The University of Nottingham

Quantification of Microstructural Damage in Asphalt

by

Rawid Khan

Department of Civil Engineering

Thesis submitted to the University of Nottingham for the degree of Doctor of Philosophy

May 2009

ABSTRACT

This research is concerned with quantifying damage in asphalt mixtures at the micro level. X ray Computer Tomography (CT) a non destructive technique along with image analysis has been used to study the internal microstructural properties of asphalt.

During laboratory testing of asphalt mixtures, it has been observed that specimens lose strength without any visible cracks. UK asphalt mixtures have been tested in uniaxial compression and tension compression fatigue tests and scanned in X ray CT. In the uniaxial compression test, specimens have been tested at three different strain rates. Both monotonic and cyclic tests have been conducted at three different temperatures. Testing has been carried out both continuously and with rest periods at selected stages. The specimens were scanned in X ray before starting the tests and also during the testing at on selected stages until failure. X ray machine operation was optimized to achieve good quality of images of different types of asphalt samples. The 2D images of the specimens were collected from the X ray CT and were stacked to regenerate into 3D images of the asphalt samples. Techniques for adjusting the threshold grey values of the images and analysing the X ray images for different parameters have been developed. The images have been analysed to evaluate the microstructure of the asphalt specimens internally and non destructively. Air voids content is considered as the parameter that represents the change in microdamage during the application of loading cycles.

Moisture damage in asphalt mixtures was studied from X ray CT. Two types of mixture were investigated, one with acid aggregate and one with basic aggregate, with three different ranges of void content. Dry specimens and specimens saturated in the laboratory were scanned in X ray CT to study the internal connected air voids which cause the permeability to moisture in an asphalt mixture and result in moisture damage. Damage due to combined moisture and ageing was studied from X ray images.

From the analysis of X ray images, it was observed that a non uniform increase in air voids occurred both along the height and across the diameter of the specimens tested in monotonic compression and tension compression fatigue. This may perhaps be due

to the heterogeneous nature of asphalt. New voids developed along with a size increase and joining together of existing voids. Using continuum damage mechanics, the data from both the mechanical testing and from X ray computer tomography was compared. For specimens tested in fatigue, damage parameters were determined for a damage model. The dissipated pseudo strain energy approach was applied to the test data and the parameters for the damage model were determined. A modified model with a new parameter of adhesion between binder and aggregate was used for data analysis. Results from X ray computer tomography and from the fatigue damage model were compared.

In the case of specimens tested for moisture damage and ageing, the retained saturation was determined from X ray image analysis and was related to the stiffness of asphalt mixtures. Asphalt mixtures containing basic aggregate were found to have a high retained stiffness value after moisture and ageing tests compare to mixtures containing acidic aggregate. The stiffness values for the retained saturation were determined and it is observed that in the case of mixtures containing acidic aggregate, the retained stiffness decrease with the increase in retained saturation.

Acknowledgement

I would like to express my sincere gratitude to Professor Andrew Collop, who selected this research topic and acted as my supervisor. I gratefully appreciate what I have learnt working under his guidance far exceeds the research that is documented in this thesis. He provided me with invaluable advice, encouragement and interest throughout the project. I am greatly in his debt for reading my thesis and offering advice for corrections despite his heavy work load.

I am grateful to Professor Gordon Airey, Professor S.F. Brown and Dr N.H. Thom for extending their help during the course of this project and their fruitful technical discussions. I would like to say thanks to Dr James Grenfell for his valuable discussions on the experimental work and the provision of invaluable technical support.

I would also like thank to Professor Dallas Little, Dr Amit Bhasin and Emad Kaseem of Texas Transportation Institute for their cooperation and discussions during my stay as visiting scholar at Texas A&M University.

Thanks to Christopher Fox, who detected and solved problems during the course of this research and to all technicians of NTEC (Nottingham Transportation Engineering Centre), specifically Mick Winfield and Richard Blakemore for making countless samples for my work. I appreciate the support and company of my colleagues Junwei, Naveed, Muslich, Nono, Jiantao, Riccardo, Izzey, Said, Lelio, Muhammad, Hung, Pic and all the other researchers in NTEC.

Finally, my gratitude goes to my family for their patience and encouragement and also to Nadia Khan for her sacrifice during my studies.

DECLARATION

The research described in this thesis was conducted at the University of Nottingham, Department of Civil Engineering, between October 2005 and September 2008. I declare that the work is my own and has not been submitted for a degree of another university.

Rawid Khan,

Nottingham,

May, 2009.

TABLE OF CONTENTS

List of tables

List of Figures

Chapter 1

INTRODUCTION

1.1 Introduction

The principal function of a road pavement is to spread the traffic loads and protect the relatively weak subgrade from overstressing and premature failure. In a flexible pavement this function is mostly carried out by main structural component, the asphalt layer.

Asphalt is one of the major materials in a road pavement, whose annual new construction and rehabilitation costs reach into billions of pounds. It is a complex heterogeneous material consisting of bitumen, mineral aggregate and air voids. Its function, together with the sub base, is to distribute and spread the traffic load and thereby protect the subgrade from over stressing and premature failure under the traffic load. The load carrying behavior of this material is strongly related to the local load transfer between aggregate particles and this is taken as the microstructural response. The performance of asphalt is governed by many internal variables like the gradation of aggregate, binder content and void content.

Due to the application of repeated loading, asphalt stiffness can reduce considerably without any visible cracking. This is due to microstructure damage initiated at the micro-scale and ultimately develops into macro cracking and failure of asphalt. Researchers have explored the damage in asphalt pavements to some extent. However, accurate prediction of pavement performance is still difficult due to complex material behaviour. There is an urgent need to characterize experimentally the evolution of microstructural damage in order to understand the actual damage mechanism. Recent improvements in computer and imaging technology have now made this possible.

X-Ray Computed Tomography (CT) and Image Analysis Techniques (IAT) are fast becoming the key tools in accurately and nondestructively characterizing the microstructure of many engineering materials. It has the capacity to obtain the three-dimensional (3D) material structure that will help in exploring the characteristics of aggregates and asphalt mixtures.

1.2 Background to the problem

Unlike other civil engineering materials, damage in asphalt does not become visible suddenly. Instead, asphalt gradually deteriorates in serviceability and ultimately fails. The two main structural failure mechanisms for asphalt pavements are fatigue damage (cracking) and permanent deformation (rutting). The three key material parameters of relevance to the analytical design or evaluation of a flexible bituminous pavement are 1) stiffness modulus of the materials, 2) deformation characteristics and 3) fatigue performance (Dunhill et al. 2006).

Asphalt is a multi-phase material comprising bitumen, graded aggregates and air. Under repeated (fatigue) loading in the laboratory it is typically observed that the stiffness of the sample can reduce significantly without any sign of visible damage. This indicates that internal damage is developing at the microscale, which ultimately develops into macrocracking leading to eventual failure.

Microstructural damage is the mechanism which initiates failure in Asphalt. It results in significant degradation of the load-carrying capacity of asphalt due to discontinuities that develop at point of high stress and/or at weak regions along the binder-aggregate bond and/or within the binder. Damage is believed to begin with the nucleation of microcracks that later propagate, grow, and combine together to form macrocracks as the material is subjected to further loading (Kim et al. 1997). The growth and interlinking of cracks in the microstructure influences the stress-strain response, and eventually leads to failure (Khaleel et al. 2001).

Researchers have addressed the importance of asphalt damage and its evolution in asphalt pavement studies (Kim et al. 1997, Lee et al. 2000). They have reported that degradation in most loading ranges normally begins with nucleation followed by localization and

eventually propagation of cracks. Little et al. (1999) emphasized the importance of microcrack growth and healing on damage and performance of asphalt. Park et al. (1996) stated that asphalt experiences a significant level of microcracking under service loading, which is assumed to be a considerable source of the nonlinear behavior. In addition, they stated that any mathematical model that describes the constitutive behavior of asphalt should account for the effect of damage growth. It is noted that the majority of the previous studies on asphalt damage are limited to specific testing procedures with only few test conditions. It is necessary to investigate asphalt behaviour at micro-level in mechanical testing such as the uniaxial compression and fatigue test. Damage characterization is necessary at different load stages to quantify the development of microstructural damage within the asphalt mix. Recently X-ray Computer Tomography techniques have been developed that can investigate the damage at the micro level. Simulation in damage mechanics can be applied to correlate this microstructure damage with the asphalt pavement performance.

1.3 Objectives

This research aims to investigate asphalt damage at the micro-level. X-ray CT, a nondestructive technique for visualizing features in the interior of solid objects, will be used to obtain digital information on the microstructure of asphalt specimens. This tool can be used to characterize the damage in asphalt mixtures and monitor the progression of damage.

Specific objectives are

1) Develop an improved technique for obtaining a 3D image of asphalt microstructure

2) Investigate the nucleation and progression of damage using X ray tomography, at different loading stages and

3) Quantify the micro level damage, and relate it to changes in macrostructural properties such as stiffness of asphalt.

1.4 Work plan

The work plan consisted of X ray computed tomography (CT) trials for different (size, material) asphalt specimens to get clear images and develop a 3D image from 2D slices (images).This also involved working on different image analysis techniques for getting reasonable information about the microstructure of asphalt mixtures.

Testing of UK asphalt specimens in a monotonic compression test at three temperatures (5°C, 23°C, 40°C) using three strain rates ($0.1sec^{-1}$, $0.01sec^{-1}$, $0.001sec^{-1}$). Stopping testing at several stages, and X ray CT scanning to catch the internal changes due to mechanical loading.

Constant stress tension compression fatigue testing of asphalt mixtures at three different temperatures, similar to the monotonic tests. Stopping the test after certain number of load cycles and X ray scanning, then restart of testing for a further selected number of load cycles. Keeping the procedure continue until failure of the sample. Determining the microdamage parameters from fatigue testing and X ray CT.

X ray CT of moisture saturated asphalt specimens, one with granite and other limestone aggregate, prepared with three different design void contents. Scanning the samples dry (before saturation) and after saturation within water. Testing these samples in the SATS (saturation ageing tensile stiffness) test and rescanning to study the internal microdamage due to moisture. Comparing data from mechanical testing and from X ray CT and relating to the stiffness of asphalt mixtures. The layout of thesis is shown in Figure 1.1 and Figure 1.2.

1.5 Research description

Chapter 2 describes definitions and details of different parameters relevant to this work. Introduction to X ray computed Tomography (CT), its principle of working, application to damage in material, specifically in asphalt mixtures, is given. Literature is reviewed on application of X ray CT, using X ray CT for materials and applying X ray CT for damage in asphalt mixtures consistently. Previous work on using X ray in different mechanical (uniaxial monotonic and cyclic) testing of asphalt mixtures is included. Different modeling approaches are also mentioned. Experiments on application of X ray CT in moisture study of asphalt are included at the end.

Chapter 3 explains specifically about setting parameters of the X ray CT and development of a procedure and different options for getting good quality images. The techniques are mentioned to improve the quality of X ray scanning specifically for asphalt mixtures. Image analysis techniques are described for converting 2D images (slices) into a 3D image of the original sample. Slice interval on the original samples and its effect on precision of data is illustrated.

Chapter 4 contains experimental testing program of X ray use for monotonic compression tests of asphalt mixtures. Testing protocol, design of asphalt mixture, sample preparation, testing of specimens and X ray scanning at selected stages are described. The testing and scanning procedure for different strain rates at different temperature conditions is given. Results from mechanical testing and from X ray CT are described. A relation has been described between stiffness and microdamage values for asphalt mixtures.

Chapter 5 gives details of microdamage due to fatigue testing. Development of specimens for tension compression fatigue test and the procedure for testing and X ray scanning of samples in the middle of a test is described. It contains test details for constant stress fatigue testing at different temperatures. This chapter describes the test detail of stopping cyclic loading at several selected stages and X ray scanning of specimens. X ray image analysis for damage study due to increase in number of load cycles is concluded. A damage model for fatigue failure and application of different parameters in microdamage model is described.

Chapter 6 explains the application of X ray CT in moisture study of asphalt mixtures. It includes detail of samples prepared at different design void contents and with two different types of aggregate i.e. granite and limestone. The process of dry scanning and then scanning within water is included. The details of samples tested in SATS (saturation aging tensile stiffness) is explained together with the change in stiffness for both acidic and basic (granite is acidic and limestone is basic) aggregate asphalt mixtures. Details about the effect of void content and void connectivity on stiffness of asphalt mixtures are given.

Chapter 7 summarizes the major conclusions of the work and makes recommendations for the future research.

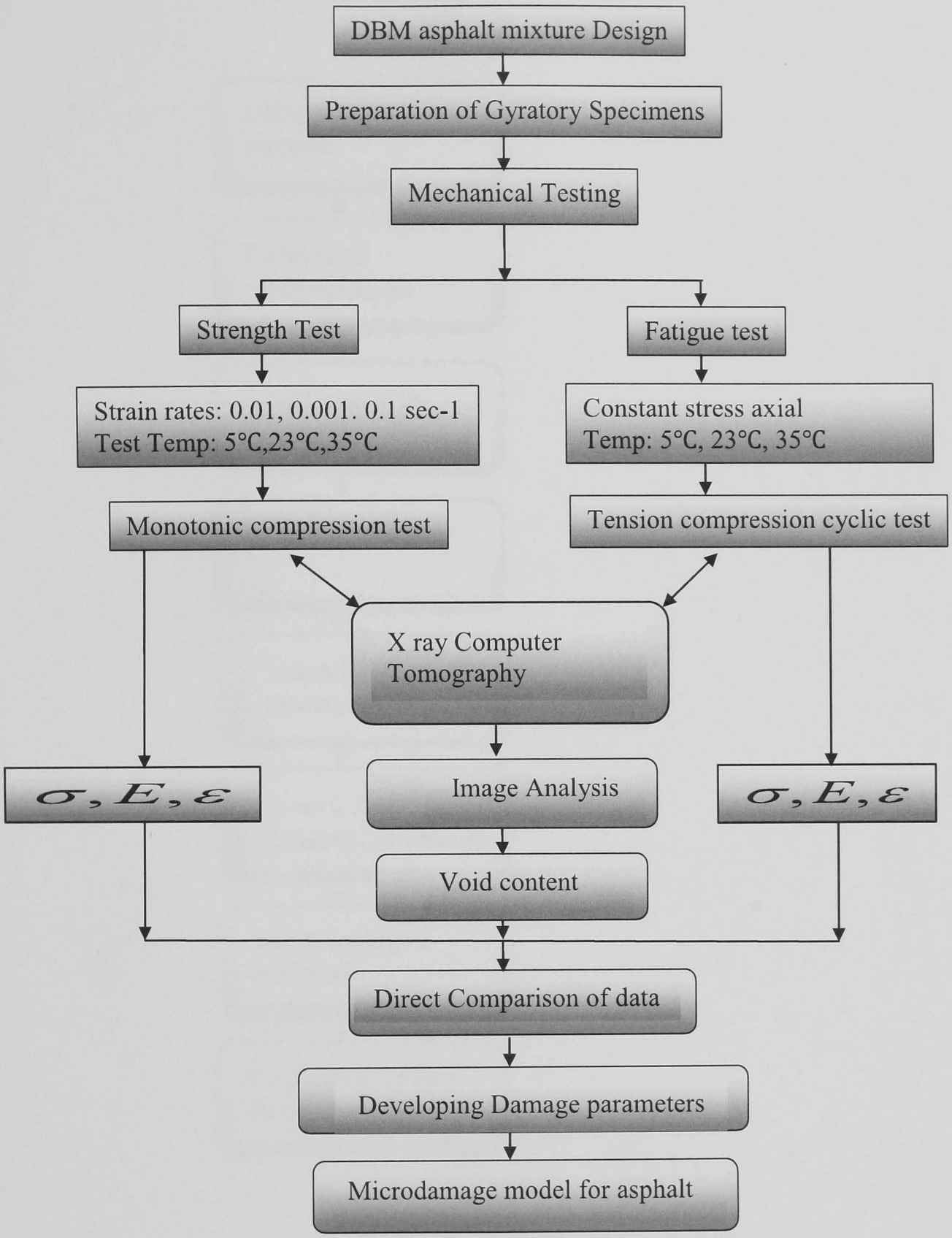

Figure 1.1 Thesis layout

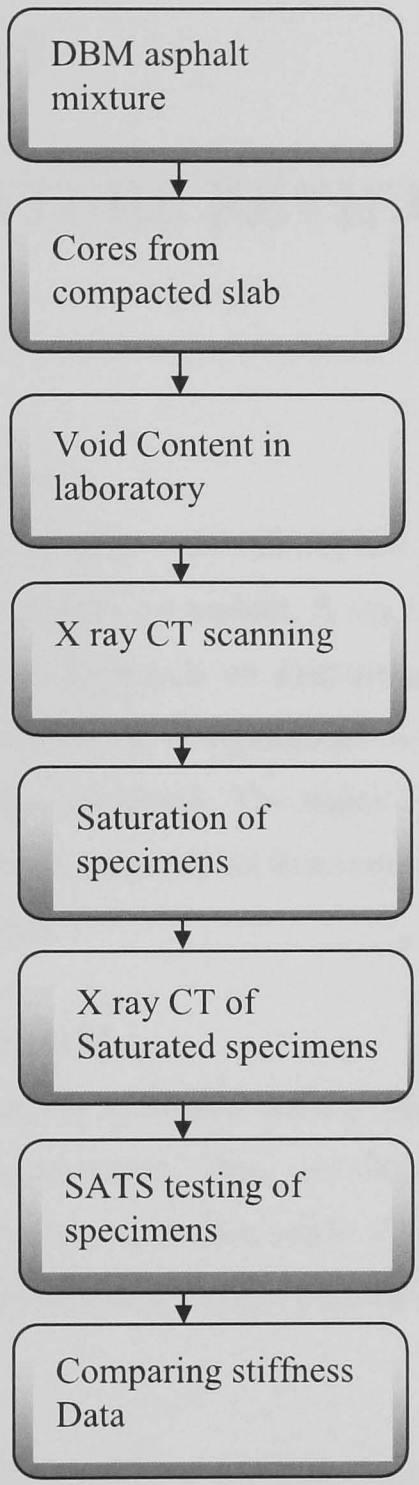

Figure 1.2 Thesis layout

Chapter 2

LITERATURE REVIEW

2.1 Introduction

In this chapter, some relevant asphalt parameters are defined first, followed by an introduction to damage in asphalt, X ray Computer Tomography techniques and specimen scanning process. Research on microstructure damage in engineering materials such as metals, concrete, soil etc is highlighted. A detailed literature review of research on damage in asphalt is then presented. The major findings of previous investigations are identified separately. A brief summary of literature on microstructural damage in asphalt is given at the end of chapter.

2.2 Road pavement

A road pavement is a durable surface which sustains traffic loading. There are two main types of road pavement. They are flexible (asphalt) and rigid (concrete) pavements. Flexible pavements are constructed of bituminous and granular materials. The main structural component of a flexible pavement is generally the bituminous layer.

2.3 Asphalt

Asphalt is a thoroughly controlled, engineered mixture made by heating bitumen and mixing it with aggregates and mineral fillers. The range of possible compositions for an asphalt mixture is infinite; however the two types of mixtures traditionally used in the greater part of UK road construction are dense bituminous macadam (DBM) and hot rolled asphalt (HRA). They are also called continuously graded and gap graded asphalt (Figure 2.1).

2.4 Asphalt stiffness

2.4.1 Bituminous binder stiffness

The stress-strain relationship for a bituminous binder is both loading time and temperature dependent, and has both elastic and viscous behaviour. The concept of Young's modulus (E), which is applied to purely elastic solid materials, and is the ratio of stress to strain, may not be applied to bitumen. As bitumen is considered as a visco-elastic material, the term stiffness modulus (or stiffness) is applied, which is the ratio of stress to strain at a particular temperature and loading time (Van der Poel, 1954). This ratio is defined as:

$$Stiffness_{(T,t)} = \frac{\sigma}{\varepsilon}$$

where T is the temperature, t is time, σ is stress and ε is strain.

The stress-strain relationship is linear for bituminous binders at low temperature and for short loading times, where bitumen behaves as an elastic solid, becoming 'glassy'. The linear relationship is also maintained at high temperatures and for long loading times, when the material behaves almost entirely as a Newtonian fluid. At moderate temperatures and/or loading times, non linear effects occur and this trend increases with increase in deformation. Van der poel also developed a nomograph which can be used to estimate the stiffness of bitumen (Van der poel, 1954).

2.4.2 Asphalt mixture stiffness

The stiffness of an asphalt mixture is an indicator of its ability to spread loads and protect the underlying layers by distributing the wheel loads and so influencing the level of stresses and hence strains within the pavement structure (Figure 2.2(a), Figure 2.2(b)). Determination of the stiffness modulus of an asphalt mixture is complex due to the heterogeneous nature of the mixture components. Generally the stiffness of asphalt may be (1) elastic, under conditions of low temperatures and/or short loading times, and is used to calculate critical strains in traditional analytical pavement design, (2) viscous, at high temperatures and/or long loading times, and is used to assess the mixture performance and (3) visco-elastic, at the intermediate temperature, stiffness has both an elastic and viscous components (Hunter, 2003).

2.5 Damage in asphalt

Generally all real materials contain voids or micro cracks. During the deformation process these internal voids / cavities may grow and cause new micro defects. This changes the macro properties of the material and its strength decreases. Such a process of structural deterioration of material which results from the creation, growth and coalescence of micro defects is called damage (Dietmar et al. 2006).

A simple way to describe damage in a material is presented here. Consider an element of cross section dA as shown in Figure 2.3. The area of the defect in this element is denoted by A_D with unit normal vector n and the amount of damage can be represented by the area fraction as

$$\omega(n) = \frac{dA_D}{dA} \quad \text{with } 0 \le \omega \le 1$$

where $\omega = 0$ corresponds to undamaged material and $\omega = 1$ describes a totally damaged material with complete loss of stress carrying capacity.

Damage may be either of microscale or macroscale. At the microscale level, damage is the accumulation of micro stresses in the neighborhood of the defects or interfaces and the breaking of bond between aggregate and bitumen. At the macroscale level, damage is the growth of micro damage into visible cracks. Microdamage may be studied through the damage variables of the mechanics of continuous media. Macrodamage is studied through fracture mechanics with variables defined at the macroscale level (Huang, 2004).

Researchers have addressed thoroughly the importance of damage and its evolution. Kim et al. (1997), Lee et al. (2000) and Collop et al. (2003) reported that performance failure in most loading ranges normally begins with nucleation followed by localization, and eventually propagation of cracks. Little et al. (1999) has highlighted the importance of microcrack growth and healing on damage and performance of asphalt.

Park et al. (1996) stated that asphalt experiences a significant level of microcracking under service loading, which is assumed to be a considerable source of nonlinear behaviour. Some researchers have considered stereology and fabric tensor as important parameters to

determine the microstructural properties of asphalt (Wang et al. 2003, Voyiadjis et al. 2007).

2.5.1 Stereology

Stereology is a collection of tools that make measurements of geometric properties of real world microstructure particles. In its typical application, information about the structure under study is available as a collection of images prepared from that structure. In stereology information about the 3D object is determined from the information on a 2D image. The geometry of features in the image may be quantified by measuring one or more geometric properties that may be defined for individual features, or for a set of features. Although most uses of stereology seek geometric information about microstructure, its application is not limited to microstructure. Stereology has been used to study the geometry of rock structures, metals, soils and other engineering materials (Russ, 1999).

2.5.2 How Stereology works

The basic principle of stereology is: "the information in a 2D image can be extended to give information about the actual shape of the sample". The general relation is presented as $P_p = V_v$, where V_v is the volume fraction occupied by an object and P_p is the area fraction in 2D. This relation may be read: "the expected value of the fraction of the population of points that exist in the volume of the structure under study that lie in the phase of interest is equal to the fraction of the volume of the structure occupied by that phase" (Russ, 1999).

2.6 X ray CT techniques

X ray Computerized Tomography (CT) is a powerful tool for the evaluation of the microstructure of materials. It was developed in 1970 by G. Hounsfield (Braz et al. 1999). Researchers in civil engineering have been using the technique in the characterization of soil-water systems, rock, cement and asphalt concrete, and reinforced concrete structures (Braz et al. 1999, Masad et al. 2002, Wang et al. 2003, Tashman, 2004, Song, 2004). Compared with other imaging methods, X ray CT has several advantages including the ability to acquire 3D data sets, no need for sample preparation, and non-destruction to suit unique requirements of sample analysis.

Basically a CT scanner consists of a light source from which an X- or gamma-ray beam is transmitted through an object and is detected, manipulated electronically, and stored in a computer (Figure 2.4). These transmitted ray beams have a varying intensity dependent on the overall linear attenuation characteristics of the material scanned. This varying intensity with respect to distance is referred to as a profile. This profile information is then manipulated to produce a reconstructed image of an object (X Tek, 2005).

The reconstructed image is then displayed on a viewing monitor for evaluation and interpretation. In a computed tomography (CT) scanner, a number of profiles of narrow-beam transmission are made at different orientations around a subject. From these measurements a 3-D image is created. When a beam of mono energetic X- or gamma- rays traverses a specimen, part of the radiation is absorbed by the specimen, part is scattered and part is transmitted (Braz et al. 1999). The study of the scattered or of the transmitted radiation allows one to deduce information on the composition of the crossed volume, particularly of the physical density. The transmission tomography is based on the study of the radiation transmitted through a specimen, and other forms of tomographic images are based on the study of the scattered radiation (Wang et al. 2004).

The data collected as the X rays attenuate while penetrating a material medium and may be used to obtain images of the medium (Figure 2.5). The contribution of the attenuation coefficient μ(x,y,z) along the X ray's path is:

$$I = I_o e^{-\int_0^l \mu(x,y,z)dl} \tag{2.1}$$

where I_o is the incident X ray intensity and I is the X ray intensity after traveling a distance l through the specimen.

Mathematical software uses reconstruction techniques such as Fourier reconstruction or an iterative method to solve Equation (2.1) and estimate the distribution of the coefficients of attenuation along the travel length l and generates slices of 2-D images. The 2-D slices may be compiled to generate 3-D images. From the image given, one can observe the location of voids, defects, or inclusions (Daigle et al. 2005).

Image pro plus software has also been used which has developed using Visual Basic. It converts the gray color image into binary images and counts the number of voids or area of aggregates (Wang et al. 2003).

2.7 Application of X ray Tomography in damage characterization

X ray Computed Tomography (CT) is a nondestructive tool for characterizing the microstructure of concrete, soil, rocks, metals and asphalt. Although some of these materials vary significantly in their microstructural composition and distribution, researchers favour this new technology due to its accurate results even for a more complex microstructure.

Perzyna (1984) found that damage in metals (brittle) grows at a small rate at the beginning of the deformation process. Thereafter, damage grows rapidly at a very high rate leading to ultimate failure. However, asphalt concrete at relatively high temperatures typically behaves as a ductile material. It is, therefore, expected that damage does not evolve in such an exponential pattern, as is the case in brittle metals.He modified his simple model of an elastic-viscoplastic solid with internal damage due to the nucleation, growth and diffusion of voids and introduced additional information about the final stage of the necking process. He stated that the rate of damage is a function of the rate of viscoplastic energy, confinement pressure, and effective viscoplastic strain:

$$\xi = f(W_{vp}, I_{I,} \bar{\varepsilon}_{vp}) \tag{2.2}$$

where W_{vp} is the rate of viscoplastic energy, I_I is the rate of change in the first stress invariant, and $\bar{\varepsilon}_{vp}$ is the effective viscoplastic strain rate.

Mummery et al. (1993) used X ray microtomography to characterize the damage occurring on plastic straining silicon carbide particle-reinforced aluminum alloys. Their characterization was based on density measurements as a function of strain in addition to imaging of the internal structure. Imaging allowed for a more accurate determination of microstructural damage in terms of air void growth.

Shi et al. (1999) used X ray CT to monitor the evolution of internal failure in different soils, particularly the formation of shear bands. CT images were then taken on different cross-sections inside the specimens at different loading stages to monitor soil deformation continuously. They showed that X ray CT is a powerful non-destructive tool for studying the deformation patterns and capturing the formation of cracks and shear bands in soils.

Landis and Keane (1999) used X ray computed microtomography to measure internal damage and crack growth in small cement mortar cylinders loaded in uniaxial compression. In their experiment, small mortar cylinders were inserted into a small loading frame that could be mounted directly on the X ray rotation table. This was done in order to scan the specimens at varying strain values so that internal damage could be quantified and correlated with load deformation information. Aluminum was chosen for the loading frame because of its relatively low X ray absorption leading to better X ray absorption resolution in the specimens. Multiple tomographic scans were made of the same specimen at different levels of deformation applied through a purpose-built loading frame, and image analysis of the scanned images was used to measure the internal crack growth during each deformation increment.

Landis and Keane further showed that under monotonic loading of concrete, deformation was elastic for loads up to 30% of the peak load. Beyond this point, cracks occurred at the cement-aggregate interface. At about 70% of the peak load, these distributed cracks concentrated at certain points, and matrix cracking occurred macroscopically and became large-scale axial splitting. Post-peak response was studied by additional matrix cracking and frictional mechanisms. However, post-peak behaviour was found to be highly dependent on the testing set up and specimen geometry.

Maire et al. (2001) carried out 3D Computer Tomography of light metal. They detected cracks up to 0.5μm opening, which was below their voxel (volume element) size. In their experiment, a first scan was performed without any applied load, in order to characterize the initial non deformed state. Thereafter, the load was applied and another scan was performed while the crosshead position was maintained constant. Five scans with increasing strain levels were performed on the same sample. Their analysis gave valuable

information about the internal structure and its evolution during the deformation of the samples studied.

Sinclair et al. (2004) have identified fatigue crack closure as an important factor in determining crack growth rates. They carried out synchrotron radiation X ray micro tomography at a high resolution of 0.7 μm to provide unique three-dimensional in situ observation of steady state plane strain fatigue crack growth in an aluminum alloy. Using such high resolution imaging, the details of fatigue cracks are readily observed, along with the occurrence of closure. A novel microstructural crack displacement gauging method was used to quantify the mixed mode character of crack opening displacement and the closure effect. They used a liquid gallium grain boundary wetting technique in conjunction with the microtomography to study the correlation between the three-dimensional structure of the grains and the fatigue crack behaviour.

Voyiadjis et al. (2007) developed a procedure for quantifying the microcracks and damage in a metal matrix composite material. They tested some samples in tension up to different load levels to understand how a microcrack develops with applied load. Images of each load case were captured. Fabric tensors of zero, second, fourth, sixth, eighth, and tenth order were used to approximate these damages. They used the fabric tensor approach and continuum damage mechanics by selecting the orientation of each micro crack as shown in Figure 2.6. In order to determine damage, they considered a uniform bar subjected to a uniaxial tensile load T as shown in Figure 2.7. The cross sectional area is A and it was assumed that the cracks and voids that appeared as damage were denoted by A^d, the uniaxial tensile force was expressed as $T = \sigma A$ and the undamaged effective stress was expressed as $T = \bar{\sigma}\,\bar{A}$, they derived the uniaxial stress as

$$\bar{\sigma} = \frac{\sigma}{1-\phi} \tag{2.3}$$

where $\phi = \frac{A-\bar{A}}{A} = \frac{A^d}{A}$

2.8 Microstructural damage in asphalt

The understanding of the deformation process is extremely limited without a clear understanding of the evolution of microcracking. Thus, it is necessary to directly measure and quantify damage in asphalt in order to understand and account for damage using mechanics-based concepts supported by measurements. This would allow relationships between the microstructural features which control damage behaviour to be developed. Recently, several successful attempts to study microstructure of asphalt mixtures using imaging technology and X ray CT have been made (Masad et al. 1999, Tashman et al. 2001, Wang et al. 2001 and Masad et al. 2002). X ray CT is fast becoming a powerful nondestructive tool by which to characterize the microstructure of asphalt and other engineering materials without damaging the specimens being tested. X ray CT sectional images are used to reconstruct the three-dimensional microstructure of a sample for computer simulation. Meanwhile the sample remains intact and can be used for determining other macro properties (Wang et al. 2004).

Kim et al. (1997)

Kim et al. (1997) used a constitutive damage approach for studying damage in asphalt concrete mixtures. They searched out different failures such as adhesive failure at the binder- aggregate interface and cohesive failure within the

binder. They used continuum damage theory to detect the damage during cyclic loading and healing during rest periods. Their continuum damage model consisted of a pseudo strain energy density function (Equation 2.4), a stress-strain relationship and a Damage evolution law (Equation 2.5). (2.4)

$$W^R = W^R\left(\varepsilon^R, S_m\right)$$

where W^R is the pseudo strain energy, ε^R is the pseudo strain, S_m is the internal state variables (or damage parameters).

$$\sigma = \frac{\partial W^R}{\partial \varepsilon^R}$$

$$\dot{S}_m = \left(-\frac{\partial W^R}{\partial S_m} \right)^{\alpha_m} \tag{2.5}$$

where $\dot{S}_m$ is the damage evolution rate and α_m is a material constant.

The value of pseudo strain ε^R was calculated from pseudo strain energy. The dissipated pseudo strain energy is the energy that has been lost in loading and unloading the material minus the energy that has been lost in overcoming the viscous resistance of the material, means it is the energy that is available to damage the material. This model predicts the damage growth and healing in asphalt under monotonic loading with varying strains for both controlled-stress and controlled-strain modes of loading.

Masad et al (1999)

Masad et al. (1999) presented images captured from sections of the HMA specimens using a digital camera connected to a computer. The image resolution was 0.3 mm/pixel, and it consisted of a wide range of gray levels ranging from 0 to 255 (numerical values where integer 0 indicates complete blackness and 255 shows a white image). The gray scale image was threshold in order to highlight the different phases in the microstructure. Further image processing was applied to separate any aggregates that might appear in contact within the image. This step was necessary as aggregates in contact are treated as one larger aggregate by subsequent imaging and mechanistic analysis. The resulting black and white image was converted into a binary file consisting of '0' (i.e. black) and '255' (i.e. white) light intensities and the x, y coordinates of each pixel on an image. The white color represented aggregates greater than 0.3mm, while black represented the phase combining the asphalt binder and fine aggregates smaller than 0.3mm, which is referred to as mastic. The data was used as input in a finite element model developed in ABAQUS (1998). Each pixel on the image was transferred to an element in the model of the microstructure. It was found that shear strains within the mastic elements were 30 to 32 times the applied strain. In order to capture inside images, the asphalt specimens were cut into different sections (Figure 2.8).

Kose et al (2000)

Kose et al. (2000) utilized imaging technology and finite element analysis to analyze the strain distribution within asphalt mixes. The study used elastic properties for the binder and

the aggregate and showed that plane stress and plane strain analyses had comparable strain results. The air voids, the loading mode, and the boundary conditions were not shown to be significant in influencing the relationship between the binder strain and the mixture strain using linear elastic analysis. They also demonstrated that the strain within the binder phase could be up to 250 times more than that suggested by the macroscopic strain of the composite.

Lytton et al (2000)

Lytton et al. (2000) defined undamaged materials behaving linear viscoelastically under loading and unloading if the hysteresis does not change with repeated loading. They concluded that accumulated damage will occur when a material is subjected to repeated loading. After the material becomes damaged to the point where it cannot carry any more loads it will fail. They concluded that damage is an important component in distresses. Thus, finding out the way to characterize asphalt mixture distress in terms of relationships of damage parameters is necessary.

Masad et al. (2001)

Masad et al. (2001) used image correlation techniques to experimentally estimate the strain distribution in asphalt. The technique works by capturing images of the asphalt mixture microstructure during deformation and calculating the strain magnitudes by comparing the coordinates of points before and after deformation. The results confirmed the findings of the finite element analysis. They found that the mastic (fine aggregate particles + binder) strain was about 3-4 times the average mix strain.

Wang et al. (2001, 2003)

Wang et al. (2001, 2003) used X ray Tomography in microstructure study of Wes Track (FWHA-USA) to verify the newly developed superpave mix design procedures. The void contents of three different mixes were evaluated using X ray tomography images and stereology methods. The spatial void content variation and void size distribution for the three mixes were studied. Void surfaces were considered as damaged surfaces because they do not transmit forces. The damage tensor, mean solid path among the damaged surfaces and mean solid path tensor, which indicate damage level, were also investigated. They concluded that quantified tensors are applicable in continuum damage mechanics for

fatigue and rutting modeling. They find out the damage tensor and mean solid path tensor can be expressed as

$$S(n) = \frac{S_v}{4 * \pi}(1 + S_{ij} n_i n_j) \tag{2.6}$$

$$\lambda(n) = \lambda(1 + \lambda_{ij} n_i n_j) \tag{2.7}$$

where $S(n)$ and $\lambda(n)$ are the distribution density functions of the damage surface area and the mean solid path, respectively, n is the unit normal to unit sphere, n_i and n_j are the directional cosines, S_v and λ are the specific damaged surface (damaged surface area per unit volume) and the average distance between damage surfaces, respectively. S_{ij} and λ_{ij} are the second order damage tensor and the mean solid path tensor respectively (Figure 2.9).

Masad et al. (2002)

Masad et al. (2002) used X ray CT along with IAT (Image Analysis Technique) to characterize the statistical distribution of air void sizes at different depths in asphalt specimens. They found that air voids can be used to quantify the effect of compaction effort, method of compaction, and aggregate size distribution on air voids. They also found that the air void size distribution in Superpave gyratory compacted specimens exhibited a "bath-tub" shape where higher air voids were present at the top and bottom parts of a specimen. This shape was more pronounced at higher compaction efforts. Specimens prepared with different aggregate sizes were found to have noticeably different air void sizes. Specifically, larger air voids were present in specimens that consisted of smaller aggregate particles.

(Tashman et al 2002)

In a study by Tashman et al. (2002) X ray CT along with image analysis techniques were shown to provide a non- destructive and accurate tool to analyze the air void distribution in asphalt mixes. Air voids were found to be non-uniformly distributed along the horizontal and vertical directions in Superpave gyratory compacted specimens. More air voids were present in the outer region and in the top and bottom regions of a specimen. This

phenomenon was strongly noticed at high compaction efforts, where 80% of air voids were concentrated in the top and bottom regions of a specimen and 85% in the outer region. The vertical difference in percent air voids was between 2.0 and 3.5%, and the horizontal difference was between 2.0 and 5.0% depending on the compaction effort. The aggregate gradations used in this study had little effect on the vertical and horizontal distributions of air voids. The Superpave gyratory compaction seemed to create uniform distribution of air voids in a specimen core (Middle–Inner region). In order to get more precise values, Tashman et al. divided the image into inner and outer regions (Figure 2.10). They also investigated field cores and concluded that in the case of field cores, air voids were uniformly distributed in the horizontal direction and non-uniformly distributed in the vertical direction. Most air voids were present in the top region. Furthermore, air voids were less uniform in the middle region of field cores compared with that in gyratory specimens.

Papagiannakis et al. (2002)

Papagiannakis et al. (2002) presented a consistent procedure to process an asphalt mix image for modeling purposes. FEM (Finite Element Method) was used to simulate measurements by the Superpave shear tester (SST). A non-linear viscoelastic model was used to model the mastics, and a linear elastic model was used to model the aggregate. The effect of the bitumen film thickness on the apparent mastic stiffness was studied, and data was presented showing the effect of image processing on the predicted macro-mechanical behaviour using this numerical technique. In order to obtain reasonable predictions, the binder stiffness was multiplied by a factor of 30. This was rationalized based on the combined effect of the presence of fines in the binder and the thickness of the binder film in the image analyzed

Nelson et al. (2003)

Nelson et al. calibrated an irrecoverable microstructural damage model for asphalt. A constant rate of strain test to failure was used to calibrate the damage behaviour. They developed viscoelastic, viscoplastic, and damage modeling of asphalt concrete in unconfined compression. In this study the model parameters were obtained from three different mechanical testing on unmodified asphalt. A superpave mix was selected in the study. The three types of laboratory tests were 1) small strain dynamic modulus test, 2) cyclic creep

and recovery test to failure and, 3) constant rate of strain test to failure. They worked out that the total strain is the sum of viscoelastic and viscoplastic strain (ε_{vp} *and* ε_{ve}).

$$\varepsilon_{total} = \varepsilon_{vp} + \varepsilon_{ve} \tag{2.8}$$

where $\varepsilon_{vp} = \left(\frac{P+1}{A}\right)^{\frac{1}{P+1}} \left(B\sigma^{q}\right)^{\frac{1}{p+1}} . t^{\frac{1}{p+1}}$ or

$$\varepsilon_{vp} = \left(\frac{P+1}{Y}\right)^{\frac{1}{P+1}} \left[\int_{0}^{1} [\sigma(t)]^{q} dt\right]^{\frac{1}{p+1}}$$

and $\varepsilon_{ve} = E_R \int_{0}^{tR} D(t_R - \tau_R) \frac{\partial\left[\frac{\partial}{C(S)}\right]}{\partial \tau_R} d\tau_R$

A, P, q are material constants, $Y = A/B$

where σ is physical stress, E_R is an arbitrary reference modulus that is constant, t_R is reduced time, τ_R is retardation time, and $C(S)$ is a damage function defined in terms of an internal state variable S.

This damage model was developed on the basis of mechanical testing. Nelson et al. recommended that further study on images of microstructure damage was necessary to find out the precise parameters for a reliable damage model.

Tashman (2003)

Tashman (2003) investigated the viscoplastic behaviour of asphalt mixtures and proposed an empirical power law for damage evolution:

$$\xi = \xi(W_{vp}, I_I, \varepsilon_{vp}) = \xi_o + Hc(W_{vp})^{H_p} + Lc(I_I)^{L_p} + Ec(\varepsilon_{vp})^{E_p} \tag{2.9}$$

where ξ_o is the initial damage value, W_{vp} is the viscoplastic energy, I_1 is the first invariant of the stress tensor, ε_{vp} is the effective viscoplastic strain, and H_c, H_p, L_c, L_p, E_c, E_p are fitting coefficients.

Tashman investigated the asphalt microstructure with X ray CT in a triaxial strength test at room temperature. In his experimental work, two-dimensional images (slices) of the microstructure of the asphalt specimens were captured at every 1mm across the height of a specimen with a slice thickness of 1mm. The resolution of the X ray CT images was 0.191mm/pixel in the undeformed specimens and 0.234mm/pixel in the deformed ones. He conducted a triaxial compression test at a constant displacement rate of 2.5mm/min. Each two replicates were loaded to a specified strain level under a constant confining pressure. The confining pressures were 0psi, 15psi, and 30psi and the strain levels were 1%, 2%, 4%, and 8%. The void content of the specimens was measured after they were deformed. All tests were conducted at a single temperature (130°F). The digital images were analyzed using IAT (image analysis technique) to characterize different aspects of the void properties including the void content, size (void area), aspect ratio, eccentricity, roundness, and length of voids in each slice, where

$$Void\ Content = \frac{\sum_{M} V}{A}, \qquad Aspect\ Ratio = \frac{Major\ Axis}{Minor\ Axis},$$

and $Eccentricity = \sqrt{x^2 + y^2}$

where V is the area of void in an image (slice), M is the total number of voids in a slice, A is the slice cross sectional area, x is the horizontal distance of a void's centroid from the center of the slice (specimen's core), y is the vertical distance of a void's centroid from the center of the slice, and p is the perimeter of a void in the slice.

Song (2004)

Song (2004) concluded that the physical meaning of the damage can be considered as the crack length and/or dissipated energy due to crack development with increasing number of loading cycles. He defined damage based on the amount of voids and stiffness changes. In his work, the two main approaches used to study damage in asphalt concrete mixtures were

1) - the void area approach and 2) - constitutive damage approach. The void area approach is based on the area of void and crack in the mixture and the constitutive damage approach is a microscale level study of damage. He included two damage parameters which were introduced by Perzyna (1984) and Kim et al. (1997). Cyclic creep test data and dynamic mechanical analysis test (the test in which shear stress is applied to a 12 mm diameters sample) data were used in this study.

Following the procedure proposed by Tashman et al. (2002) and Lee et al. (2000a), Song determined two damage parameters ξ and S for asphalt concrete mixtures. Damage parameter ξ is the ratio of area of crack and voids to the total cross sectional area S:

$$\xi = \frac{Av}{S} \qquad \text{where} \quad S = Av(\text{area of voids}) + As(\text{area of solid})$$

Damage parameter ξ was developed from the Perzyna (1984) model of an elasto-visco-elastic solid with internal imperfections due to the nucleation, growth and diffusion of voids:

$$\xi = (\xi)_{nucleation} + (\xi)_{growth} + (\xi)_{transport} \tag{2.10}$$

$$(\xi)_{nucleation} = \frac{h}{1-\xi} tr(\sigma D^p) + lJ_1 , \qquad (\xi)_{growth} = (1-\xi) tr(\Xi D^p),$$

and $\xi_{transport} = D_0 \nabla^2 \xi(x,t)$

where h, l are the nucleation material function, J_1 is the first invariant of the Cauchy stress tensor, D^p is rate of permanent deformation tensor, Ξ is the matrix of the materials function, D_0 is diffusion constant for the constant temperature, and ∇^2 is Laplasian operator.

Song (2004) noted that the damage parameter S can be defined from the evolution law and the pseudo strain energy density function. Combining the two equations by using the chain rule yields another equation as follows:

$$\frac{dC}{dS} = \frac{dC}{dt}\frac{dt}{dS} \tag{2.11}$$

$$\frac{dS}{dt} = \left[-\frac{1}{2}\frac{dC}{dS}(\varepsilon_m^R)^2\right]^{\alpha} \tag{2.12}$$

Substituting Eq. 2.11 into Eq. 2.12, we have

$$\frac{dS}{dt} = \left[-\frac{1}{2}\frac{dC}{dt}(\varepsilon_m^R)^2\right]^{\alpha/(1+\alpha)}$$

Finally, the equation is rearranged by means of integrating.

$$S \cong \sum_{i=1}^{N}\left[\frac{1}{2}(\varepsilon_{m,i}^R)^2(C_{i-1}-C_i)\right]^{\alpha/(1+\alpha)}(t_i - t_{i-1})^{1/(1+\alpha)}$$

Substituting γ_m^R for ε_m^R in their torsional controlled–strain mode fatigue test, then

$$S \cong \sum_{i=1}^{N}\left[\frac{1}{2}(\gamma_{m,i}^R)^2(C_{i-1}-C_i)\right]^{\alpha/(1+\alpha)}(t_i - t_{i-1})^{1/(1+\alpha)} \tag{2.13}$$

where S is the damage parameter at each discrete cycle, $\gamma_{m,i}^R$ is the peak pseudo strain, C_i is the pseudo stiffness, t_i is the corresponding time, N is the number of loading repetitions, α is the material constant.

Microstructure damage was investigated only in the Dynamic Mechanical Analyzer (DMA) for a sand mix and in the cyclic creep test for asphalt mixes. Asphalt specimens were scanned at four test stages.

Wang et al. (2004)

Wang et al. (2004) investigated the microstructure of granular materials with X ray CT. They confirmed that X ray computer tomography, with high penetration capability and relatively high resolution, is a workable tool for imaging the true 3D microstructure of granular materials nondestructively. Quantitative studies of particle kinematics to obtain

particle motions i.e., particle translations and rotations are more complex than characterization studies. In general, the reconstruction of true 3D structure that includes detailed representation of the individual particles is essential for applications, such as the quantification of fabric, local void ratio, contact normal distribution, branch vector distribution, particle kinematics, and numerical behaviour modeling in a 3D form. They presented methods to represent the microstructure of granular materials using X ray tomography imaging. The representation is vectorial and each of the individual particles is represented. The motions of individual particles including particle translation and rotation can be easily presented. This approach was applied to the reconstruction of specimens consisting of sandstone aggregate particles in the range of 4.75 mm to 9.50 mm sieve size (Fig. 2.11).

(Tashman et al. 2005, Tashman et al. 2007)

Tashman et al. (2005, 2007) developed an asphalt model for permanent deformation at high temperatures. They linked the microstructure properties with continuum damage mechanics. The microstructure parameters were included in the model in order to determine the effect of anisotropy distribution of aggregates and damage in terms of voids. They used image analysis techniques to investigate the aggregate distribution on cut sections of asphalt and determine the vector magnitude. An effective stress theory based damage parameter was included to study the effect of voids and cracks.

2.8.1 Dissipated pseudo strain energy for damage in asphalt

There have been several attempts to develop a viscoelastic model for asphalt mixtures using constant strain and constant stress monotonic tests. Constant strain tensile tests were conducted for asphalt mixtures (Lee et al. 1998). The data was analyzed applying Schapery's elastic viscoelastic principle. This was done to evaluate the time dependent damage growth in the asphalt mixtures. Using a linear viscoelastic constitutive equation they calculated the linear viscoelastic stress as

$$\sigma(t) = \int_0^t E(t-\tau)\frac{d\varepsilon(\tau)}{d\tau}d\tau \qquad (2.15)$$

where σ(t) is time the dependent viscoelastic stress, $E(t-\tau)$ is the relaxation modulus at time t-τ under the undamaged condition, t is the present time and τ is the time history at which strains were measured. ε(τ) is the measured strain at the previous time τ.

The pseudo strain for the nonlinear viscoelastic asphalt can be calculated if the linear viscoelastic stress is divided by nonlinear reference modulus E_R. The value of E_R was taken as the ratio of the maximum applied stress during the first load cycle to the strain recorded during first cycle.They identify that the model for a controlled stress test is different from the controlled strain case due to the increase in strain the stress strain loop displaces from its original position. The equation for strain in constant stress tests was described as consisting of two portions (Lee et.al 1998).

$$\varepsilon_1(t) = B_0 + B_1 t^{\alpha} + \sum_{i=2}^{i} B_i t^i \tag{2.16}$$

$$\varepsilon_2(t) = \varepsilon_0(t)\sin(\omega t + \theta) \tag{2.17}$$

here t is the time that has elapsed from first application of loading, $\varepsilon_2(t)$is the amplitude of the sinusoidal function which is a function of time, ω is the angular velocity, B_0, B_1, B_2, α and θ are constants.

The pseudo strain was calculated by adding these two components. The stress strain loops are shifting toward the right. Also there is reduction in dissipated energy calculated from the area inside the stress strain curve. The stress-pseudo strain behaviour is linear as shown in Lee et al. (1998). The shift in the pseudo strain is denoted by ε_S^R. The first term B_0 and the last term $\sum_{i=2}^{i} B_i t^i$ in the equation 2.16 have little effect on the average strain in each cycle. So the $\varepsilon_1(t)$ is simplified as $\varepsilon_1(t) = B_1 t^{\alpha}$. Also in equation 2.17 constant strain amplitude ε_0 is assumed instead of $\varepsilon_0(t)$for simplifying the analysis. Using the derivative of these strain functions and the relaxation modulus in the form of pure a power law i.e. $E(t) = E_1 t^{-m}$ the pseudo strain can be obtained as

$$\varepsilon^R(t) = P_0 t^{(\alpha-m)} + P_1 \sin(\omega t + \phi) \tag{2.18}$$

where P_0 and P_1 are constants depending on B_1, E_1, m, α, ε_0 and ω. The Paris law has been modified for determining the microdamage and healing characteristic of asphalt mixtures (Si et al. 2002). Paris law is expressed as $(dc/dN) = AK^n$, where c is the crack length, N is the number of applied load cycles, K is the stress intensity factor, A and n are the material constants (Tada et al. 2000). The equation was developed to calculate the number of cycles at a certain crack radius (Si et al. 2002).

$$N_i = \frac{\frac{n+1}{2n+1} c_i^{2n+1/n+1}}{A^{1/n+1}\left(\frac{b}{4\pi}\right)^{n/n+1}} \tag{2.19}$$

where N_i is the critical number of load cycles at c_i which is the critical mean radius of the circular shape and is assumed. A , n and b are the Paris law parameters.

A constant strain tensile test was conducted to study the moisture damage of asphalt concrete (Arambula et al. 2007). X ray images were taken before testing and after testing in a tension test. They studied the permeability and moisture damage of asphalt mixtures.

A unified method approach was applied to model the failure in controlled strain and controlled stress fatigue testing (Masad et. al. 2007). The dynamic mechanical analyzer (DMA) was used and the fine portion of the asphalt mixture was selected for testing. In the unified method the dissipated pseudo energy is assumed to consist of three parts: the energy due to an increase in phase angle, energy due to permanent deformation caused by loading and unloading, and the third part is due to the difference between the pseudo stiffness of the undamaged and damaged materials.

$$W_R = W_{R1} + W_{R2} + W_{R3} \tag{2.20}$$

$$W_{R1} = \pi G \gamma_0^2 \sin(\phi_n - \phi) \tag{2.21}$$

$$W_{R3} = \frac{1}{2}\frac{\tau_0}{G_R}(\tau_0 - \tau_N) \tag{2.22}$$

$$\Delta R(N) = \left(\left(\frac{2n+1}{nb+1} \right)^{n+1} \left(\frac{G_R bc}{4\pi G_1 \Delta G_f} \right)^n N^{nb+1} \right)^{\frac{1}{(2n+1)}} \tag{2.23}$$

The acoustic emission technique was used to study micro damage due to fatigue in asphalt (Youngguk et. al. 2008). Acoustic emission (AE) is a non destructive technique in which a picture of the specimen is taken and recorded during each load cycle (Figure 2.12). The fracture process zones (FPZs) are determined from image data. Two sensors are attached to the sample to record data during the load cycle. Acoustic emission counts are used to determine the propagation of fatigue cracks. The method cannot compute the damage that already present in the sample as it considers damage only during the load cycle.

2.9 X ray CT for moisture damage of asphalt mixtures

X ray CT was used to determine the flow paths and permeability of water in asphalt (Al Omari et al. 2004). They tested specimens in water and scanned them for moisture transport. They found that the moisture flow can be related to the connected air voids in asphalt. They developed a program to calculate the air voids connected throughout the depth of the specimen. The program considers only the voids continued throughout the specimen from one face to the other side.

The effect of compaction angle on the moisture susceptibility of asphalt mixes from X ray CT has also been investigated (Arambula et al. 2007). Two different compaction angles (1.5° and 2.5°) were used in the gyratory compaction method. The specimens were scanned in X ray CT before and after saturation. The difference in air void distribution was determined from image analysis. The saturated specimens were tested in a tensile test to determine the damage parameters from saturated samples.

Surface energy and adhesion between aggregate and binder were considered as the main parameters in a moisture damage study of asphalt mixtures (Amit, 2006, Caro et al. 2008). Water permeability and capillary rise were determined for asphalt mixtures. Specimens

from three different mixtures were prepared and kept in a 10mm deep water bath. The voids were found filled due to capillary rise. The specimens were scanned in X ray CT after every five days. The procedure was followed for thirty five days and the flow path was plotted for selected mixtures.

2.10 Summary

Researchers have explored damage in asphalt pavements to some extent. However, the accurate assessment of pavement performance is still difficult due to the complex nature of asphalt materials.

Microstructural damage is the key factor responsible for asphalt failure. It causes a significant decrease in load-carrying capacity due to adhesive failure and/or cohesive failure. Damage is believed to begin with the nucleation of microcracks that later propagate, grow, and coalesce to form macrocracks as the material is subjected to loading (Kim et al. 1997, Wang et al. 2003).

There have been attempts to study the internal structure of asphalt mixes using imaging techniques and X ray tomography systems. Images of the internal structure have been used to understand the deformation mechanisms of asphalt mixes (Masad et al. 1999), for statistical study of the air void distribution (Masad et al. 2002), and to compare different compaction methods (Masad et al. 1999, Tashman et al. 2002). These advances have helped to improve the quality of images that can be used to define the asphalt mix geometry in the FEM (finite element method) and the DEM (discrete element method).

Although the microstructure of asphalt plays an important role in affecting its stiffness, its study has been very limited until recently. The reason might be due to the absence of appropriate techniques to obtain the actual microstructure of the materials. X ray tomography, a relatively new technique, provides visualized microstructure of the materials while causing no destruction to specimen. Since X ray tomography has only recently been

used in research on microstructures of construction materials, the number of papers on this topic is very limited.

Mostly researchers have developed asphalt damage models only based on mechanical testing (Nelson et al. 2003, Dunhill et al. 2006 etc.). Few have investigated microstructure of asphalt with X ray CT. The focus of using X ray CT in asphalt has primarily been on characterizing internal particle distribution, internal aggregate arrangement, and moisture effects on asphalt and air void during compaction of fresh mix.

Masad et al. (1999, 2001, 2002) have studied compaction performance with X ray CT. Tashman (2002, 2003, 2004) focused on the triaxial strength test for microstructure study at a single temperature (130°F). Song (2004) concentrated on DMA (dynamic mechanical analysis) and cyclic creep tests for superpave mixes only. He modified Tashman's equations with help of CDM (continuum damage mechanics). 2D images were used for determining the microstructural properties of asphalt while it has been shown for metals that 2D image data for microstructural properties gives an approximate value and true microstructure can be only determined from 3D. This approach was used by Voyiadjis et al. (2007) for metals. They develop a relation between 3D data of the sample and damage due to load. A damage tensor was developed for composite metals. Damage models have been developed from the experiments on sand asphalt mixtures in the dynamic mechanical analyzer (DMA) test, for further detail see Masad et al. (2007). Also for the asphalt mixtures fatigue damage model, parameters have been determined from indirect fatigue test or fatigue.

Fatigue tests for specimens in direct tension compression test have also been evaluated using acoustic emission (AE). These tests were conducted at pilot scale and have limited application as the technique cannot compute damage present in the specimens (Youngguk et al. 2008).

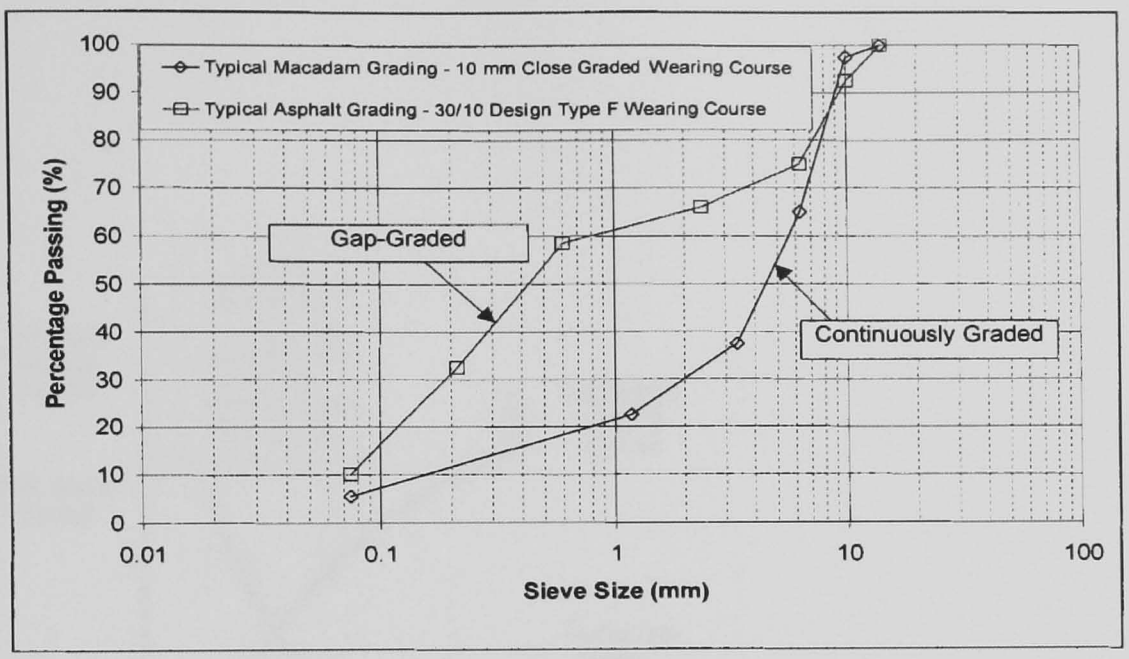

Figure 2.1 Aggregate gradation for DBM (Continuously graded asphalt) and HRA (Gap graded asphalt) (Dunhill, 2002)

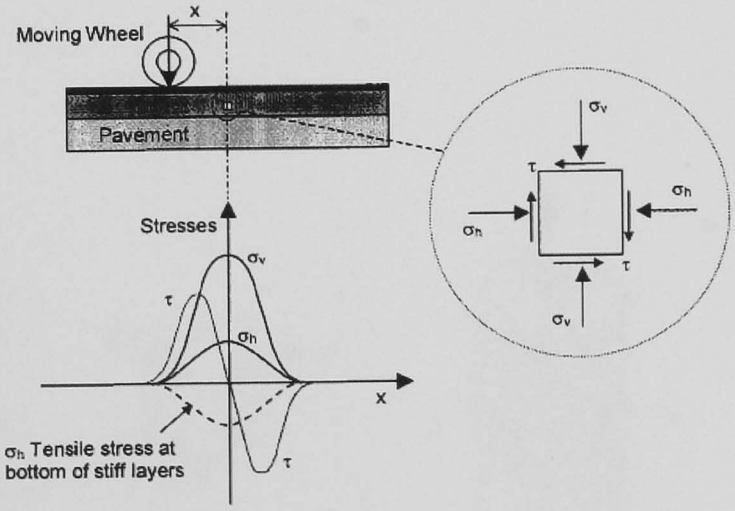

Figure 2.2 (a) Stress distributions in asphalt pavement due to wheel load (Dunhill, 2002)

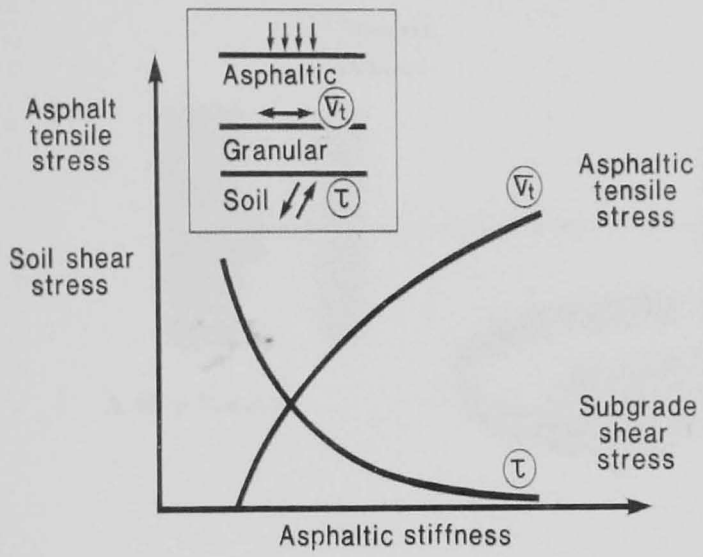

Figure 2.2 (b) Stress distributions in asphalt pavement due to wheel load (Collop, 1996)

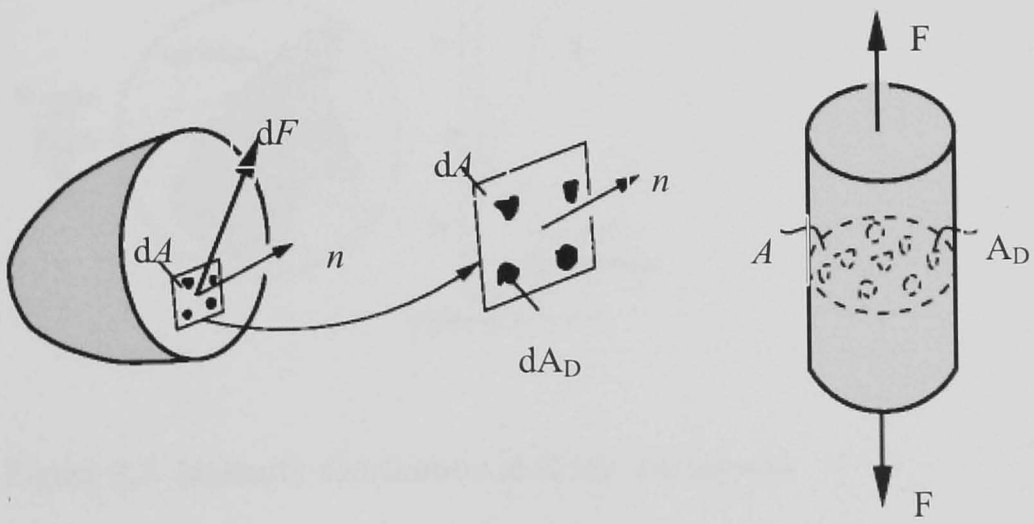

Figure 2.3 Definition of Damage (Dietmar et al. 2006)

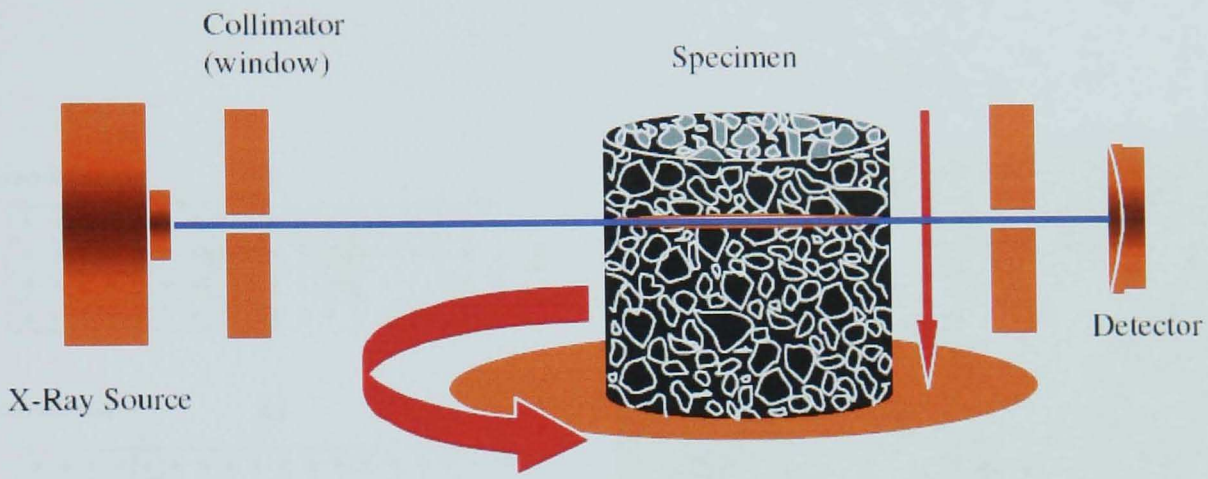

Figure 2.4, X ray Tomography process (Tashman, 2003)

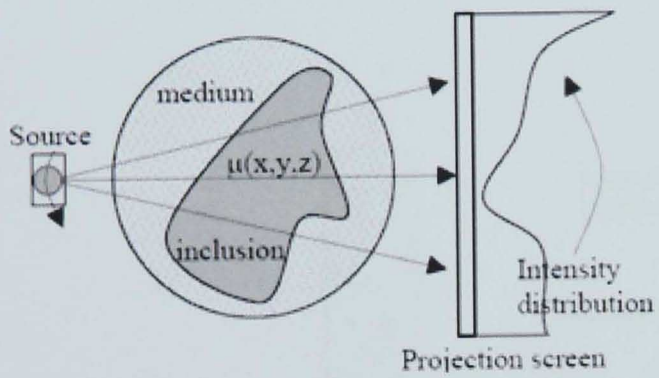

Figure 2.5 Intensity distribution in X ray Tomography (Daigle et al. 2005)

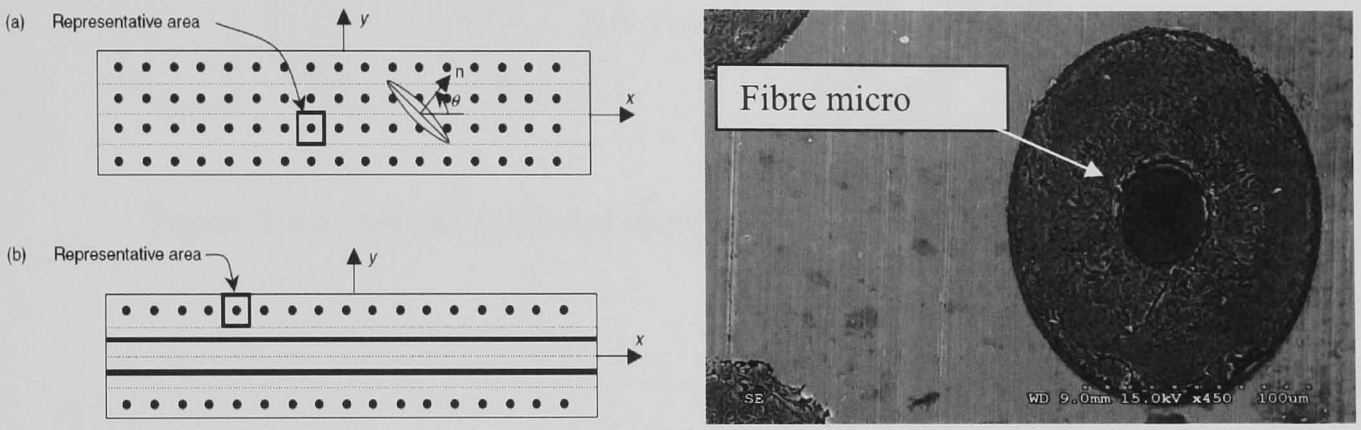

Figure 2.6 Microcracks in metals (Voyiadjis et al. 2007)

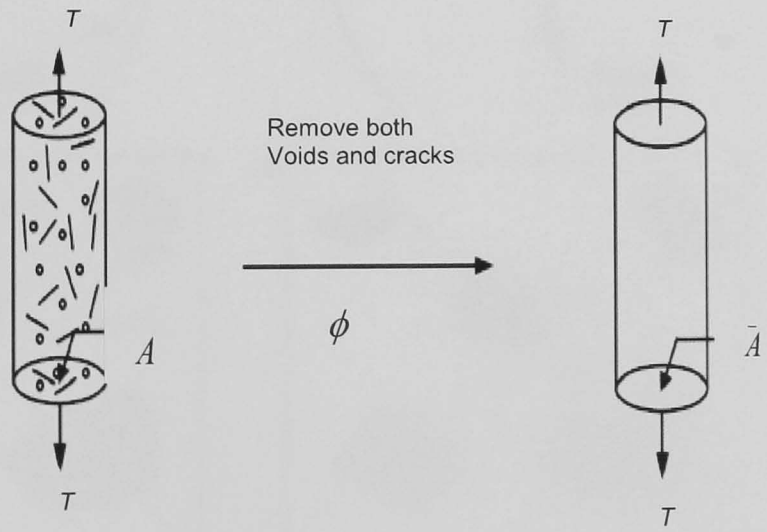

Figure 2.7 Microcracks in metals

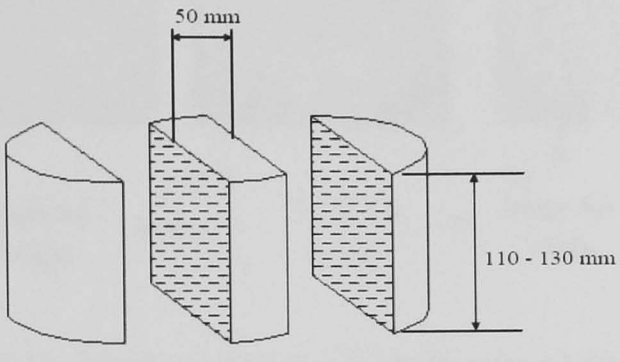

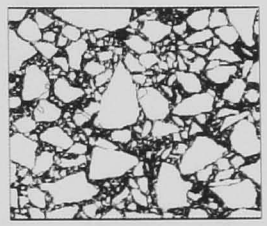

Figure 2.8 a) Asphalt specimen sections b) Processed binary image

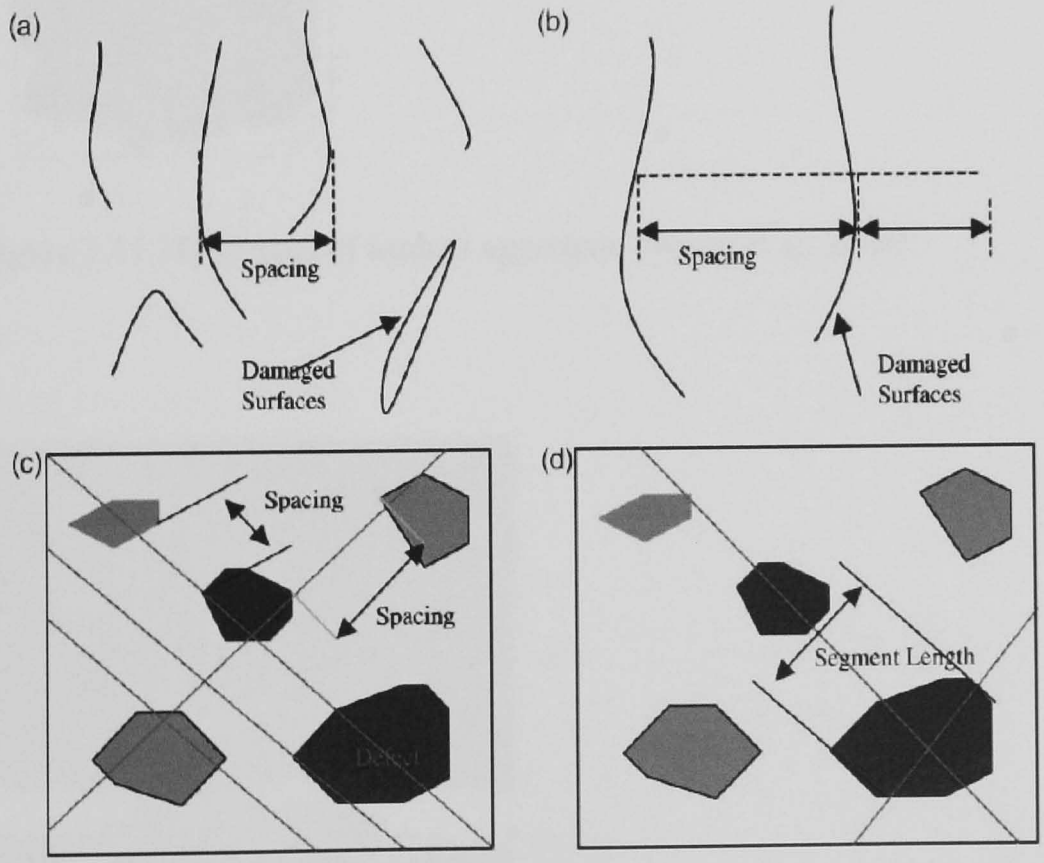

Figure 2.9 Damage approach in Wes Track project (Wang et al. 2001)

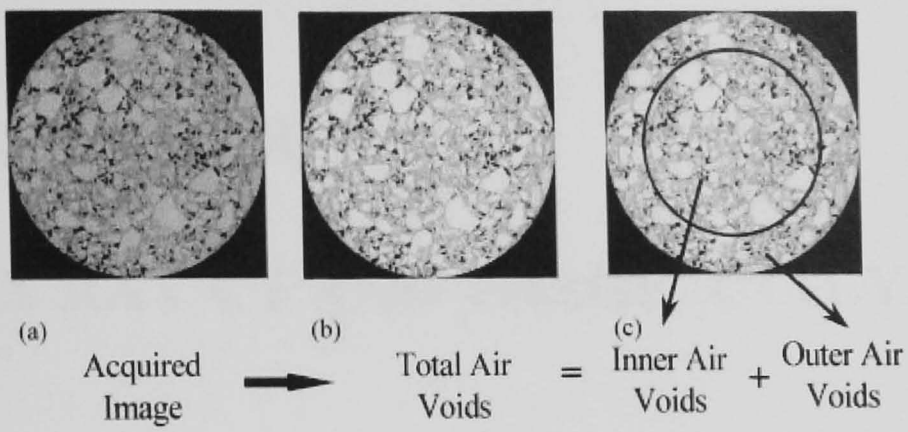

Figure 2.10 Void content in 2D image of asphalt sample (Tashman et al. 2002)

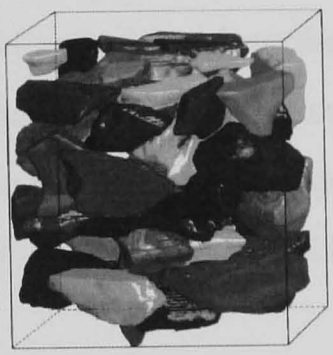

Figure 2.11 3D images of asphalt aggregate (Wang et al. 2004)

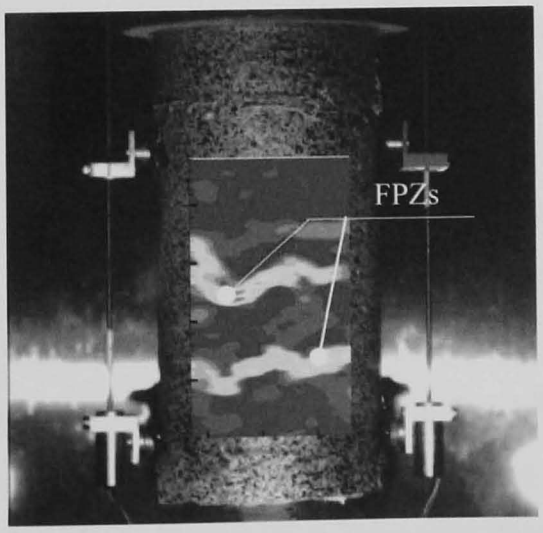

Figure 2.12 Image from acoustic emission technique (Youngguk et al. 2008)

CHAPTER 3

X RAY CT AND IMAGE ANALYSIS

3.1 Introduction

Being the first project on the recently commissioned X ray CT in NTEC (Nottingham Transportation Engineering Centre), the working methodology developed is described here. Parameters require to obtain a clear image, and precautions against scanning errors and correction of images are discussed. Later on the procedure of image analysis, image enhancement and development of 3D image from 2D slices are included.

3.2 X ray CT operation

In X ray CT, the X rays, after passing through the sample, are saved on a detector which measures the attenuation of the X rays which is related to density and size of sample. The data from the detector is used to create 2D images which are also called slices. The X ray CT facility in NTEC is shown in Figure 3.1.

The prime factors in X ray CT are the X ray energies generated and the X ray intensity. The energy is the ability of the X rays to penetrate the sample and then their relative attenuation as they pass through materials of different densities. High energy X rays penetrate more efficiently compare to low energy X rays. At the same time high energy X rays are less sensitive to material changes due to density differences (X Tek, 2005). The energy of the X ray is quantified in term of kV. The intensity of the X ray relates to the clarity of the image. It affects the relation between signal and noise on the image. In addition there are other factors relating to scanning such as filters, source filter and back filter (the source filter is a 2mm thick copper plate and is kept in front of X ray beam (Figure 3.2 (a)) before passing

into the sample while back filter is fixed in front of the detector (Figure 3.2 (b)) such that the rays after passing through the sample will pass through the back filter. The thickness of filters is varying depending on the thickness of the sample scanned.

3.3 X ray 2D image acquisition

The fundamental principle in X ray CT is to acquire multiple sets of views of an object over a range of angular orientation. View is the set of X ray intensity measurement for a given position of specimen. These data are used to create two dimensional images called slices because they corresponds what can be seen if the object were slices along the scan plane (X Tek, 2005). Intensity is measured as the power from a source that is directed into a particular direction. Mathematically it is expressed as , $I = P/\Omega$, where I is intensity, P is power (Watt) and is the product of voltage (kV) and current (mA), Ω is solid angle which remain constant, thus intensity is directly proportional to power.

In order to obtain reasonable 2D image data from the sample, the sample is fixed on the turn table to ensure that it does not move while the X ray is scanning. For the acquisition of two dimensional images X rays are emitted simultaneously across the object's width. The CT scanner parameters are fixed for a certain required resolution. The number of slices and slice spacing is selected according to the required resolution. The energy of the X ray, primary and secondary filters, X ray source intensity are selected according to sample size and density of material. Steps followed for X ray CT and image analysis are shown in Figure 3.3. Several trials were made to fix the scanning parameters (Voltage, Current, primary and secondary filters) (Table 3.1, Figure 3.4). Primary filters of 1mm, 1.5mm and 2mm thick copper plates were used to improve the quality of scans.

A uniform circular / cylindrically shaped sample was found to produce noise-free images compared to a rectangular shape. This is because while rotating the sample during the X ray CT the X rays travel similar path lengths and have uniform intensity in the case of a circular sample while this was not the case for rectangular shaped specimens (Figure 3.5).

The position of 2D images was mapped onto a paint brush image of the sample (Figure 3.6). The paint brush image is a picture of the sample (geometry) which is obtained before

taking any scans. The thickness of the slice is the maximum resolution which is 83 microns in this case and the same slice interval was fixed on the paint brush image. In order to cover the whole specimen the positions of the slices were marked such that the slice interval is also 0.083mm (83 microns), equal to the resolution of the system. This covered the whole specimen (Figure 3.7).

3.3.1 X ray Attenuation

When the X rays enter a sample, the energy of rays is reduced is due to scattering over the sample and due to absorption in the sample. The intensity of X rays at the detector after attenuation is expressed as a function of the initial intensity, the X-ray path length, and the attenuation coefficient. This can be expressed in form of Beer's law as (Richard et al. 2001)

$$I = I_0 e^{-\mu L} \tag{3.1}$$

where I_0 is the initial intensity, μ is the attenuation coefficient and L is the path length.

For composite materials such as asphalt mixtures which composed of different materials the intensity is expressed as

$$I = I_0 e^{\sum_i (-\mu_i L_i)} \tag{3.2}$$

where i is the increment for a material having attenuation coefficient μ_i over X ray path L_i.

Attenuation coefficients for all materials are relatively high at low voltages and reduce exponentially as voltage increases. Therefore it can be said that attenuation coefficients are inversely proportional to the exponential of voltage.

$$\mu = Qe^{-KV} \tag{3.3}$$

where μ is the attenuation coefficient, Q and K are constant material factors and V is voltage.

3.4 Image construction

In the X ray CT process, the 2D sinograms (raw data for image which is reconstructed and results 2D image) obtained are converted into 2D images in which the intensity data is converted into a computer tomography number such as 8 bit (256 grey values) or 16 bit image (65536 grey values). Intensity data is converted into image using filtered back projection (X Tek, 2005). Filtered back projection is an algorithm in which, the intensity data is first filtered to reduce the noise and then each view is successively superimposed over a square grid at angle corresponding to its acquisition angle (Ramachandran et al. 1971).

Tomography combines the information of many radiographs, each taken at a different sample orientation and is related to the movement of X ray Manipulator. The Manipulator is the base that seats the sample, and it can be adjusted to specific horizontal, vertical, magnification and tilt axes. Whilst scanning, it rotates the sample through 180°. Rotating the manipulator at a slower rate increases the number of radiographs taken, thus enhancing the reconstruction. Also, when the angular step between each radiograph is small it is possible to compute the attenuation coefficient at each point of the sample. Radiographs taken at different orientations are combined to create an image reconstruction. Reconstructed image is in the form of pixels (unit of picture in 2D) in a 2D reconstruction and cubic pixel (voxel) in a 3D reconstruction. Each pixel and voxel in the reconstruction is allocated a grey number from a grey scale as a representation of the density of the element occupying that pixel/voxel.

3.5 Defects in X ray images

In X ray computer tomography sometimes the image looks physically clear but is difficult to analyze for different material parameters as the image does not represent the actual material properties due to changes in different parts of the image. Such errors occur due to scanning artifacts (beam hardening, ring artifacts) (Richard et al. 2001).

3.5.1 Beam hardening

Hardening refers to the mean increase in X-ray energy as it passes through the scanned object. Because lower X-ray energies are attenuated more readily than higher energies, the beam loses the lower part of the energy spectrum. Therefore, although diminished in overall intensity, the beam has a higher average intensity than the incident beam which increases the further it travels through the sample. The result is that low energies are easily absorbed and therefore short X-ray paths are proportionally more absorbing than longer paths.

It has been found that sometimes the X ray CT images have non uniform brightness throughout the image although the material composition in the sample is the same (uniform). It is either dark in the centre and bright in edges or dark at the edges and bright in the centre. This is due to beam hardening (Figure 3.8a). The beam hardening effect is eliminated by using/adjusting both the source and back filters.

3.5.2 Ring artifacts

When the sinograms are converted into the 2D images, some partial or full rings are appearing on the image. These are caused by the rotation of the sample. It is due to a shift in the output of the detector which occurs on every X ray. This results in anomalous X-ray values at the same point in the line array with every radiograph. The rotation of the sample results in ring artifacts about the rotation axis. The output change, or shift, depends on detector sensitivity to changes in the scanning conditions. This could be climatic changes such temperature or humidity so it is important to keep scanning conditions under control. More critical is the sensitivity of the detector to beam hardness (energy of the beam). This is especially important with composite materials as the variation of attenuation properties caused by the rotating sample will cause variations in the beam intensity that reaches the detector. If the detector output varies greatly with beam hardness it can produce anomalous results which manifest as partial circles about the axis of rotation (Figure 3.8).

As beam hardness causes the ring artifacts, it can be corrected in the same way, though more emphasis is placed on software correction at the data processing stage. Keeping uniform temperature /air conditioning of the X ray system has been found to have good

effect on scanning data. It has been found that the consistency of results is related to climatic control of the X ray machine. The use of air conditioning to regulate the laboratory does appear to enhance the consistency of the scanning process.

3.5.3 Noise and CT acquisition time and partial volume effects

Filters in X ray CT disperse X ray energies across the spectrum, resulting in noise in the images. Increasing the acquisition time effectively increases the time to collect the X rays. This increases the sinogram data used for image reconstruction and results in reduction in noise effects (Figure 3.9). Increasing the exposure time increases the image acquisition time (Richard et al. 2001).

In the case of an asphalt mixture which is a complex multiphase material, some of the pixels (voxels in 3D) comprise part aggregate stone and part mastic or mastic and air void. For image analysis every pixel in the X ray image is either considered as aggregate stone, mastic or air void. In the case of a pixel or voxel divided between two or three different components this is called a partial volume effect. Partial volume effects cause a similar problem to noise. In this case the value is taken as an average. The difference between noise and partial volume effects is that noise generally relates to the quality of the image while partial volume effects relate to data for individual constituents within an asphalt mixture.

3.5.4 Sample movement

Sample movement refers to the lateral movement of the sample due to manipulator vibration as it rotates. This produces incoherent alignment of the radiographs (Figure 3.10). The effects are more notable in smaller lighter objects more prone to movement. Large samples are found to be relatively less affected (Townend, 2005).

3.5.5 Centre of rotation (COR)

The centre of rotation is a function of the sample height and eccentricity about the centre of the manipulator axis. If the COR is incorrect radiographs are incorrectly aligned resulting in unsatisfactory image reconstructions.

3.6 Correction to X ray filters

It was observed from X ray scanning that quality of the image depends on primary and secondary filters, specifically the profile of the secondary filter. The primary filter is a plane plate and can be adjusted by using a thicker or thinner filter. The secondary filter is of varying thickness in form of a profile. The thickness of the profile depends on thickness of the sample and is adjusted according to the radius of sample (Figure 3.11) (X-Tek, 2005). Several specimens were scanned as a trial to obtain a good quality image for analysis. It was noted that each limestone, granite and mixed aggregate required a different filter profile. Similarly different specimen sizes of the same material require different settings of the filter's thickness and profile. Applying these correction measures resulted in images of reasonable quality which simplifies analysis and gives enough information of sample microstructure.

3.7 Image Analysis

After scanning the asphalt samples the 2D images are collected from the X ray CT. These images are converted into digital image form to study the image properties (Figure 3.12). The size of the image in pixels depends on the scanning setup in the X ray CT system which is selected before starting the scanning (taking images). This is for example in the form of 1750x1750 pixels for a uniform specimen of equal length and width and 2340x1800 for a sample of differing width and length. The size of 2D image is independent of the height of the sample. Pixel size is fixed in the X ray system according to the size of the specimen. The acquired images are digitized as 8 bit or 16 bit depending the resolution. In an 8 bit image the grey scale is divided into 256 levels and each pixel has value from 0 to 255 (Figure 3.13) where zero represents the black portion of the image and 255 represent the white portion. In the case of a 16 bit image the grey scale is 0 to 65535 where zero represents the black portion and 65535 represents the white portion. The images are converted into 8 bit as this requires less memory and can be simply analyzed for various information regarding the components of the sample.

3.7.1 Threshold of an image

This is the technique applied in image analysis to characterize the components of the mixture. It converts the representative grey scale of a component into a value. This value is

then the only value associated with an element and so it can be identified in the mixture. The image is thresholded so that a grey value can be assigned to air voids mastic and aggregate within the asphalt mixture. These different grey values are applied to specific number of the image, distinguishing the microstructural components of the asphalt mixture. Grey value changes with the density of different components in the mixture and it has different values (Figure 3.13, Figure 3.14).

Since the accuracy of the data from the image depends on the quality of the image such as the brightness, contrast, noise etc, therefore more effort and care is necessary in enhancing the image and reduce the noise.

When images are collected from the X ray there are usually black rings outside the image (Figure 3.15) although these were reduced during X ray scanning trials and are not considered in analysis. Figure 3.16 illustrates the result of including the outer ring, they are automatically considered as air voids. Due to noise outside the image it is selected as the part of image and values are calculated considering the outer ring as the part of the image. In this case sides of the image were trimmed, so that only the specimen itself can be considered for analysis.

Threshold grey values are adjusted in Image J, the image analysis tool. Image size in pixels can be modified using image analysis tools. Once the grey value is selected the image can be analysed for mixture components (Figure 3.17a, Figure 3.17b). The complex nature of asphalt can be confirmed as grey value profile varies due to density differences between asphalt mixture components (Figure 3.18).

While analyzing the image in 3D using in VG studio max 1.2.1, the resolution of the image and slice interval have been considered. Resolution is the measure of output quality of the image usually represented as pixels per linear inch, many pixels per inch gives a high resolution image with good quality while fewer pixel numbers per inch gives a low resolution image of comparatively poor quality comparatively. Slice interval is the distance between consecutive 2D images along the height of the specimen. As in the X ray scanning setting, 0.083 mm intervals (i.e. next slice taken at 0.083 mm from the centre of the

previous slice), so in regeneration in 3D, 0.083mm, 0.083mm, 0.083mm values have been used for x, y, z resolution values respectively (Figure 3.19). A detailed methodology has been developed for X ray CT and image analysis (See appendix A).

Using resolution values in mm in x, y and z directions reduces the calculation, which results in output data in mm, mm^2 and mm^3 instead of pixels and voxels. The x, y and z coordinates of every single air void is determined in 3D image and the volume of air void can be calculated (see Table 3.2).

3.8 Summary

Asphalt specimens of various diameters made from different types of aggregate and binder contents were scanned in X ray CT. X ray CT scanning parameters for a good quality image was determined by adjusting the energy of X rays, intensity and primary and secondary filters. Defects and noise in images were found to have affected the output data of the sample. 2D slices were stacked to generate 3D image of the original sample. To get a uniform 3D image for the specimen, the scanning (slice) interval between 2D slices were fixed equal to the resolution of the system for 2D images.

Image analysis techniques were applied to develop the 3D digital image and convert it into a set of parameters describing the internal microstructure of the original sample. Grey values for different components of asphalt mixture were fixed from trials and from laboratory air voids. Expertise in image analysis can provide maximum information about the internal structure of a scanned sample.

Table 3.1 X ray CT energy parameters for sample scanning

Energy (kV)	Intensity (mA)	Energy (kV)	Intensity(mA)
90	7.1	185	3.5
95	6.8	190	3.4
100	6.4	195	3.3
105	6.1	200	3.2
110	5.8	205	3.1
115	5.6	210	3.1
120	5.3	215	3
125	5.1	220	2.9
130	4.9	230	2.8
135	4.7	235	2.7
140	4.6	245	2.6
145	4.4	255	2.5
150	4.3	265	2.4
155	4.1	275	2.3
160	4	295	2.2
165	3.9	300	2.1
170	3.8	315	2
175	3.7	335	1.9
180	3.6	350	1.8

Table 3.2 Data for air voids from 3D image of asphalt specimen (slice No. 01)

Void No.	X-co-ordinate (mm)	Y-co-ordinate (mm)	Z-co-ordinate (mm)	Volume (mm^3)	Surface (mm^2)
1	43.99	52.95	0.17	0.5144	4.865
2	21.75	13.45	0.17	0.0735	0.884
3	71.55	70.55	0.17	0.2204	1.99
4	42.33	53.29	0.17	0.1837	1.879
5	62.25	7.8	0.17	1.0288	6.077
6	82.5	1.49	0.17	0.1837	1.436
7	65.57	5.81	0.17	0.9553	6.964
8	33.03	26.39	0.17	0.2572	2.1
9	57.6	55.61	0.17	1.8003	12.266
10	44.32	12.12	0.17	0.0735	0.884
11	15.77	8.13	0.17	0.147	1.659
12	34.36	31.04	0.17	0.1837	1.658

Figure 3.1 X ray CT system in NTEC

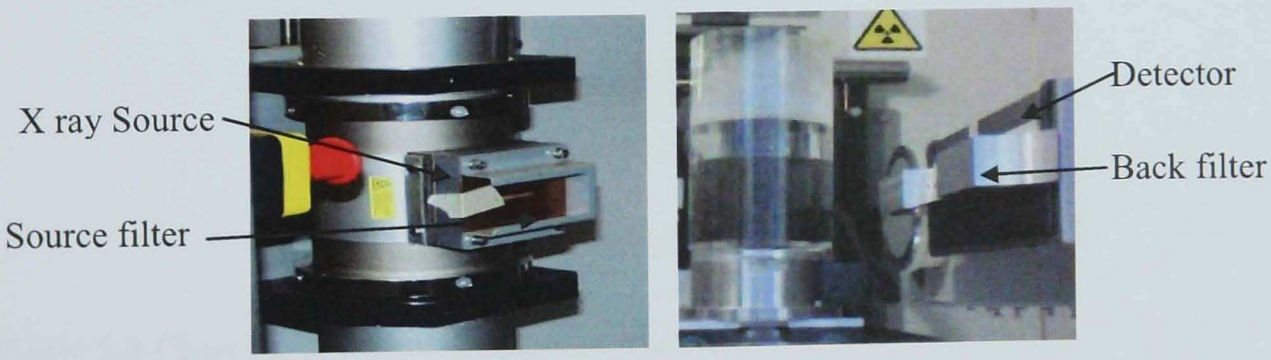

Figure 3.2 a) Source filter, and b) back filters used in the X ray CT

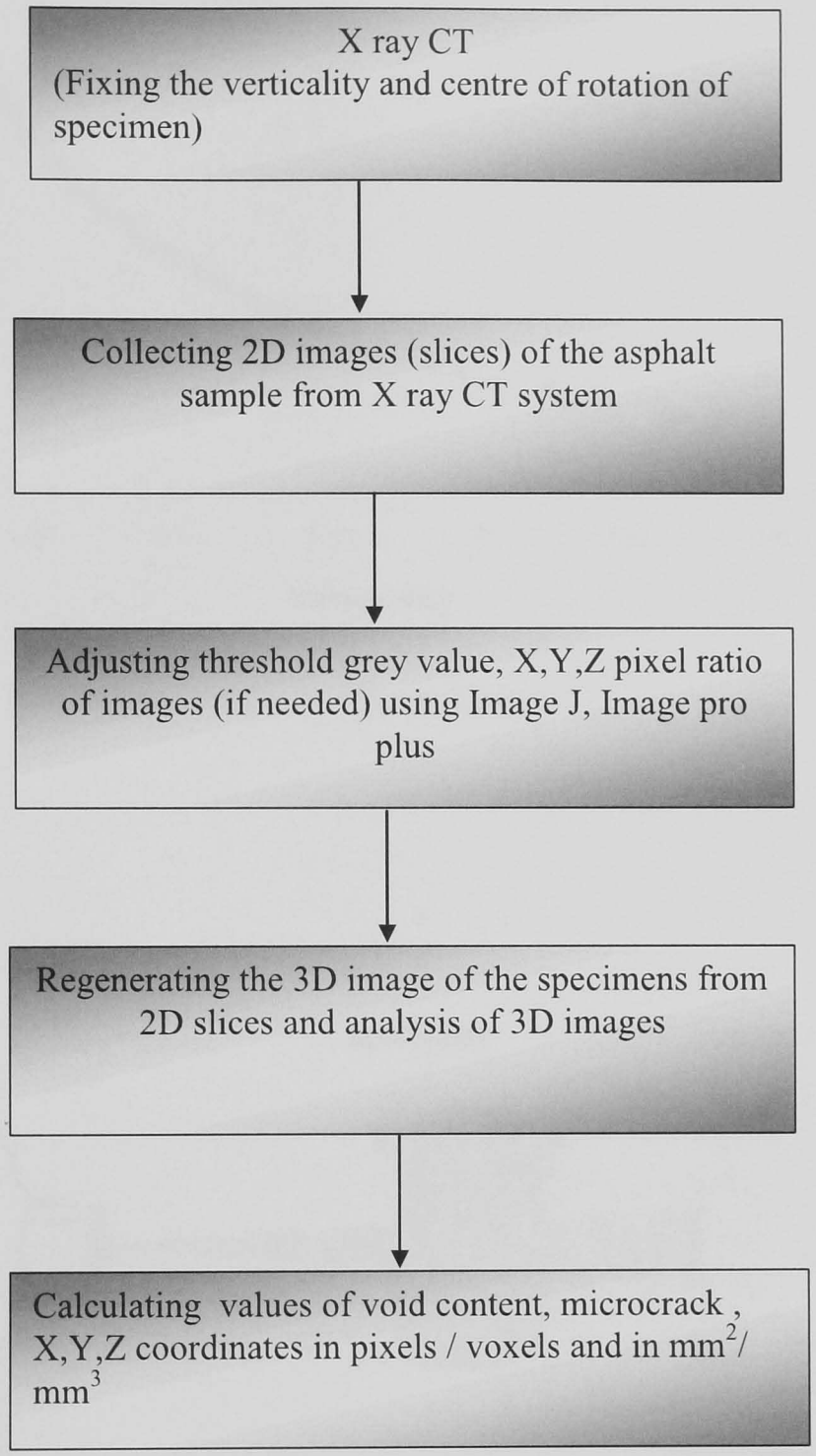

Figure 3.3 Chart for X ray CT and image analysis

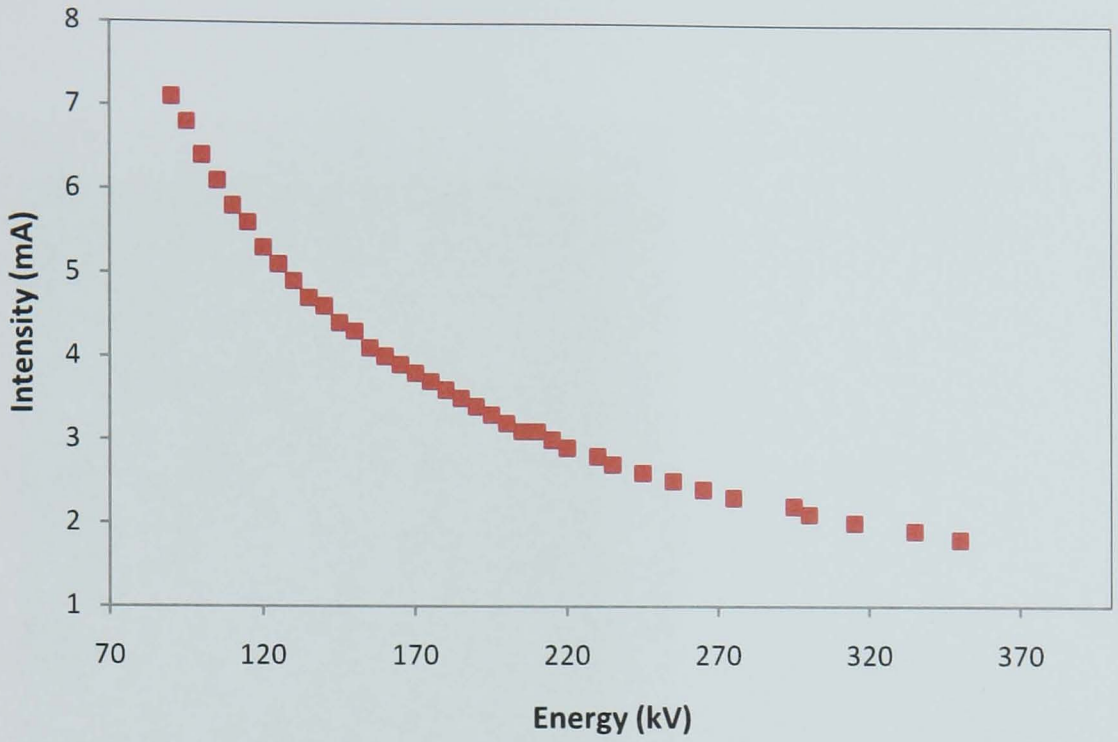

Figure 3.4 Variation of Intensity with Energy in X ray CT

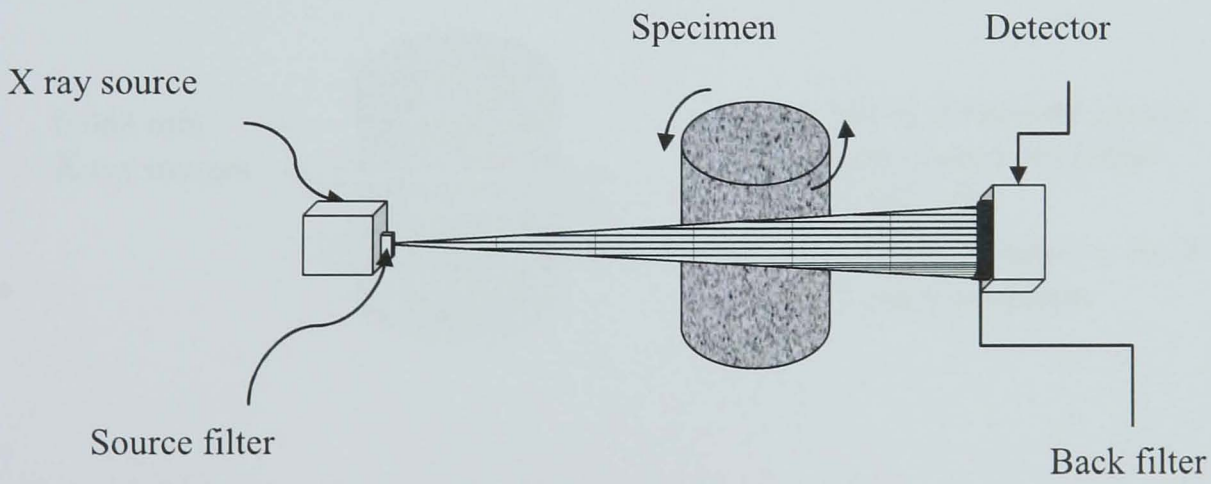

Figure 3.5 X ray arrangement used in the project

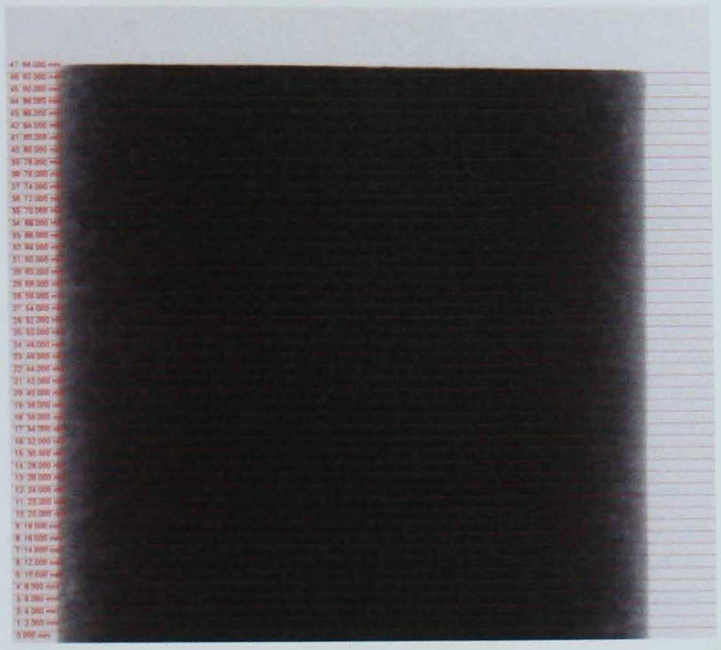

Figure 3.6 Slice positions on paint brush image of asphalt sample

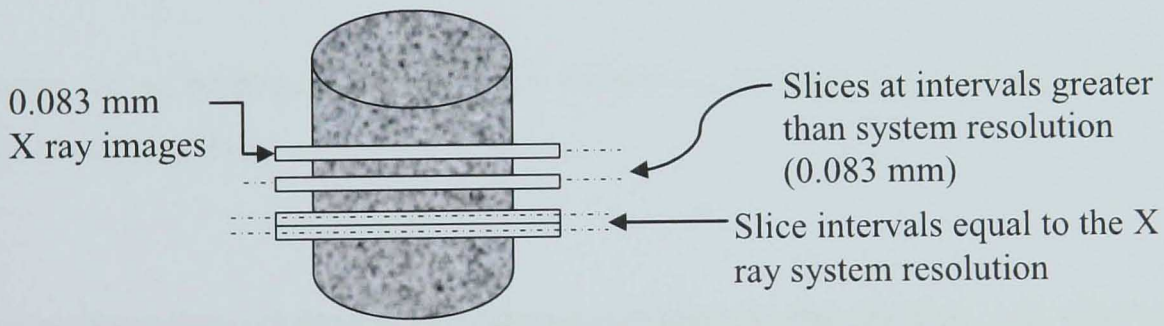

Figure 3.7 Slice position on asphalt specimen

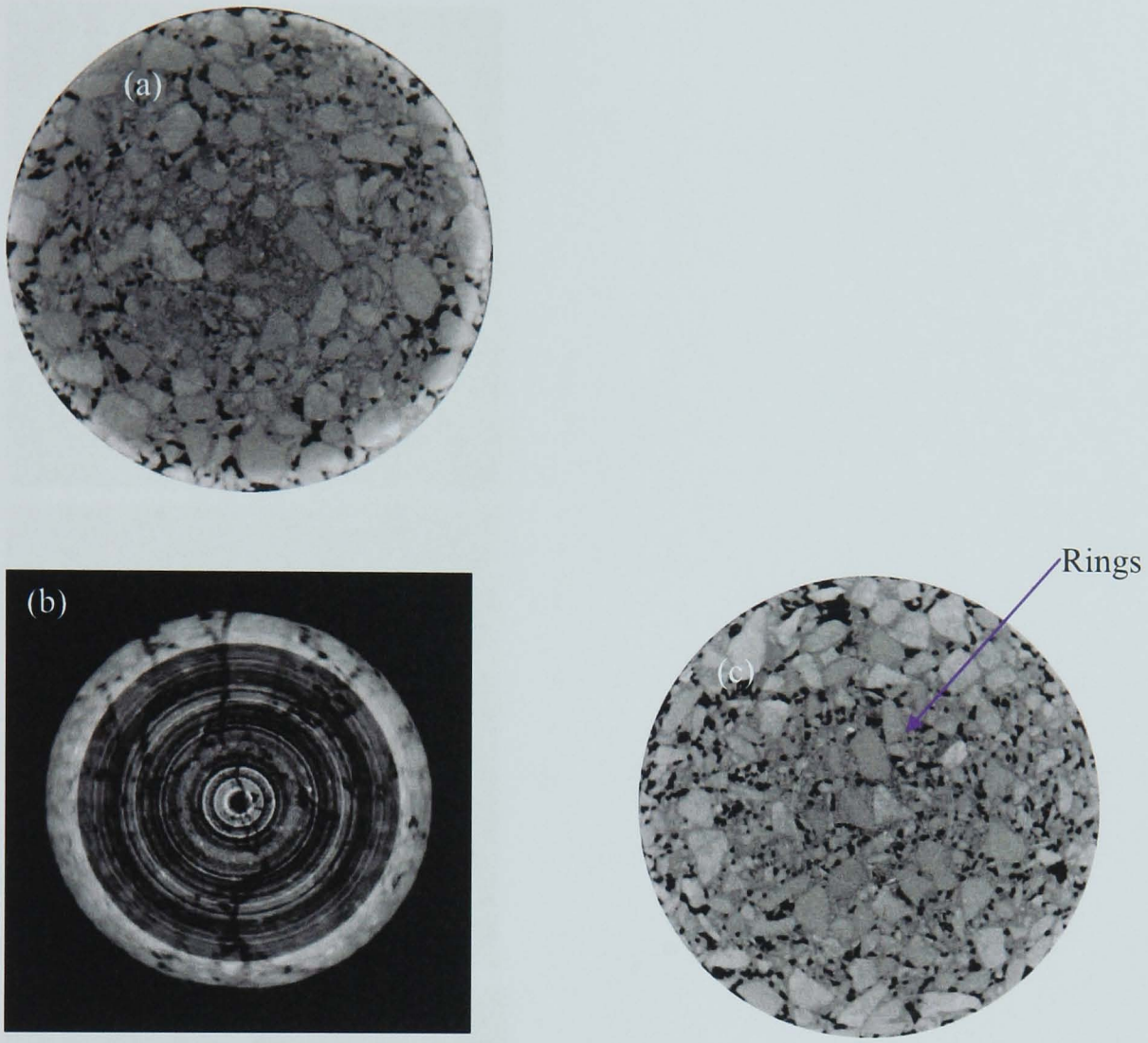

Figure 3.8 a) Brightness due to Beam hardening, b) High ring artifacts (Townend, 2005), c) Low ring artifacts

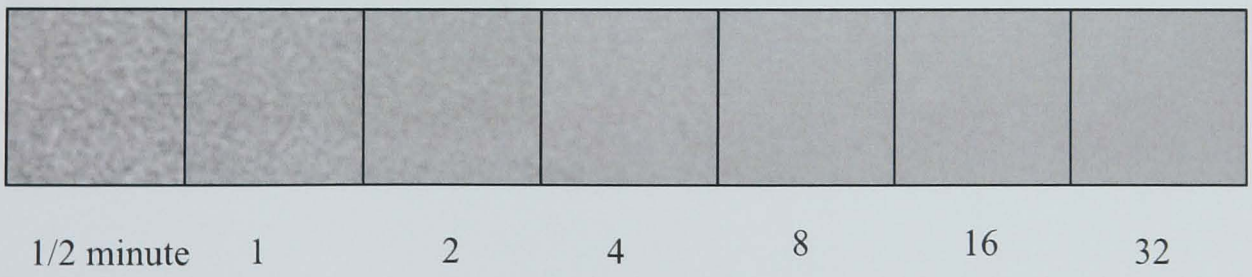

Figure 3.9 Reduction in the noise with increase in acquisition time

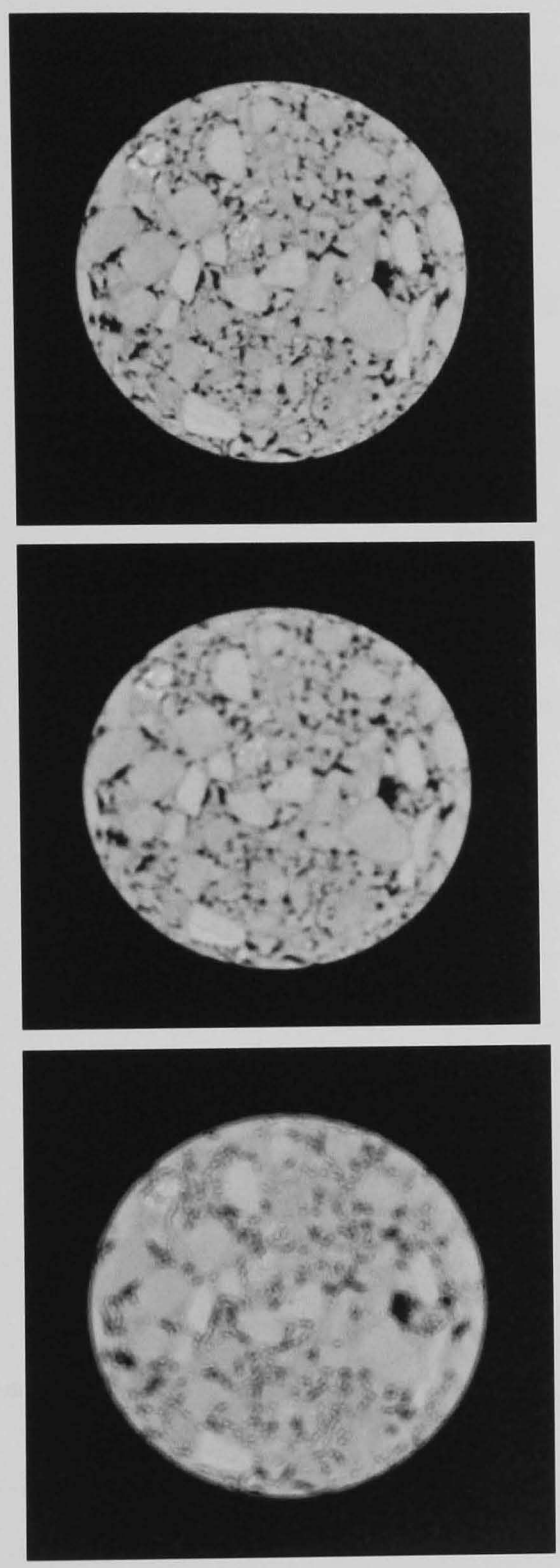

Figure 3.10 Effect of sample movement on image quality

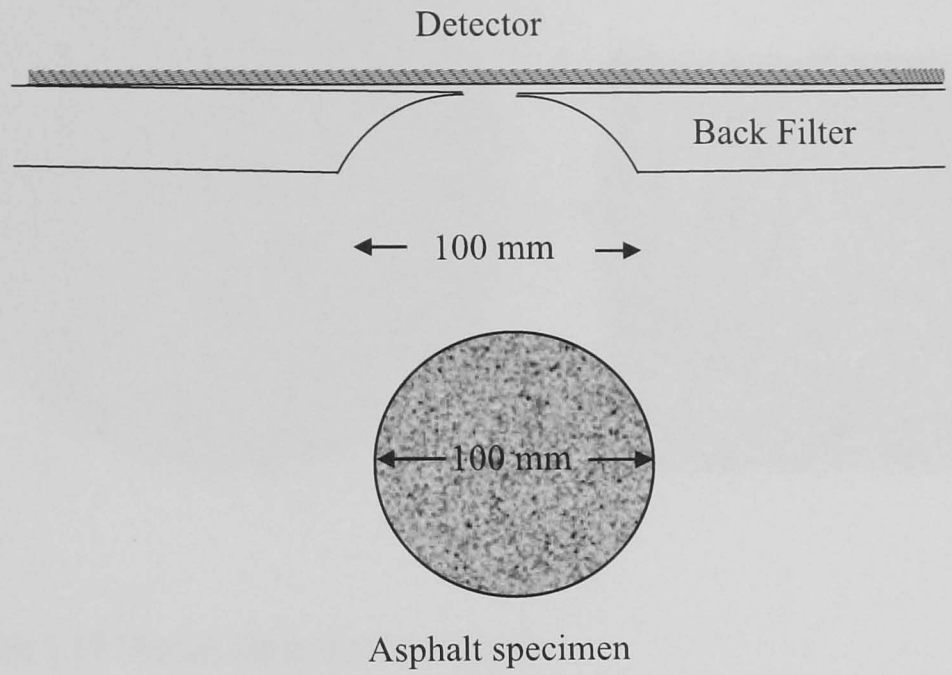

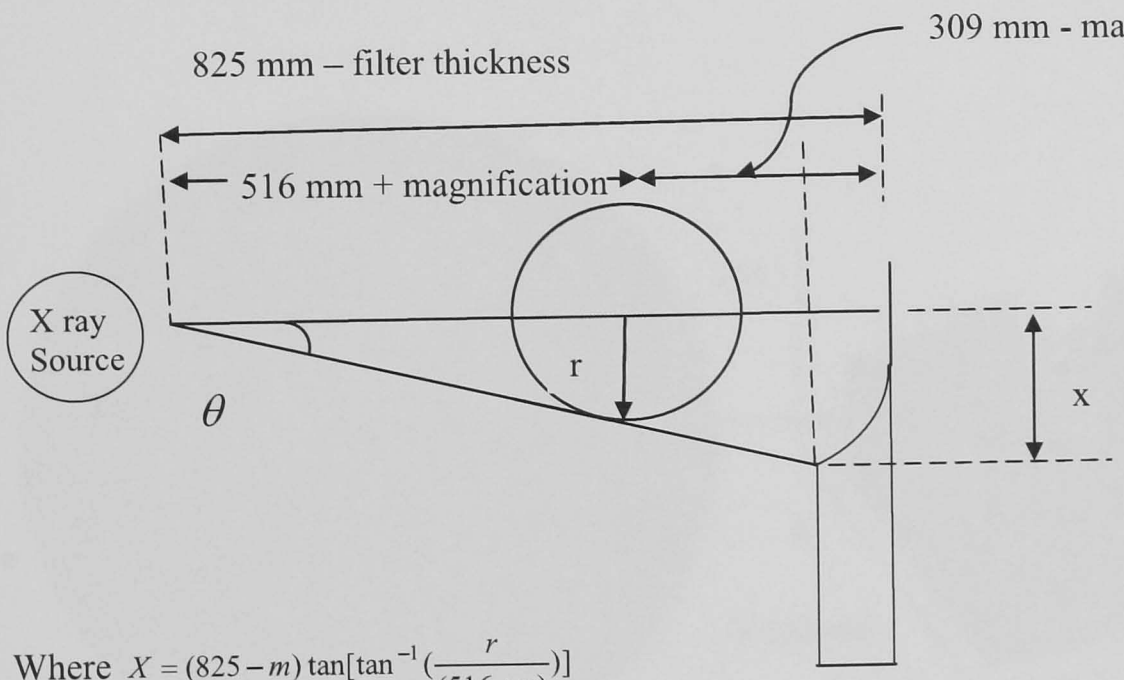

Where $X = (825 - m)\tan[\tan^{-1}(\frac{r}{(516+n)})]$

Figure 3.11 Profile of back filter (X Tek, 2005)

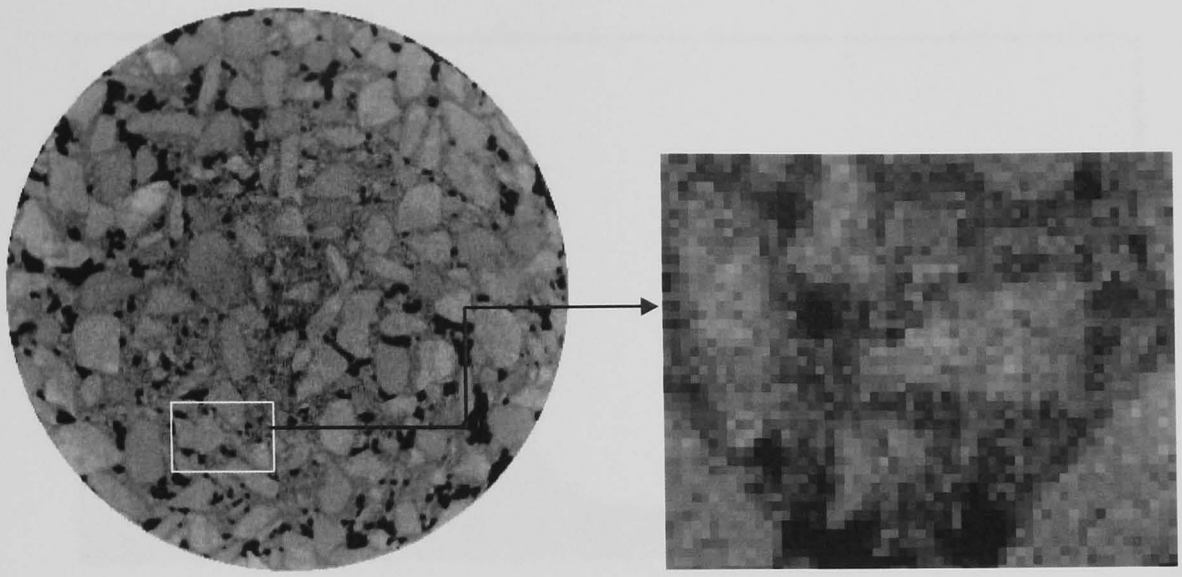

Figure 3.12 Digital image to show pixels

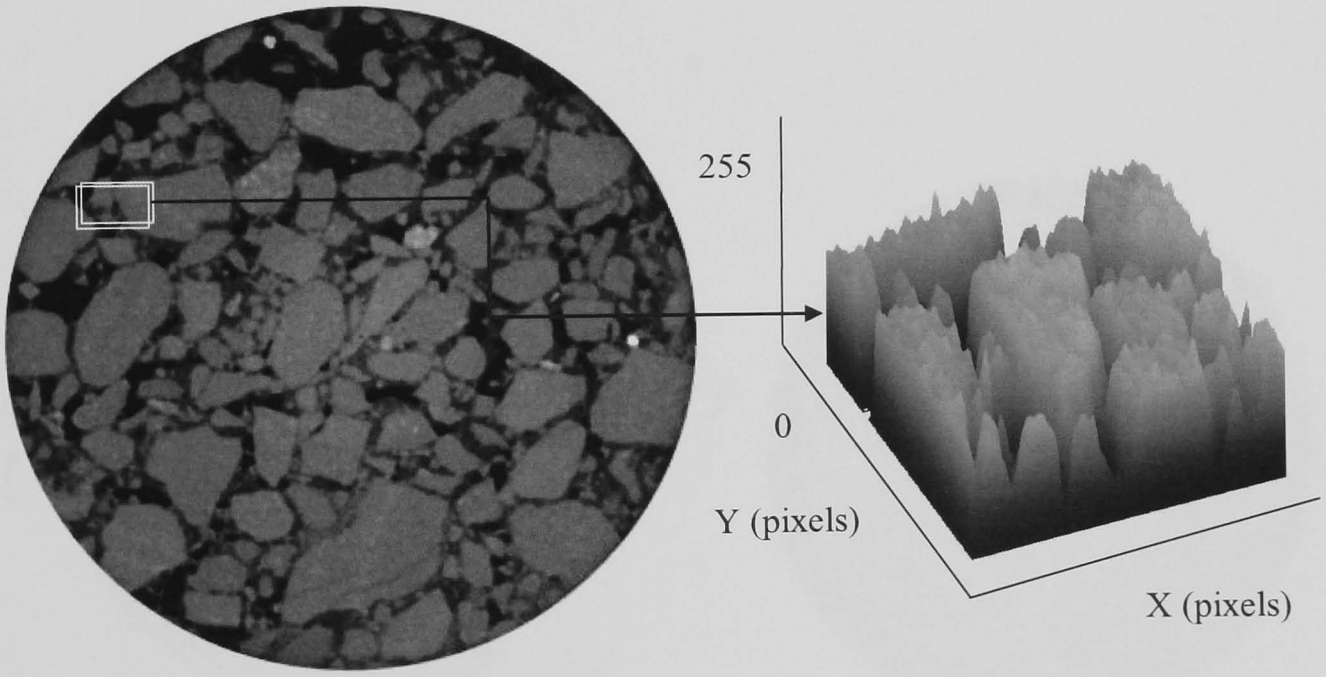

Figure 3.13 The plot of grey values for an asphalt image

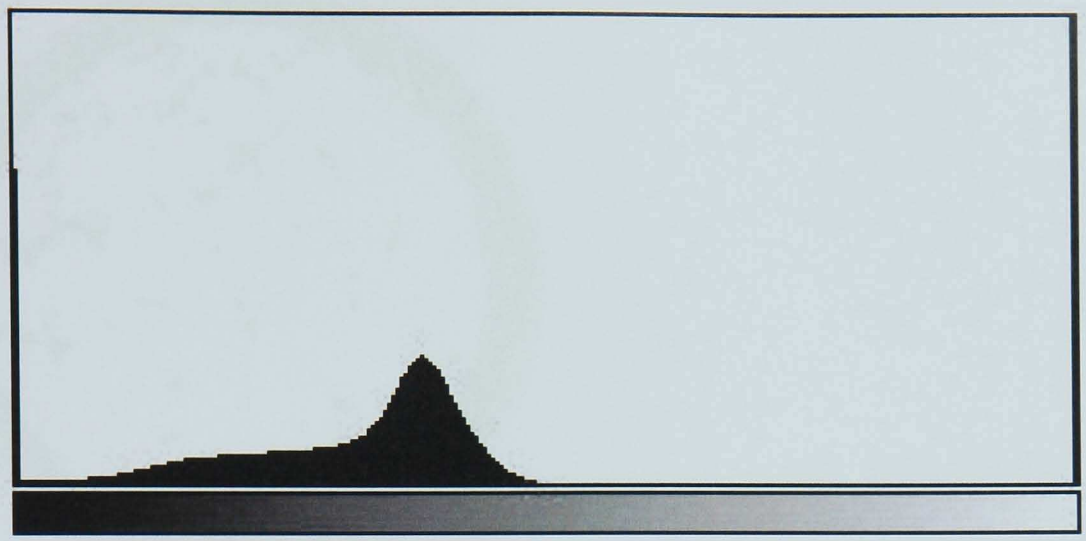

Figure 3.14 grey value distribution in an image

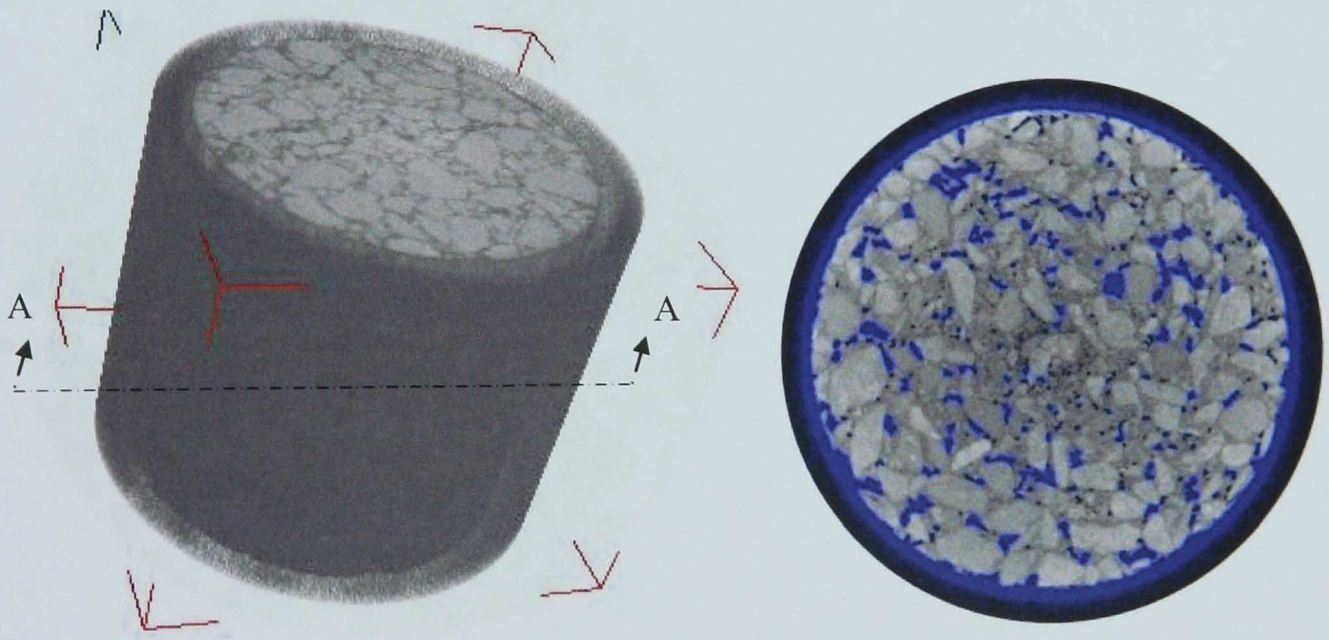

Figure 3.15 a) Outer ring in 3D image of asphalt b) 2D section AA

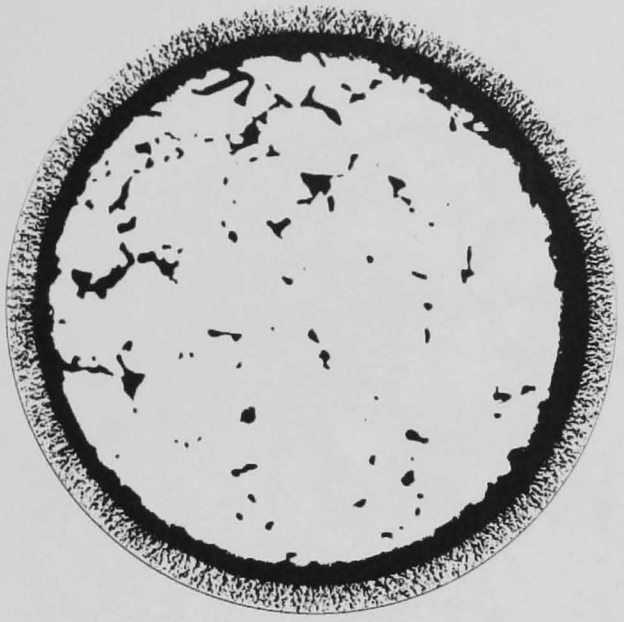

Figure 3.16 The black outer ring selected as part of air voids

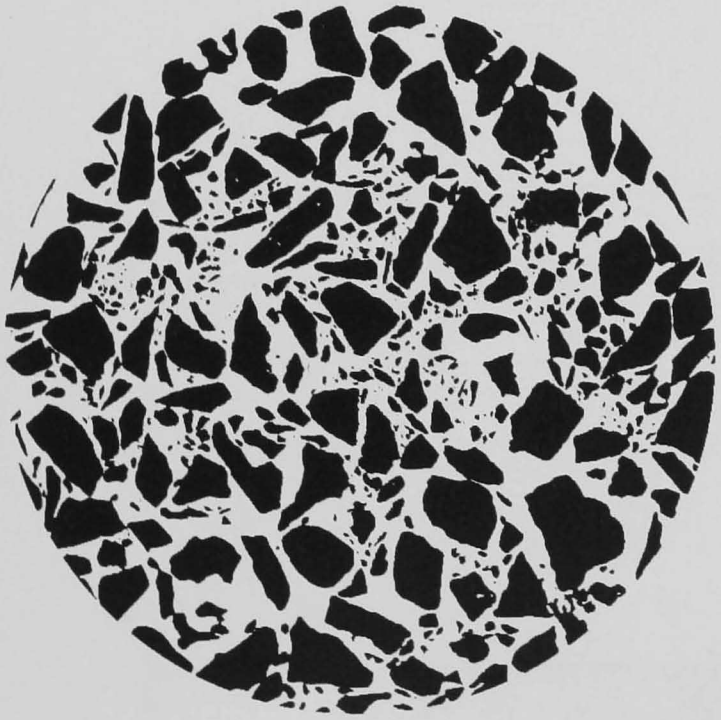

Figure 3.17(a). Aggregate component extracted in image analysis from 2D image analysis

Figure 3.17(b). Aggregate component from 2D image of asphalt mixture

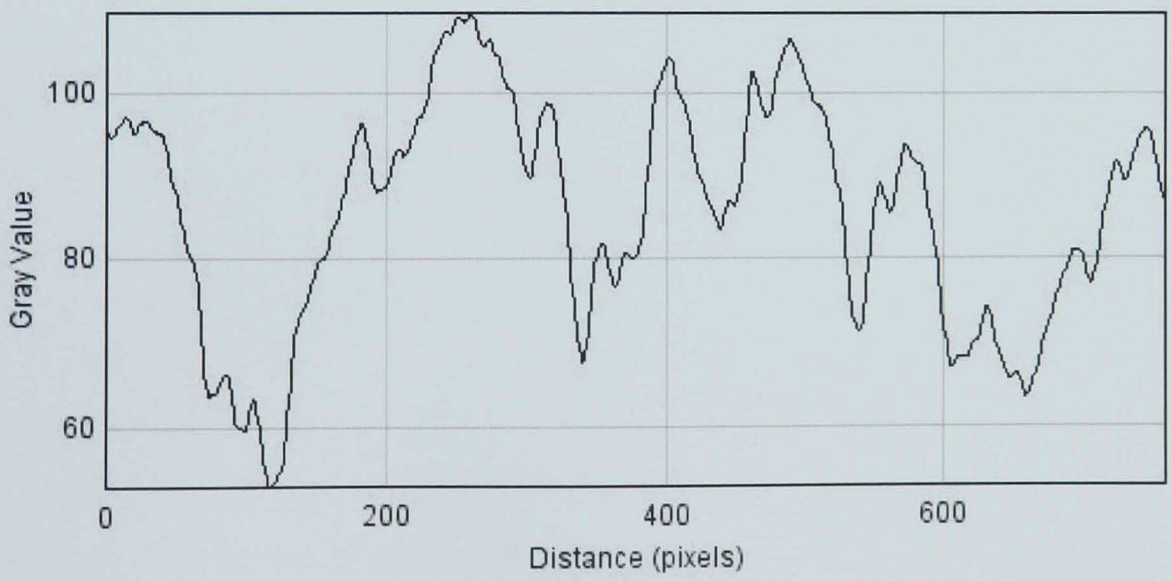

Figure 3.18 plot of grey value profile in DBM asphalt mixture

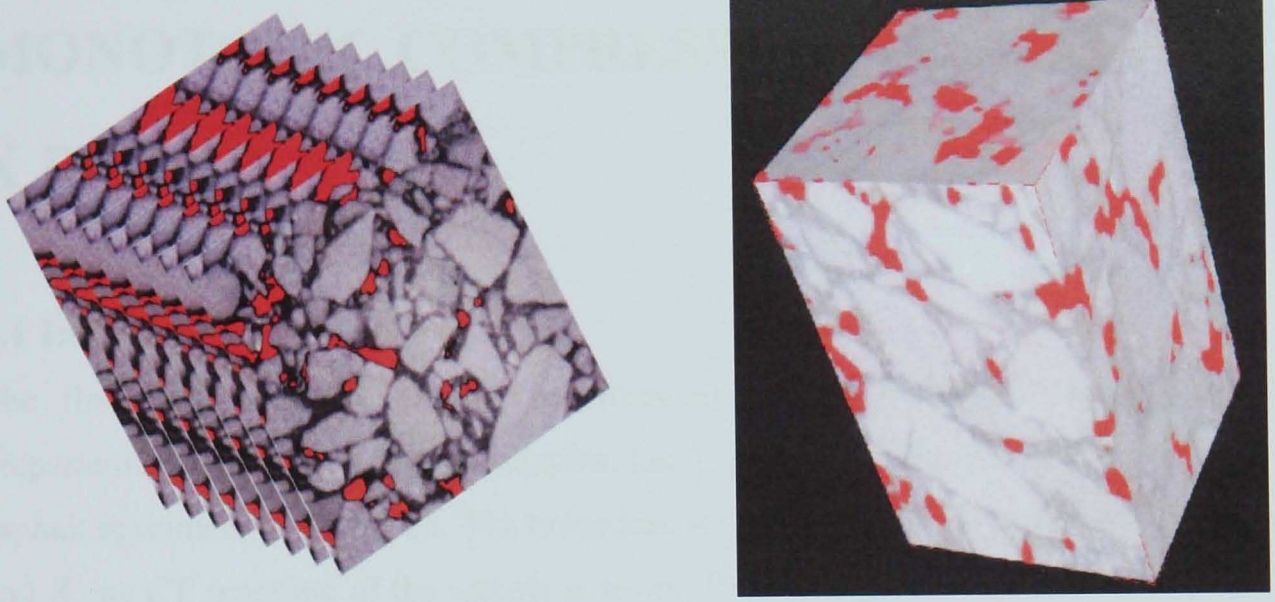

Figure 3.19 3D image from 2D images

Chapter 4

MONOTONIC COMPRESSION TEST AND X RAY CT

4.1 Introduction

The first section of this chapter describes material mix design, densities, specimen preparation and testing of asphalt samples. Later on the test protocol for the strength test of asphalt specimens is discussed. The procedure for stopping the test at different strain levels and X ray CT scanning of the sample is given. Developing 3D images and image analysis for asphalt mixtures are included. Analysis of data for microdamage during strength testing of asphalt mixtures and the relation between damage from X ray CT and from mechanical testing has been included.

4.2 Specimen Preparation and test Equipment

A close graded Dense Bitumen Macadam (DBM) surfacing was selected for testing (BS 1993). Granite aggregates and a 100 Penetration grade bitumen were used to produce the mixture. To be consistent with previous work, the binder content and air void content were selected to be 5.5% and 6% respectively (Dunhill et al. 2006). Cylindrical specimens were selected to provide a uniform stress distribution under the applied load. Specimens, 100mm in diameter and 100mm in height, were prepared using a gyratory compactor (Figure 4.2). The mould surface was oiled for each specimen before pouring the mix. In order to obtain uniform results, it was confirmed that the specimens should have similar height and diameters. The dimensions of specimens confirmed to the criteria that the minimum dimension of the specimen should be five times the maximum aggregate size.

The overall air void contents for all the specimens were determined in the laboratory prior to testing and scanning. This information was used for calibration of the grey-scale images. The aggregate gradation and mix design curve is given in Table 4.1 and Figure 4.1

respectively. Mixing was carried out according to the procedure of the Asphalt Institute (1988).

A 6mm diameter steel ball bearing was put in the centre of each specimen. The ball was used to locate the centre of specimen while scanning the sample in the X-ray machine. The ball was located in the first few trials and used as a reference for full scanning of the sample. In order to make sure that the steel ball was positioned correctly in the middle of the specimen, it was put in after half of the mould had been filled with the mix. As the density of steel is different from the asphalt mix, it can be seen and differentiated from asphalt mix in the X ray images. It was observed that due to the steel ball bearing the density of the asphalt specimen and the design void content were slightly changed. The weight correction due to the steel ball was adjusted in mixture weight for each mould.

In order to characterize the stress strain behaviour of asphalt microstructure under different conditions, three strain rates and temperatures were selected (Table 4.2).

4.3 Laboratory void content

The void content of specimens was determined in the laboratory before taking the specimen for X ray scanning. For determining the void content the bulk densities of the specimens were determined according to BS 598 part 3. The specimen was first weighed dry in air and then weighed when sealed in an aluminum foil. After that the specimen was weighed in water. The following equation was used to determine the bulk density.

$$\rho = \frac{M_{au} \cdot \rho_w}{M_{ac} - M_{wc} - \left(\frac{M_{ac} - M_{au}}{S_{gf}} \right)} \tag{4.1}$$

where ρ is bulk density, ρ_w is density of water, M_{au} is mass of the specimen in air uncoated, M_{ac} is mass of the specimen in air sealed in aluminum foil, M_{wc} is mass of the specimen in water coated with aluminum foil and S_{gf} is relative density of aluminum foil.

The maximum density and void content for DBM was determined using equations 4.2, 4.3 respectively.

$$\rho_{\max} = \frac{M_A + M_B}{\left(\frac{M_B}{G_b}\right) + \left(\frac{M_A}{G_a}\right)} \cdot \rho_w \qquad (4.2)$$

$$V_v = \frac{(\rho_{\max} - \rho)}{\rho_{\max}} .100 \qquad (4.3)$$

where $M_A + M_B = 100$, $\rho_{\max}$ is maximum theoretical density, M_A is aggregate content percent by mass of the total mixture, M_B is binder content percent by mass of the total mixture, G_b is specific gravity of the bitumen, G_a is specific gravity of the aggregate and ρ_w is density of water.

4.4 Testing and X ray Scanning

Monotonic compressive testing to failure was conducted at 5°C, 23°C and 35°C using strain rates of 0.1sec^{-1} , 0.01sec^{-1} and $0.001\ \text{sec}^{-1}$. Three specimens were tested at each temperature using an Instron testing machine and stress strain data was plotted. The stress strain curve for asphalt mixtures can be divided into four distinct areas, a linear elastic part, inelastic hardening, peak strength response and a descending strain softening part (Figure 4.3). In early stages of the test, the stress increase in proportion to the strain, there is then small region of hardening where slop of stress strain curve decrease as the peak stress is approached. Beyond the peak, the material then softens and the stress decreases rapidly as failure occurs (Dunhill, 2002).

Results were used to produce reference stress-strain curves (Table 4.3, Figure 4.4a). To get consistent strain values from the testing and X ray CT scanning of specimens, friction reduction treatment was done which resulted uniform failure in the specimens (Figure 4.4b). Additionally two specimens at each temperature and strain rate were then tested but the procedure was stopped at pre-selected strain values so that scanning could be

undertaken (Figure 4.5). The detail of specimens tested with rest periods is given in Table 4.4. The data was plotted for each individual test condition (Figures 4.6-4.10). For specimens tested with rest period, the peak stress was slightly lower because of the induced damage before reaching peak stress point. Scanning at each pre-selected strain level takes approximately 12 hours during which some recovery was observed to occur. Consequently, the height of each specimen was measured before and after scanning using a purpose built rig.

Scanning setup

An X-ray CT system (Venlo H -350/225) with IMPS operating software was used for scanning the specimens (Figure 4.11a). The machine has Venlo 5 Axis manipulator with high precision turntable (Figure 4.11b).

The 350kV source was used to obtain the 2D images (slices) (Figure 4.12). Slices were taken at 0.083mm interval (which is equal to the system resolution) along the height of the specimen. After several trials it was found that the clearest images were obtained using the following parameters:

Voltage: 342kV

Current: 2.0mA

Exposure: 7.5 minutes

Primary filter: Copper, 2mm in thickness

Back filter : Aluminium, thickness varied from 0mm to 50mm.

Using these parameters the specimens were taken into X ray CT and scanned at every stage of predefined strain.

4.5 Aggregate gradation from X ray images

In order to determine the minimum particle size that can effectively be determined from the X-Ray CT images, specimens were scanned at three different positions ensuring that the intervals between scans were greater than the maximum size of the aggregate in mixture. To separate the aggregate portion from the X-Ray CT image, the threshold gray value for the aggregate was selected and the other components were removed (Figure 4.13). The dimensions of each aggregate particle were then determined from the 2-D images (the third dimension was determined from the principle of stereology. Stereology is the information

about the 3D shape of an object from available 2D data by considering the object as homogenous (Underwood,1970). Aggregate sizes from the X-Ray images using three different specimens were determined and average values were calculated. The resulting reconstructed aggregate grading curve is shown in Figure 4.14 where it is compared to the initial grading curve. It can be seen from this Figure that agreement is generally good above 5mm below which the grading curve obtained from the X-Ray CT images tends to under predict the number of particles. In order to determine whether this is related to the bitumen films present between aggregate particles obscuring the smaller sizes, the aggregate was mixed without bitumen and scanned in the X-Ray CT (Figure 4.15). Results are also shown in Figure 4.14 from where it can be seen that the aggregate grading is very similar to that obtained from the mixture that included the bitumen. The aggregate particle histogram was plotted as shown in Figure 4.16. Using X ray images from asphalt samples the distribution of aggregate in asphalt mixture was also determined (Figure 4.17).

4.6 Microstructure of asphalt from X ray images

2D images were stacked using VG Studio max 1.2.1 software to generate 3D images of the asphalt samples. The 3D image can be cut to study the internal structure of the compacted asphalt specimens non-destructively (Figure 4.18). The air voids were identified by appropriate thresholding (adjusting the grey value) so that the volume of voids in the scanned image was the same as the measured void content. Using image analysis techniques, the volume of void content can be separated from the 3D image of the compacted specimen (Figure 4.19). The volume, 3D co-ordinates, surface area and size of each individual void were calculated from the image data. It was determined from the X ray CT image analysis that the size of air voids in the gyratory compacted asphalt specimens varied. Five different samples were scanned and the data of air void size in the middle and near the edges were plotted (Figure 4.20).

Images from specimens tested at three different temperatures (5°C, 23°C and 35°C) and scanned at selected test stages were analysed for void content. Generally a trend of increase in void content was observed in compression testing of asphalt (Figure 4.21). The increase in void content and number of total voids corresponding to various test stages were determined from X ray images (Figure 4.22, Figure 4.23, Table 4.5). It can be seen from these figures that the increase in void content due to increase in strain is not uniform

through the height of the specimen; also the increase in total number of air voids is varying. The void content values of three test temperatures were plotted on stress strain curves (Figure 4.24). The maximum stress for 5°C, 23°C and 35°C curves in the Figure is 14.80MPa, 8.01MPa and 3.82MPa respectively. Similar procedure was followed for the image analysis of specimen tested at 0.1 sec^{-1} and 0.001 sec^{-1} strain rate and scanned at selected test stages. The increases in void content values were calculated as shown in Figure 4.25. The maximum stress for 0.1 sec^{-1}, 0.01 sec^{-1} and 0.001 sec^{-1} curves in the Figure is 14.2MPa, 8.19MPa and 4.87MPa respectively (Figure 4.25a).

It can be seen from these figures that the air voids were found to increase with increasing strain as damage accumulates in the specimen. It can also be seen from these figures and from figure 4.26 that there is a greater increase in damage (void content) for the specimens tested at the higher temperatures and lower strain rates-. It was observed from X ray CT images that some new voids were generated along with size increase and interlinking of existing voids. For specimens tested at low temperature, the size increase in existing air voids was found dominant compared to developing new voids.

4.7 Microstructure Anisotropy

3D images of the asphalt specimens were analyzed for void content and it was found that the internal void content is not uniform throughout the specimen. Also for specimens tested in compression the increase in void content was not uniform across the height and diameter of specimen. The difference in void content before starting the test and at failure is shown in Figure 4.27 and Figure 4.28. It was observed that the increase in void content was comparatively greater in the middle of the specimen. This indicates that microstructural data parameters from 2D images may represent an average value for a sample. For some specimens a few aggregate particles were found to have broken at the maximum stress (Figure 4.29).

4.8 Microdamage in Asphalt (Continuum damage mechanics)

According to continuum damage mechanics, damage is caused due to nucleation, growth and coalescence of microvids. During the deformation process the internal voids / cavities may grow and cause new micro defects. Considering the damage in the cross section area

of the damaged body as an area of element dA with unit normal vector n (Figure 4.30), the area of the defects in this element is denoted by dA_D and the amount of damage then can be characterized by the fraction area w as (Dietmar et al. 2006)

$$w(n) = \frac{dA_D}{dA} \quad \text{With } 0 \le w \le 1 \tag{4.9}$$

If w=0 the material is considered as undamaged and if w=1 the material is considered as fully damaged. If the damage is constant across the finite area, for example in case of a uniaxial test, the relation can be written as

$$w = \frac{dA_D}{dA} \tag{4.10}$$

This relation can be applied for void-like defects. If the stresses are replaced by the effective stresses the stress-strain behaviour of the damaged material can then be described by the constitutive law of the undamaged material (Dietmar et al. 2006).

$$\varepsilon = \frac{\tilde{\sigma}}{E} = \frac{\sigma}{(1-w)E} \tag{4.11}$$

where E is the Young's modulus of the undamaged material

Hence the damage can be determined by measuring the effective Young modulus

$$E = (1-w)E_o \quad \text{or} \quad w = 1 - \frac{E}{E_o} \tag{4.12}$$

Considering the asphalt mixture as a homogenous material, the increase in void content has been calculated for asphalt specimens in the compression test. At the beginning of the test the entire void content is taken correspond to w=0. The void content at specimen failure is to be taken w=1 i.e. if the void content in a specimen is 6.3% at the beginning of the test

and 9.7% at specimen failure 6.3% voids is taken correspond to w=0 and 9.7% is taken as w=1. The value of relative stiffness E/E_o has been determined from mechanical testing at each test stage and that of damage parameter w has been determined from void content calculated from X ray computer tomography. The data has been plotted for three different test temperatures (Figure 4.31). The relative stiffness and damage parameters were also determined for three different strain rates and the data was plotted (Figure 4.32).

The damage parameter w determined from X ray image analysis was plotted against the strain data from mechanical testing. Initially there is little or no change in the damage parameter, followed by an increase. The trend of increase in damage with increase of strain in mechanical testing is approximately similar for three different test temperatures (Figure 4.33). Trend of increase in void size generally due testing at six defined stages can be seen from X ray CT images (Figure 4.34).

4.9 Summary

From advances in X ray CT, it is now possible to study asphalt specimens internally non-destructively. A procedure of scanning the asphalt specimens in the middle of testing is developed. Because of different densities, the components of asphalt mixture (aggregate, binder, mastic and air voids) were found to be identified separately. Aggregate stone of different sizes were separated from the other components within image of compacted asphalt specimen and were compared to the aggregate grading curve of the original mix design.

Increase in void content due to increase in load was calculated from X ray CT scanning and was found not uniform through the height of the specimen. The maximum increase in void content value was found in the middle of the specimen. Strain produced due to applying load was related to increase in design void content from X ray images. Trend of high increase in void content was found for specimens tested at high temperature. Similarly the increase in void content was higher for specimens tested at low strain rate. The change in internal structure and damage propagation due to mechanical loading were determined from X ray image analysis. The resultant output data was related to macro properties such as stiffness of asphalt mixtures.

Table 4.1 Aggregate gradation for mix design

Aggregate for mix design	
Sieve (mm)	Percent passing
14.0	100
10.0	97.11
6.3	69.56
5	57.54
3.35	39.04
2.36	31.54
1.18	22.54
0.60	16.48
0.30	12.55
0.21	11.09
0.15	9.88
0.075	7.92

Table 4.2 Detail of test conditions

Asphalt mixture	Test temperature (°C)	Strain rate ($1/sec^{-1}$)
DBM	5	0.1,0.01,0.001
	23	0.1,0.01,0.001
	35	0.1,0.01,0.001

Table 4.3 Detail of samples tested without rest period

Specimen No.	Temperature	strain rate (sec^{-1})	Maximum stress (MPa)
07-321	5°C	0.1	30.2
07-518			31.4
07-320		0.01	14.31
07-520			14.7
07-522		0.001	7.67
07-521			8.2
07-523	23°C	0.1	14.1
07-319			13.7
07-517		0.01	7.94
07-519			7.75
07-322		0.001	5.1
07-323			4.8
07-526	35°C	0.1	8.8
07-525			8.23
07-524		0.01	3.98
07-527			3.78
07-528		0.001	3.54
07-317			3.21

Table 4.4 Specimens tested with rest period at selected stages for X ray CT

Specimen No.	Void content (%)	Test temperature	strain rate (sec^{-1})
1992	7.82	23°C	0.1
1995	6.0		
1223D	7.9		0.01
1223E	8.0		
2096	6.2		0.001
2349	8.6		
1223F	7.8	5°C	0.01
2350	8.10		
1928	6.0	35°C	0.01
1929	6.1		

Table 4.5 Detail of void content values (%) from six testing stages

Specimen No.	Void content (%)	Void content at 0 .5 % strain	Void content at 1. 0 % strain	Void content at 1 .5% strain	Void content at 2.0 % strain	Void content at 2 .5 % strain
1992	7.82	7.82	8.09	8.48	8.76	8.90
1995	6.0	5.85	6.10	6.35	6.63	7.05
1223D	7.90	7.80	8.10	8.38	8.75	9.01
1223E	8.00	8.00	8.19	8.43	8.67	8.96
2096	6.20	6.38	6.90	7.80	8.60	9.10
2349	8.60	8.73	9.08	9.70	10.65	11.52
1223F	7.50	7.50	7.66	7.91	8.08	8.14
2350	8.10	8.10	8.23	8.52	8.69	8.98
1928	6.0	6.11	6.65	7.23	7.91	8.78
1929	6.10	6.05	6.52	7.35	8.11	8.91

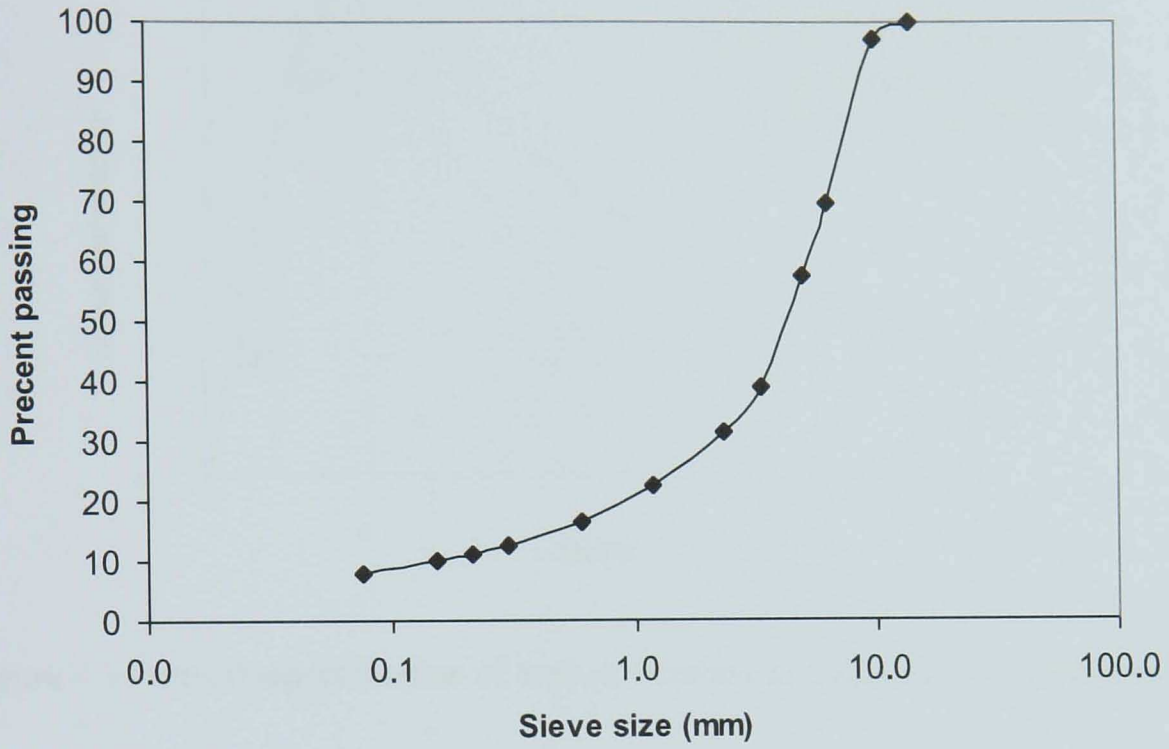

Figure 4.1 Aggregate grading curve for 10mm DBM mixture

Figure 4.2 Specimen for monotonic compression test

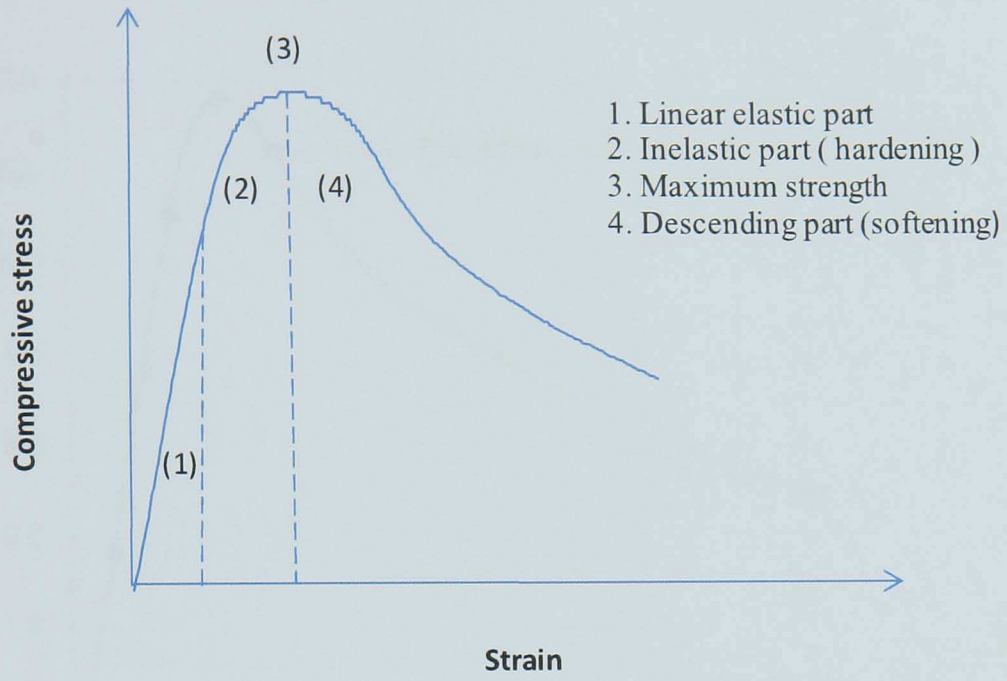

Figure 4.3 General representation of asphalt response in monotonic compression test

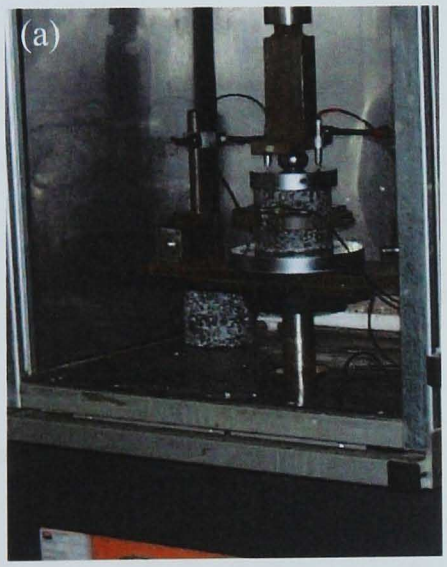

Figure 4.4 a) Sample in monotonic compression test, b) Typical failure of sample in monotonic compression test

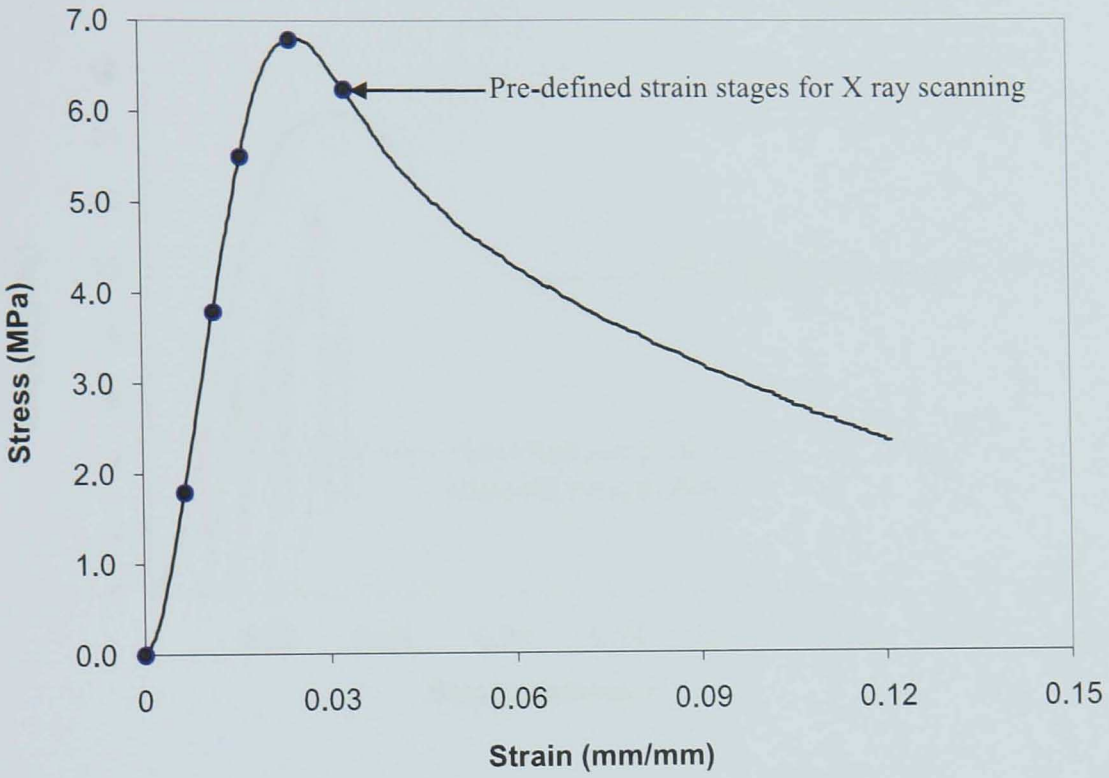

Figure 4.5 Proposed stages for testing and X ray scanning

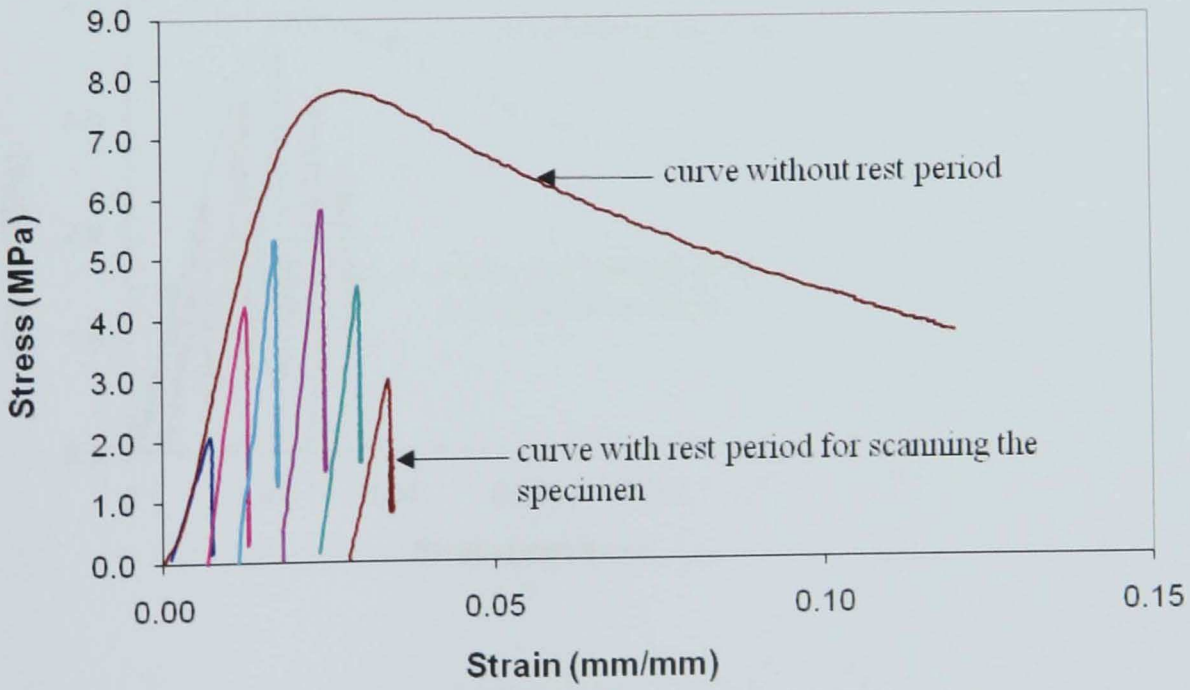

Figure 4.6 Curve for specimens tested at 23°C and scanned ($0.01sec^{-1}$)

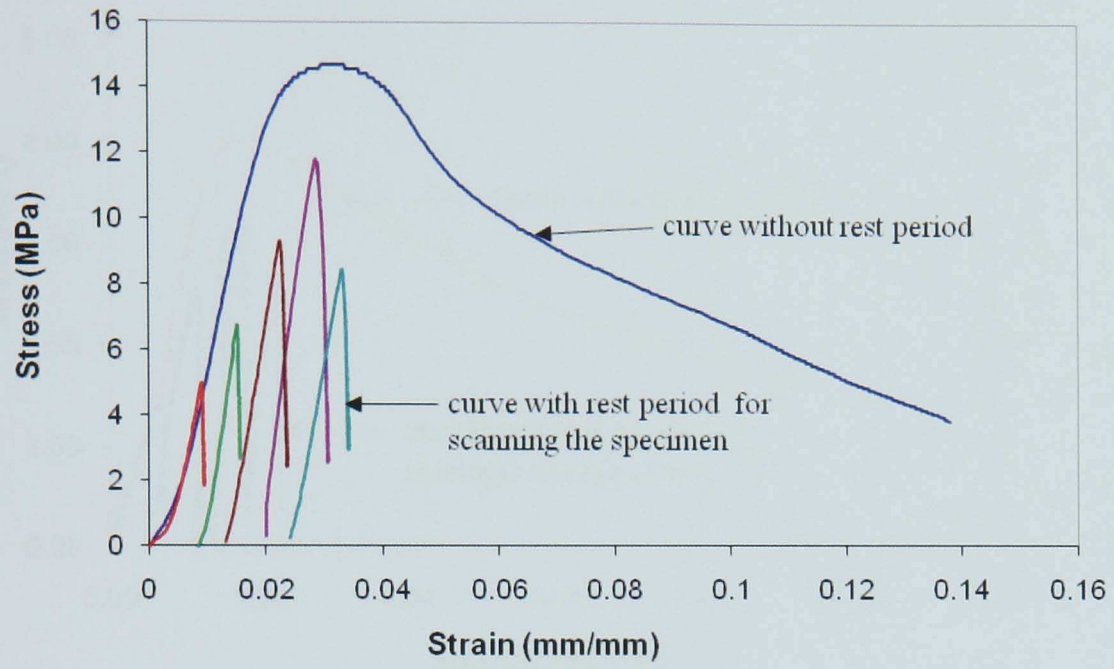

Figure 4.7 Curve for specimens tested at 5°C and scanned ($0.01 sec^{-1}$)

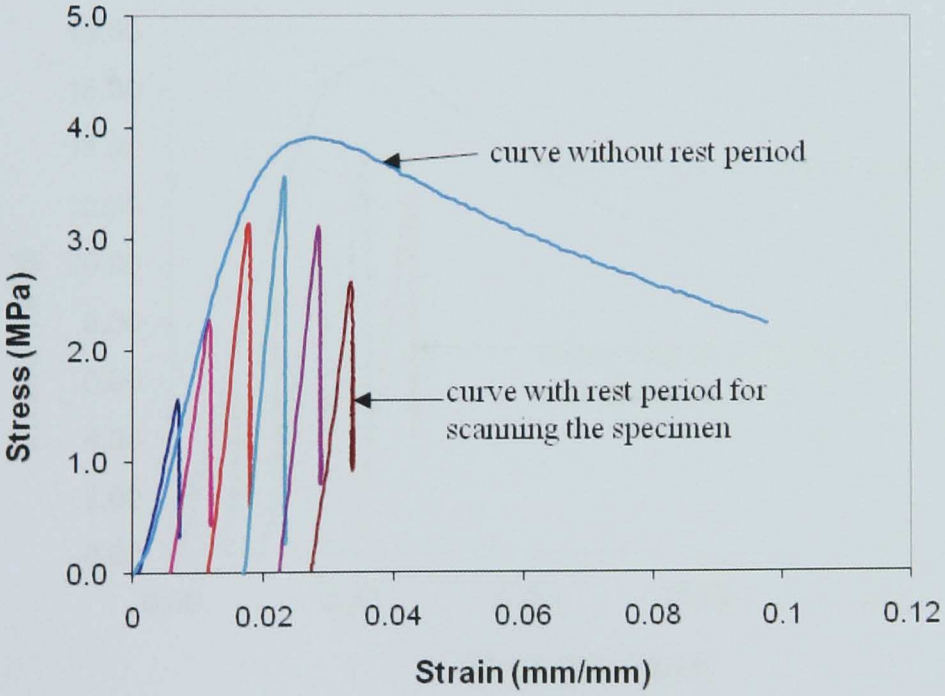

Figure 4.8 Curve for specimens tested at 35°C and scanned ($0.01 sec^{-1}$)

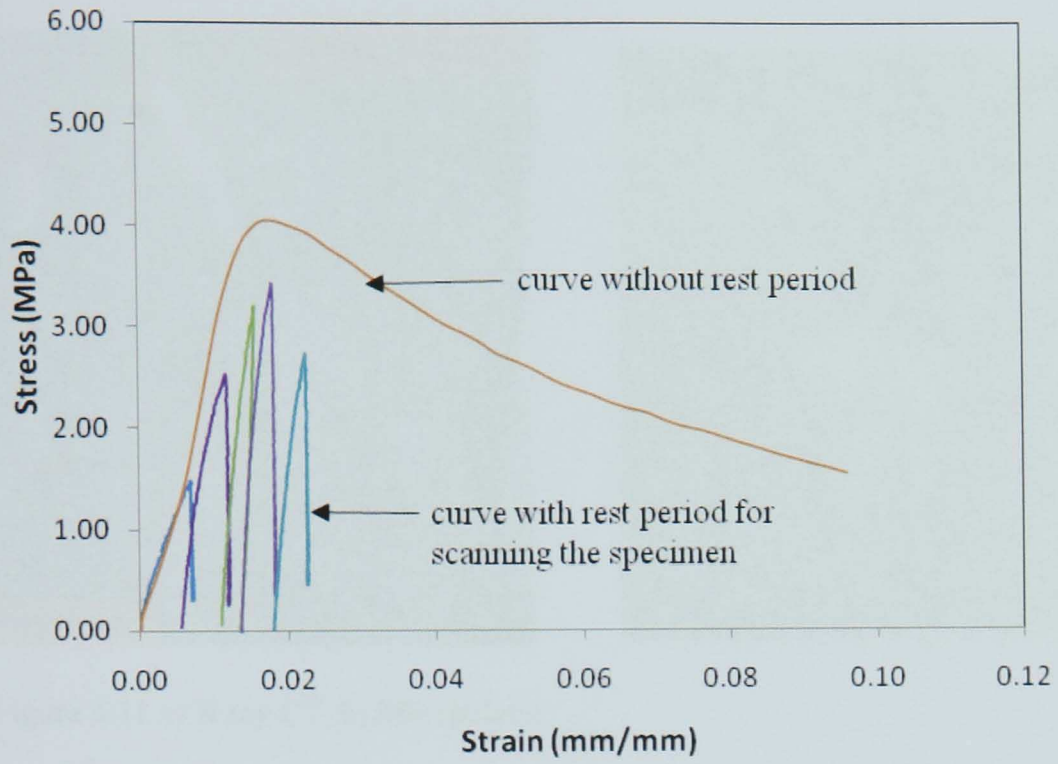

Figure 4.9 Curve for specimens at 23°C and scanned ($0.001 sec^{-1}$)

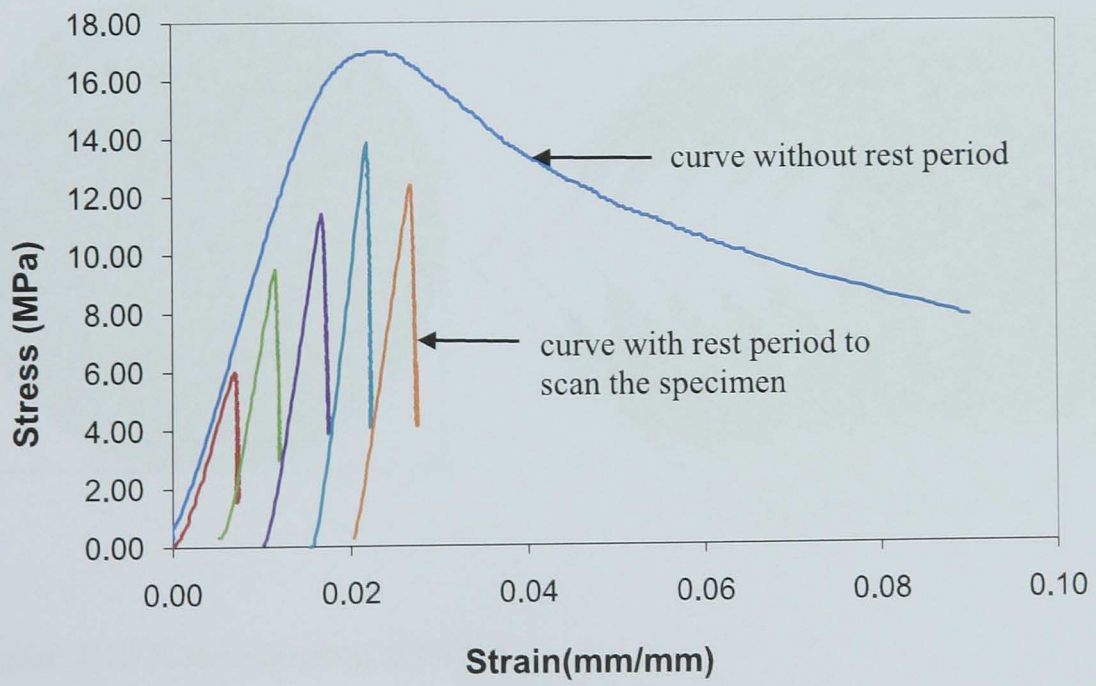

Figure 4.10 Curve for specimens tested at 23°C and scanned ($0.1 sec^{-1}$)

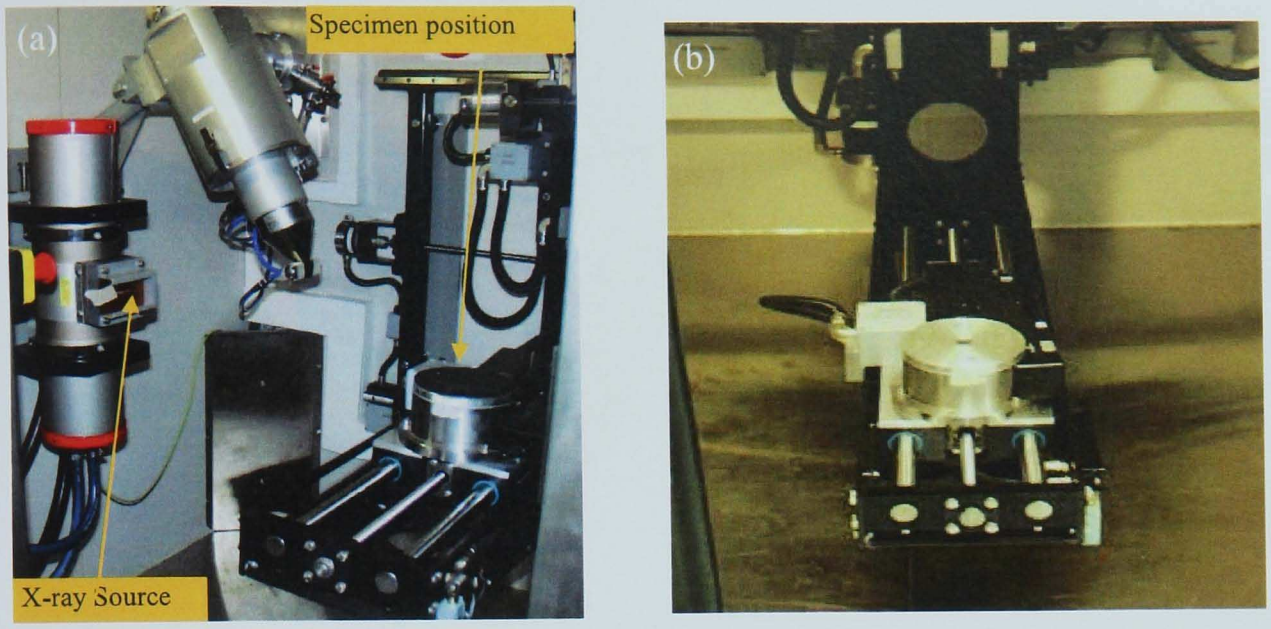

Figure 4.11 a) X ray CT, b) Manipulator

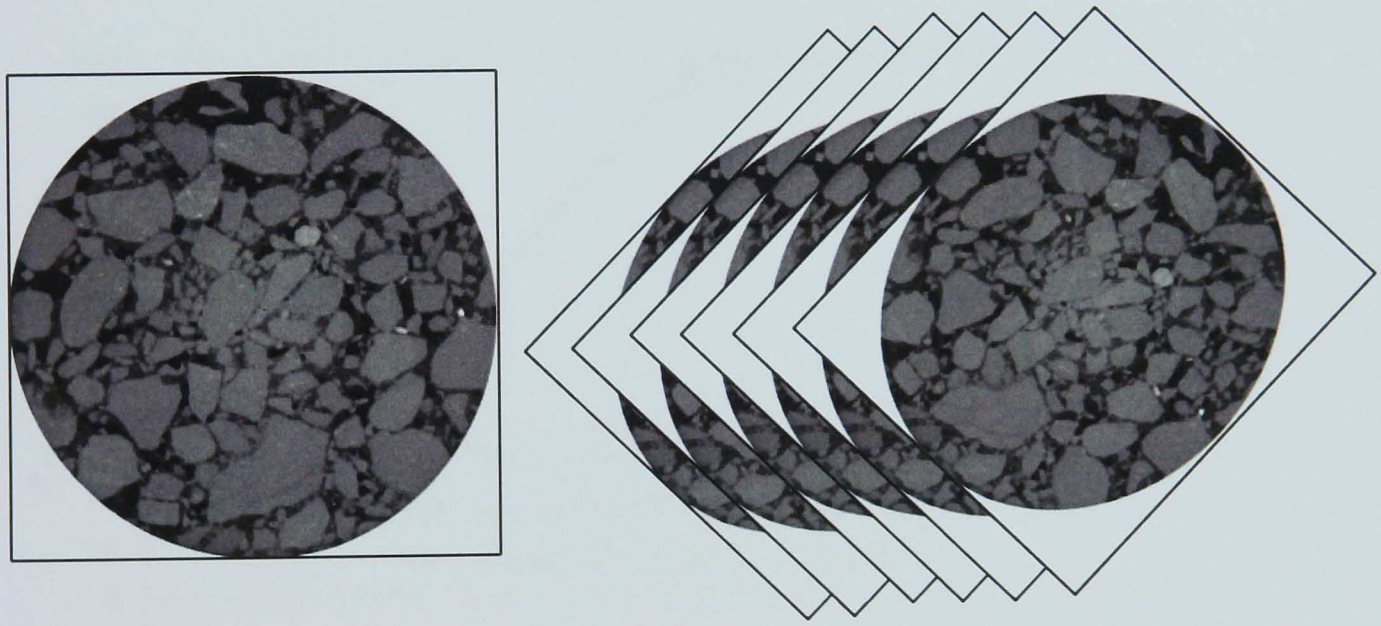

Figure 4.12 X ray scanning 2D slices

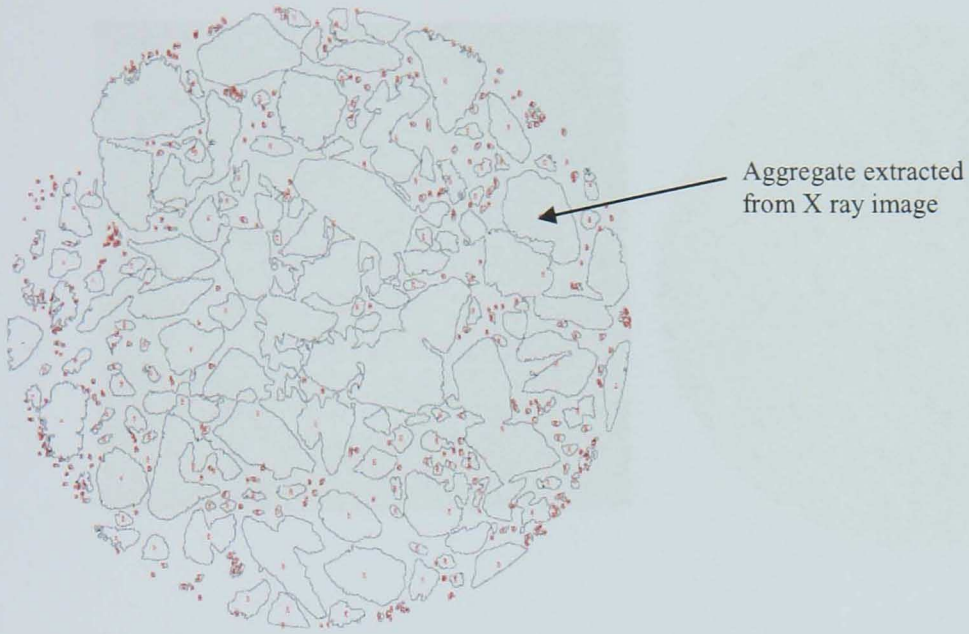

Figure 4.13 Aggregate particles extracted from X ray image

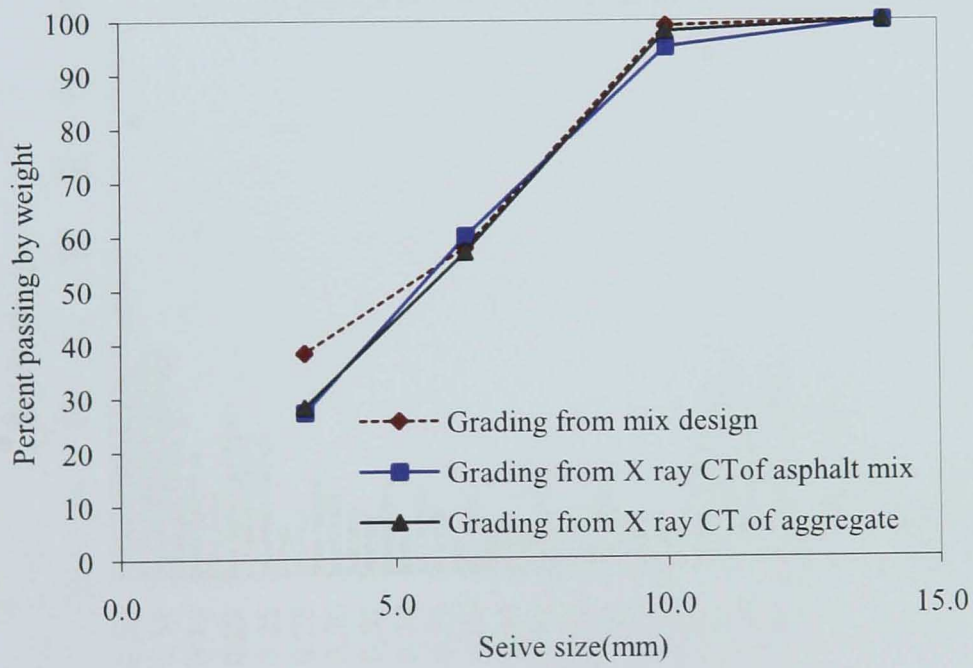

Figure 4.14 Comparison of aggregate grading from sieve analysis and from asphalt mixture X ray Images

Figure 4.15 a) Aggregate mix for X ray scanning, b) X ray image of aggregate without binder

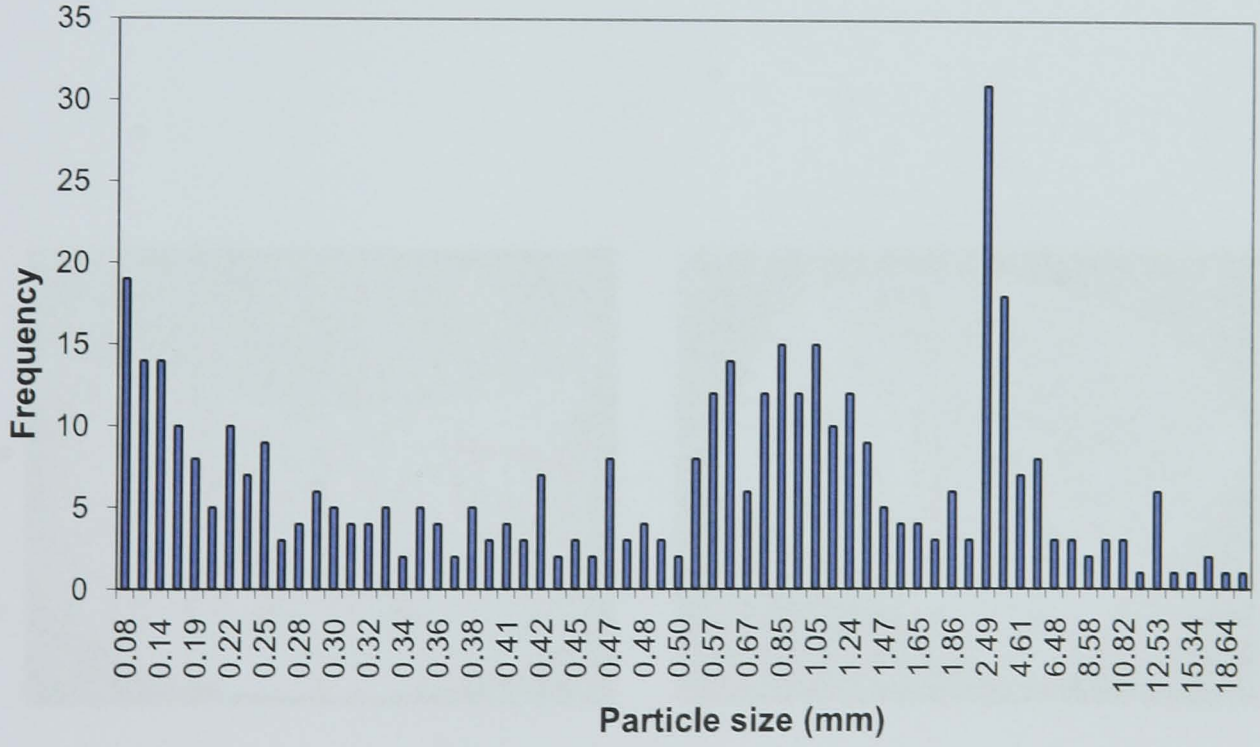

Figure 4.16 Histogram of aggregate particles in asphalt mixture

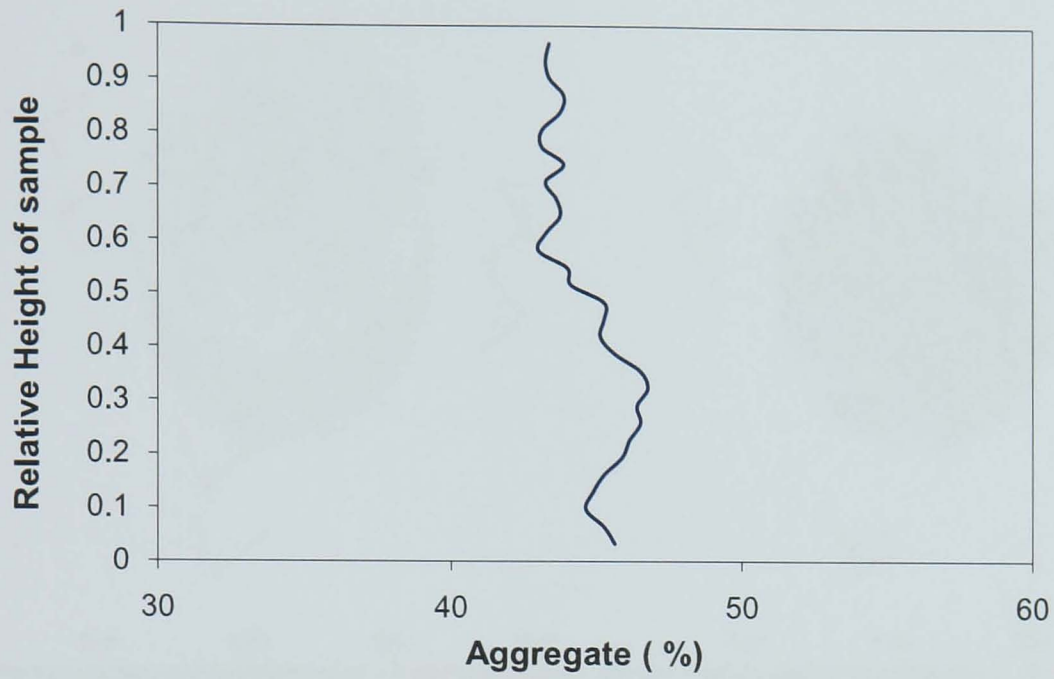

Figure 4.17 Distribution of aggregate in asphalt specimen

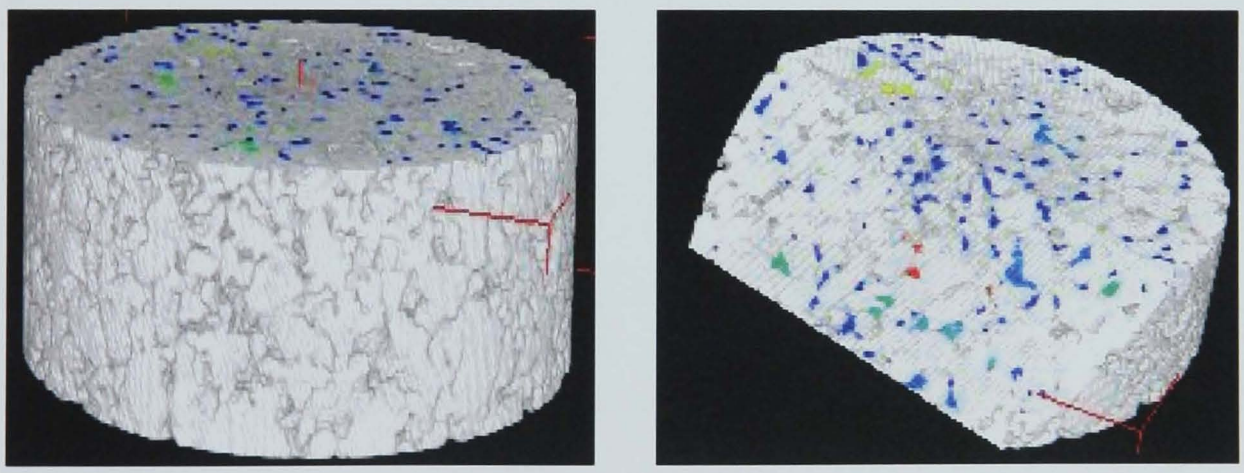

Figure 4.18 3D image of compacted asphalt specimen

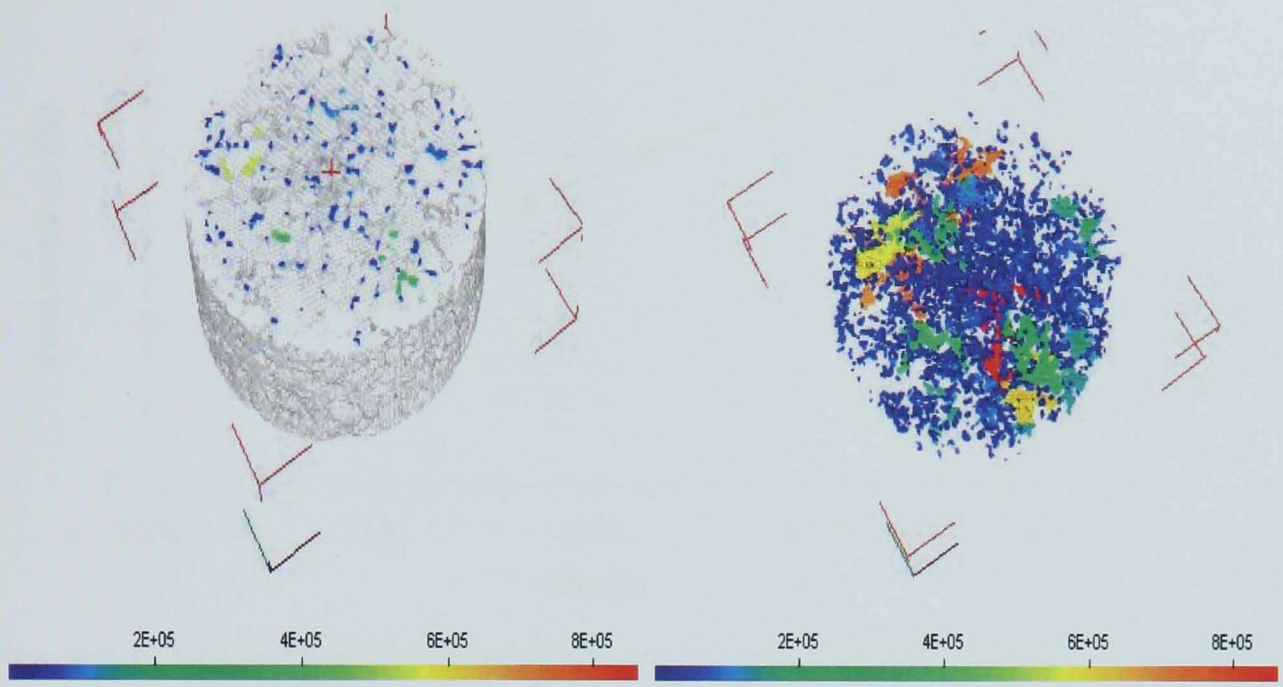

Figure 4.19 Air voids in asphalt 3D image (scale represent void size in voxels)

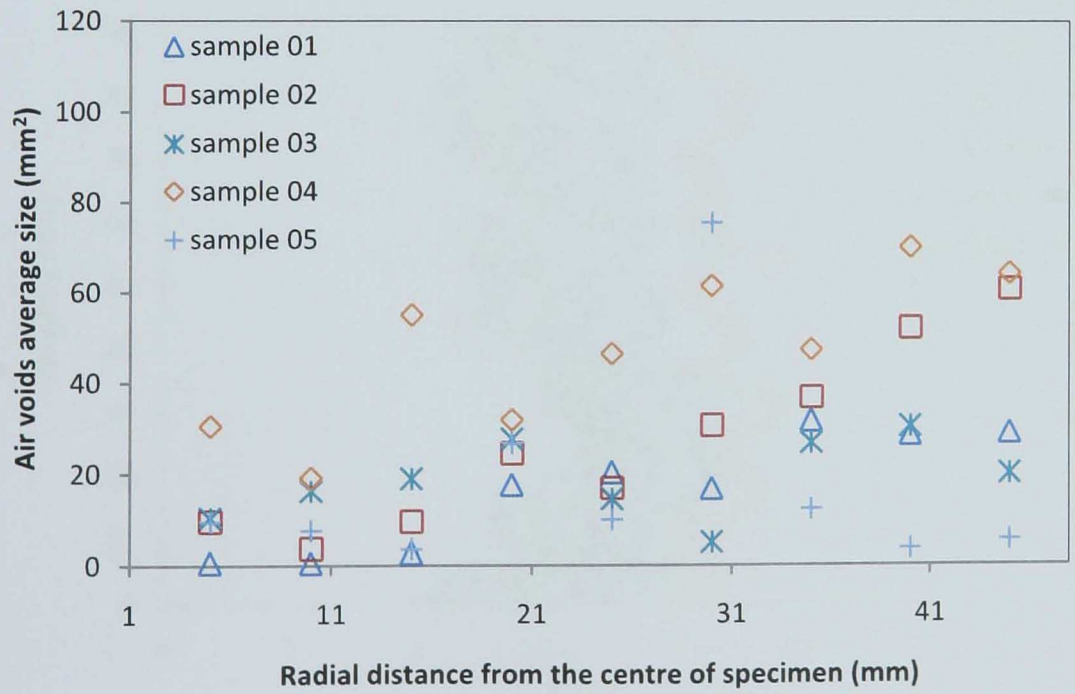

Figure 4.20 Air voids distribution in 100 mm gyratory compacted specimen

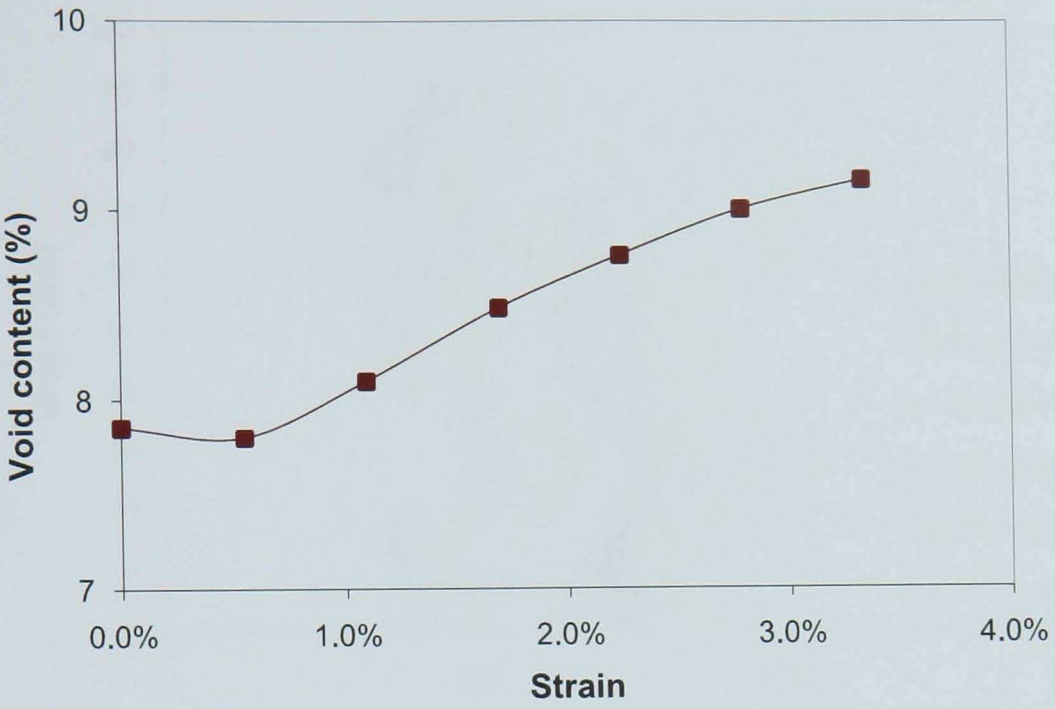

Figure 4.21 General trend of increase in Void content in compression test

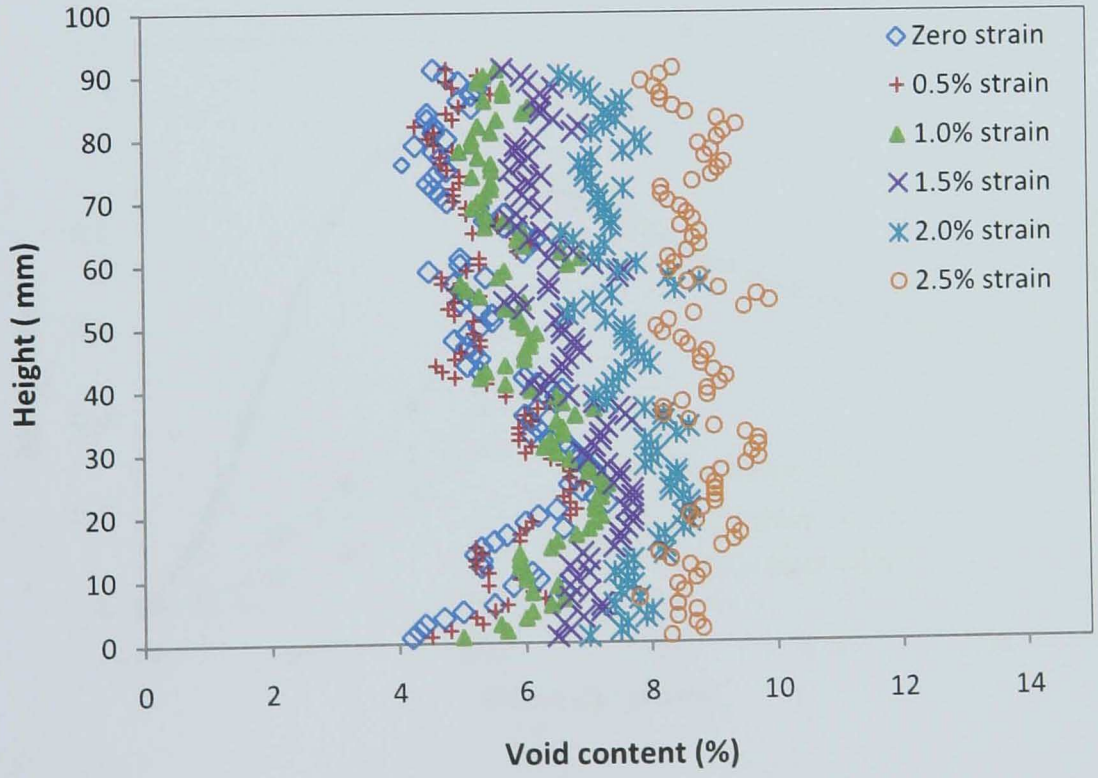

Figure 4.22 Void content corresponding to increase in strain

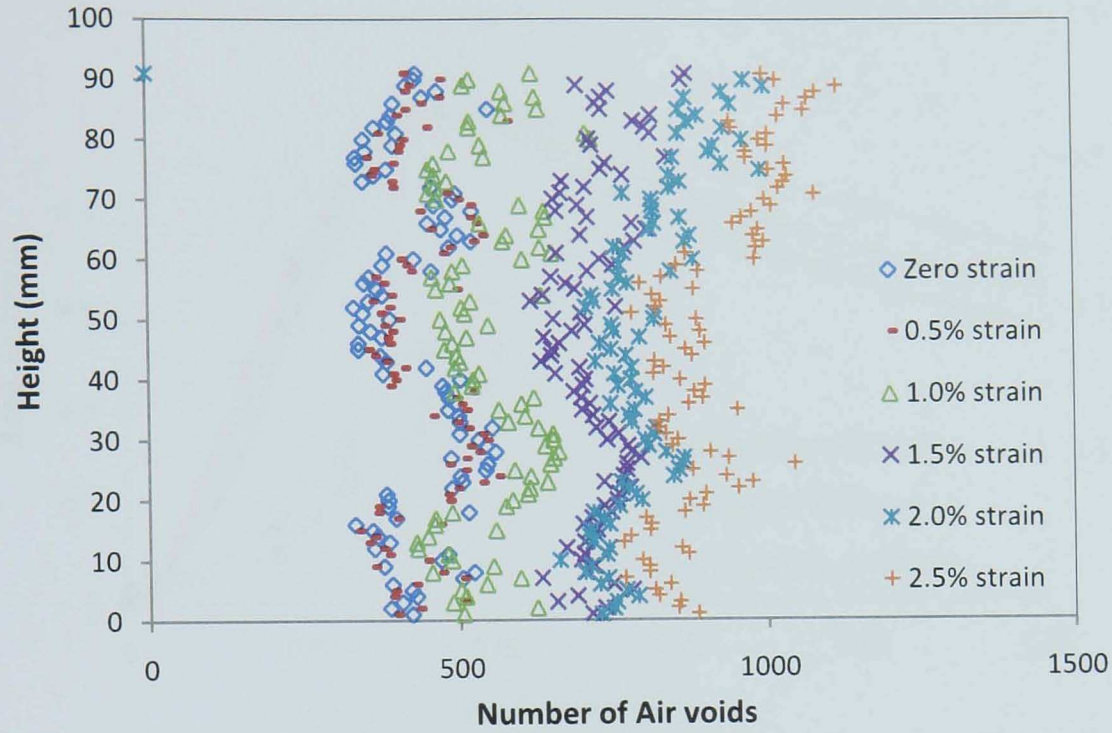

Figure 4.23 Number of air voids corresponding to increase in strain

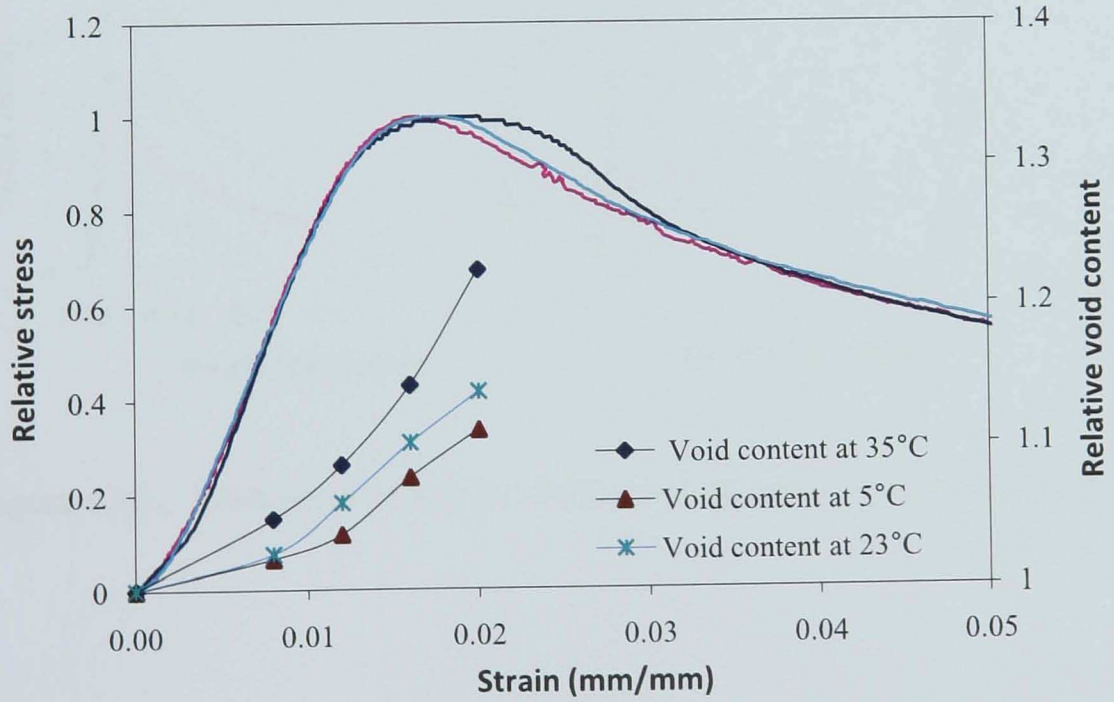

Figure 4.24 Void content with increase in strain at different temperatures at strain rate of 0.01/s

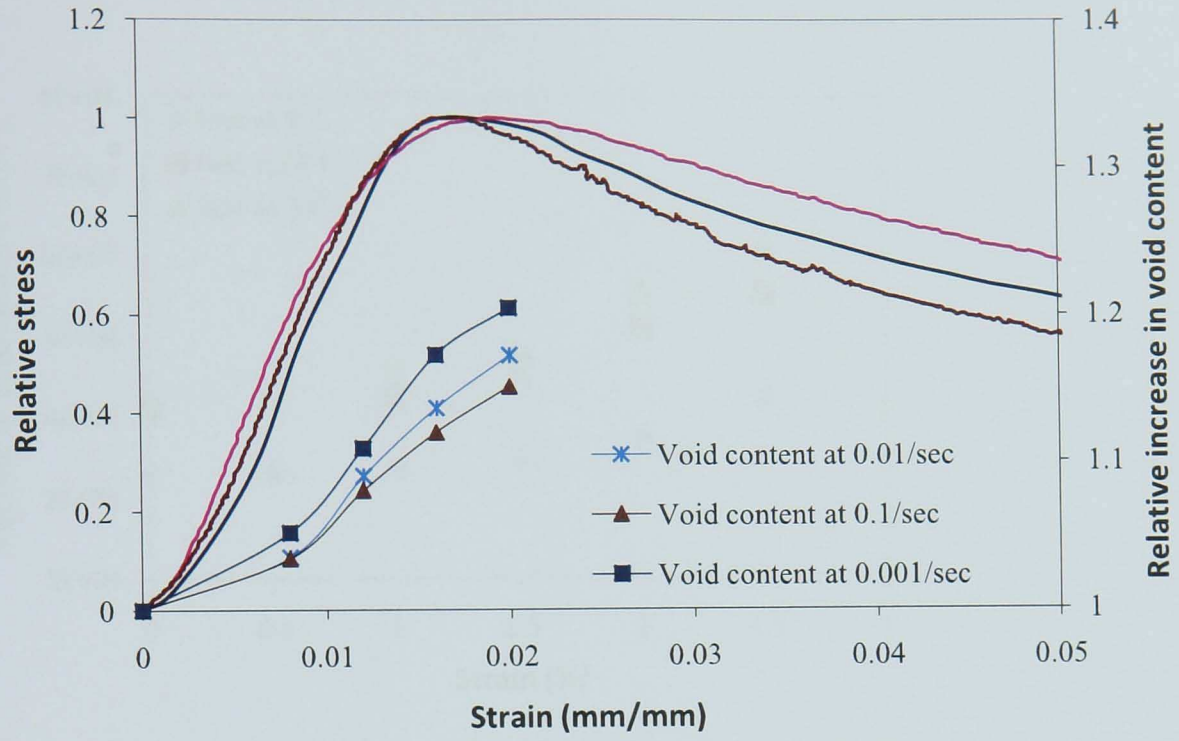

Figure 4.25 Void content with increase in strain at different strain rates at 23°C

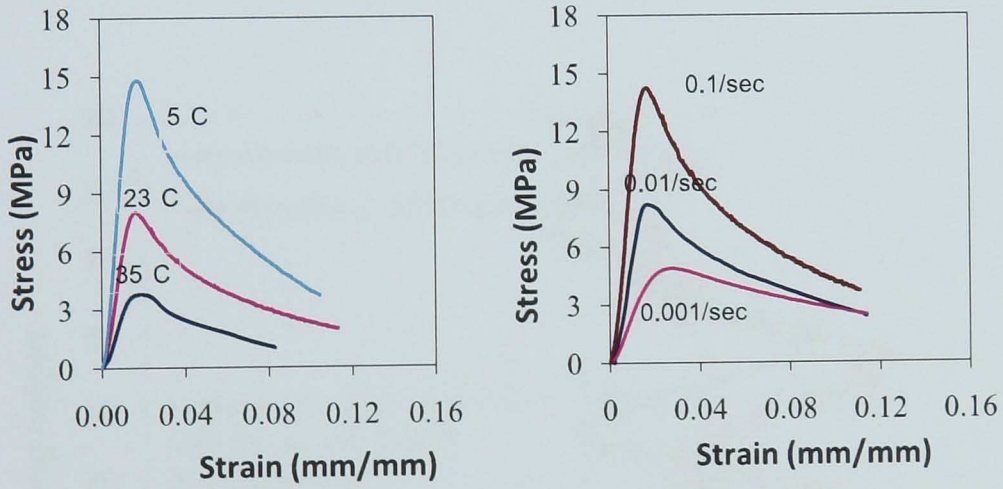

Figure 4.25a. Peak stress values for different temperature and strain rate testing

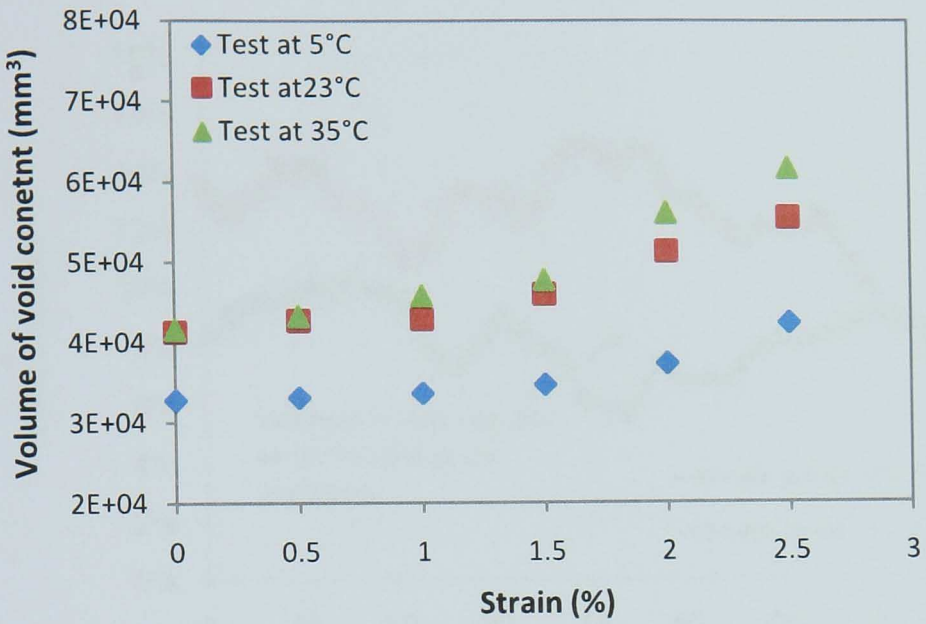

Figure 4.26 Increase in volume of voids with increase in strain

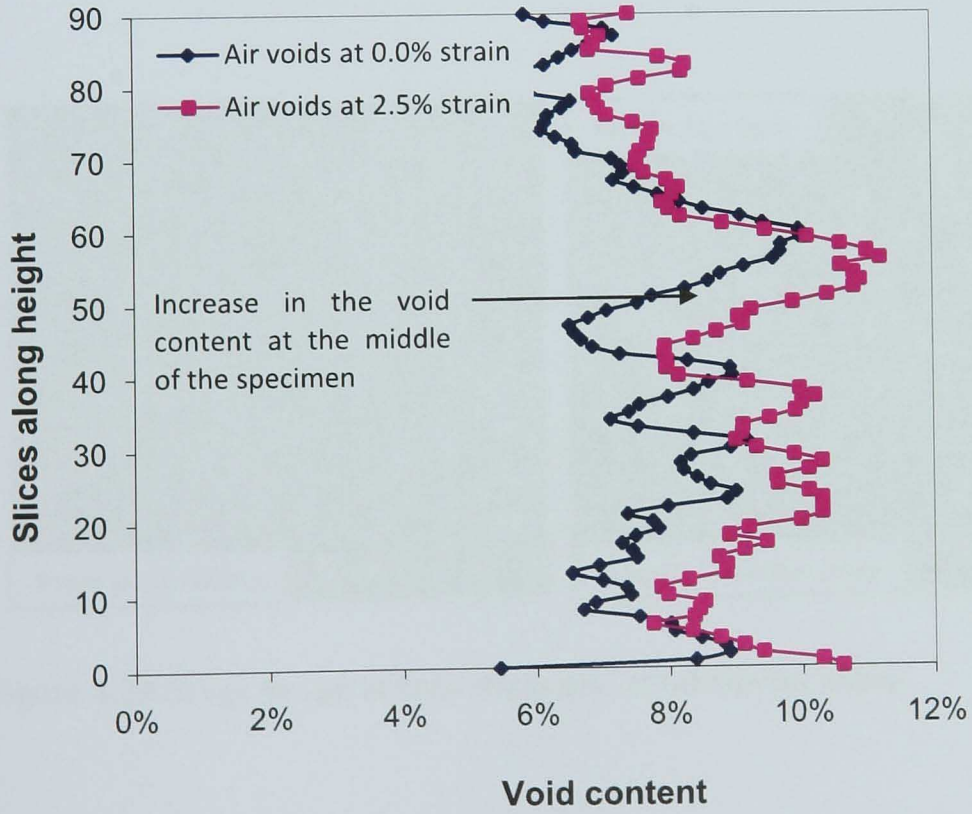

Figure 4.27 Air voids variation along the height at 23°C

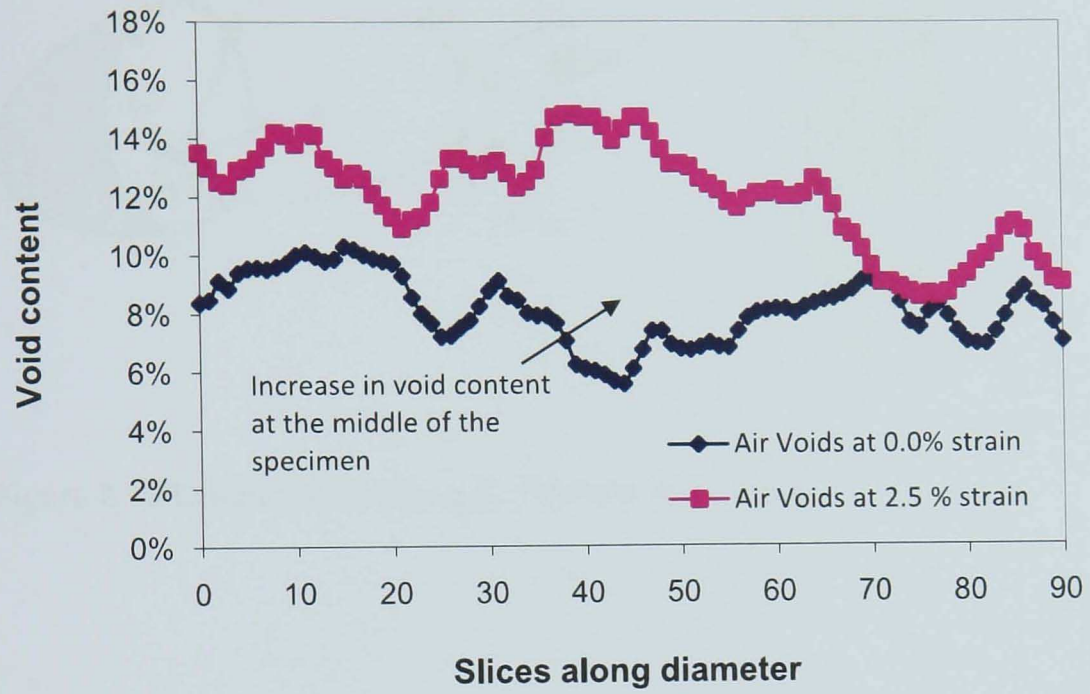

Figure 4.28 Air void along the diameter at 23°C

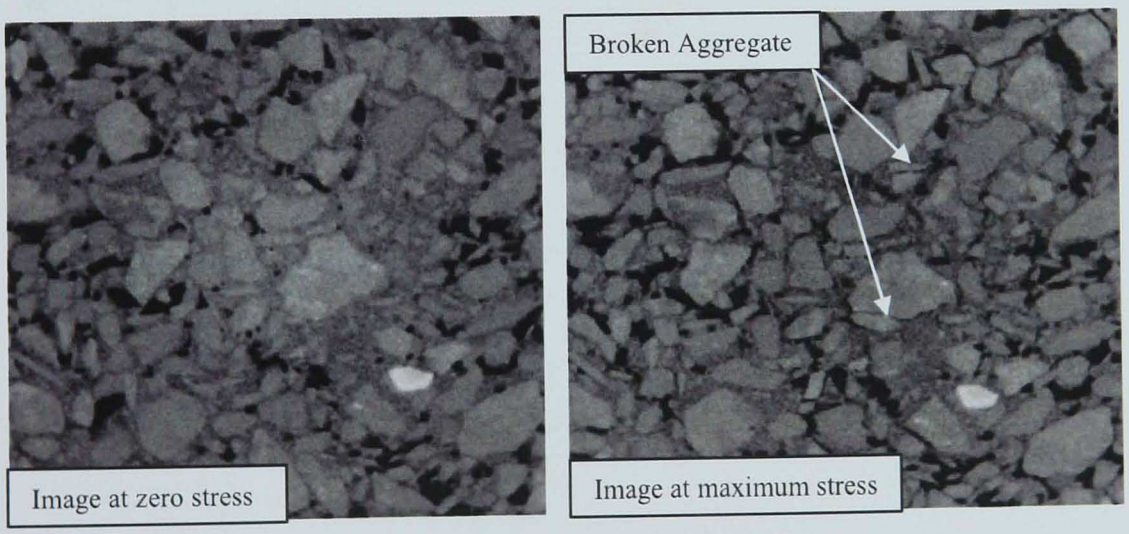

Figure 4.29 X ray image at zero stress and at maximum stress

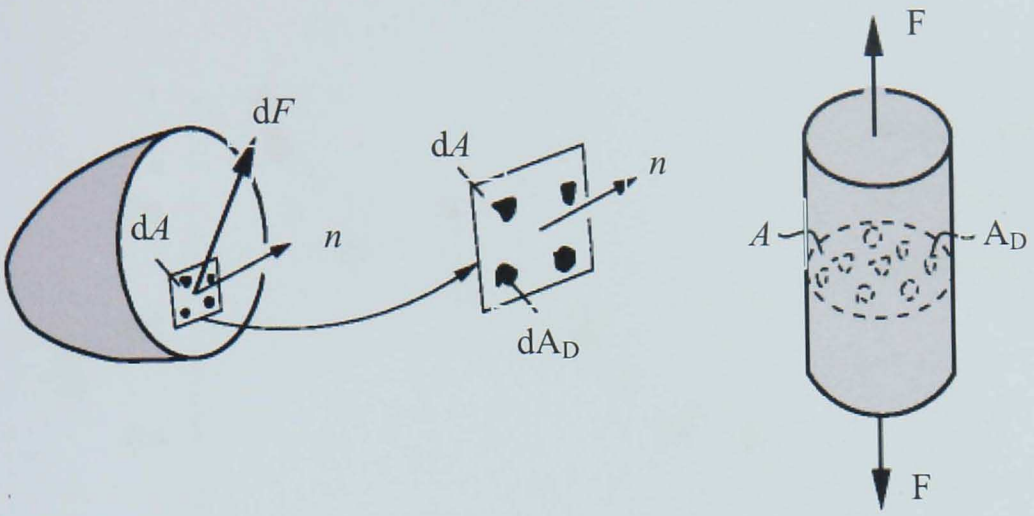

Figure 4.30 Definition of Damage (Dietmar et al. 2006)

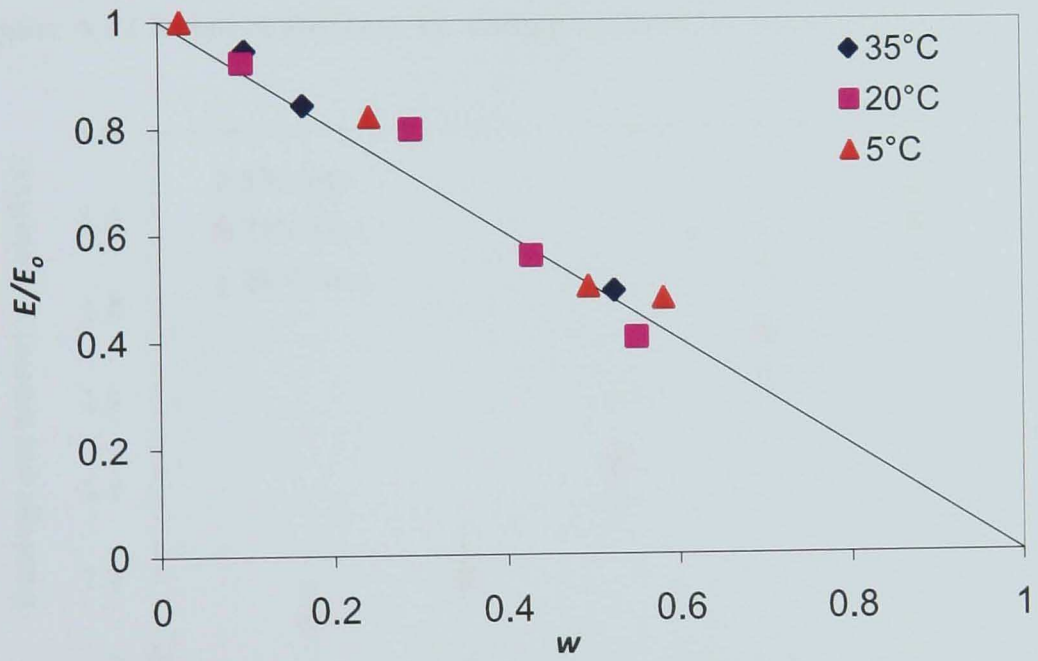

Figure 4.31 Relative stiffness vs. damage parameter from X ray CT

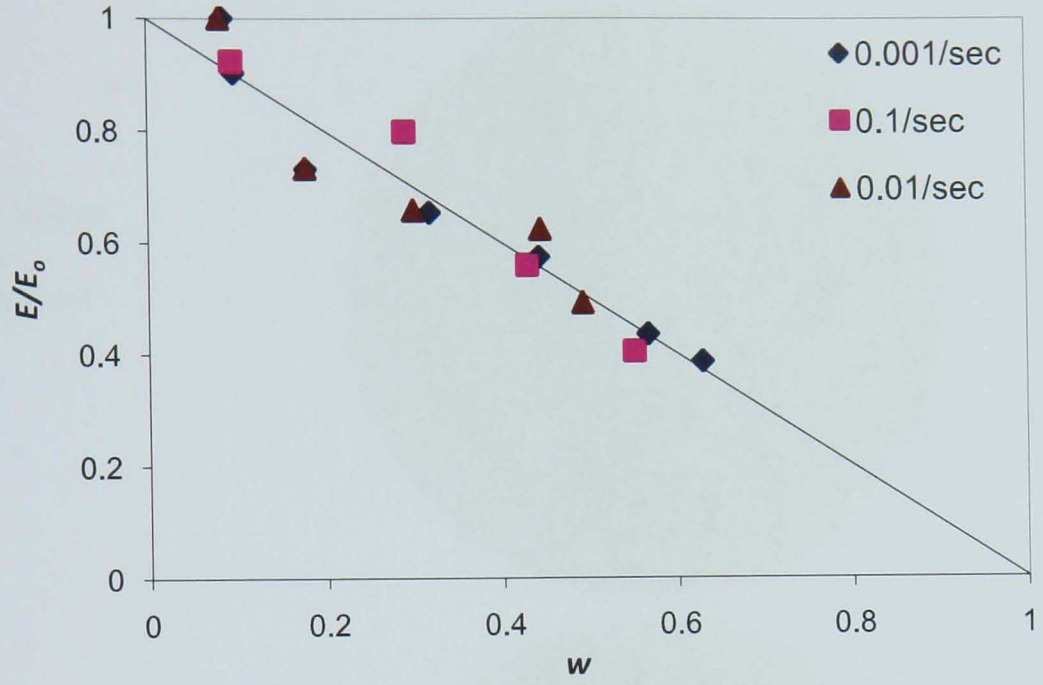

Figure 4.32 Relative stiffness vs. damage parameter from X ray CT

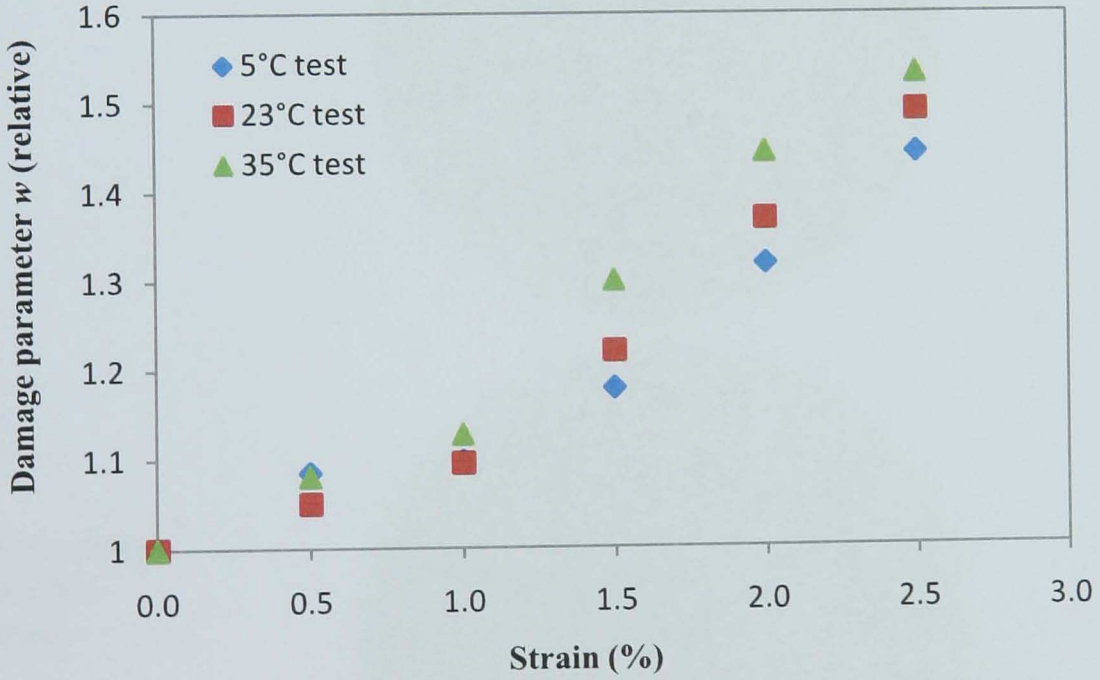

Figure 4.33 Relative Damage parameter from X ray CT vs. Strain from mechanical testing

X ray Image
before
starting test

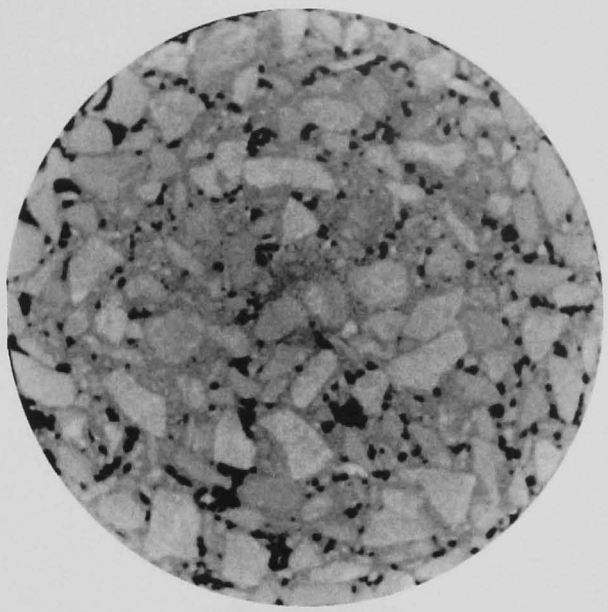

X ray Image
at 0.5%
strain

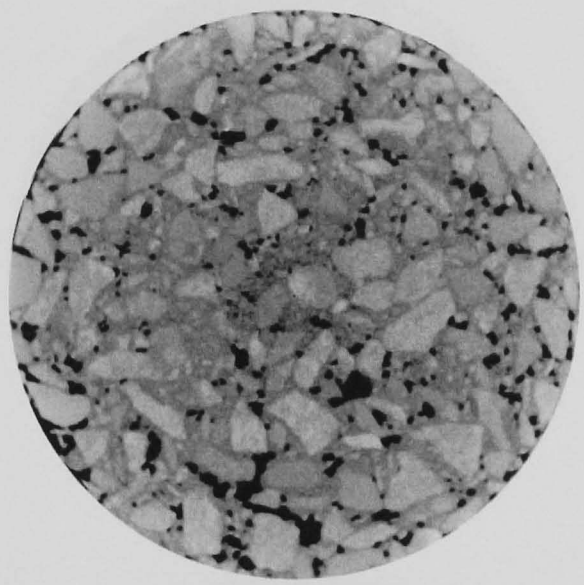

X ray Image
at 1.0%
strain

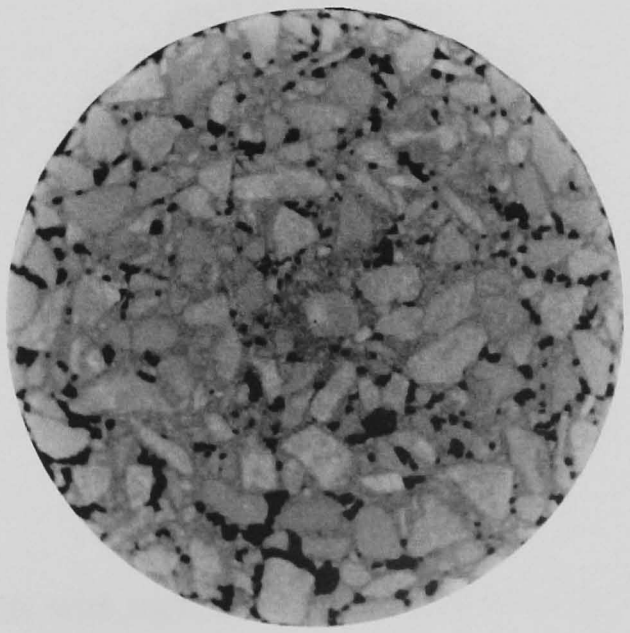

Figure 4.34 Air voids with increase in strain (Air voids are black presumably)

X ray Image
at 1.5%
strain

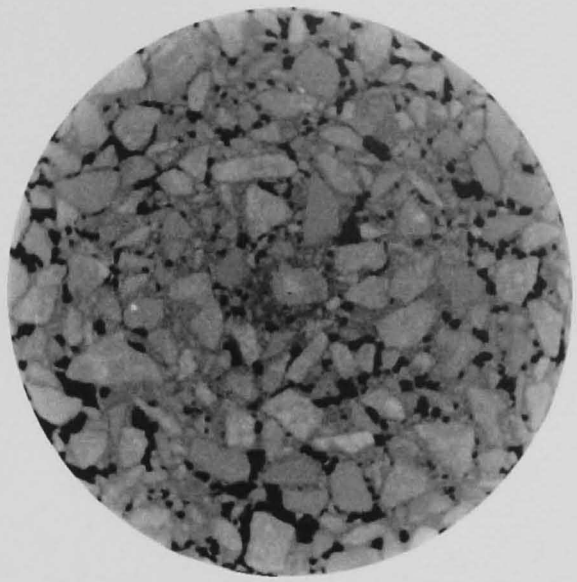

X ray Image
at 2.0%
strain

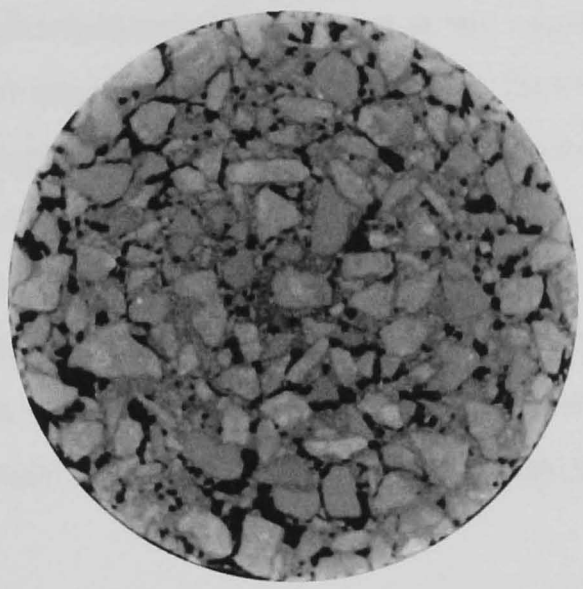

X ray Image
at 2.0%
strain

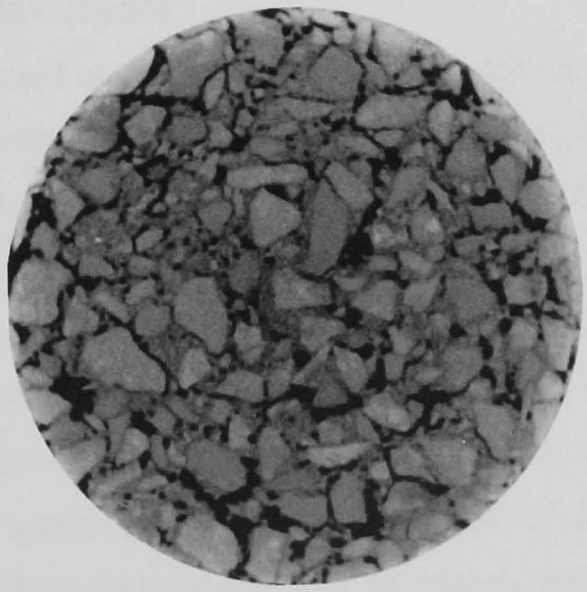

Figure 4.34 Air voids with increase in strain (Air voids are black presumably)

Chapter 5

TENSION COMPRESSION FATIGUE TESTING

5.1 Introduction

This chapter includes an introduction to the constant stress, constant strain fatigue test and tension compression fatigue testing. Preparation of samples for tension compression fatigue testing and testing of samples without rest periods is described. The methodology for stopping the fatigue test and X ray scanning the sample is given. Constant stress testing at three different temperatures is described. The air void contents at different numbers of load cycles has been determined from image analysis and related to the stiffness of the asphalt mixture. Parameters have been determined for damage modelling of asphalt and an adhesion parameter is included as required for the modified damage model.

5.2 Fatigue in asphalt pavements

A road pavement is subjected to short term loading each time a vehicle passes over it. As the number of passes increases toward a certain limit, there is a decrease in the stiffness of the asphalt material which ultimately leads toward the failure of the pavement in the long term. This shows that fatigue failure should be studied properly to ensure adequate structural design. Fatigue failure is commonly linked to the tensile strain at the bottom of the asphalt layer caused by repeated traffic load (Di Benedetto et al. 2004). It is different from permanent deformation as it decreases the rigidity of the asphalt and causes a decrease in modulus (Figure 5.1). Accurate prediction of fatigue behaviour can be determined by understanding the characteristic of asphalt under repeated loading. The behaviour of asphalt may be considered as linear or non linear viscoelastic. A typical plot of elastic and viscoelastic behaviour of asphalt is shown in Figure 5.2.

Actually fatigue failure starts as microcracks. These cracks propagate, densify and coalesce to form macrocracks (Wen, 2001). Laboratory cyclic tests on asphalt mixes allow a designer to predict and to take into account the fatigue performance of material while designing the mixture and the asphalt pavement.

Different approaches to assess the fatigue behaviour of asphalt have been developed such as, tension compression fatigue test, two point bending fatigue test, three point bending fatigue test, four point bending fatigue test and indirect tensile test (Di Benedetto et al. 2004).

In a controlled stress fatigue test, the specimen fails quickly due to the high rate of crack propagation in this mode of test as this is a function of the stress magnitude at the crack tip. In controlled strain mode, on the other hand there is a gradual reduction in the applied stress as the material weakens.

Fatigue testing commonly shows the existence of a stage during the test characterized by an approximately linear reduction in the stiffness modulus E with number of cycles (Artamendi et al. 2005). Based on this linear reduction in the stiffness a damage parameter D can be introduced, thus

$$D(N) = \frac{E_0 - E(N)}{E_0} \tag{5.1}$$

The rate of damage growth can be calculated by differentiating this equation (Artamendi et al. 2005)

$$\frac{dD}{dN} = -\frac{1}{E_0}\frac{dE}{dN} = -a_T \tag{5.2}$$

where E_0 and dE/dN are the intercept and slope of the fitted line for the stiffness data.

5.3 Specimen preparation

For X ray CT of tension compression fatigue testing, samples of 100 mm diameter and 100 mm height were prepared (Figure 5.3). Aggregate grading and asphalt mix design were

similar to that used for specimens in the compression test as mentioned in Chapter 4. The design void content and binder were 6.5% and 5.5% respectively. In order to fix the specimens for tension compression cyclic testing, the specimens were glued with specifically designed steel plates both at the top and bottom (Figure 5.4a). The plates had grooves inside to increase the bonding of the specimen to the plates (Figure 5.4b). The specimens were glued and kept clamped for 24 hours in a fixing machine specially designed to properly fix at the bottom and top. Similar to the compression test, three test temperatures were selected for fatigue testing

Modifying test plates for low temperature fatigue testing

For fatigue testing at low temperature, sample failure tended to occur when the bond broke between the sample and the top or bottom plate. The existing end plates with a 10 mm deep ring and a single channel were therefore modified and replaced by plates with a 20 mm deep ring and two channels (Figure 5.5). This increased the contact bond area between the sample and the steel plate. To ensure parallel alignment of the plates with each other and with specimen, a right angle jig was used (Figure 5.6).

5.4 Test equipment

An Instron testing machine with 100 kN loading frame, servo-hydraulic actuator, an axially mounted load cell and on-specimen instrumentation was used for the tension compression fatigue test. The apparatus consists of the specimen housed within a 5°C to 50°C temperature controlled cabinet. The load frame is controlled by a Rubicon digital control system that was also used for data acquisition. Using the loading platens the specimen is fastened to the upper and lower actuator crosshead and a system of bolts positioned between the top loading plates and the hydraulic ram are adjusted to compensate for any load eccentricity.

5.5 Fatigue testing

The sample was taken from the conditioning environment and was instrumented with an axial strain transducer and fastened with bolts to the actuator at the lower crosshead using the bottom loading platen and to the stationary crosshead using the top loading plate (Figure 5.7). The door of the temperature controlled cabinet was closed for enough time to

ensure a constant temperature regime within the cabinet. Before starting the test, the sample with attached plates was placed in a temperature controlled environment, and set at the required testing temperature for at least 12 hours. At the end of the test, it was confirmed that the sample failure was at middle of the specimen (Figure 5.8).

A force controlled tension compression cyclic test using a frequency of 5Hz was selected at three temperatures, 23°C, 35°C and 5°C. In order to obtain a reference curve three specimens were tested at 23°C. After making several trials it was determined that for 350 N the specimen failed between 24000 and 40000 cycles. A reference stiffness curve was plotted. The same procedure was followed for 35°C testing. Three specimens fixed between steel plates were tested at 35°C and a reference curve was plotted (Figure 5.9).

For testing at 5°C several attempts were made to obtain a reference curve, but in all the cases the specimens broke at the bond between plate and specimen. This is due to the increase in strength of the asphalt specimen at low temperature which exceeded the bond strength of the epoxy used to glue the sample to the loading plates. This manifested in failure taking place at the specimen epoxy bond interface. This was overcome by modifying the loading plates to include another lip into which the specimen would fit. Using this procedure new specimens were fixed to the plates and, after 24 hours kept in a cold store were then fixed to the Instron machine for testing at 5°C. Three specimens were tested in the cyclic fatigue test at a frequency of 5Hz. It was found that the specimens failed in the middle after between 24000 and 40000 cycles. The reference stiffness curve for tension compression fatigue testing at 5°C was then plotted.

The stages for stopping the test and scanning the specimens for X ray CT were marked on the reference curves for testing at the three different testing temperatures (Figure 5.9). In order to test the specimens with rest periods at selected stages, specimens were fixed in the Instron testing machine and testing continued at 23°C until 6000 cycles, the bolts were then released and the specimen was removed and taken for X ray scanning. The specimens were re-fixed in the testing machine for a further 6000 cycles and scanned again. Each time the sample was conditioned at test temperature again before starting the next stage of testing.

The results were taken and stress strain and stiffness curves were plotted with rest periods (Figure 5.10).

A similar procedure was followed for specimens tested and scanned at 35°C and 5°C and scanned. The test was stopped after 6000 cycles and samples were released and were taken for X ray CT. After completing the scans the samples were kept at the test temperature for 12 hours before starting the next stage. The specimens were then fixed with bolts into the testing machine and the test was continued for a further 6000 cycles. After a total of 12000 cycles the specimens were again taken for X ray scanning. The process continued until the specimens failed and curves with rest periods were plotted for samples tested at 35°C and 5°C (Figure 5.11, Figure 5.12). Typical stress strain curves and the increase in strain due to load cycles are shown in Figure 5.13 and Figure 5.14.

It is noted from all the curves at three different temperatures that the decrease in relative stiffness ($E_{Failure}/E_{Initial}$) increases with increase in the temperature. Specimens tested at 5°C and 35°C have approximately similar trend of decrease in stiffness to that tested at 23°C. There is rapid decrease at the start followed by continued slow decrease and then a final acceleration. Thus the curve becomes S-shaped (Di Bendetto et al. 2004).

5.6 X ray CT of fatigue specimen

In order to study the microdamage of asphalt mixtures during fatigue, the specimens along with the steel plates at top and bottom, were scanned in X ray CT before starting the fatigue test. The specimen was taken into the X ray machine (Figure 5.15). The scanning parameters were fixed according to the size of the specimen including the steel plates at top and bottom. After several trials the position of the specimen along with plates was fixed to obtain the clearest possible image. Due to the plates it was difficult to fix the specimen in the already built frame in the machine, and the specimen was therefore fixed by manually rotating the table of the manipulator. This was done by shifting the X ray mode from automatic to manual and, using the handles fixed on the main desk, the turntable was rotated through 90 degrees and the specimen was centred. The X ray scans of samples before testing were collected for further analysis.

As the test consists of scanning at several stages, specimen testing was stopped after 6000 load cycles, the bolts were loosened and the specimen was removed from the Instron machine. The sample along with the steel plates was fixed for X ray scanning. After scanning in the X ray, the specimen was again put in the conditioning store to gain the testing temperature before starting the next testing stage and further X ray scanning. The process of testing and scanning was continued after each 6000 cycles unless the specimen failed. Specimens tested at 23°C, 35°C and 5°C were scanned at each selected test stage. For specimens tested at low temperature and scanned in the X ray, it required comparatively more time as, after scanning in the X ray, the specimen had to be kept in a cold store to bring it to 5°C before the next test stage.

The scanning data was collected from the X ray machine and was analysed in VG studio max for increase in void content. Increase in void content with increase in number of load cycles was observed. The values of void content at different stages are shown in Figure 5.16. The void content data along with stiffness curves for the three test conditions are plotted (Figure 5.17).

It can be seen from the Figure 5.16, that void content value increases with increase in number of load cycles. The increase in void content value is comparatively high at high temperature. From the graph of specimens tested at low temperature and scanned, there is almost negligible increase in void content initially, followed by an increase after 6000 load cycles.

5.7 Fatigue damage from test data

The data from the three tests plotted against the relative stiffness have shown that there is a trend of increase in void content with increase in number of load cycles. It can be seen from the fatigue curve that at the start of the curve there is a drop in stiffness followed by a continuous slow decrease and a sudden drop in stiffness near the failure of the specimen. At the start, microcracks are created in the binder film between aggregates. The initial curve drop illustrates this process, superposed onto a thermo-mechanical transient regime due to viscoelastic dissipation. In the continuous smooth portion of the curve, the thermal regime is permanent and the initiated cracks grow leading to a progressive macrocrack pattern.

Finally a single macrocrack propagates with an increasing rate until fracture of the specimen. The elastic based damage approach can be used to describe the modulus decrease due to developing microcracks (Bodin et al. 2004).

As described in Chapter 4, damage in the cross sectional area of the body with an an area of element dA, and the area of the defects in this element denoted by dA_D can be characterized by the area fraction w as (Dietmar et al. 2006),

$$w(n) = \frac{dA_D}{dA} \quad \text{with} \, 0 \le w \le 1 \tag{5.3}$$

If w=0 the material is considered as undamaged and if w=1 the material is considered as, totally damaged. If the damage is constant across area dA, for example in the case of a uniaxial test, the relation can be written as

$$w = \frac{dA_D}{dA} \tag{5.4}$$

This relation can be applied for void-like defects. If the stresses are replaced by the effective stresses the stress-strain behaviour of the damaged material can then be described by the constitutive law of the undamaged material (Dietmar et al. 2006).

$$\varepsilon = \frac{\tilde{\sigma}}{E} = \frac{\sigma}{(1-w)E} \tag{5.5}$$

where E is the Young's modulus of the undamaged material. Hence the damage can be determined by measuring the effective Young's modulus

$$E = (1-w)E_o \quad \text{or} \quad w = 1 - \frac{E}{E_o} \tag{5.6}$$

where E_0 is the initial stiffness and E is stiffness at a certain number of load cycles.

Considering the asphalt mixture as a homogenous material, the increase in void content has been calculated for asphalt specimens in the tension compression fatigue test. At the beginning of the test the entire void content is taken correspond to w=0. The void content at specimen failure is to be taken w=1, i.e. if the void content in a specimen is 7.1% at the beginning of the test and 8.6% at specimen failure 7.1% voids is taken to correspond to w =0 and 8.6% is taken as w=1.

The initial stiffness E_o and stiffness E (ratio of change of stress to change of strain) were calculated for specimens tested in fatigue test. The value of relative stiffness E/E_o has been determined from mechanical testing at each test stage and that of damage parameter w has been determined from void content calculated from X ray computer tomography. The relative stiffness and damage parameters were determined for three different temperature tests. Values of void content at 6000, 12000, 18000 and 24000 cycles were used to calculate damage parameters and the data was plotted for relative decrease at these cycles (Figure 5.18). Values of damage parameter were considered after the first test stage, as initially there is a sudden drop in stiffness while the damage parameter does not increase so suddenly. This initial drop in stiffness during the fatigue test is not solely considered as damage in the mixture and is rapidly recoverable if the test is stopped (Di Benidetto et al. 2004). Also, due to tension compression load cycles, the air voids initially reduces followed by an increase with increase in load cycles. Most of the specimens failed by splitting into two pieces during the fifth or sixth test stage and it was not possible to scan the sample in X ray CT.

5.8 Micromechanics for fatigue damage model of asphalt

There are two different approaches to fatigue modelling of asphalt, one is phenomenological in which the fatigue characteristic is usually expressed as a relationship between the initial stress or strain and the number of load repetitions to failure. The other is the mechanistic approach in which the fatigue behaviour of asphalt is considered as a damage process and fracture mechanics/damage mechanics principles are used to investigate the cracking of asphalt mixtures (Si et al. 2002). Fatigue life, under a given state of stress, is defined as the number of loading cycles during which damage increases according to a crack propagation law from an initial state to a critical level. The flexural

stresses due to load induce microcracks and these microcracks can be represented in the form of voids or discontinuities. The procedure followed for calculating fatigue damage model parameters is shown in Figure 5.19

Dissipated pseudo strain energy

Applying stress to a material induces strain. The energy being input into the material is represented by the area under the stress strain curve. The strain will recover when the stress is released from the material. If the loading and the unloading curve coincide then this means all the energy applied is recovered. If the loading and unloading energy do not coincide then some of the energy is lost. The energy is dissipated in mechanical work, heat generation and damage in the material in such a manner that it cannot be recovered from the material. This difference in energy is the dissipated energy in the material caused by each load cycle. For viscoelastic material, a certain amount of energy is used in overcoming the viscous resistance of the material and is not contributing to the damage of the material. In order to have the correct amount of the energy, the concept of pseudo strain has been introduced. The dissipated pseudo strain energy is the energy that has been lost in loading and unloading the material minus the energy that has been lost in overcoming the viscous resistance of the material and therefore it represents the energy that is available to damage the material (Kim, 2009).

The dissipated pseudo strain energy approach has been applied to quantify the microdamage in asphalt. Since asphalt is a viscoelastic material, the performance under constant stress or constant strain is dependent on time and history. By using the dissipated pseudo strain energy the time dependent viscoelastic behaviour can be eliminated. In order to separate and deduct the time dependent viscoelastic behaviour from the real damage within the material during the fatigue test, instead of strain, pseudo strain is used (Kim et al. 1997, Si et al. 2002). A typical plot of a stress pseudo strain loop is shown in Figure 5.20.

For the case of controlled stress sinusoidal loading, the applied stress and the strain response for undamaged viscoelastic material can be expressed as (Masad et al. 2007)

$$\sigma = \sigma_0 \sin(\omega t) \qquad (5.7)$$

$$\varepsilon = \varepsilon_{0N} \sin(\omega t - \phi_N) \tag{5.8}$$

For the case of undamaged material, the corresponding undamaged stress for this strain will be

$$\sigma = E_{VE}\varepsilon_{0N} \sin(\omega t - \phi_N + \phi_{VE}) \tag{5.9}$$

And the pseudo strain for the controlled stress loading is the function in the above equation divided by the reference modulus (Masad et al. 2007)

$$\varepsilon_R = \frac{E_{VE}\varepsilon_{0N} \sin(\omega t - \phi_N + \phi_{VE})}{E_R} \tag{5.10}$$

where ε_R is the pseudo strain, E_{VE} is the dynamic modulus, ω is the load frequency, t is the time, ϕ_{VE} is the viscoelastic phase angle between the stress and strain response and E_R is the reference modulus and taken as the ratio of the applied stress during the first load cycle to the strain recorded during the first cycle, VE shows material viscoelastic properties, and N indicates the loading cycles. The typical stress strain response for a stress controlled fatigue test is shown in Figure 21.

There are three stages in the fatigue process which are initiation, propagation and failure. During the stage of propagation, the crack growth rate can be expressed using the Paris law (Si et al. 2002)

$$\frac{dc}{dN} = \bar{A} K^{\bar{n}} \tag{5.11}$$

where c is the crack length, N is the number of loading repetition, $\bar{A}$ and $\bar{n}$ are parameters dependent on the material and on the experimental conditions and K is stress intensity factor. In order to reduce some of the testing and calculations required for determining the stress intensity factor K, the Paris law is modified by replacing it with a

J-integral. The modified Paris law can be written as $dc/dN = AJ^n$ and for pseudo *J*-integral as (Arambula et al. 2007)

$$\frac{\partial c}{\partial N} = A(J_R)^n \tag{5.12}$$

The pseudo *J* -integral is defined as the rate of change of pseudo strain energy per unit area of crack growth.

$$J_R = \frac{\partial W}{\partial (csa)} = \frac{\partial W / \partial N}{\partial (csa) / \partial N} \tag{5.13}$$

csa is the crack surface area and is considered to be $2\pi c^2$ for a circular crack with an equivalent radius c (Si et al. 2002, Masad et al. 2007, Kim, 2009). Here c is considered as average radius of air voids determined from X ray image. The value of crack growth rate is determined as $\partial(csa)/\partial N = 4\pi c(\partial c/\partial N)$, and that of $\partial W/\partial N$ is calculated from the graph between dissipated pseudo strain energy and logarithm of the number of load cycles. The data from the graph comes in the form of a straight line and is expressed as $W = a + b\ln(N)$, where a is the intercept. The rate of dissipated energy comes out as $\partial W/\partial N = b/N$. Putting values of $\partial W/\partial N$ and $\partial(csa)/\partial N$ into equation (5.13)

$$J_R = \frac{b}{4\pi c N(\partial c/\partial N)} \tag{5.14}$$

Putting the value of J_R into the modified Paris law

$$\frac{\partial c}{\partial N} = A\left(\frac{b}{4\pi c N(\partial c/\partial N}\right)^n \tag{5.15}$$

Integrating both sides of the equation and for micromechanics modelling of fatigue, putting the value of A (Masad et al. 2007) as $A = k(E_R/E_1\Delta G\sigma_t^2)^n$.

$$\int_{c_0}^{c} c^{n/(n+1)}\partial c = \left(A\right)^{1/(n+1)}\left(\frac{b}{4\pi}\right)^{n/(n+1)}\int_{1}^{N}\frac{\partial N}{N^{n/(n+1)}} \tag{5.16}$$

$$c = \left((2n+1)\left(\frac{bE_R}{4\pi E_1 \Delta G \sigma_t^2}\right)^{n/(n+1)}\left(N^{1/(n+1)} - 1^{1/(n+1)}\right) + c_0{}^{(2n+1)/(n+1)}\right)^{(n+1)/(2n+1)} \tag{5.17}$$

where E_1 is the initial modulus, E_R is relaxation modulus, ΔG is the adhesion bond energy due to interfacial strength between binder and aggregate and is introduced in the modified fatigue damage model, c is the average radius of crack (void in this case) corresponding to number of load cycles N, c_0 is the initial average radius of void and σ_t is the tensile strength of asphalt mixture.

Detail derivation of equation 5.17 is given in Arambula et al. (2007). The initial average radius of void c_0 is determined from X ray CT images data as, $c_0 = \sqrt{A_{Voids}/\pi n}$, where $A_{Voids} = V_{image} / A_{total}$ and $V_{image} = V_{total} / N$, where V_{image} is the average void content in an image, N is the number of X ray images, A_{Voids} is the area of void content in an image, V_{total} is the total void content, n is the number of voids in a CT image (Kaseem et al.2008).

Determining equation parameters

Dissipated Pseudo strain Energy

For 5 Hz load frequency, and ω which comes out as 10π radians per second (Figure 5.22) in this case, the pseudo strain was calculated at every 500 cycles. The values of pseudo strain were plotted against the stress and the hysteresis loops were plotted (Figure 5.23). The area inside the loop represents dissipated pseudo strain energy W and is determined using the area by coordinate method (Wolf et al. 2002). The value of pseudo strain energy W was plotted against the number of load cycles N and the unknown value of b was determined from the slope of the line (Figure 5.24).

Relaxation modulus E_R

In a relaxation modulus test, a constant axial strain is applied on the asphalt samples (Figure 5.25) either in tension or in compression for a specific time and then the strain is released for some time which allows the specimen to relax. During this rest period the sample undergoes elastic recovery. In this case 0.0025mm/mm elastic tensile strain is applied and kept for 60 seconds followed by unloading / relaxation for 600 seconds, then elastic strain in compression for 60 seconds followed by unloading as shown in the test protocol diagram. 60 seconds of strain is selected as a reasonable value as increased strain time may result irrecoverable strain and a 600 seconds rest period is selected which is adequate for elastic recovery of the sample. Too small a value of strain will not give reasonable results while too large strain values will result the complete failure of the sample (Walubita et. al. 2006). The actual test curve is trapezoidal in shape and the total test (tension, compression and relaxation) is completed in 25 minutes. A power law equation was used to obtain the relaxation modulus as function of loading time

$$E_R(t) = E_1 t^{-m} \tag{5.18}$$

$E_R(t)$ is the time dependent relaxation modulus, E_1 is the initial relaxation modulus, t is the reduced time and m is the relaxation modulus rate. The value of m is determined from this equation and is related to n as $n = 1 + 1/m$ for controlled stress testing (Masad et al. 2007). Stress and relaxation modulus test data is shown in Figure 5.26 and Figure 5.27 respectively.

In order to determine the model parameter σ_t which is the tensile strength, specimens were tested at 23°C temperature at a rate of 1mm/sec and the value of tensile strength parameter σ_t was calculated as $\sigma_t = P/\pi r^2$ where P is the maximum tensile load in kN, r is the radius of the cylindrical asphalt specimen.

ΔG (adhesion between binder and aggregate)

ΔG is the measure of bond strength between aggregate and binder and is determined from the surface energy of binder and surface energy of aggregate (Amit, 2006).

$$\Delta G = -\gamma_{ba}^{LW} + \gamma_b^{LW} + \gamma_a^{LW} - \gamma_{ba}^{AB} + \gamma_b^{AB} + \gamma_a^{AB} \qquad (5.19)$$

where $\gamma_b^{AB} = 2\sqrt{\gamma^+\gamma^-}$

$\gamma_a^{AB} = 2\sqrt{\gamma^+\gamma^-}$

$\gamma_{ba}^{LW} = (\sqrt{\gamma_b^{LW}} - \sqrt{\gamma_a^{LW}})^2$

$\gamma_{ba}^{AB} = 2(\sqrt{\gamma_b^+} - \sqrt{\gamma_a^+})(\sqrt{\gamma_b^-} - \sqrt{\gamma_a^-})$

γ_b represents the surface energy of binder, γ_a represents the surface energy of aggregates. Equation (5.19) is the total adhesive bond strength energy also called the Gibbs free energy and is the combination of polar energy AB and non polar energy LW $\gamma = \gamma^{LW} + \gamma^{AB}$. AB is for acid-base component, $+ve$ for acid component of surface interaction and $-ve$ for base component of surface interaction. $\gamma_{ba}^{LW}, \gamma_{ba}^{AB}$ are interfacial surface energies between binder and aggregate due to LW and AB respectively.

Surface energy measurement for binder

Surface energy of bitumen is determined using the Wilhelmy plate method. This method is based on kinetic force equilibrium when a very thin plate is immersed and withdrawn from a liquid solvent at very slow constant speed. The contact angle between bitumen and a liquid solvent measured during the immersion process is the advancing contact angle and that measured during withdrawal is the receding contact angle (Figure 5.28). The total surface energy is calculated from the contact angle. The recently commissioned Dynamic Contact Angle (DCA) analyzer in NTEC was used for determining the surface energy of the binder (Figure 5.29) (Kibuuka, 2007).

In the test half a gram of hot liquid bitumen was coated on a 0.15 mm thick 32mm by 24 mm glass slide. The slide is suspended from the microbalance, is immersed in liquid solvent and then withdrawn. The test involves the automatic cycle of immersion and

withdrawal process which is controlled by the software within the DCA analyzer and takes about 15-20 minutes.

The test liquids used in the process were de-ionised water, Methylene Iodide (di-iodomethane) and Glycerol (see Table 5.1). These solvents were selected because they have comparatively higher surface energy than bitumen, as required in this method. The contact angle is automatically calculated from $\cos\theta = (\Delta F + (\rho_L - \rho_{air} g) / P\gamma_L$, where p is the parameter of the plate coated with bitumen, γ_L the surface energy of the probe liquid (known), θ is the dynamic contact angle of liquid onto the bitumen surface, V is the volume immersed into the probe liquid, ρ_L is the density of the probe liquid, ρ_{air} is the density of air, g is the gravitational force and F is the applied force (Amit, 2006).

The dynamic contact angle is determined either in advancing or in receding. The value of force F applied during the immersion and withdrawl process is measured from the automatically controlled DCA analyzer balance and the contact angle is calculated. During testing advancing and receding contact angles are obtained.

Using known values of γ_L^{LW}, γ_L^- and γ_L^+ for the three liquids and the measured contact angle to determined the values of unknown γ_L^{LW}, γ_L^- and γ_L^+.

$$\gamma_L(1+\cos\theta) = 2(\sqrt{\gamma_b^{LW}\gamma_L^{LW}} + \sqrt{\gamma_b^-\gamma_L^+} + \sqrt{\gamma_b^+\gamma_L^-}) \tag{5.20}$$

The equation is re-arranged as

$$(1+\cos\theta) = 2\sqrt{\gamma_b^{LW}}\frac{\sqrt{\gamma_L^{LW}}}{\gamma_L} + 2\sqrt{\gamma_b^-}\frac{\sqrt{\gamma_L^+}}{\gamma_L} + 2\sqrt{\gamma_b^+}\frac{\sqrt{\gamma_L^-}}{\gamma_L} \tag{5.21}$$

$$1+\cos\theta = Y_i, \quad 2\sqrt{\gamma_b^{LW}} = X_1, \quad 2\sqrt{\gamma_b^-} = X_2, \quad 2\sqrt{\gamma_b^+} = X_3$$

For any liquid i, $\quad A_{1i} = \frac{\sqrt{\gamma_L^{LW}}}{\gamma_L}, \quad A_{2i} = \frac{\sqrt{\gamma_L^+}}{\gamma_L}, \quad A_{3i} = \frac{\sqrt{\gamma_L^-}}{\gamma_L}$

$$\begin{bmatrix} A_{11} & A_{12} & A_{13} \\ A_{21} & A_{22} & A_{23} \\ A_{31} & A_{32} & A_{33} \end{bmatrix} \begin{bmatrix} X_1 \\ X_2 \\ X_3 \end{bmatrix} = \begin{bmatrix} Y_1 \\ Y_2 \\ Y_3 \end{bmatrix}$$

where the 'A' matrix comprises the known surface energy components of the three liquid solvents. The 'X' matrix comprises the required unknown surface energy components of the binder and 'Y' matrix is a known function of the measured contact angles of the binder in the three liquid solvents (θ_{water}, $\theta_{\text{Methylene Iodide}}$, θ_{Glycerol}).

Solving these equations, the required binder surface energy is obtained (see Table 5.2).

Surface energy measurement for the aggregate

The recently commissioned dynamic vapour sorption system DVS in NTEC laboratory was used for the surface energy measurement of aggregates (Figure 5.30). This method is comparatively suitable because it considers the irregularity in shape, mineralogy and surface texture of the aggregate. A solvent of known surface energy is used for comparison and the gas absorbed by this solvent is an indirect measure of surface energy of the aggregate.

The equipment works on the gravimetric adsorption principle and consists of a balance (measuring up to 10 grams), temperature control unit and vapour / gas flow controller. In order to determine the surface energy of the aggregate an aggregate sample passing 4.75mm and retained on 2.36mm, is suspended in the sample chamber. The size of aggregate is restricted by the capacity of the equipment. A solvent vapour is injected into the aggregate. The balance measures the quantity of solvent adsorbed onto the surface of the aggregate. At the same time the vapour pressure at the surface of the aggregate is measured.

Three different solvents with known surface energy are used in the test and the adsorbed quantity is measured for each solvent. In this case octane, ethyl acetate chloroform were used (Table 5.3). The surface energy of the aggregate is calculated after measuring the

quantity adsorbed for all the three solvents. The vapour pressure and adsorbed gas mass are collected from the attached computer software. In order to achieve reasonable data the aggregate was first washed with distilled water and dried in an oven. The surface energy of the aggregate is calculated from the equation (Walubita et al. 2006)

$$\gamma_a = \gamma_a^{LW} + 2\sqrt{\gamma_a^+ \gamma_a^-} \tag{5.22}$$

where $\gamma_a^+ = \dfrac{(\pi + 2\gamma_L - \sqrt{\gamma_a^{LW}\gamma_L^{LW}})^2}{4\gamma_L^-}$,

$$\gamma_a^- = \frac{(\pi + 2\gamma_L - \sqrt{\gamma_a^{LW}\gamma_L^{LW}} - 2\sqrt{\gamma_a^+\gamma_L^-})^2}{4\gamma_L^+}$$

$$\gamma_a^{LW} = \frac{(\pi + 2\gamma_L)^2}{4\gamma_L^{LW}}$$

where a is for aggregate and L is for solvent.

Values were put into equation 5.22 and surface energy of aggregate was calculated (see Table 5.4).

In order to determine the value of model parameter ΔG , surface energy components from Table 5.2 and Table 5.4 were put into equation 5.19.

Values of model parameters from Table 5.5 were put into the equation 5.17 and the increase in damage due to increase in load cycles was calculated at test temperature 23°C. The increase in average radius of air voids from the damage model and that from X ray CT at selected load cycles were plotted as shown in Figure 5.31. Using a similar procedure, model parameters for fatigue testing at 5°C and 35°C can be determined and plotted along with microdamage data from X ray CT. The increase in void content due to fatigue load can be seen in X ray images (Figure 5.32).

5.9 Summary

Tension compression fatigue testing along with X ray CT was applied to investigate microdamage in asphalt mixtures. Testing was stopped in the middle at several defined test stages and increase in void content due to cyclic load was calculated from X ray scanning of the sample. The relative decrease in stiffness with increase in damage was determined for samples tested at three different test temperatures 23°C, 35°C and 5°C. The concept of dissipated pseudo strain energy and its application to specimens tested in tension compression fatigue and X ray CT has been described. The values of increase in average radius of air voids was calculated from the model and from X ray CT. A relationship between values from a damage model and from X ray CT was determined. Data from model was found to compare well with data from X ray CT. The procedure required several repeat samples as some specimens failed without completing the predefined selected number of load cycles and data from some specimens was very scattered. Repeatedly stopping the test and X ray CT scanning the specimens along with top and bottom plates requires care as a single disturbance will affect subsequent behaviour.

Table 5.1 Surface energy components (known) of water, Methylene Iodide and Glycerol

Liquid	γ_{total}	γ^{LW}	γ^{+}	γ^{-}	γ^{AB}
Water	72.80	21.8	25.5	25.5	51
Methylene Iodide	50.80	46.50	0.00	0.00	0
Glycerol	48.30	29.0	1.92	47.00	30

Table 5.2 Surface energy components for 100 penetration bitumen (erg/cm^2)

Bitumen	γ_{total}	γ^{LW}	γ^{+}	γ^{-}	γ^{AB}
100 pen	19.06	19.06	0.00	0.78	0.00

Table 5.3 Surface energy components of octane, ethyl acetate and chloroform

Liquid	γ_{total}	γ^{LW}	γ^{+}	γ^{-}	γ^{AB}
octane	21.62	21.62	0	0	0
ethyl acetate	23.9	23.9	0	19.2	0
chloroform	27.15	27.15	3.8	0	0

Table 5.4 Surface energy components for Aggregate

Aggregate	γ_{total}	γ^{LW}	γ^{+}	γ^{-}	γ^{AB}
Granite	60.01	56.55	1.58	1.90	3.46

Table 5.5 Model parameters

Mixture	n	m	ΔG J/m^2	E_1 (MPa)	E_R (MPa)	a J/m^3	b	σ_t kPa
DBM	3.293	0.436	0.068	1289	2034	0.89	0.001	1280

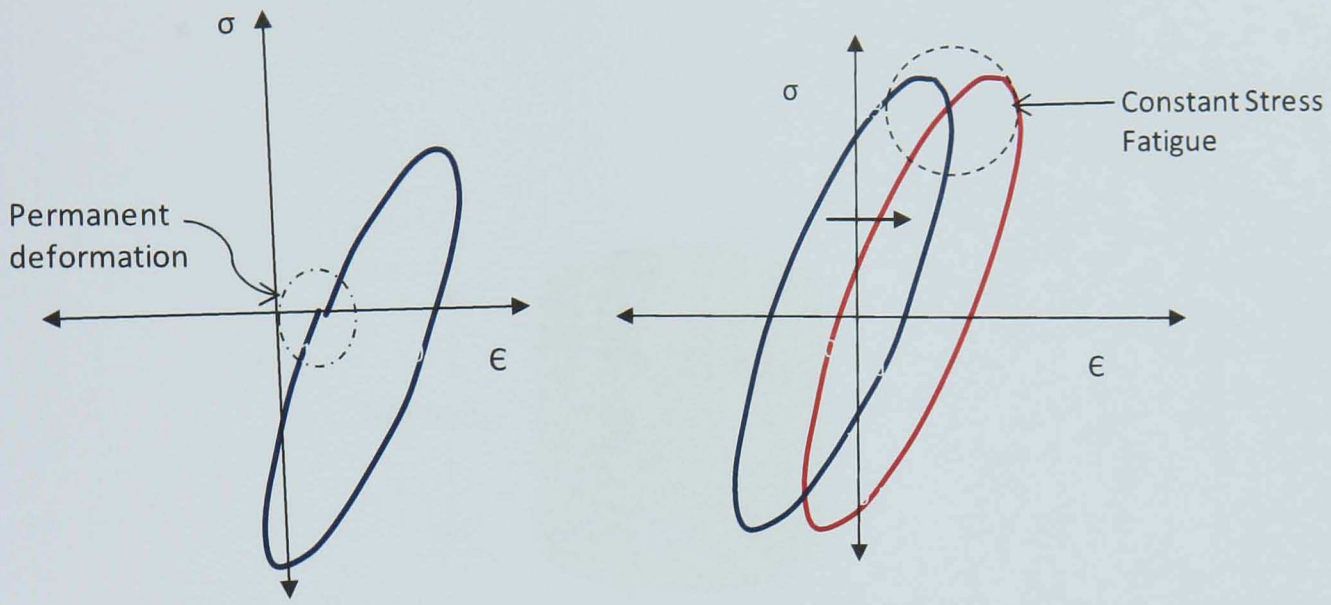

Figure 5.1 a) Permanent deformation, b) Fatigue failure

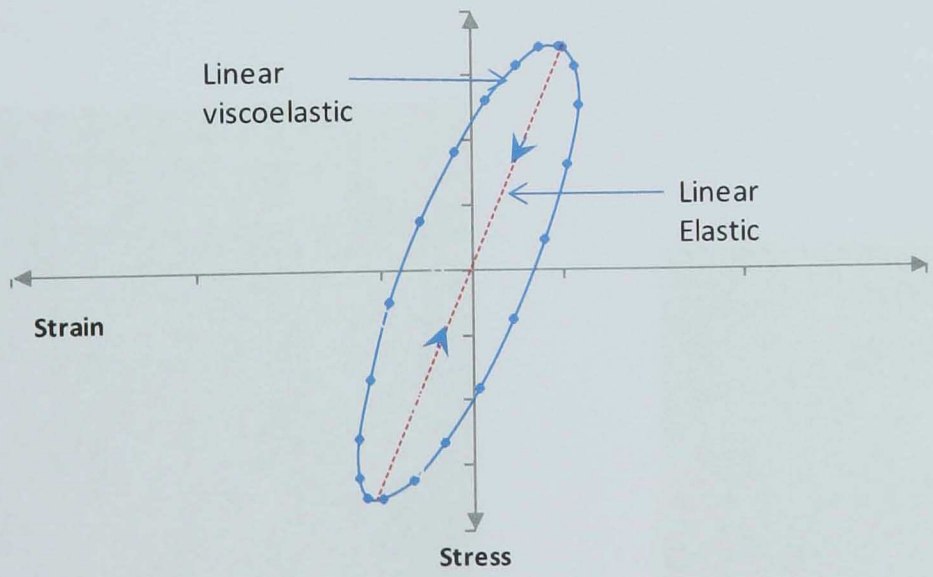

Figure 5.2 Linear elastic and viscoelastic stress strain curves

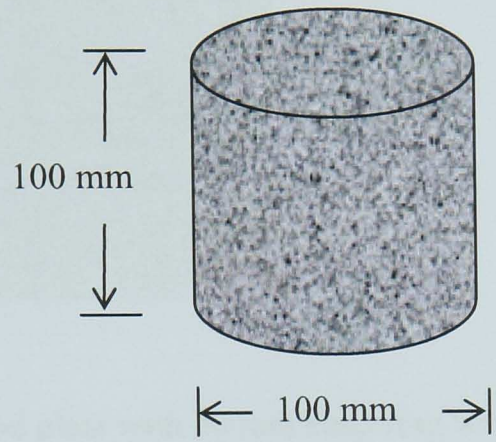

Figure 5.3 Typical dimensions of asphalt specimen tested in fatigue test

Figure 5.4 a) Specimen glued between in steel plates, b) End plate with 10 mm deep ring with grooves inside

Figure 5.5 Modified end plate with 20 mm deep ring with two groves inside

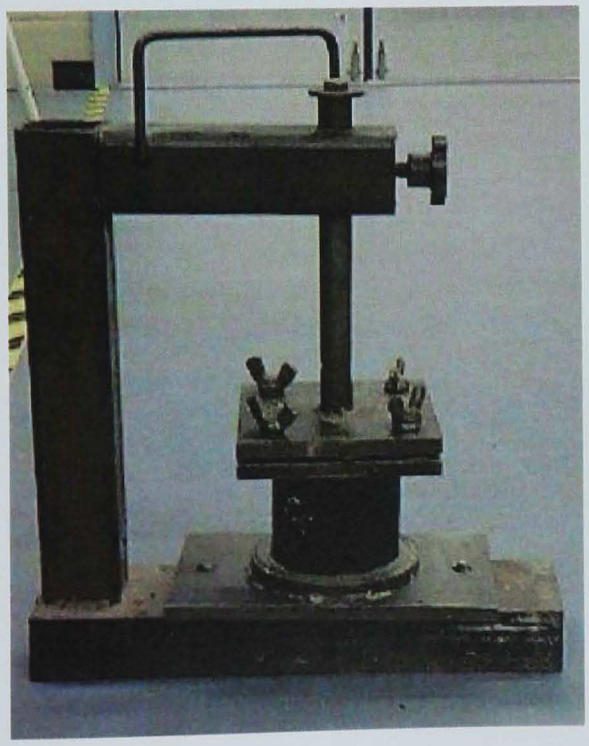

Figure 5.6 Specimen fixed in purpose built right angle jig

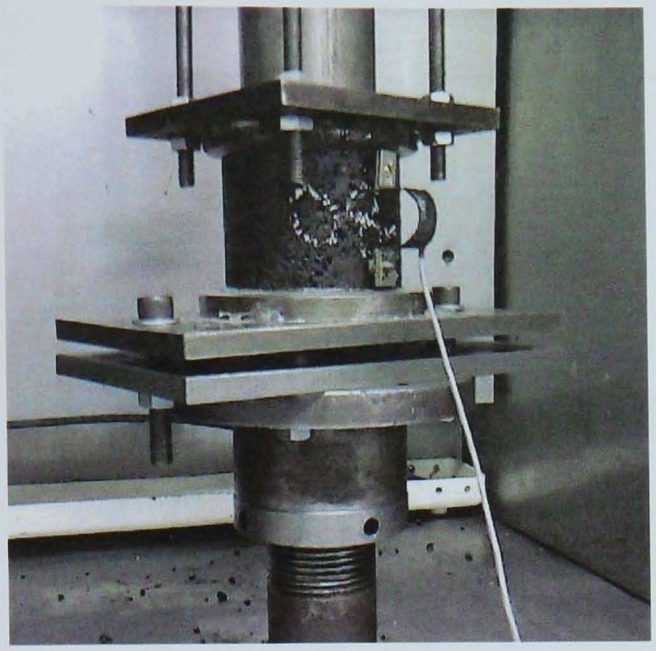

Figure 5.7 Specimen in fatigue test showing strain transducer

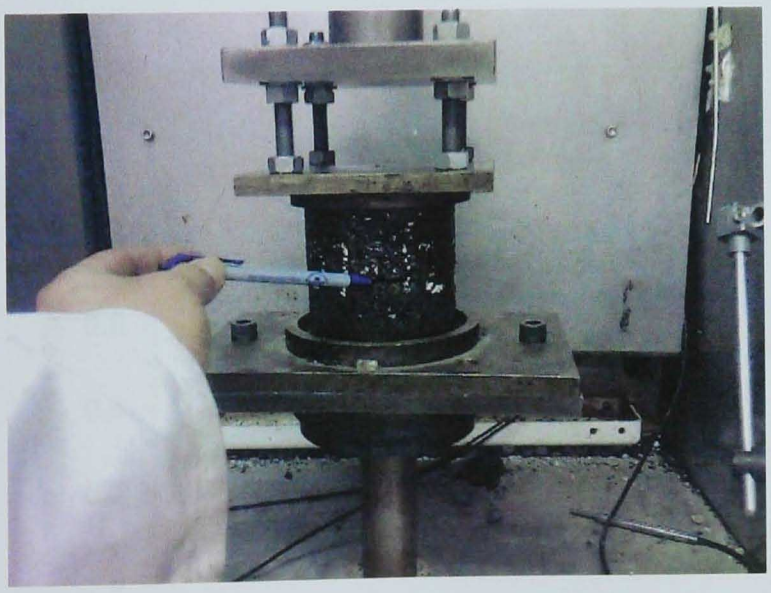

Figure 5.8 Specimen showing failure location after fatigue testing

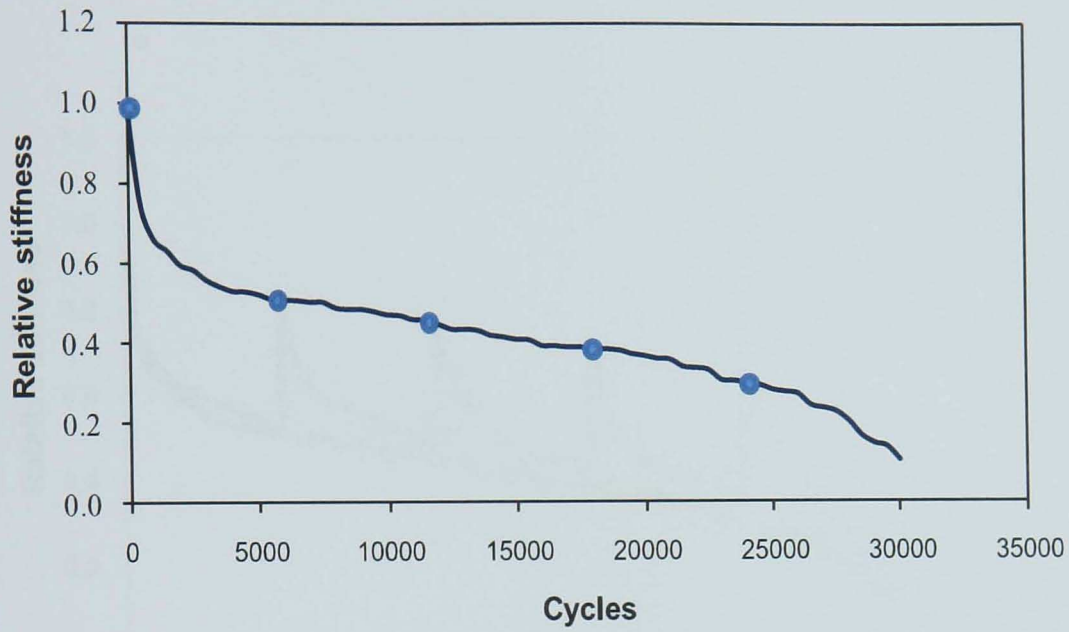

Figure 5.9 Scanning positions marked on stiffness curve

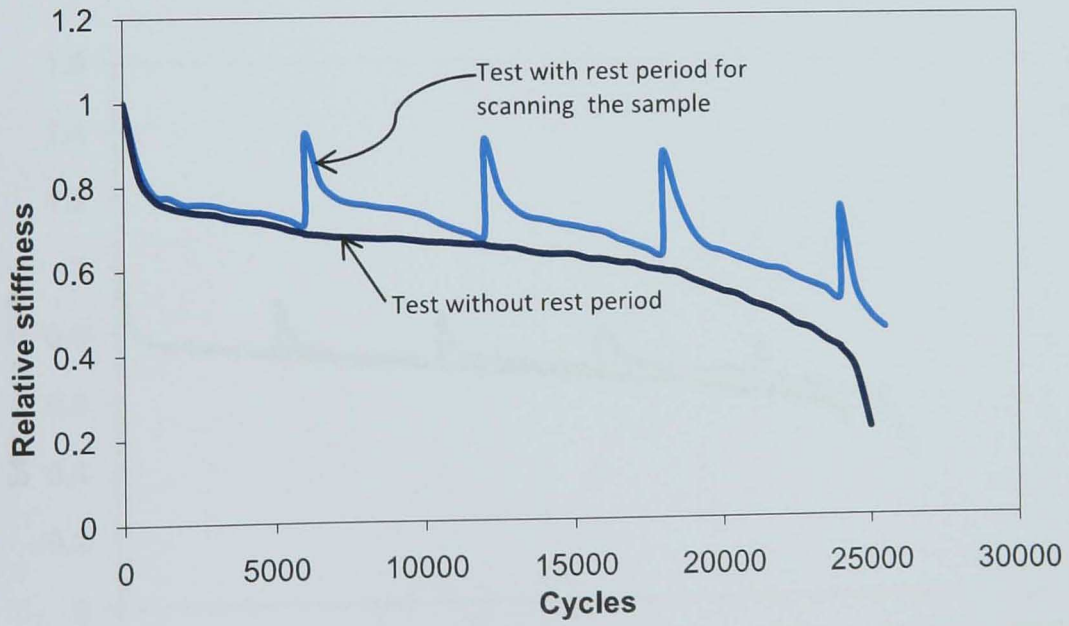

Figure 5.10 Fatigue test at 23°C with rest periods for scanning the sample

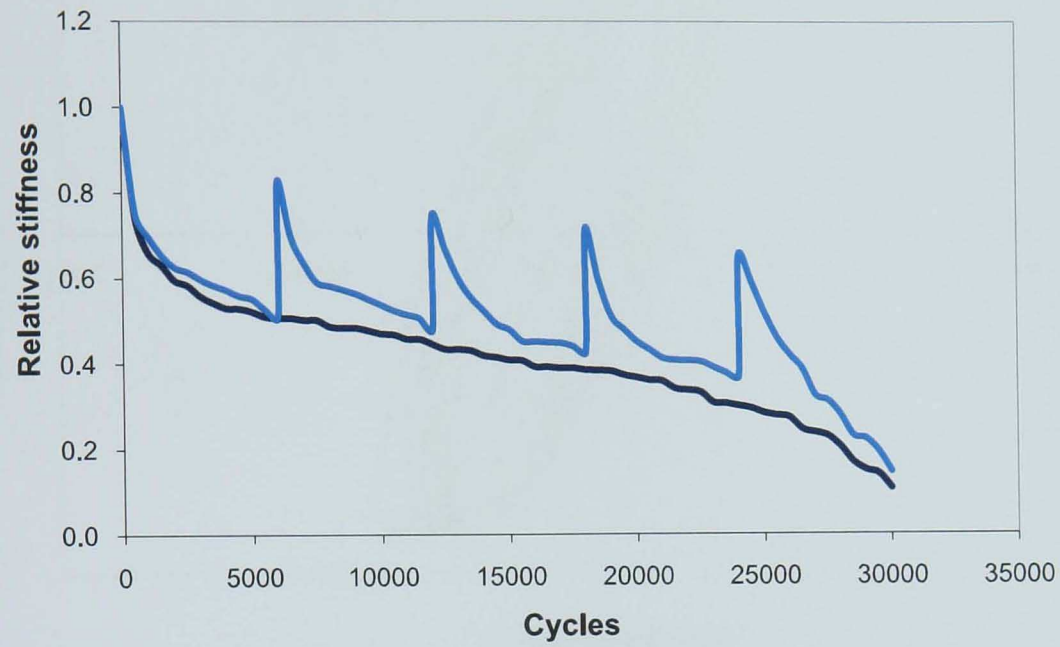

Figure 5.11 Fatigue test at 35°C with rest periods for scanning the sample

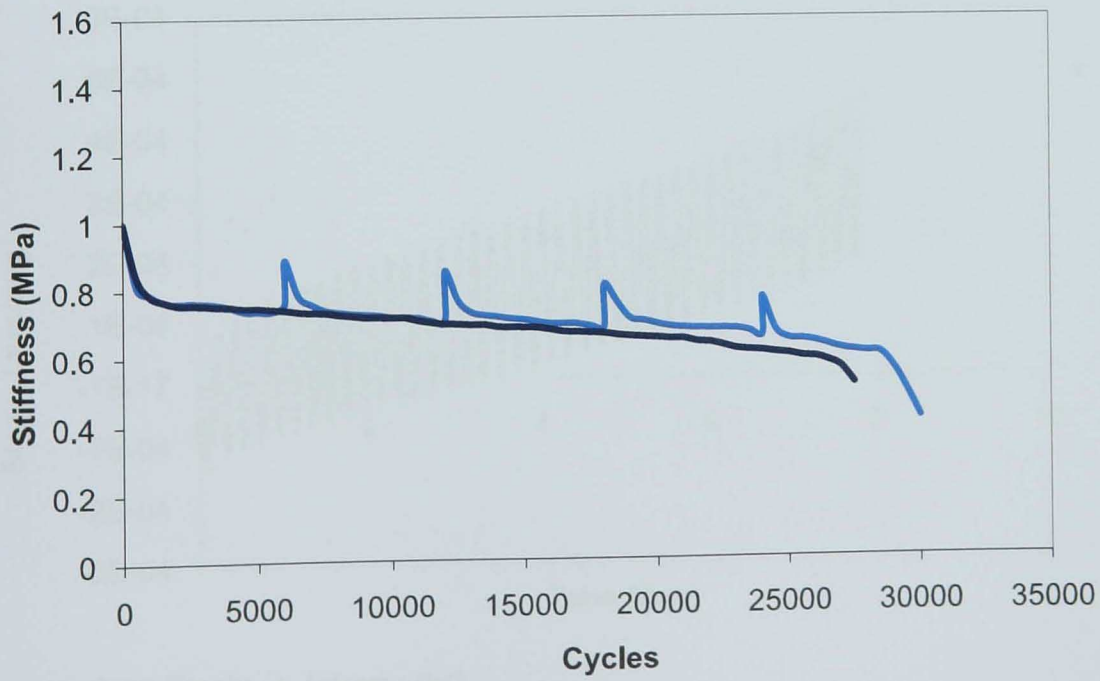

Figure 5.12 Fatigue test at 5°C with rest periods for scanning the sample

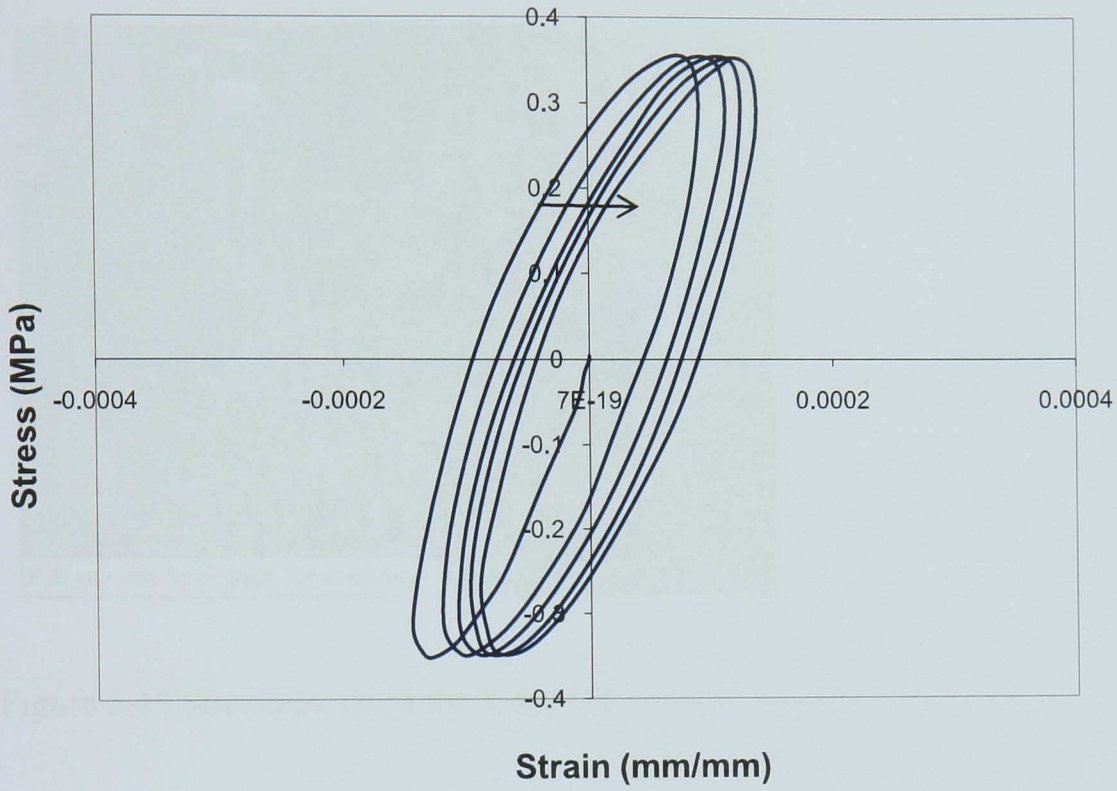

Figure 5.13 Stress strain curve in tension compression fatigue test

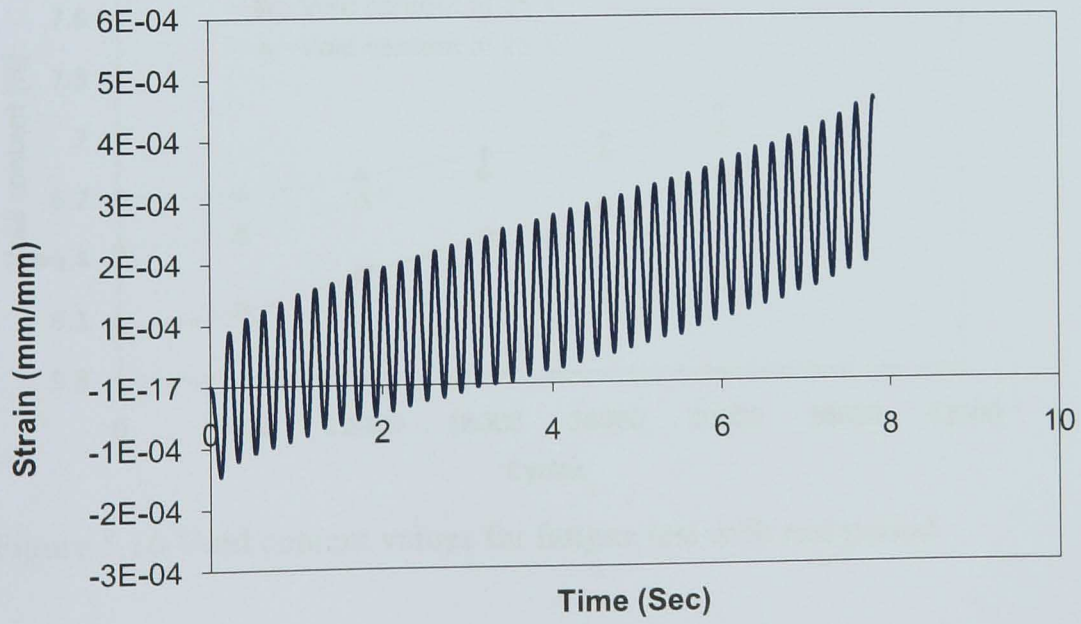

Figure 5.14 Strain in fatigue test

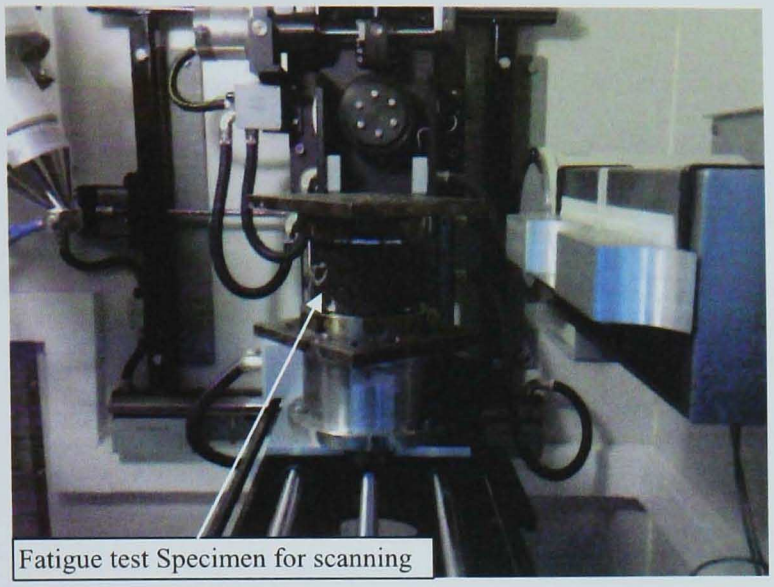

Figure 5.15 Specimen fixed for X ray CT

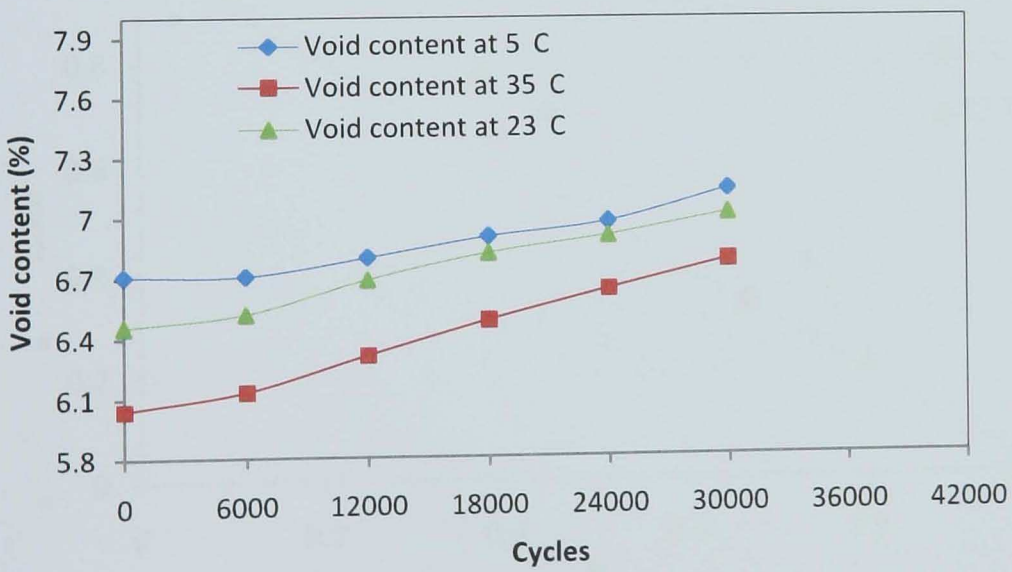

Figure 5.16 Void content values for fatigue test with rest period

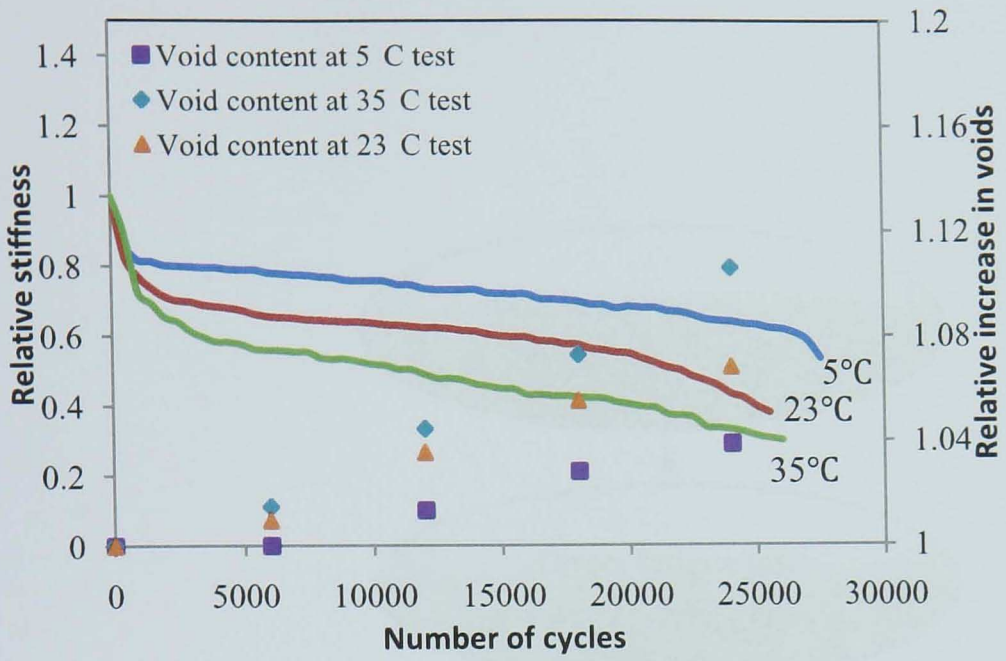

Figure 5.17 Data from fatigue test and from X ray CT

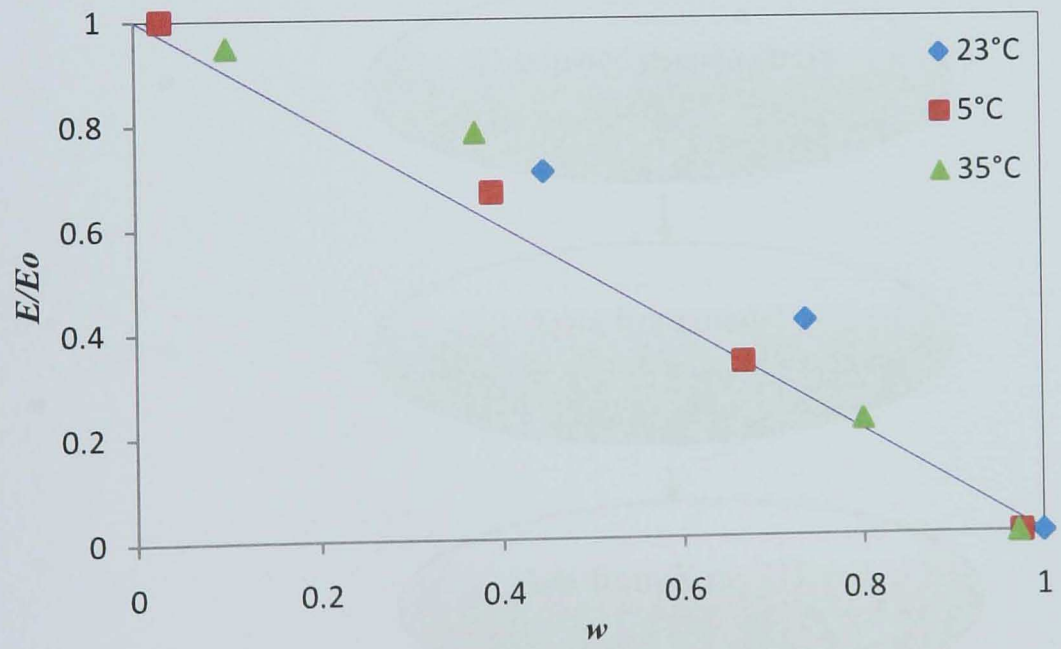

Figure 5.18 Damage parameters from X ray CT and fatigue test

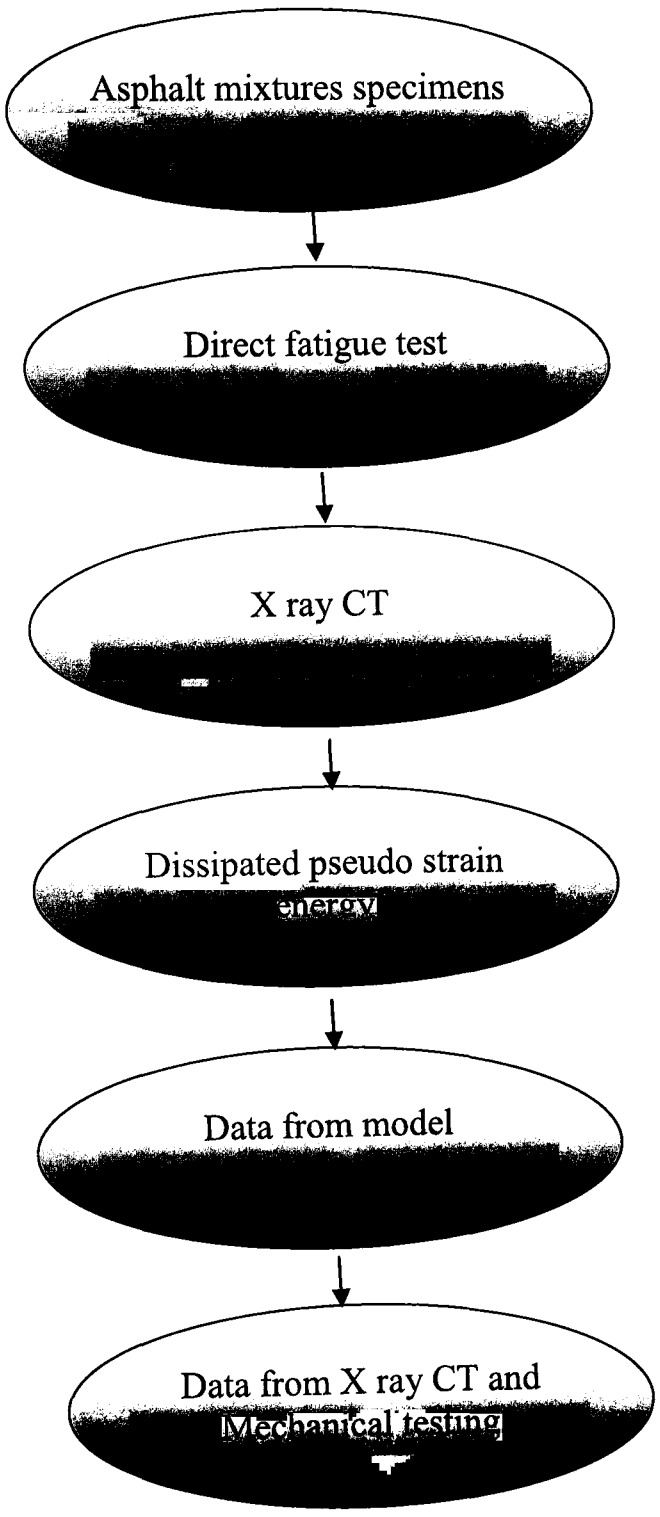

Figure 5.19 Steps for damage calculation from X ray CT

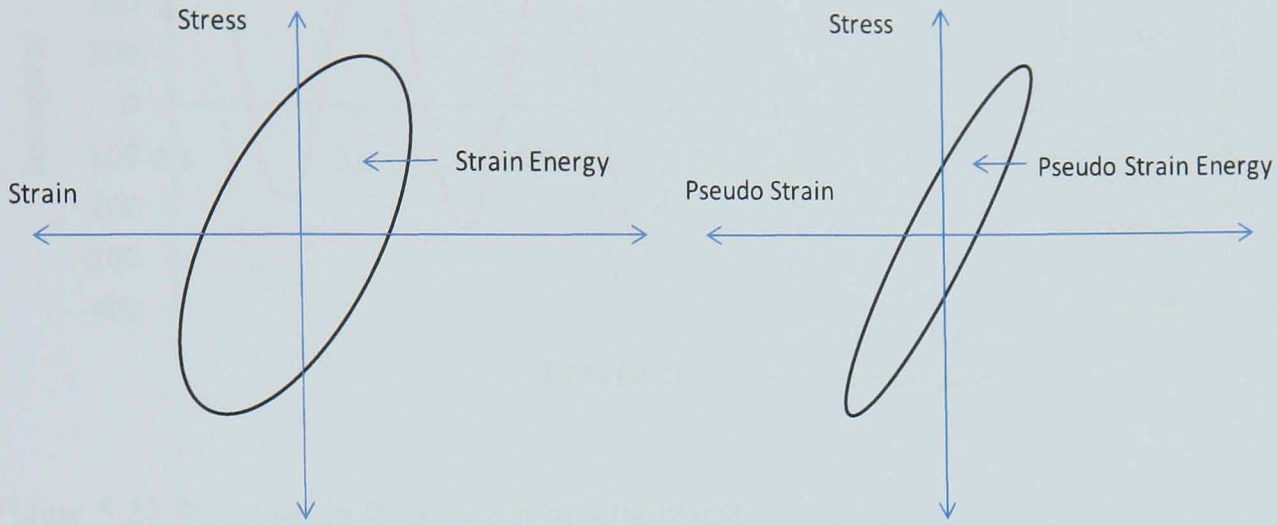

Figure 5.20 a) stress strain curve, b) stress pseudo strain curve

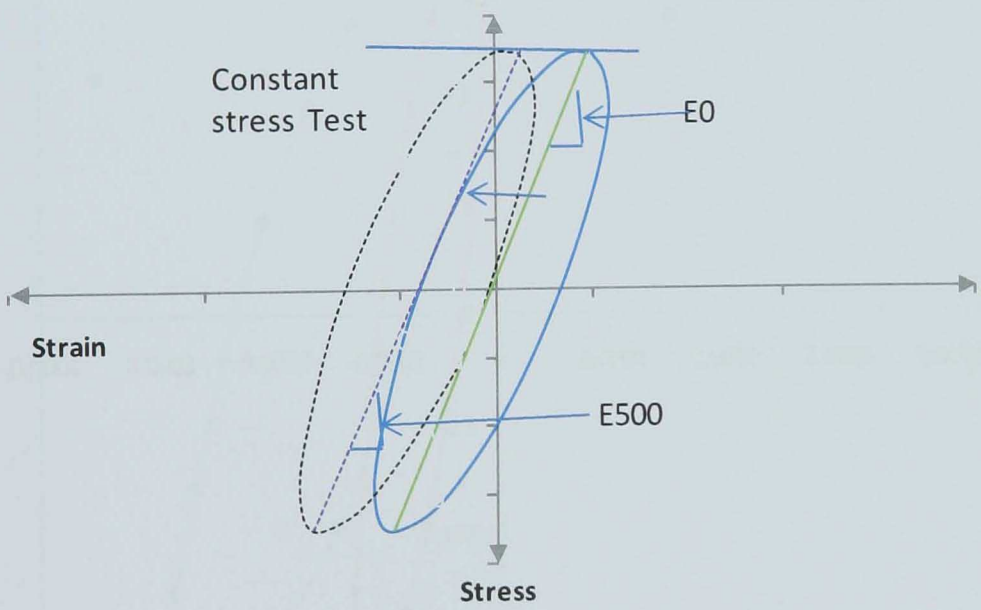

Figure 5.21 Constant stress fatigue test for asphalt mixtures

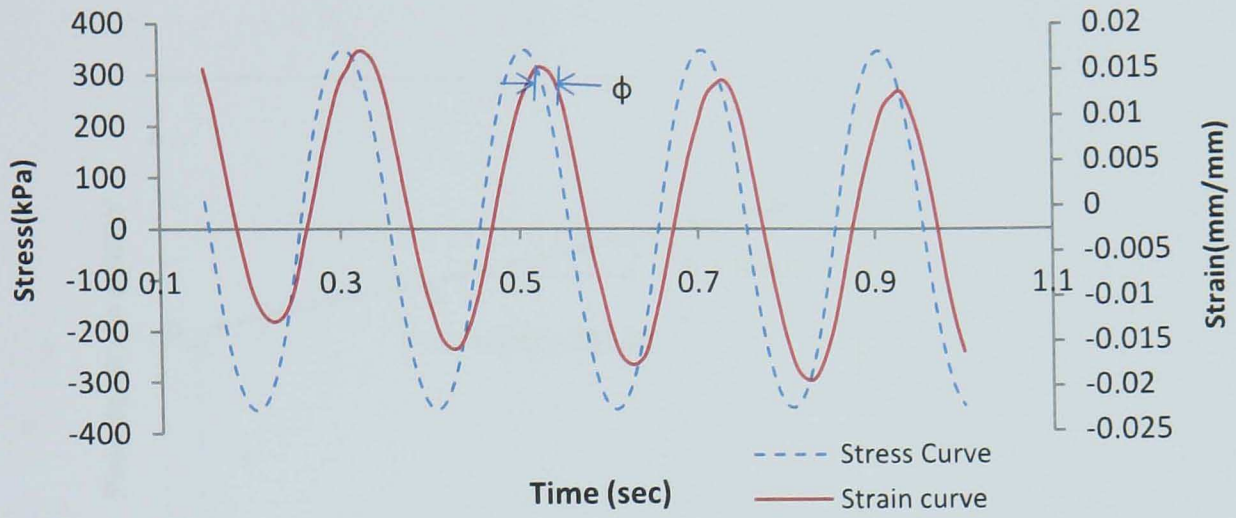

Figure 5.22 Stress strain distribution in fatigue test

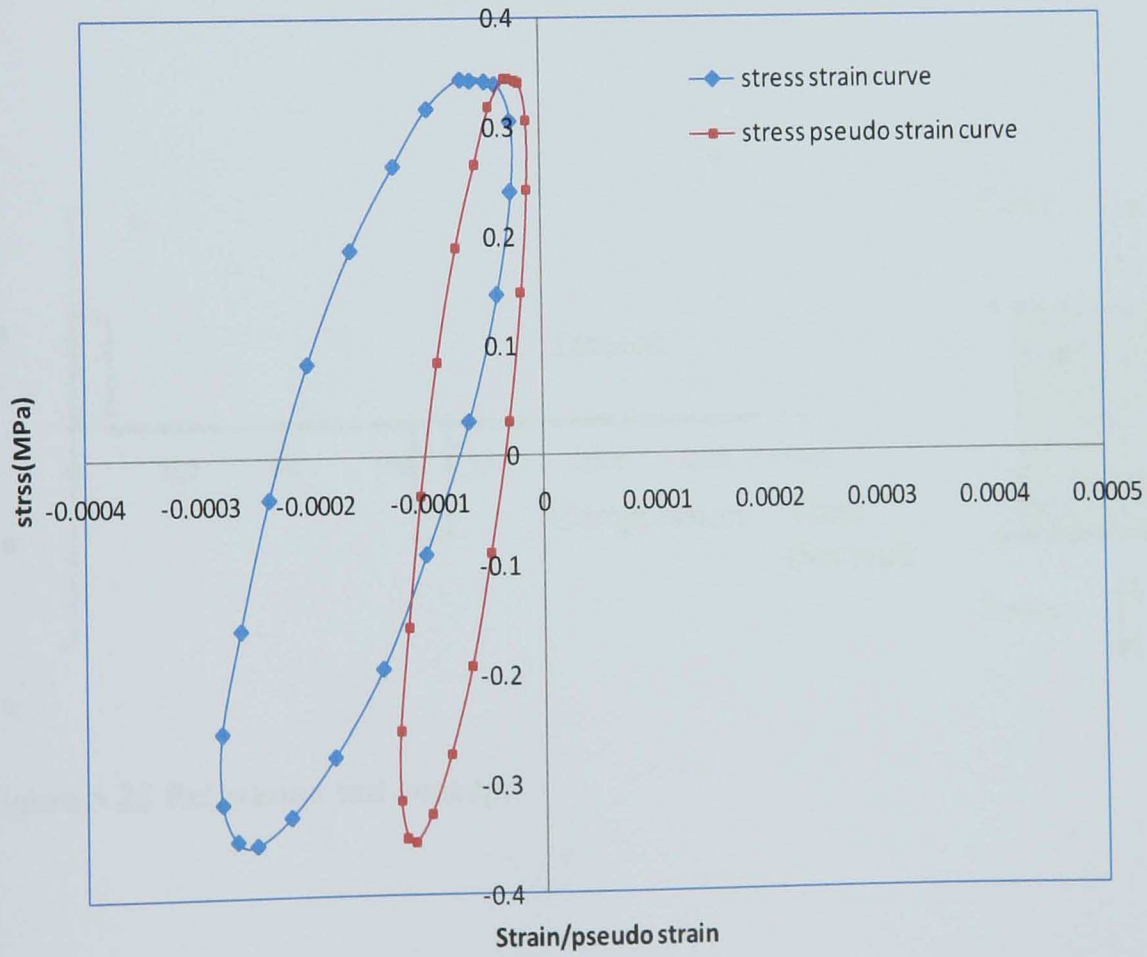

Figure 5.23 Stress strain and stress pseudo strain distribution in fatigue test

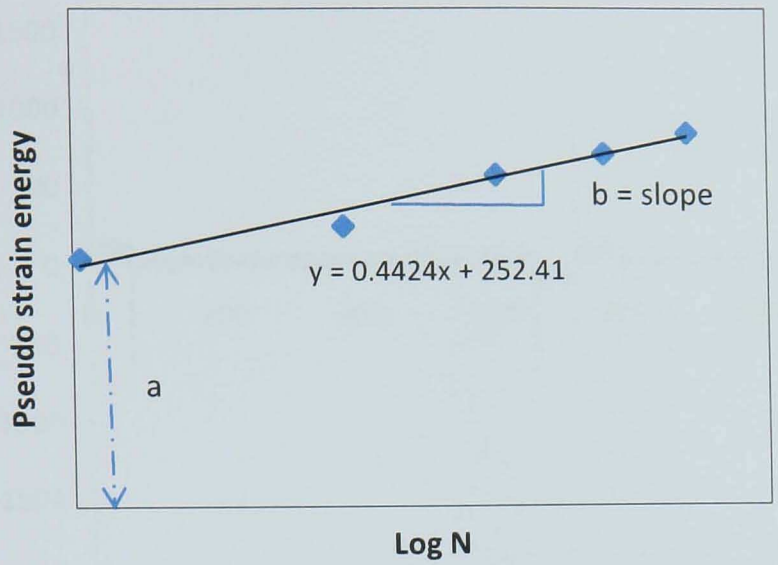

Figure 5.24 Typical plot of pseudo strain energy in constant stress fatigue test

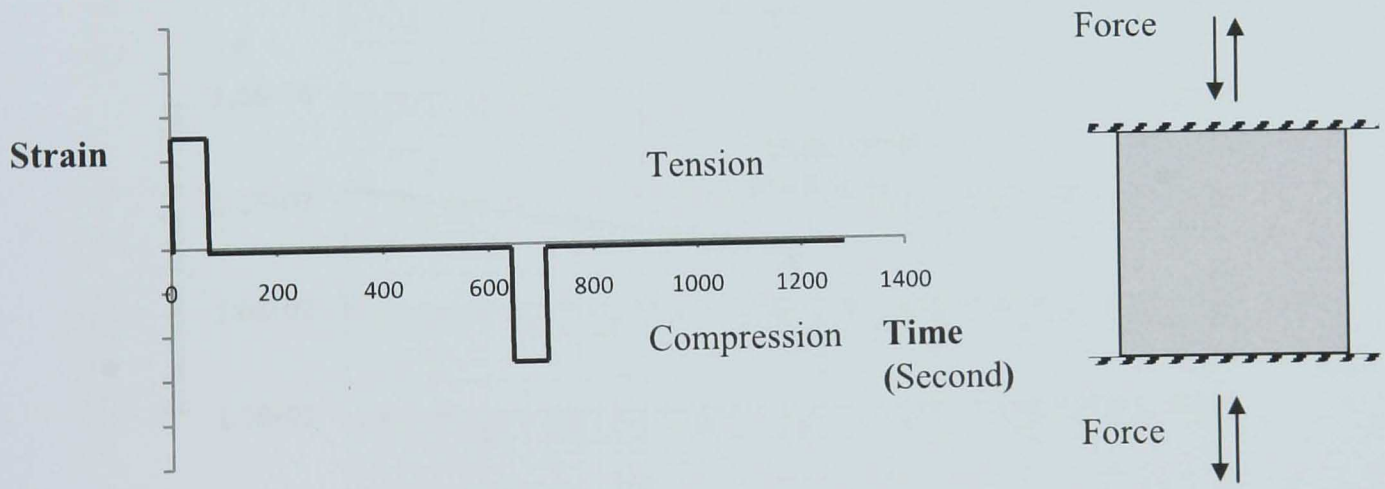

Figure 5.25 Relaxation test concept

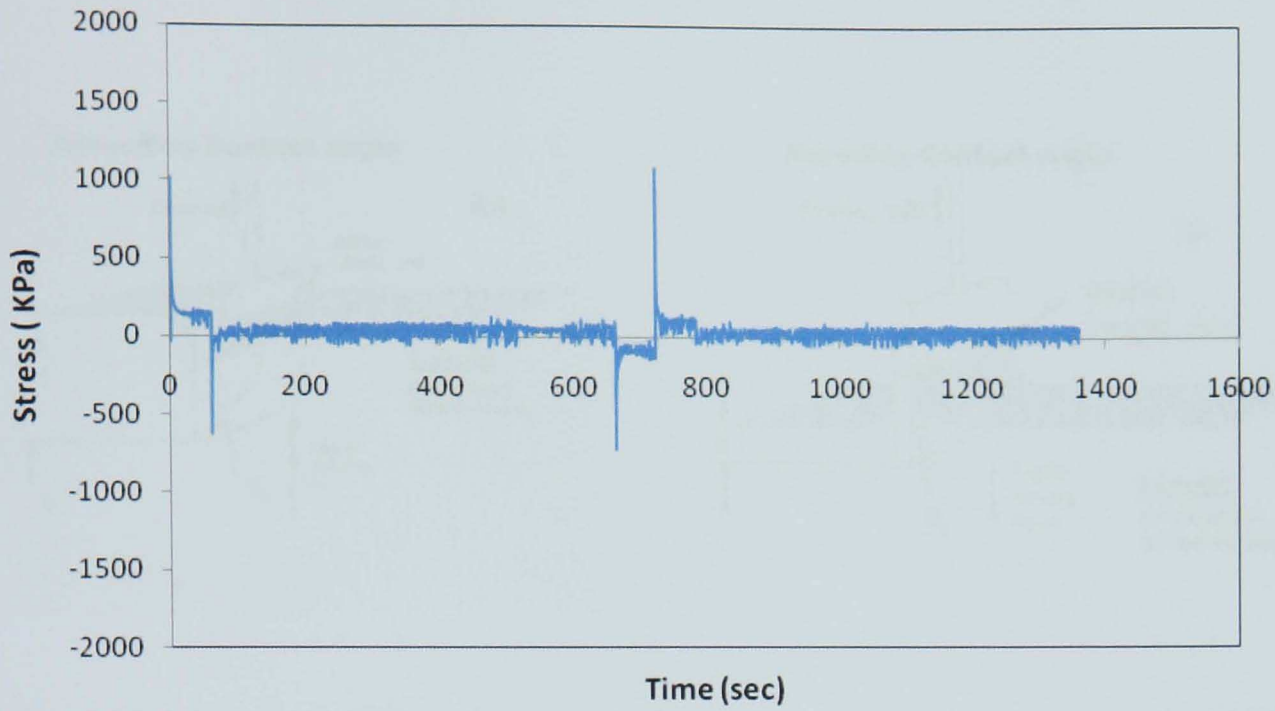

Figure 5.26 Stress vs. time in relaxation test

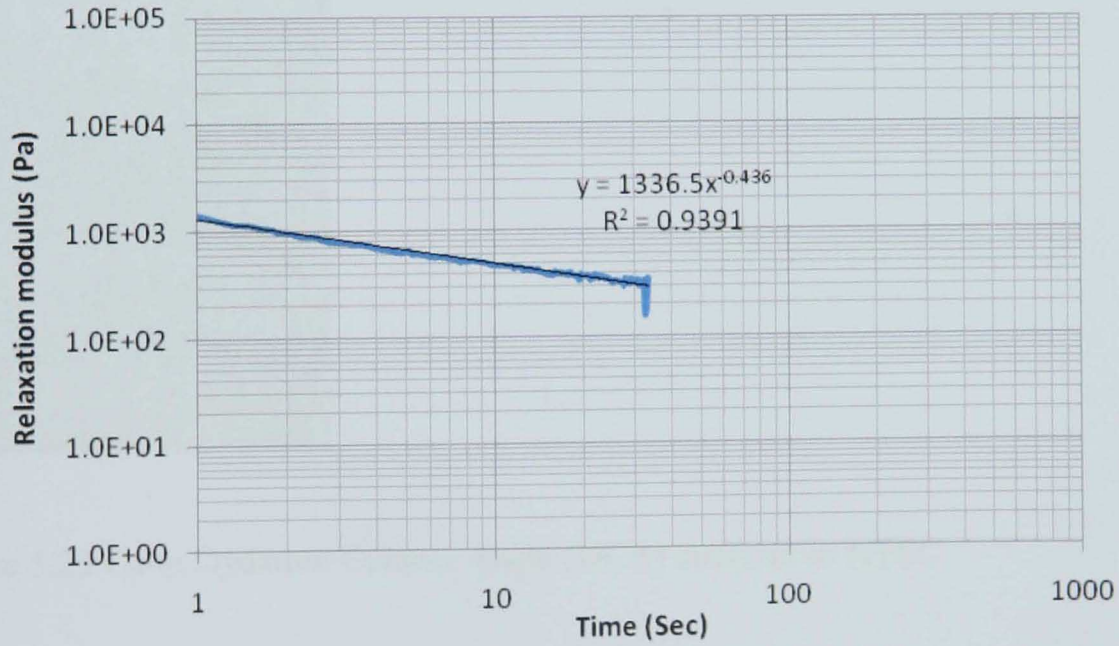

Figure 5.27 Relaxation test data

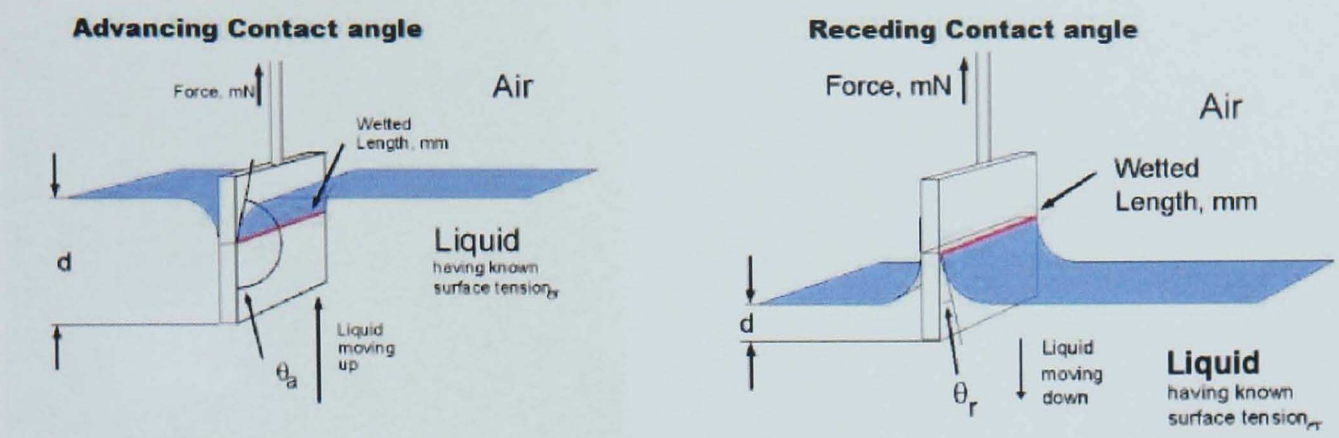

Figure 5.28 Advancing and receding process for surface energy of binder (Kibuuka, 2007)

Figure 5.29 Cahn Dynamic Contact Angle (DCA) analyzer in NTEC

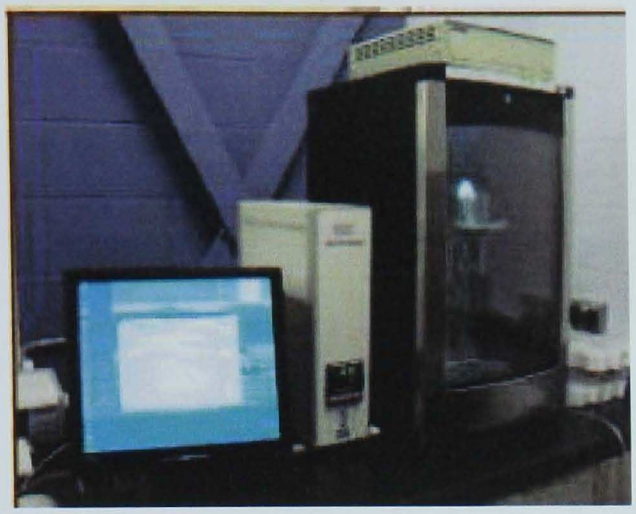

5.30 Dynamic vapour sorption system DVS in NTEC

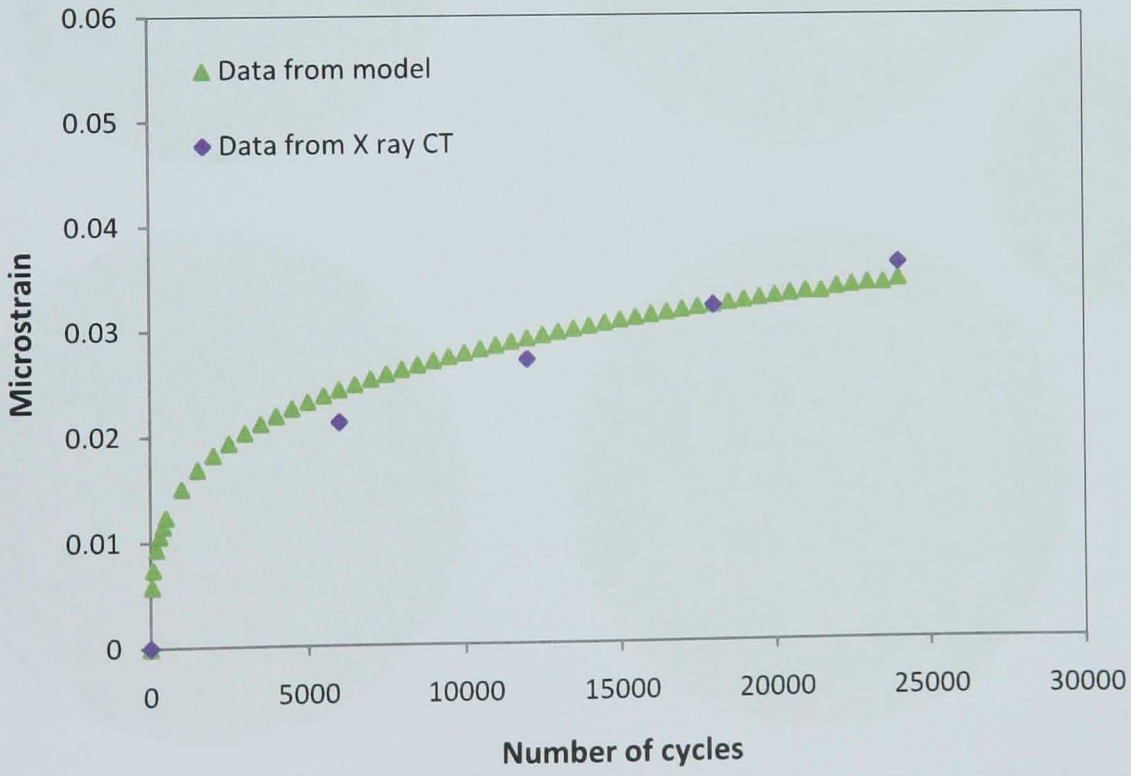

Figure 5.31 Data from constant stress fatigue model and from X ray CT

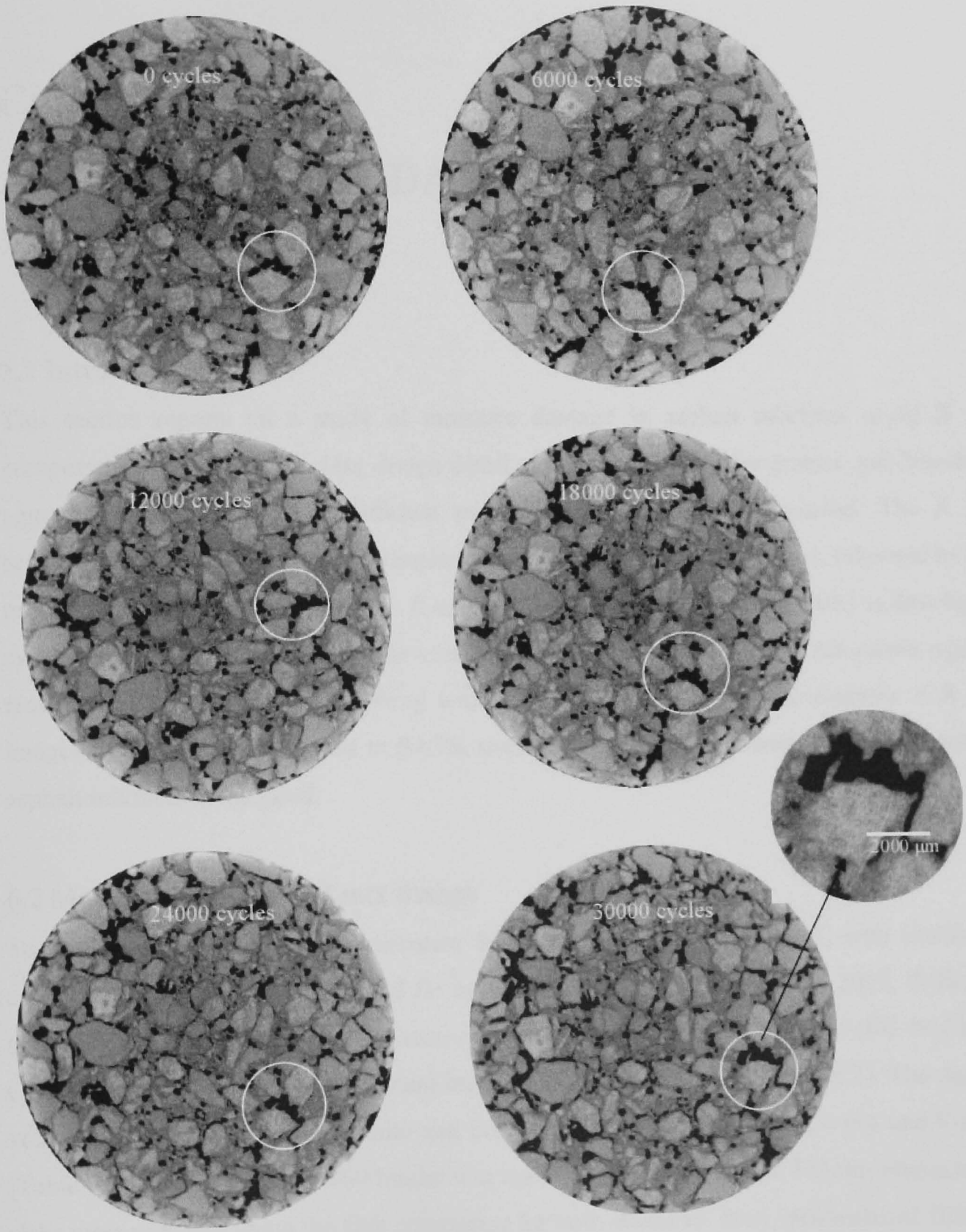

Figure 5.32 Damage from X ray CT images with increase in number of load cycles

Chapter 6

ASPHALT MICRODAMAGE DUE TO MOISTURE

6.1 Introduction

This section reports on a study of moisture damage in asphalt mixtures using X ray computer tomography (CT). Mix design detail of asphalt mixtures for granite and limestone aggregates considering three different ranges of void content is included. The X ray scanning of dry specimens and specimens after saturation is then described, followed by the procedure for saturation of samples. A methodology for moisture permeability is developed using the volume of connected air voids. Later on the procedure for saturation ageing tensile stiffness (SATS) testing along with X ray CT is described. The analysis of X ray images from the samples tested in SATS, useful for studying the internal microdamage in asphalt mixtures is included.

6.2 Material selection and mix design

To be consistent with previous research, dense bitumen macadam (DBM) with limestone and granite aggregate were selected for asphalt mix design (Gregory et al. 2009, Collop et al. 2003). Aggregate grading was determined for these two types of mixture (BS 4987) for 0/32mm dense bitumen macadam road base (Table 6.1, Figure 6.1, Figure 6.2). The design void content ranges for both granite and limestone mixtures were 2-4%, 4-6% and 8-10% (Table 6.2). 4.0% of grade 40/60 binder was used in the mix. 305mm x 305mm 60mm thick slabs were prepared using the slab compactor for both mixtures. Four specimens of 100mm diameter and 60mm height were cored from each slab.

A total of 24 cores were prepared from both limestone and granite aggregate mixes. Density and void content of all cores were determined in the laboratory. These values were used as reference for analysis of X ray images.

6.3 Saturation and moisture damage from X ray CT

Moisture damage affects the performance and durability of asphalt mixtures. Due to loss of cohesion in binder or failure of adhesion between binder and aggregate, the structural performance of the mixture is affected. Thus both mechanisms cause damage to asphalt mixtures which reduces the stiffness modulus, and hence causes a reduction in the strength of an asphalt pavement (Collop et al. 2004). The non destructive technique of X ray CT can be applied to study the permeability and moisture damage of asphalt mixtures.

In order to study moisture transport in asphalt mixtures, samples were scanned in the X ray CT and then saturated with distilled water at 20°C using a partial vacuum of 680mbar pressure for 30 min (Figure 6.3). The weight of the specimen before and after saturation was determined. The mass of the specimen was determined and the percentage saturation calculated using equation 6.1.

$$\text{Percent saturation} = \frac{100(M_w - M_d)}{((M_d / G_{mb}) - (M_d / G_{mm}))} \qquad (6.1)$$

where G_{mb} is dry bulk density, G_{mm} is maximum density, M_d is mass of dry core and M_w is the mass of wet core.

The saturated specimens were taken into the X ray CT for scanning. In order to avoid water draining out of the sample, the specimens were kept in the X ray CT along with a container. The size and material of the container was selected such that it can be fixed into the X ray system without affecting the scanning parameters (Figure 6.4).

2D images (slices) were taken at 1mm intervals and data was saved for image analysis. The image data was analysed using image analysis techniques. The threshold grey value was fixed according to the void content values from the laboratory density test.

6.4 Saturation from X ray CT

Saturation was determined from X ray CT based on the difference between the air void content values before saturation and after saturation. The same threshold value was used for the X ray image analysis of samples before and after saturation. For example a grey value of 40 was selected for image analysis of a dry specimen according to the void content value from the laboratory; the same value was applied in image analysis of saturated specimens. The decrease in the void content value for the sample was determined. This decrease in void content indicate that some voids filled with water due to saturation and were not selected as air voids in X ray image analysis. The percent of voids filled with water was considered as percent saturation of the specimen.

The images were analysed for moisture study in the image analysis software VG studio max, image J and Image pro plus. Distribution of water over the height of the sample was determined (Figures 6.5 - 6.10). It was found that due to non uniform void content in specimens, the water permeability was also not uniform. For specimens containing high void content, the initial saturation was high compared to specimens of low void content. In order to study the effect of void content on permeability, specimens with different void content values were saturated and scanned from mixtures with both granite and limestone aggregates. The trend of increase in saturation with increase in void content is similar in case of both mixtures (Figure 6.11). Due difference in density of water (1 gm/cm^3) and air (0.00129 gm/cm^3), the grey values are different for water and air and thus the volume of air replaced by water can be determined from X ray CT. A typical X ray scan before the saturation and after saturation is shown in Figure 6.12.

6.5 X ray CT for Saturation Ageing Tensile Stiffness (SATS) Test

The SATS test is a combined ageing and moisture sensitivity laboratory test. The idea of its use is to age a compacted asphalt mixture not with loading damage but with moisture damage. Moisture damage creates a loss of cohesion in a mixture caused by a loss of adhesion between the bitumen and the aggregate and it therefore ages the asphalt, resulting in a reduction in a pavement's ability to support traffic-induced stresses and strains. Failure of the bond between the bitumen and aggregate also results in increased stress in the pavement foundation.

The SATS test has been used to evaluate the performance of coated macadam binder course and base mixtures with relatively low binder contents and relatively high air void contents. Oxidation and volatile loss tend to be universally accepted as the dominant factors affecting age-hardening. Short-term age hardening is associated with the loss of volatile components and oxidation of the bitumen during asphalt mixture construction. Long-term age hardening is due to progressive oxidation of the material in the field. Both oxidation and volatile loss cause an increase in viscosity of the bitumen which gives the material a higher stiffness. Age hardening can have two effects, either increasing the load-bearing capacity and permanent deformation resistance of the pavement by producing a stiffer material, or reducing pavement flexibility, resulting in the formation of cracks with the possibility of total failure (Vallerga et al. 1982).

The SATS test procedure was developed in NTEC (Collop et al. 2004, Collop et al. 2007). The purpose of the SATS test is to speed up the ageing process by addition of high pressure and high temperature.

To study the SATS results under different conditions, four sets of specimens were tested with five specimens in each set. 50 penetration (40/60) paving grade bitumen was used in all the specimens. Two sets of specimens were from acidic aggregate and two from basic aggregate. All the specimens were scanned before starting the SATS test. This was done to compare later on the X ray CT data before and after the specimens tested.

The SATS test procedure was required to first test the specimens for indirect tensile stiffness modulus using the Nottingham asphalt tester (NAT). The specimens were then immersed in distilled water at 20°C and saturated using a residual pressure of 68kPa for 30 minutes. After removal of any surface water, the wet mass of each specimen was determined by weighing and the percentage saturation (or initial saturation) is calculated. The PAV (pressure aging vessel) was partially filled with distilled water until the level is between the fourth and fifth specimens (Figure 6.13). The vessel and water were maintained at the target temperature of 85°C for at least 2 hours before the conditioning procedure commences. The saturated specimens were placed into the vessel using the

specimen tray and the conditioning procedure is performed at a pressure of 0.5 MPa and a temperature of 85°C for 24 hours (Nicholls et al. 2009). The test holds five cores at a time, four of which are above water and one is under water (Figure 6.14). This is the modified form of the previous standard procedure developed in NTEC, as the modified form can be used for testing asphalt specimens with a higher penetration grade of binder. As the cores used in this study were produced with 50 pen binder, the new 24 hour SATS procedure was performed. Positions for both mixtures containing granite (acidic) and limestone (basic) aggregate were fixed. Specimens with different void content ranges were also fixed at different positions (see Table 6.3).

After completing 24 hours of testing, the temperature was reduced to 70°C in about 3 hours and the specimens were taken out and surface dried. The mass and percentage saturation of the specimens were determined. The specimens were taken to the X ray CT and scanned using the previous set of scanning parameters applied to scanning before starting the test. The values of saturation determined at the end of test are termed retained saturation. Finally the specimens were tested in the NAT to determined the final stiffness of these specimens.

6.6 X ray image analysis and SATS test data

The values of saturation from X ray CT were found to be up to 10% higher compared to the values computed from the mass method before and after saturation. This was because the specimens were scanned in X ray CT along with the container and there was no drainage from the specimen, while in the case of mass calculation the sample was taken out of the water and some of the saturated water drained.

From X ray image analysis of scans at initial saturation and scans after SATS test, increase in void content values was found. This increase in void content was due to decrease in saturation during SATS test. Using the data at initial saturation and at final saturation, the retained saturation of specimens in the SATS test was determined. The difference in void content from X ray CT of scans dry specimens, after initial saturation and at the end of SATS test is shown in Figure 6.15. Retained saturation was calculated as the amount of saturation maintained in asphalt specimens after completing the SATS test.

Consistent with the results of previous research, the general trend found was for retained saturation to decrease for specimens located lower down the vessel except for position 5 (Collop et al. 2004). For the case of specimens in position 5 in the vessel, the saturation value was high as the specimen was immersed in water. Due to water inside the vessel, the air inside is fully saturated.

For specimens, containing acidic and 2-4% void content, the retained saturation was minimum, for 4-6% void content, the saturation were more than the first range and was maximum for 8-10% void content (Figure 6.16, Figure 6.17, Figure 6.18, see). In case of specimens containing basic aggregate the general trend was similar to the specimens containing acidic aggregate (Figure 6.19, Figure 6.20, Figure 6.21).

The test involved X-ray scanning the same core three separate times, once when the core was dry, once when the core was initially saturated and the third time after the SATS test. The retained saturation values were found different for specimens at different positions in the test tray. Except specimens at position 5, the values of retained saturation was high for specimen at position 1 in SATS test and decrease for specimens downward until position 4.

Computer programming for void connectivity

Moisture can penetrate on asphalt mixture if the air voids in the specimen are internally connected. In order to study the moisture effect on asphalt mixture internally, the connectivity of air voids was determined from X ray CT. A Matlab program was developed to determine the volume of connected air voids in the asphalt specimens (Appendix A-2). Separate sheets consisting of void coordinates, size and maximum radius/diameter were prepared for each slice. Similarity index (SI) method was used to identify individual air voids

$$SI(i,z)\min = \min(\left|x_{i,z-x} - x_{j,z+1}\right| + \left|y_{i,z-y} - y_{j,z+1}\right|)$$

where value of i is from 1 to n, also value of J is from 1 to m. n and m represent the number of air voids in cross-sections of two adjacent slices z and $z+1$.

The minimum *SI* is defined to check whether the void with minimum *SI* overlaps with on the void in next slice or not. If connectivity is found, the volume of the connected voids is saved. The air void shape is considered circular and the diameter of each void was determined from X ray images. The program is run twice, first from top (considering top slice as first slice) toward bottom (considered as end slice as last slice) and then from bottom (considering bottom slice as first slice) toward top (considering top slice as end slice). The values of void connectivity from computer programming was found slightly lower (28%, compare to 34% from laboratory saturation method), because the program calculates the connected air voids only from one face to the other face of the sample and voids if connected from the sides is not considered. The flow chart for the program can be shown as:

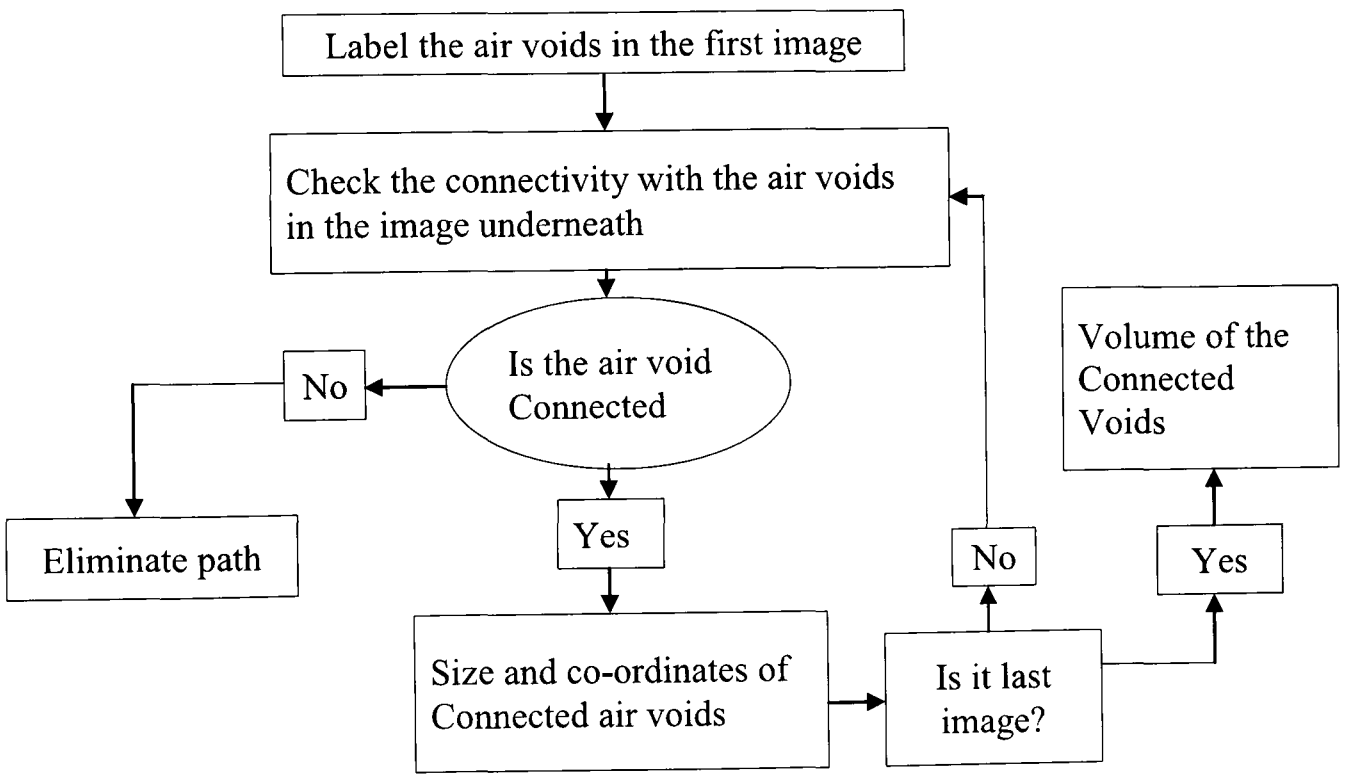

6.6.1 Stiffness values

From the values of initial stiffness (before specimens were kept in SATS vessel) and final stiffness (at the end of test), it was observed that for specimens containing acidic aggregate the general trend for retained stiffness modulus decreased with increase in retained saturation while for specimens containing basic aggregate, the trend is different. Also the

retained stiffness is higher for specimens contain basic aggregate compare to specimens containing acidic aggregate. The positioning inside the PAV was shown to make a difference in results in previous studies (Collop et al. 2004, Collop et al. 2007). It was observed from analysis of X ray scanning that retained saturation at position 5 is either equal to or slightly higher than initial saturation.

From X ray CT and from NAT test data it was observed that increasing void content value resulted in a lower stiffness. The trend is similar for both mixtures with basic and acidic aggregate (Figure 6.23).

It was found from final stiffness results and from the connectivity results determined using the Matlab program, that for specimens of high void connectivity the relative stiffness is less compare to specimens of low connectivity. For similar void connectivity, the relative stiffness of mixture containing acidic aggregate is lower compare to mixture containing basic aggregate. (Figure 6.24).

It can be seen from Figure 6.25 that for specimens containing the acidic aggregate, the general trend is for the retained stiffness modulus to decrease as the retained saturation level increases. Generally the decrease in relative stiffness is smaller for mixtures containing basic aggregate compare to mixtures containing acidic aggregate. Some scaling (seen as colour change) was also observed after SATS test on few specimens contain acidic aggregate (Figure 6.26).

6.7 Summary

Using X ray CT, an improved methodology for saturation and moisture damage of asphalt is developed. The saturation values from X ray CT were found in comparison with the values from laboratory weighing method. As the specimens are scanned within water, the water does not drain out from the outer face voids of the specimen and is considered in the saturation data from X ray CT. Cores of different void contents were considered for testing and X ray scanning and their effect on moisture damage of asphalt was studied. Mixtures containing different types of aggregate were found to have different performance in saturation and moisture damage. Design void content values and chemistry of aggregate

were found the important parameters for studying the moisture damage of asphalt. Mixtures of high design void content were found to have high saturation and high internal void connectivity.

Combined moisture damage and ageing of asphalt specimens was investigated from X ray CT by scanning the samples at three different stages of SATS testing. The retained saturation from X ray images and from weighing specimens was determined and related to the retained stiffness at the end of testing. Mixture containing limestone aggregate was found to have high stiffness compare to granite aggregate, means mixtures containing basic aggregate are good to resist moisture damage and aging.

Table 6.1 Aggregate gradation

Sieve size (mm)	Lower limit	Upper limit	Percentage passing	
			Limestone	Granite
40	100	100	100.0	100.0
31.5	90	100	100.0	99.8
20	71	95	81.9	86.1
14	58	82	69.7	72.7
6.3	44	60	44.8	52.7
2	20	40	25.5	32.8
0.25	6	20	10.6	13.2
0.063	2	9	7.3	7.0

Table 6.2 Detail of specimens prepared

Void content	Granite samples	Limestone samples
2-4%	09-216	09-212
	09-217	09-213
	09-218	09-214
	09-219	09-215
4-6%	08-3696	08-3925
	08-3697	08-3926
	08-3698	08-3927
	08-3699	08-3928
8-10%	08-3692	08-3929
	08-3693	08-3930
	08-3694	08-3931
	08-3695	08-3932

Table 6.3 Detail of specimen positions for SATS test

Sample ID	Sample position*	Aggregate Type	Void Content (%)	Target Air Voids (%)
09-216	P1	acidic	2.8	2-4
09-217	P2	acidic	2.5	2-4
09-219	P2	acidic	3.5	2-4
08-3696	P3	acidic	6.7	4-6
08-3697	P2	acidic	5.1	4-6
08-3698	P1	acidic	6.5	4-6
08-3692	P1	acidic	8.8	8-10
08-3693	P3	acidic	8	8-10
08-3694	P4	acidic	10.4	8-10
08-3695	P5	acidic	8.6	8-10
09-212	P3	basic	3.2	2-4
09-213	P1	basic	4.1	2-4
09-214	P2	basic	3.2	2-4
09-215	P3	basic	3.3	2-4
08-3925	P1	basic	6.2	4-6
08-3926	P4	basic	5.7	4-6
08-3927	P5	basic	6.4	4-6
08-3928	P1	basic	6.3	4-6
08-3929	P2	basic	11.5	8-10
08-3930	P2	basic	9.7	8-10
08-3931	P3	basic	10.2	8-10
08-3932	P4	basic	8.8	8-10

* some samples omitted where X ray scanning was not completed

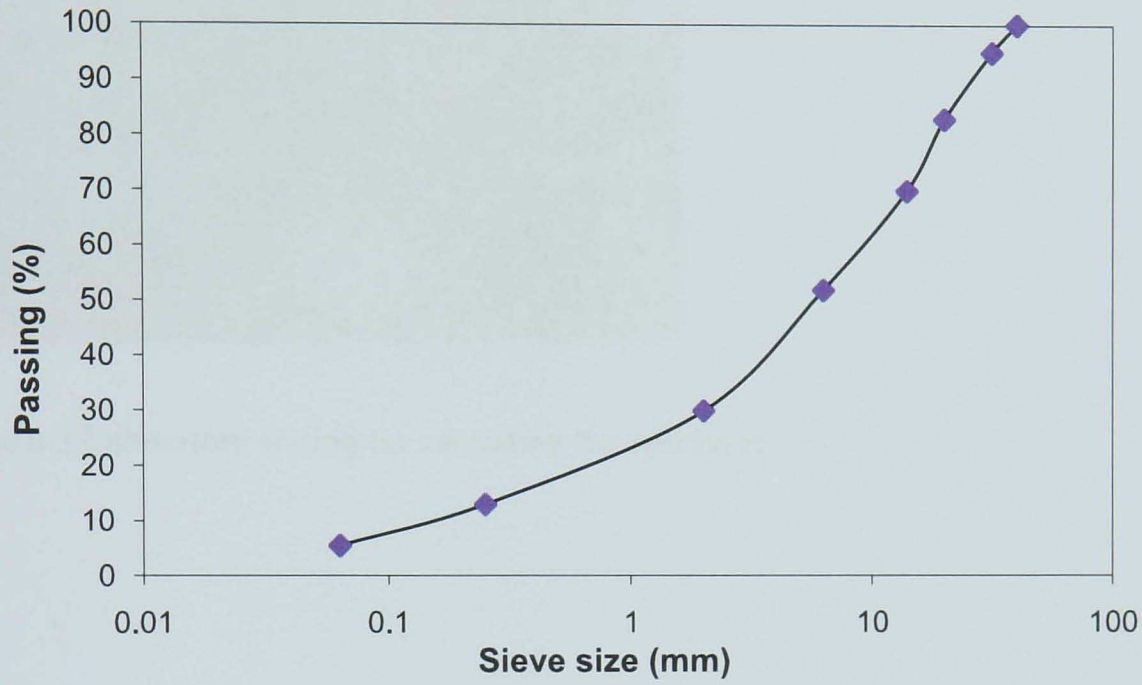

Figure 6.1 Mix design curve (Granite aggregate)

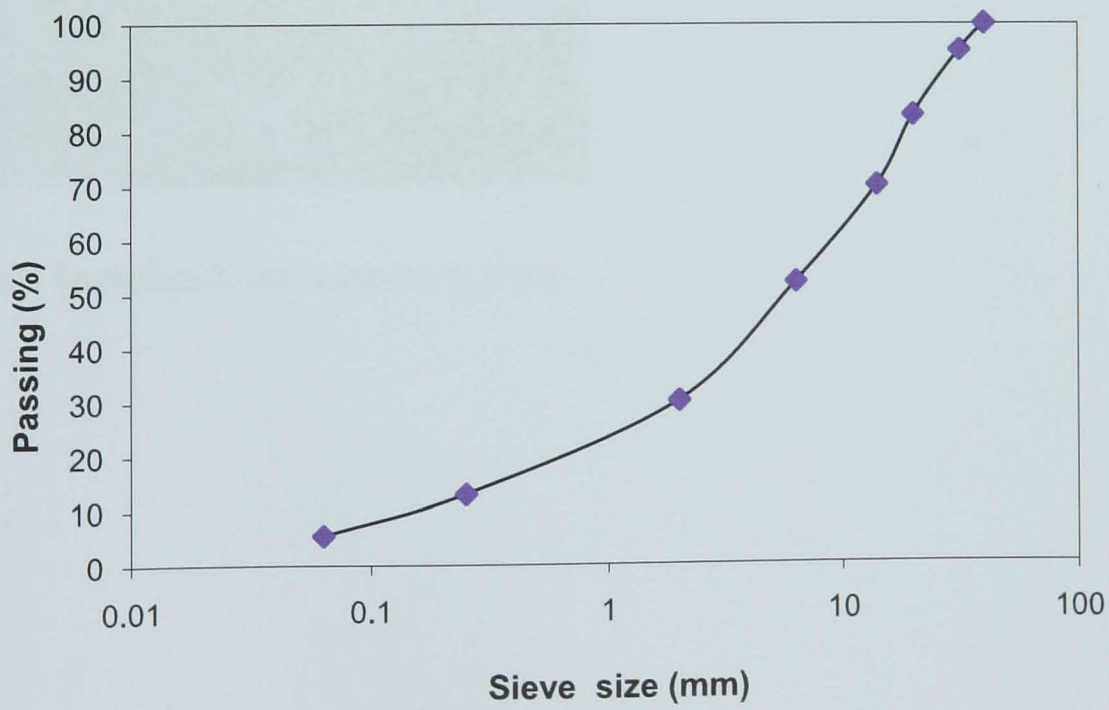

Figure 6.2 Mix design curve (Limestone aggregates)

Figure 6.3 Laboratory setting for saturating the specimen

Figure 6.4 Specimen X ray scanning in water

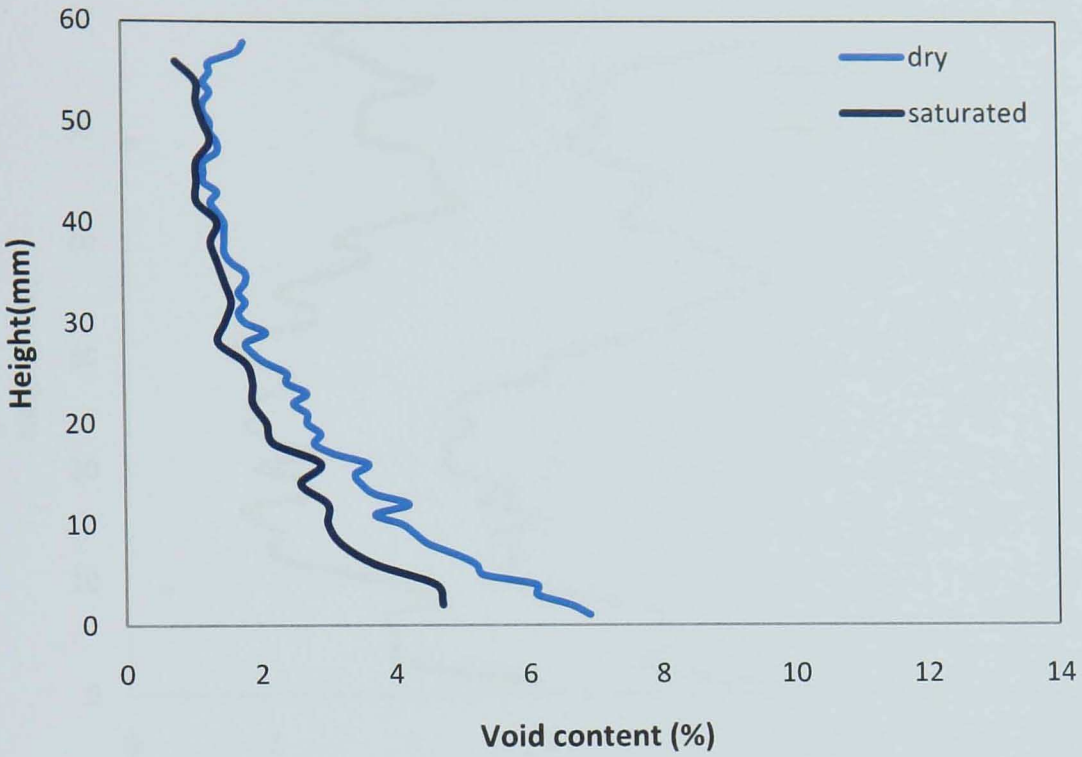

Figure 6.5 Void content in saturated specimen (Acidic aggregate, 3.5% void content)

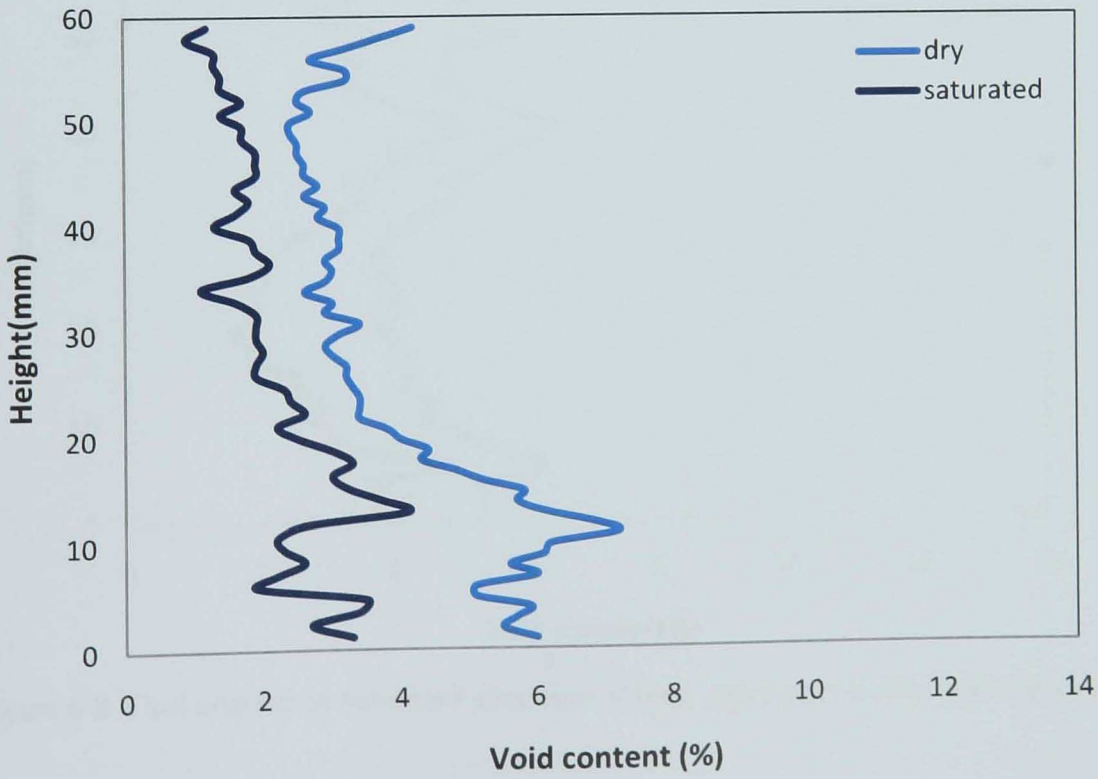

Figure 6.6 Void content in saturated specimen (Acidic aggregate, 5.1% void content)

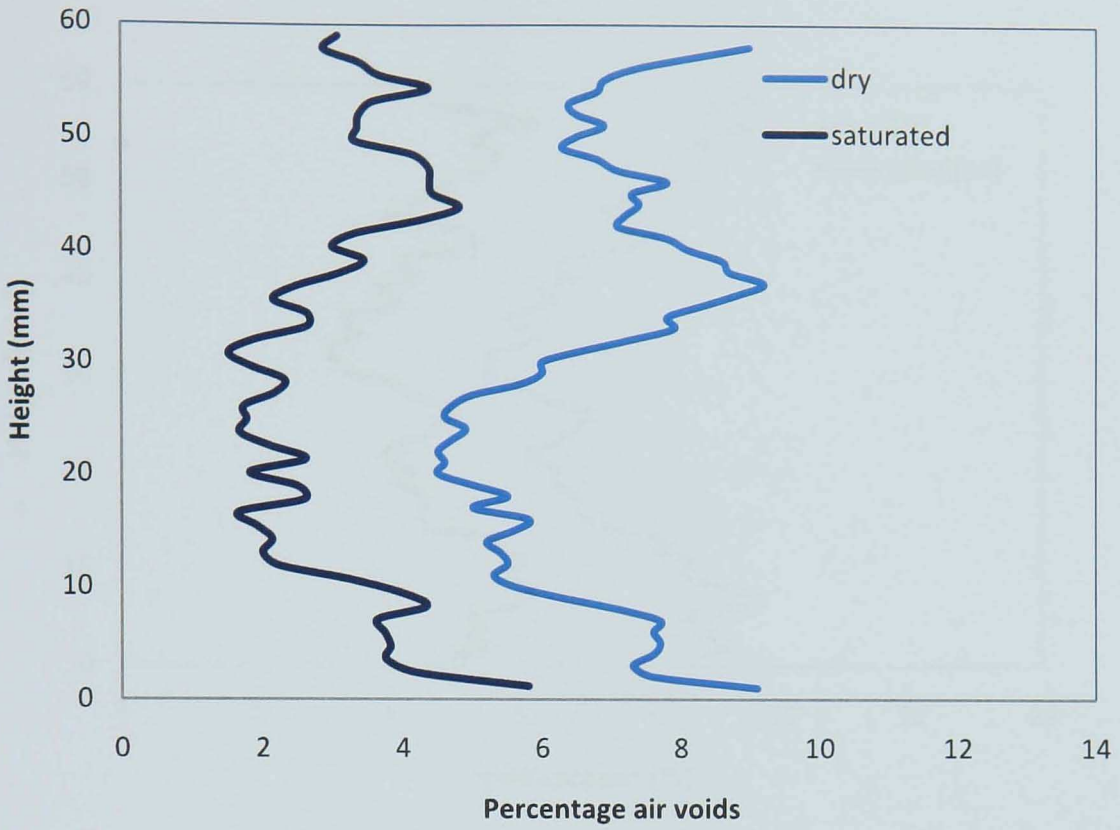

Figure 6.7 Void content in saturated specimen (Acidic aggregate, 7.8% void content)

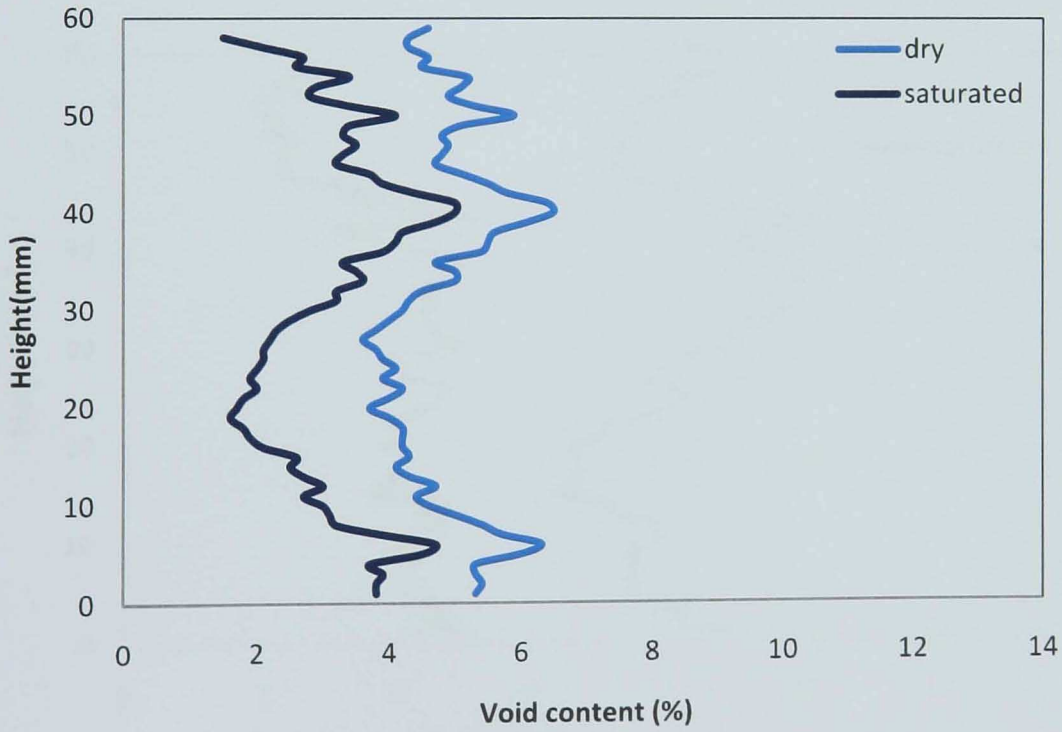

Figure 6.8 Void content in saturated specimen (Basic aggregate, 4.8% void content)

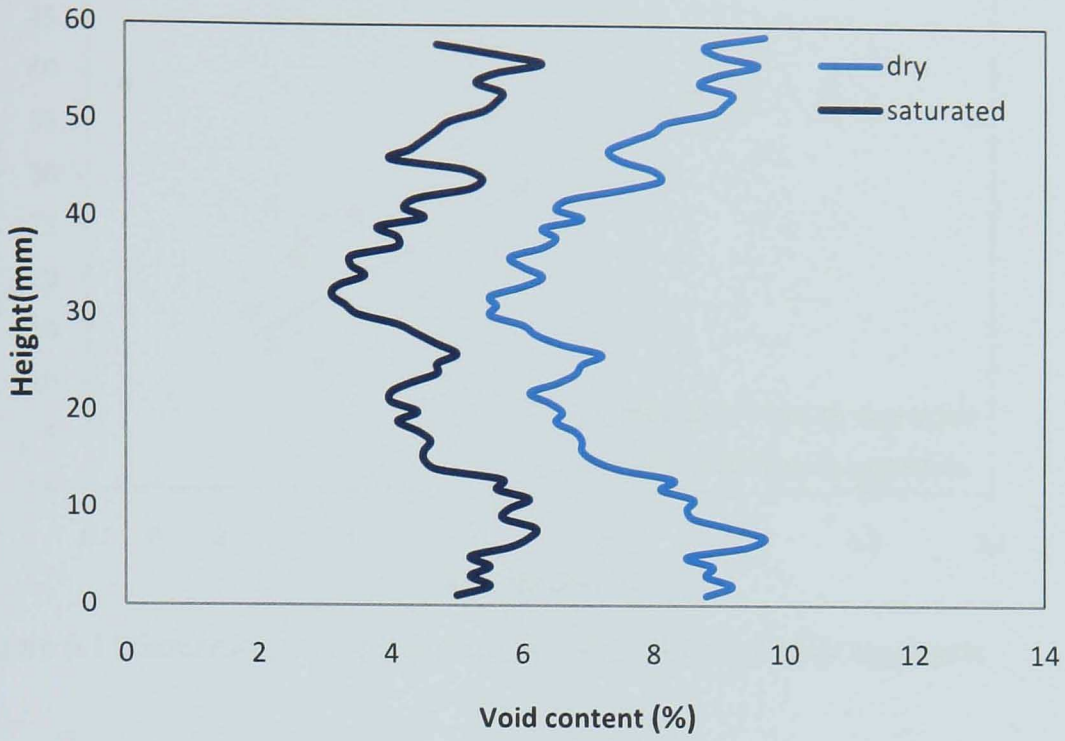

Figure 6.9 Void content in saturated specimen (Basic aggregate, 8.2% void content)

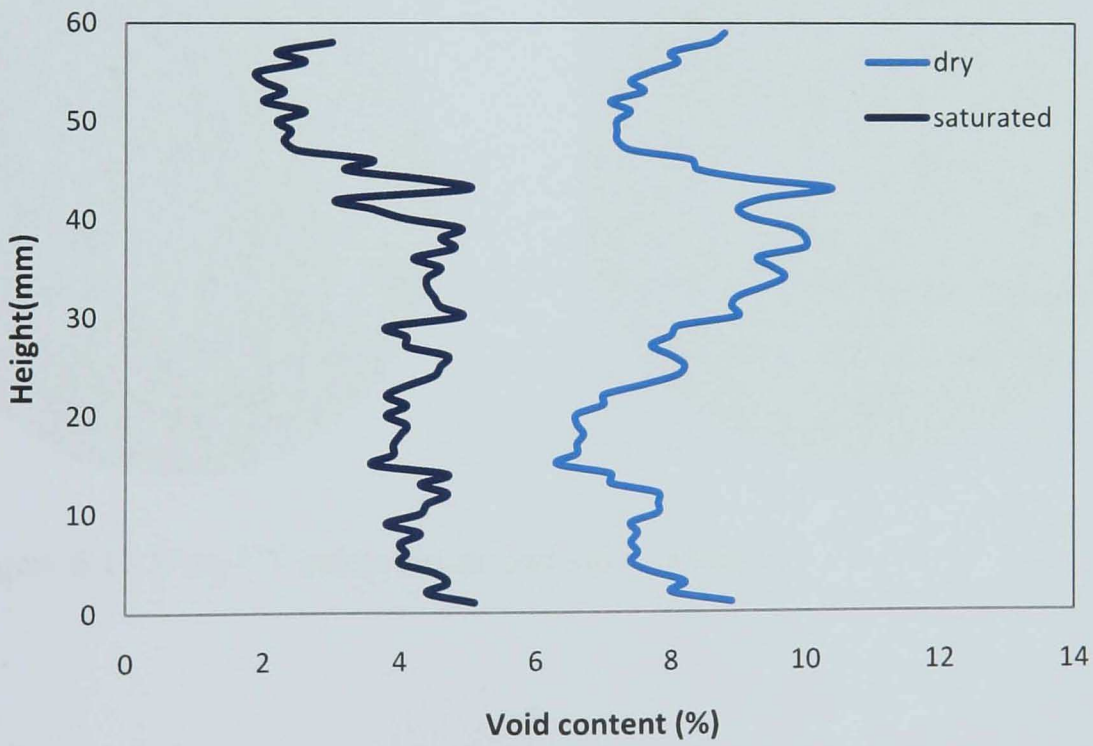

Figure 6.10 Void content in saturated specimen (Basic aggregate,9.2% void content)

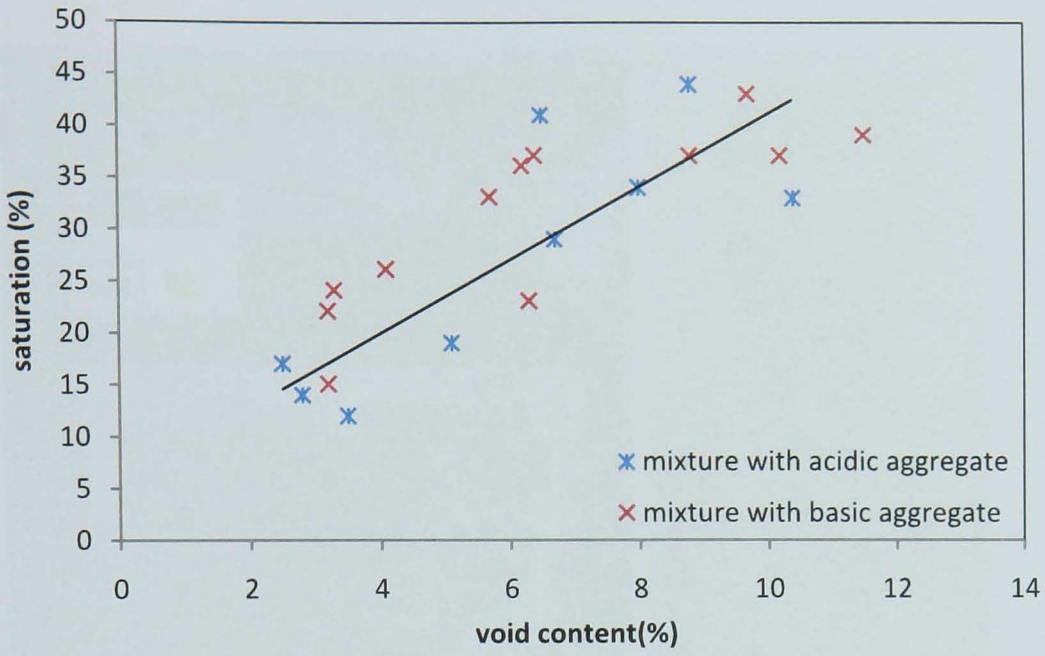

Figure 6.11 Saturation for asphalt mixtures with acidic and basic aggregate

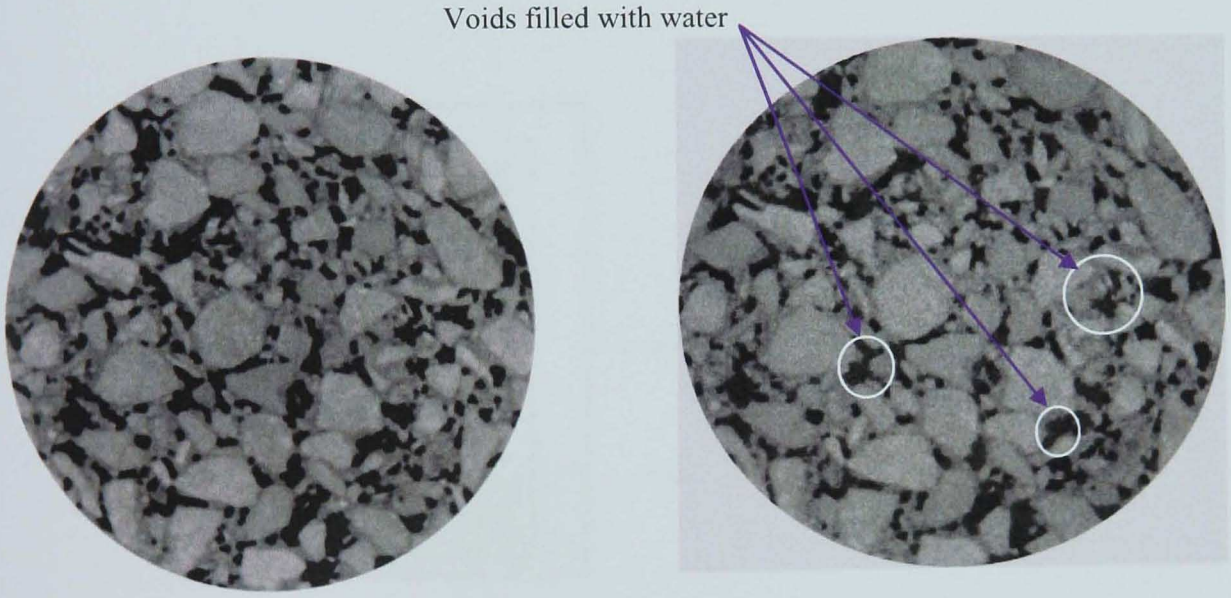

Figure 6.12 X ray CT image before and after saturation

Figure 6.13 (a) Pressure ageing vessel used in the SATS test, (b) specimen rack in vessel

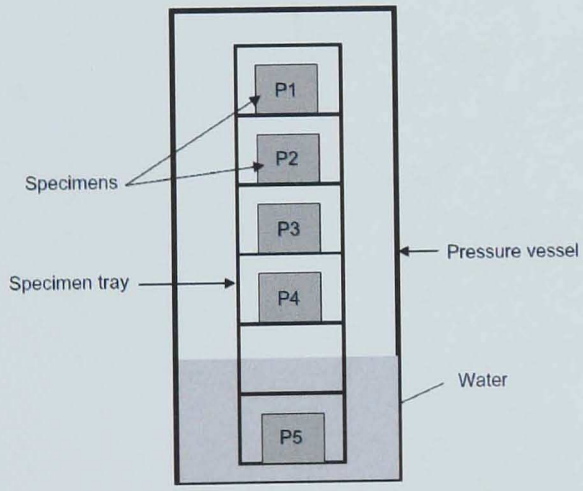

Figure 6.14 Schematic of SATS test configuration (Collop et al. 2004)

Figure 6.15 Void content from X ray scanning at different stages of SATS test

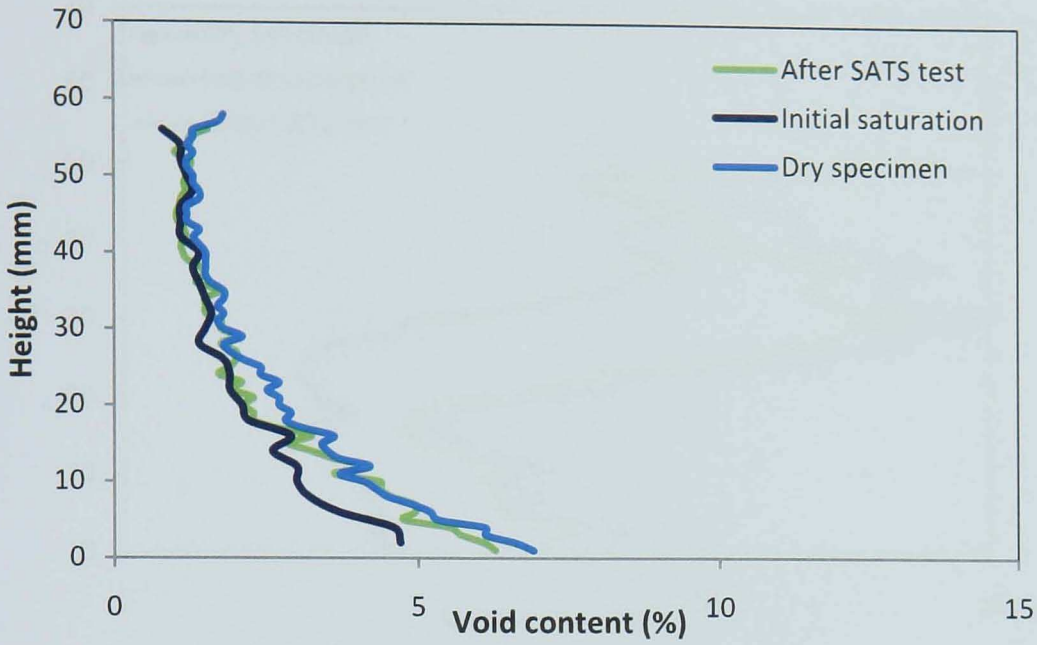

Figure 6.16 Void content in SATS test (Acidic aggregate, 3.5 % void content)

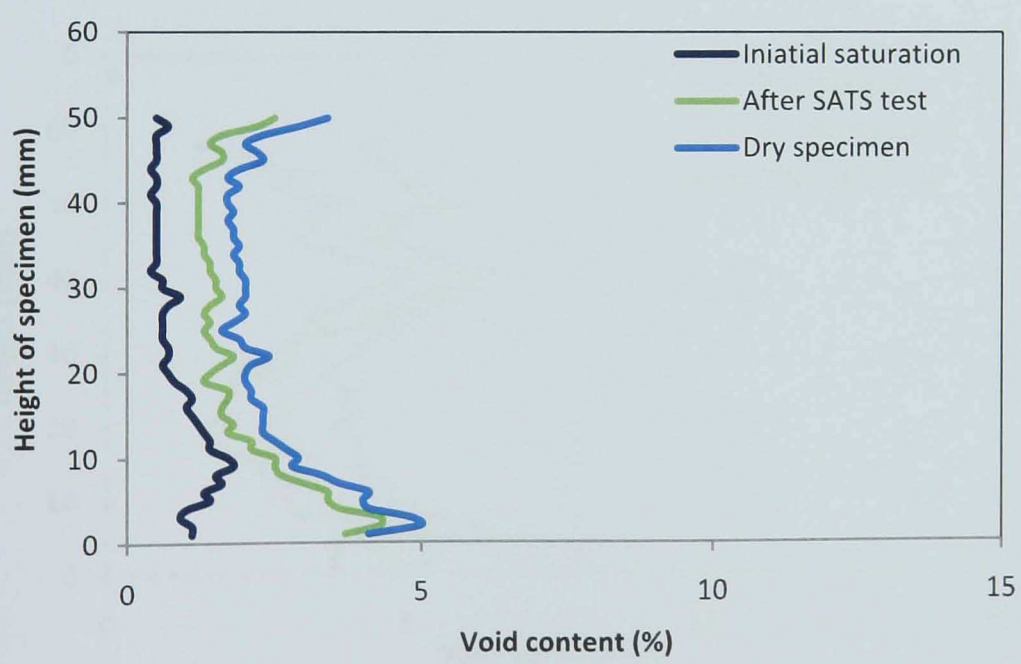

Figure 6.17 Void content in SATS test (Acidic aggregate, 4.3 % void content)

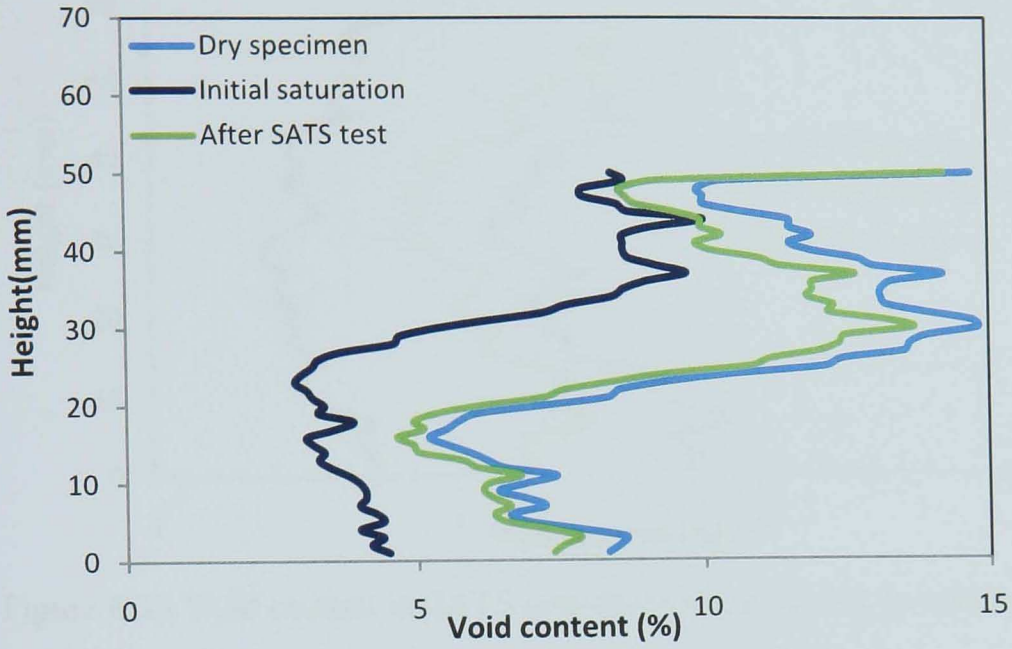

Figure 6.18 Void content in SATS test (Acidic aggregate, 10.1% void content)

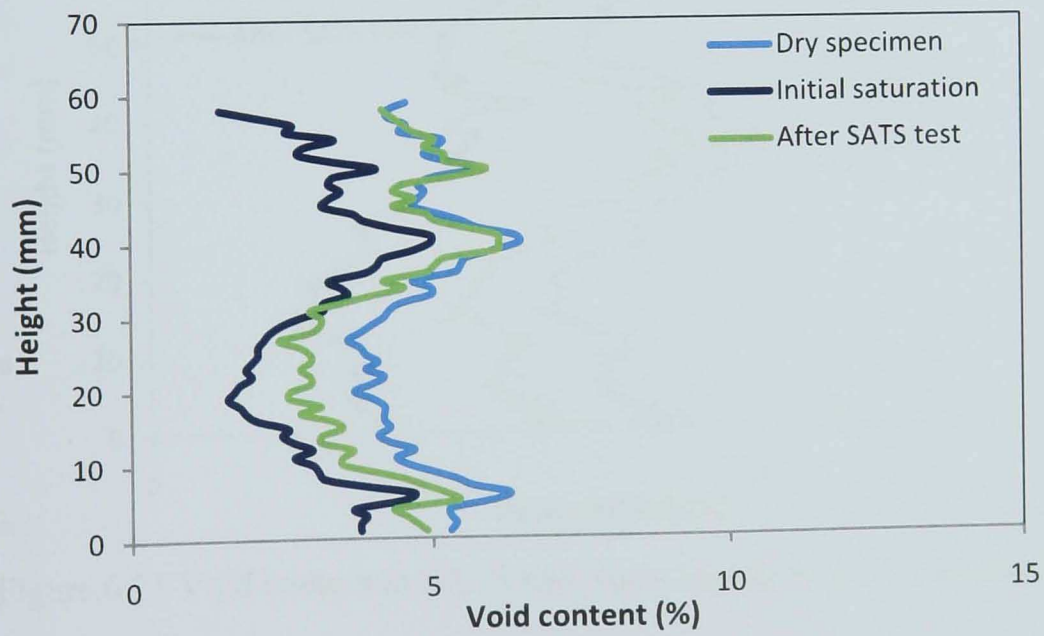

Figure 6.19 Void content in SATS test (Basic aggregate, 6.2 % void content)

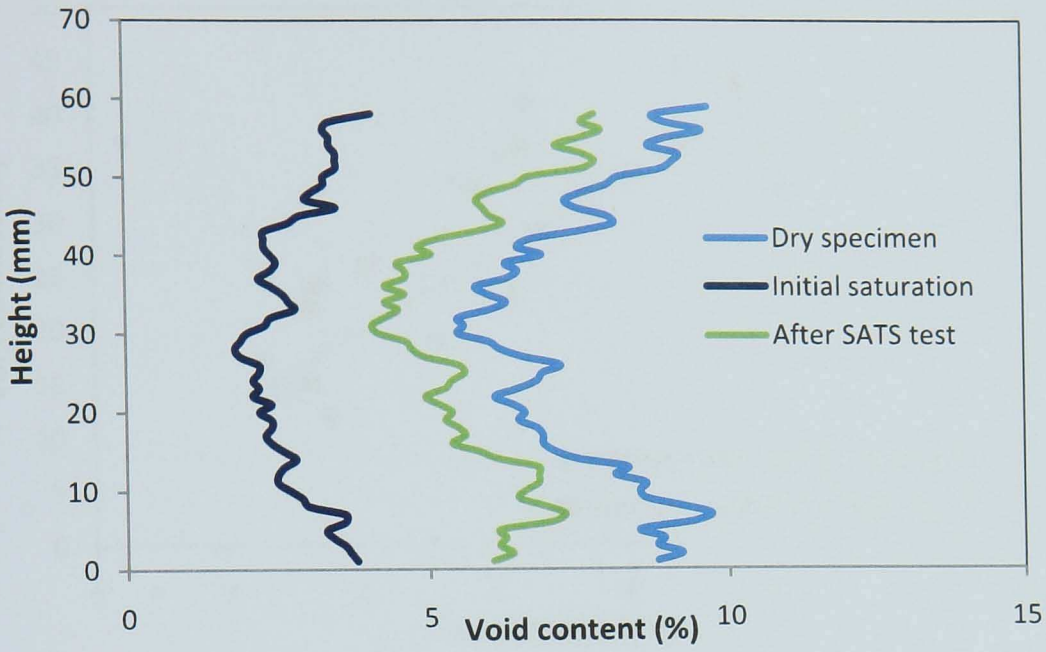

Figure 6.20 Void content in SATS test (Basic aggregate, 9.1 % void content)

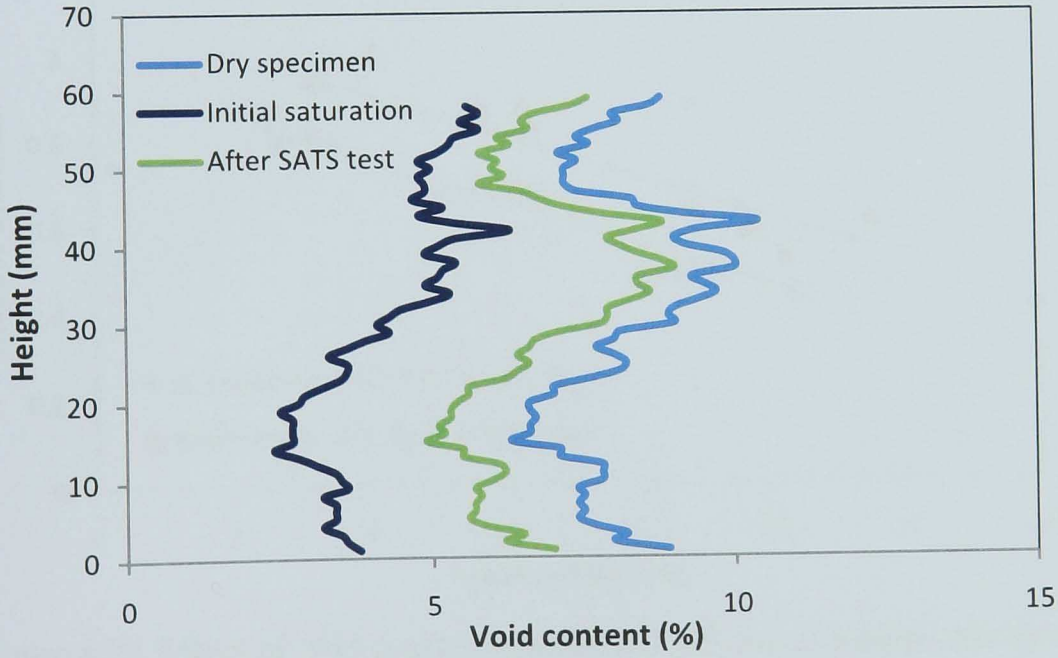

Figure 6.21 Void content in SATS test (Basic aggregate, 9.8 % void content)

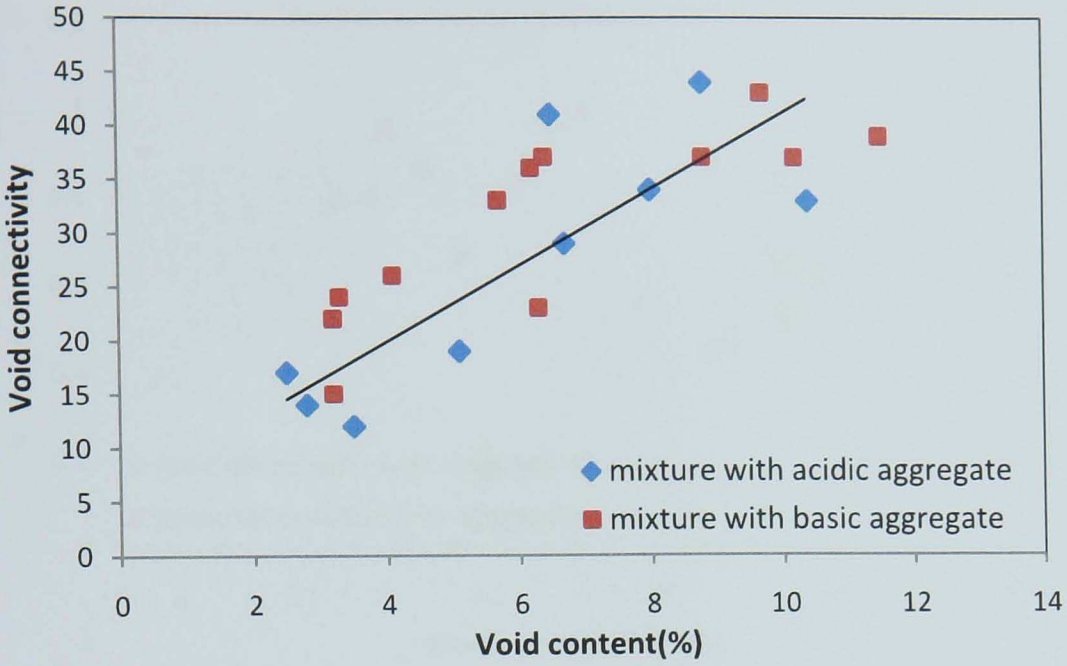

Figure 6.22 Effect of void content on connectivity of air voids

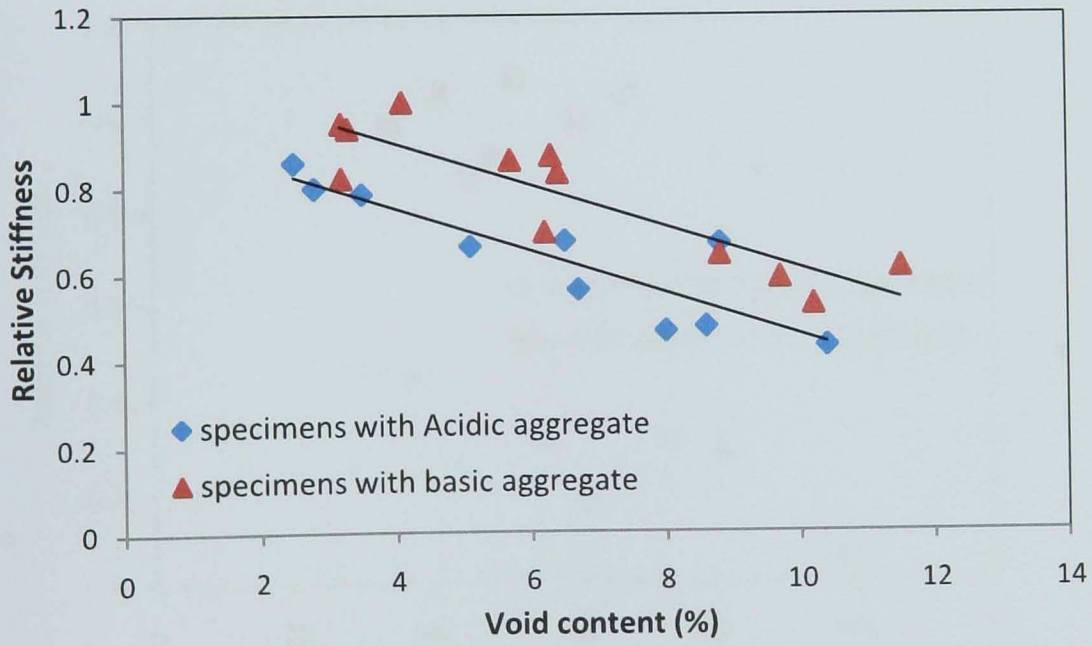

Figure 6.23 Effect of void content on relative stiffness of asphalt mixtures

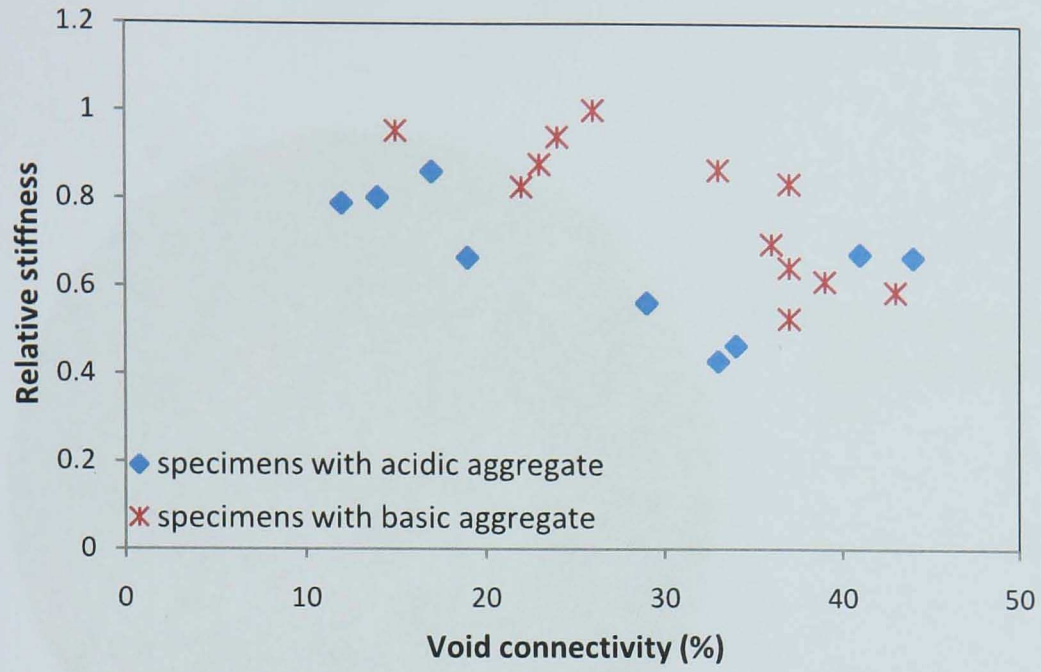

Figure 6.24 Effect of void connectivity on relative stiffness of asphalt mixtures

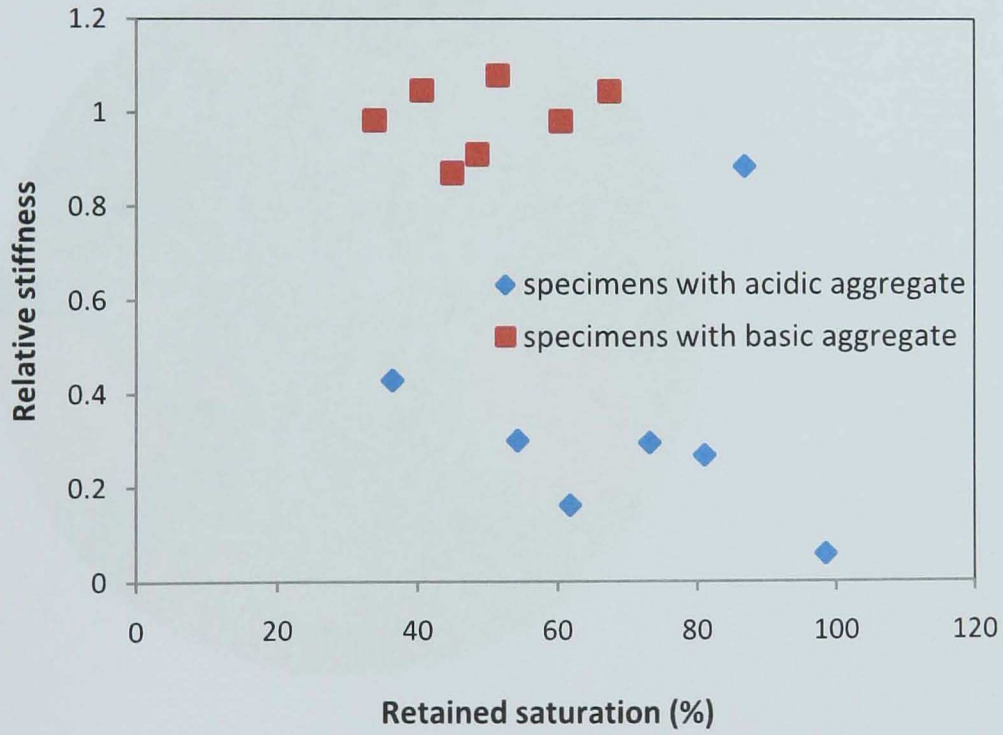

Figure 6.25 Effect of retained saturation on relative stiffness of asphalt mixtures

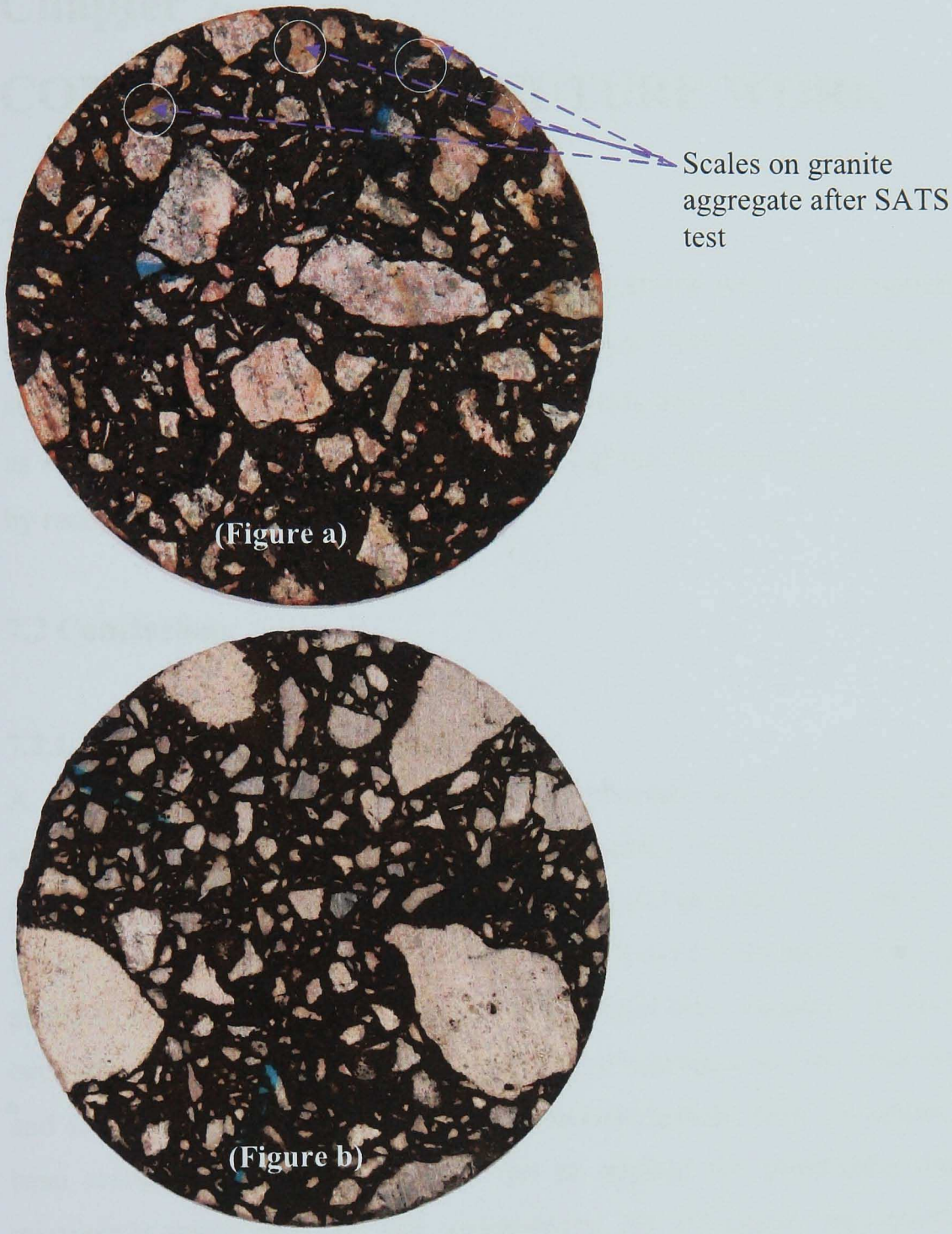

Figure 6.26 Specimens contain (a) Granite, (b) Limestone aggregate after SATS test

Chapter 7

CONCLUSION AND FUTURE WORK

7.1 Introduction

Microstructural properties of UK asphalt mixtures were investigated in monotonic compression tests, tension compression fatigue tests and in combined moisture and saturation ageing tensile stiffness (SATS) tests and related to macro properties such as stiffness of asphalt. This chapter consists of the conclusion from this research followed by recommendation for future work.

7.2 Conclusions

7.2.1 Review of literature (Chapter 2)

A review was carried out of the relevant literature concerned with understanding the application of microstructural properties of asphalt mixtures, introduction to X ray CT, application of X ray CT for studying the microstructure of asphalt mixture during laboratory testing. Applications of imaging and X ray CT for studying the microstructure of material, including different imaging options, have been compared. X ray CT images have been used previously for studying the texture of aggregate and air voids in asphalt mixtures and scanning has been performed during certain specific tests of asphalt mixtures. It has been recommended that X ray CT can be applied for quantifying damage in asphalt mixtures at micro level and that, compared to 2D, 3D images may provide more reliable results.

The microstructure of asphalt mixtures has been studied for certain specific testing parameters using reference images. Asphalt being complicated in nature, it is observed that asphalt specimens should be tested under various different test conditions. The available procedures for X ray CT and image analysis could potentially be developed further to increase the information from data analysis. For studying microdamage during fatigue

testing of asphalt mixtures, a sound recording technique has also been applied but with limited application.

The dissipated pseudo strain energy concept for modeling fatigue tests has been introduced. Literature was also reviewed on the use of X ray CT for moisture damage of asphalt mixture, although because it has only recently been introduced, there is limited work on this application. Only specific parameters of moisture damage have been investigated and further investigation has been recommended.

7.2.2 X ray CT and image analysis techniques (Chapter 3)

Being recently commissioned in NTEC, guidelines for X ray scanning of asphalt specimens were developed. A detailed procedure for operating the X ray machine and obtaining clear scans for asphalt specimens was worked out. Depending on density of aggregate and size of testing sample, a methodology for setting of X ray scanning parameters was introduced. The resolution of the image which is an important parameter for microstructural study of asphalt mixtures was adjusted to the highest possible value.

While scanning specimens different image errors occurred and their effect on image analysis was observed. Slight brightness or contrast darkness in the image have let to differences in results from image analysis. These errors were corrected by modifying the X ray filters and adjusting the voltage and current of the X ray system. The machine was fixed at 83micron resolution in the x and y directions; in the z direction the slice interval (spacing) was fixed such that no information was missed between images and uniform resolution was obtained in x, y and z directions of the specimen. For developing 3D images, it is necessary to keep the slice intervals not more than three times the resolution of 2D images; this will keep the dimensions of the voxels in the 3D image uniform.

X ray parameters for scanning specimens containing granite were found to be different from specimens containing limestone. Similarly 100mm diameter scanning parameters were different from 50mm diameter parameters for the same material. Different materials require different X ray scanning settings depending on the density of aggregate materials, size of the specimen and density of the specimen.

After comparing data from 2D and 3D images, it was found that data from 3D images was generally not the same as the data from 2D and that the 3D image was most representative of the actual specimen. Also, use of high resolution will result in data without any information being missed.

7.2.3 Microdamage in monotonic tests of asphalt mixtures (Chapter 4)

A procedure for X ray computer tomography of asphalt samples along with mechanical testing has been developed. Using image analysis techniques, grading of the aggregate was carried out from the X ray images of compacted asphalt specimens. Particles down to 0.083 mm can be seen in the X ray image. 1 mm stones can be clearly seen; mostly smaller particles were found touching other particles and therefore were observed as single particles. It was found that particles larger then 5mm matched the actual mix design curve of the asphalt mixture.

The air void distribution of specimens was determined from X ray images and reasonable data was obtained. It was observed from cyclic load testing and X ray scanning of the specimens at different test stages that the increase in void content is comparatively high in the middle of the specimen. The general trend of increase in void content in compression tests of asphalt was found to be approximately similar for the specimens tested at 5°C, 23°C and 35°C. Similarly for the void contents for specimens tested using 0.1/sec, 0.01/sec and 0.001/ sec strain rates were found to have approximately similar trends. The increase in void content is high for specimens tested at high temperature and low strain rate. Relative stiffness was determined from mechanical testing and a damage parameter was calculated from the air void data determined in X ray CT of specimens. A relation between relative stiffness and damage parameter for asphalt mixtures was observed.Some broken aggregates were noted at peak load.

It has been observed that the increase in air void content is not uniform through the specimen both horizontally and vertically, they are more prominent in the middle of the specimen. The same behaviour was observed at 5°C, 23°C and 35°C. Similarly there are large size air voids near the walls of gyratory mould compared to the inside of the

specimen. This may be due to the large size stones rolling to the sides leaving the fines in the middle.

Results from testing have shown comparatively more increase in void content horizontally in the specimen may be due to the load direction. This means that under vertical loading, damage/crack growth in asphalt is more likely to extend vertically than horizontally. Quantifying damage at the micro level using X ray CT will give reasonably precise values for input into damage models of the asphalt mixture.

7.2.4 X ray CT for fatigue test of asphalt (Chapter 5)

Specimens for the tension compression fatigue test were glued to make sure that the specimen failed in the middle instead of at the joint between steel plates and specimen. Verticality and alignment were found to be important factors for X ray scanning of fatigue test specimens. The data from fatigue tests was scattered and required testing of many specimens. A relation between fatigue testing and X ray CT of specimens was developed except at the first test stage where the stiffness drop suddenly and at failure of the specimen where it splits into two parts and is difficult to scan in X ray CT.

For specimens tested at high temperature, the increase in void content due to increase in load cycles is high comparatively, while for specimens tested at low temperature, no increase was observed during first 6000 cycles, followed by a low increase until 12000 cycles.

Consistency of test temperature during starting and stopping of fatigue tests for X ray scanning is necessary as this has been found to have an effect on output data. Data from constant stress fatigue testing at 5°C, 23°C, 35°C and scanning at 6000, 12000, 18000, 24000 and 30000 cycles were found to provide a relationship between stiffness and microdamage from X ray CT. All input parameters including the newly introduced parameter of adhesion between binder and aggregate were calculated. Using the approach of dissipated pseudo strain energy, the data from a microdamage model and from X ray scanning directly were found to have approximately similar trends.

7.2.5 Moisture damage in asphalt mixtures (Chapter 6)

A methodology for determining moisture saturation using X ray CT scanning was developed. Specimens from asphalt mixtures containing both granite and limestone aggregates with three different ranges of void content were scanned dry and after saturating and were then analyzed. The specimens were scanned within water along with a container. The values of saturation from X ray image analysis were found to be higher by up to 10 %, compared to the values from weighing the surface dried saturated specimen. The results from a void connectivity program (which is considered to relative directly to degree of saturation) were also similar to the values from X ray CT. This was because no water drained out of the specimen and the real degree of saturation was therefore calculated. It was observed that for mixtures containing granite (Acidic) aggregate, the saturation was high compare to mixtures containing limestone (Basic) aggregate. Higher void content resulted in high void connectivity and smaller relative stiffness.

In the case of specimens with high void content, the percentage of connected air voids was high and the relative stiffness was small. The range 2-4% void content was found to give better resistance to saturation compared to the range 8-10% for mixtures containing both acidic and basic aggregates. The combined moisture and ageing effect was studied using X ray CT. The results from SATS testing showed that saturation values calculated from X ray CT are up to 10% higher than using the mass calculation method.

As moisture behaves differently towards granite (acidic) and limestone (basic) aggregate, two different mixtures containing these two different aggregates were tested. From SATS tests and from X ray CT image analysis, it was found that retained stiffness is higher in the case of specimens containing basic aggregate and was smaller in case of specimens containing acidic aggregate. The relative stiffness was found to decrease with increase in retained saturation in the case of specimens containing acidic aggregate while there is no clear decrease in the case of mixtures containing basic aggregate.

7.3 Recommendations for further work

7.3.1 Microdamage in monotonic tests

In the current research a DBM mixture was selected. Mixtures such as HRA (hot rolled asphalt) with different aggregate sizes, void contents and sample sizes could also be tested and scanned in X ray CT. In order to study the effect of compaction method on the distribution of aggregate and air void, specimens compacted in both the slab compactor and the gyratory compactor could be investigated using X ray CT. Specimens tested in the tension test under a similar test procedure i.e. stopping the test and scanning in the X ray CT at selected stages of testing, could further clarify the microstructural properties of asphalt mixtures.

Healing of asphalt mixtures can be investigated to develop some correction factor / guideline. This will reduce the testing effort as instead of measuring the healing which occurs each time during stopping of the test for X ray scanning, measurement can be directly adjusted.

For studying fatigue of asphalt mixtures, the current work can be taken forward under similar test conditions including X ray scanning at smaller intervals of load cycle number during the first and last parts of the fatigue test curve. It is suggested, for example, to scan the specimens every 100 cycles for the first and last 6000 cycles if there are total 30000 cycles to sample failure.

7.3.2 In situ loading frame in X ray CT

An in situ loading facility with temperature control cabinet would increases the application of X ray CT to investigate the microstructural properties of asphalt mixtures. This would reduce the time and effort of testing, removing, scanning and retesting the samples. It would also be helpful in getting results with minimum calculation without including healing effects at every test stage.

7.3.3 Moisture damage in asphalt mixtures

The current procedure developed for studying microdamage during fatigue testing can be applied in studying the combined effect of moisture and traffic load on performance of asphalt mixtures. Specimens saturated in water can be tested in direct fatigue and scanned in X ray CT at selected load cycles. Asphalt mixture microstructure can be further investigated in a combined moisture damage and ageing test of asphalt mixtures for different test conditions (pressure, temperature), and X ray CT scanning carried out.

7.3.4 Asphalt mixture damage model

The X ray image data obtained during mechanical testing of asphalt mixtures can be applied to develop an improved discrete element models for monotonic compression testing and fatigue test of asphalt mixtures. Finite element modelling along with X ray CT can also be applied to improve the existing damage models of asphalt mixtures for different environmental and load conditions. This can be done in well know packages such as ABAQUS and CAPA (computer aided pavement analysis) etc.

APPENDIX A-1

Guidelines developed for X ray scanning and image analysis:

The X-ray CT in the Nottingham Transportation Engineering Centre (NTEC), Department of Civil Engineering, University of Nottingham is shown in Figures 1 and 2. This setup includes two separate systems placed in the same shielding cabinet. The mini-focus system has a 350 kV X-ray source and a linear detector, while the micro-focus system has a 225 kV X-ray source and an area detector.

The mini-focus source can penetrate thicker and denser specimens than the micro-focus source. The micro-focus system, however, is capable of achieving a better resolution than the mini-focus system. All the experimental measurements in this study were conducted using the mini-focus 350 kV X-ray source system, which has the necessary power to penetrate the asphalt mix specimens with a reasonable resolution. The guideline herein presents the operational procedure for using the 350 kV X-ray CT system step by step.

OPERATIONAL PROCEDURE

- Turn the system and the PC on
- Press the reset button located beside the keyboard; the pump will start up.
- From the start menu select programs then open up the IMPS III (Figure 3)
- Enter the identification and the password as eng and eng respectively (Figure 4) then hit OK
- Choose manual (Figure 5)
- Press the switch button at the bottom of the main menu as shown in Figure 6 to assign 350 kV Mini Focus for this job and then hit OK

Note: 225 kV is the default selection for the X-ray system and should be switched to 350 kV

- The system should be warmed up, before it can be used for scanning. Two program can be used; 100 and 101. The 100 programs is recommend if the system is not used for less than 24 hours while the 101 program is recommend if the system is not used for more than 24 hours. However to be

certain it is recommended to warm up the X-ray system by 101 program. To warm up the system,

Open the door and slide the solid black box in front of the X-ray source as shown in Figure 2

- Close the door by pressing both closing buttons at the same time.
- Select the X-ray tab in the main menu as shown in Figure 7
- Choose program 101 then hit on. The yellow bulb will turn on for a few seconds then the red bulb will turn on afterwards for around one hour. This is an automatic warming up procedure which means that the system will be turned off once the program is completed.
- In some special cases the user might be asked by the manufacturer to run the 000 program which means manual warming up. After the user chooses the 000 program, the kV should be increased in 5 kV increment starting from 50 kV until it reach 75 kV. Around five minutes should be considered between each increment.

- After the warming up is completed. Press the 2D CT tab from the main menu as shown in Fig 8, press the icon as indicated in Figure 8 .
- Load a previous CT profile that contains the parameters which were previously found to be suitable for various scanned samples. Press the load profile button as indicated in Figure 9. Hit the browse button and then choose the 2D CT setup.xml from the previously scanned sample as indicated in Figure 10. Then select the folder containing the X-ray CT images. This folder should be created by the user on the hard drive prior this step.
- Insert the sample's dimensions; height, height from the turntable to bottom of sample and the width. Then the magnification axis inspection position should be entered. For 150mm sample -190mm is recommended, and for a 100mm sample -220mm is recommended. Then move to the next step

- Check and review the X-ray parameters; volt, current, thickness of the filter, and the exposure time as explained in Figure 12. Then hit OK. The next step will be taking a black reference image by hitting the acquire button in Figure

12. During acquiring the black reference image the X-ray will be off. Place the pointer at the middle of the screen after the black reference image is completed, the black level will be around 900 for the detector in this system. The noise can be estimated to be the square root of the 900 which is 30. After paint brush step (mentioned in the following sections) the black level at the middle of the sample should be higher than 930. This can be achieved by modifying the kV, current and the filter thickness in order to achieve the proper penetration.

- Acquiring a white reference image (figure 13) will automatically turn on the X-ray. The image should be checked in order to make sure it is not saturated. This can be done by choosing the display tool button in the main menu as show in Figure 14, and clicking the colorise icon and highlighting the saturation (Figure 14).

- Proceed by acquiring a PaintBrush Image. Hit the acquire button and then after it has completed press save profile as shown in Figure 15. Proceed to PaintBrush image 2. This step is optional and it is used for non-circular samples to make sure that the X-ray penetrates the longest path.

- The centre of rotation at the top and bottom should be entered (Figure 17). If these values are known before then they can be used directly if they were not identified before, the procedure will be given at the end of these guidelines.

- The slice setup will be the next step. The slice setup includes locating the datum and the slices needed to obtain X-ray CT images. Use the locate-datum icon to place the datum on the sample as shown in Figs. 18 and 19. The user has the choice to create a slice stack by highlighting the Slice Stack

box as indicated in Figure 18 or he can place slices wherever needed on the sample by the place-slice icon (Figure 18).

- The last step is to enter the slice acquisition time. It has been found that 2 minutes per slice is suitable in order to avoid wasting time. That can be done by assigning 15 % of the maximum turntable speed as explained in Figure 20. Hit the Save Profile button and proceed for the program to start scanning.

CENTRE OF ROTATION CORRECTION

- In order to correct the centre of rotation previously mentioned, scan two slices one at the bottom of the image (A) and one at the top of the image (B) with zero offset values as explained in Figure 17.
- Select 2D CT tab from the main menu and select the 2D reconstruction icon as shown in Figure 21
- Three files should be selected; CT Config File, Sinogram File, and CT Slice File (Figure 22). The CT Config File is selected by browsing the folder that contains X-ray CT images, created in Figure 9, as presented in Figure 23. Choose the reconstruct.xml file and then click open Figure 23.

- The Sinogram file for each slice should be selected one at a time. Start with the bottom slice (A). Hit the browse button in Figure 22 in order to select the sonogram file for slice A, and the CT Slice File is selected the same way. But give the slice another name to avoid overwriting this slice as shown in Figure 24.

- After you select the files select the setting button in Figure 24 and then select the centre of rotation tab (COR) as shown in Figure 25. Highlight incremental search for best of COR and enter -10 for the lower COR offset and +10 for the upper COR offset. There are two options by which one can minimize the range of searching. The first one is watching the COR and the clarity of the image, and selecting a smaller range, for example -3 and -1 for the upper and lower COR, in order to get the most accurate COR. And the second method is to select a COR which is associated with a higher number as shown in Figure 26. The first method is recommended. After obtaining the COR at the bottom (A) repeat the same procedure with image B in order to get the COR at the top. Use these offset values in a new run for the same sample.

Image Analysis

After getting image data from the X ray CT three different approaches have been developed for image analysis in NTEC.

1. VG Studio Max technique
2. Image pro plus technique
3. Image J

In VG studio Max Method the images are selected after opening the VG studio Max window
(Figure 26).

- Importing the image stacks: select the file menu click import and select the import slices (Figure 26)

- Select the type of images. For our case it is TFF (Figure 27)

- Next select the alphabetic order, this will make the slices in proper serial numbers. (Figure 29)

- Select the greyscale (Figure 30)

- Select the image size (Figure 31)

- Select the image scanning parameters : in the top select the 8 bit. Using this will require less memory and allow analysis of many images at a time. In the X , Y , Z boxes the resolution is input. In this case X and Y should be 83 and the Z value will be the slice interval. In the unit box select mm (Figure 32).

- In order to analyze the image for microdamage first calibrate the image. On the front open window and in the corner there is a calibrate window. After clicking calibrate the new window will open as shown. Now select the XY image window. Click the mouse on the black portion (air void) and a value will automatically appear in the calibrate window in minimum box. Similarly drag the mouse onto an aggregate stone and another value will be generated in the maximum box of the calibrate window (Figure 33).

- Next is to select the defect from the main window and open defect analysis (Figure 34) .

- Select the 3D and Unselect calibrated. The calibration values here are selected based on trials depending on the value of air voids of the actual specimen from the laboratory. The minimum value is selected as zero. The value for defects (max) is selected such that the grey value can be related to the value of air voids in the specimen. Run value can be selected as 3, 4 or 5. Increasing the number will slightly increase the value of the defects as it processes the images repeatedly. In this case an average value 3 has been selected. In the min(size) box select 0.00 and for maximum box select 1000000. These values selects the size of defects (size of air voids in our case) in the sample. Select the unit mm^3. This is the size of the defects/voids in 3D. Then select start. The images will be analyzed for different parameters and the results can be seen after the analysis (Figure 35).

The value of defects is taken as the value of air voids.

2 Image pro plus

The following steps were followed for Image pro plus

- In the main window select the file menu and click open. Select first image from the images file and open it in image pro window.
- Select 'measure' in the main window, then select calibration, then spatial. This will open a new window in which the horizontal (X) and vertical (Y) resolution are selected and the aspect ratio of the image, which is 1.0 in this case. The resolution used here was 5.03937. This is actually the image size in pixels divided by the area in mm of the actual sample. The unit will be pixel/mm.
- As for image pro analysis the images should be 8 bit type and will be TFF. This is done in the free available software image J. It is a simple software in which one can change the properties and resolution of images.
- Select macro from the main window and a new window will open. Click edit and this will open the macro developed for image void content. Change the paths of loading files and result files. This means the macro will take the images automatically using the selected path and will save the results in the specified file. Click save so that the changes made in macro are saved and close the window. The macro was developed in BASIC computer language.
- Close this window and open the macro from main window again. This time select run in this new open window. This will run the macro asking for some input parameters. Put C (for circular) and click, 'next' put '0' and click 'next'. Put image resolution/size and click 'next'. Now select a calibrated value typically 40-80 in this study. Click next. This will start processing the images and will give the result. In the result check if the air voids value is related to the air voids data from the laboratory. If not repeat the process and put a different calibrated value and check again until the value of air voids from image analysis is equal to that of the laboratory air voids. Now the image can be analysed for different properties.

Voids Connectivity using image prop plus:

- Image type and size of the images is fixed in image J.
- Analyze the images in image pro and fix a threshold value for certain air voids before analyzing for connectivity.
- During image pro analysis of images, put '-1' instead of putting '0'. This will get the aggregate white and air voids black. Make sure the air void macro is copied into the image file.
- Open image pro window. Then select macro, select permeability, select run. A new window will open.
- Enter either '1' for 4 connect or '2' for 8 connect. Here '2' was selected, which will cover the pixels on all (four) sides.
- Including borders select '1'.
- Put start image '1'.
- Put end image 'any value'.
- Put name of file saved images (image file)
- Put Base name as slice_.
- Output file.
- Go to image file and open Fortran file macro named "permeability 18f". the macro should be adjusted for images considered. Correct the 'image nos.' i.e. 100, 80 or any other figure. Correct the image size i.e. 515 or 512 or any other. The images can be included by deleting 'c' on the right hand and can be deleted by writing 'c' on the right side. This macro needs more care in form of slice, word size etc. It should be checked again and again. Three locations should be corrected 1)- input file, bit format, 2)- modify the character size according to the length of file name; this is in the text format, 3)- output file.
- Press compile to see if the there is any error.
- Run. "!". Note: If the Fortran macro gives error of "array ", increase memory to "32".
- After processing arrange the slices.
- Open image pro window now, select macro, select 'Read ASCI file', then put pixel, put again same value, put value of input directory, here enter base name, it will be named as "slice out_".

- Create a new folder in the file to keep the output and select the image name such as "slice final_", select 'Ok'.
- In the new folder there will be images of connected air voids. Analyze these images in image pro using the general procedure for determining voids. This will give an average value of connected air voids.

3 Image J

Image J is used for enhancing the image, fixing threshold grey value for images in 2D. The software is available free of cost and using its application is simple once the main window is opened. All commands are self explainatary and are available on the main window.

Figure 1. X-Ray CT System at NTEC, University of Nottingham

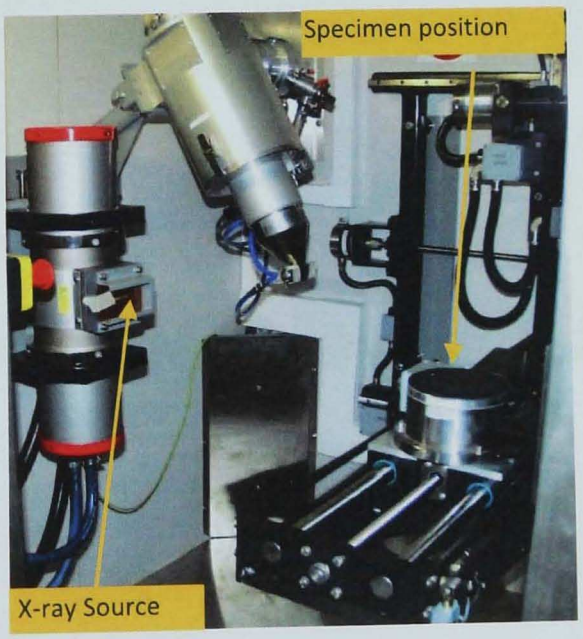

Figure 2. Components of X-Ray Computed Tomography System at NTEC

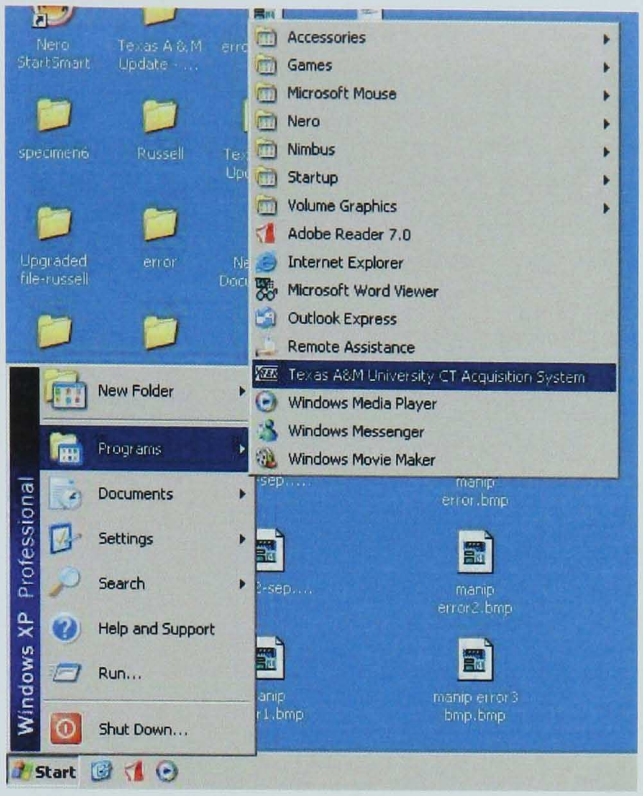

Figure 3 Open The NTEC CT Acquisition System Program

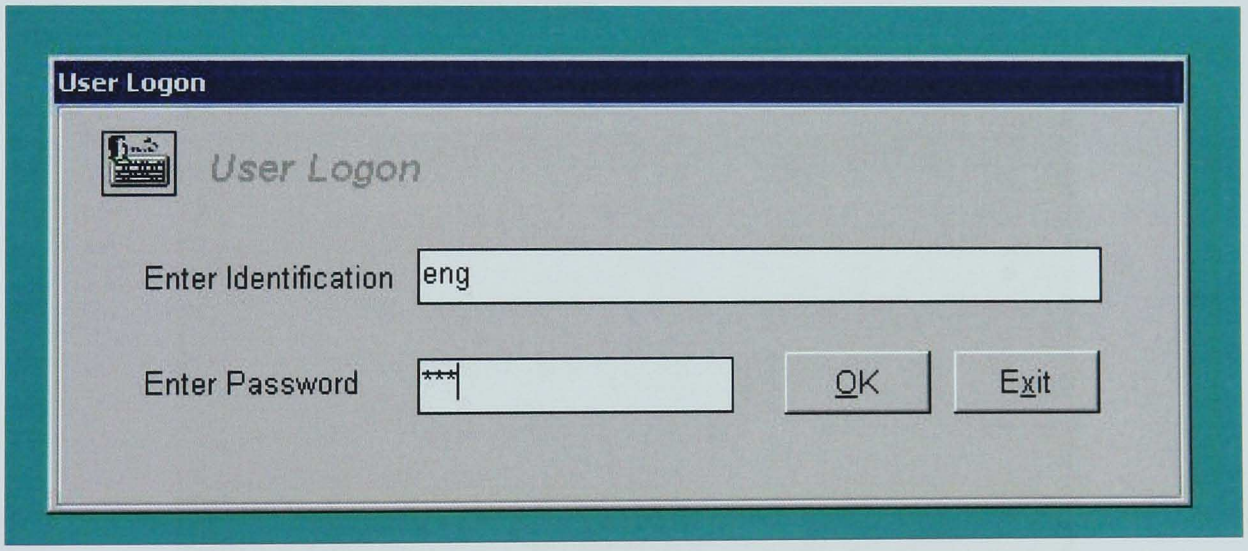

Figure 4 The Identification and The Password

Figure 5 The Manual Option

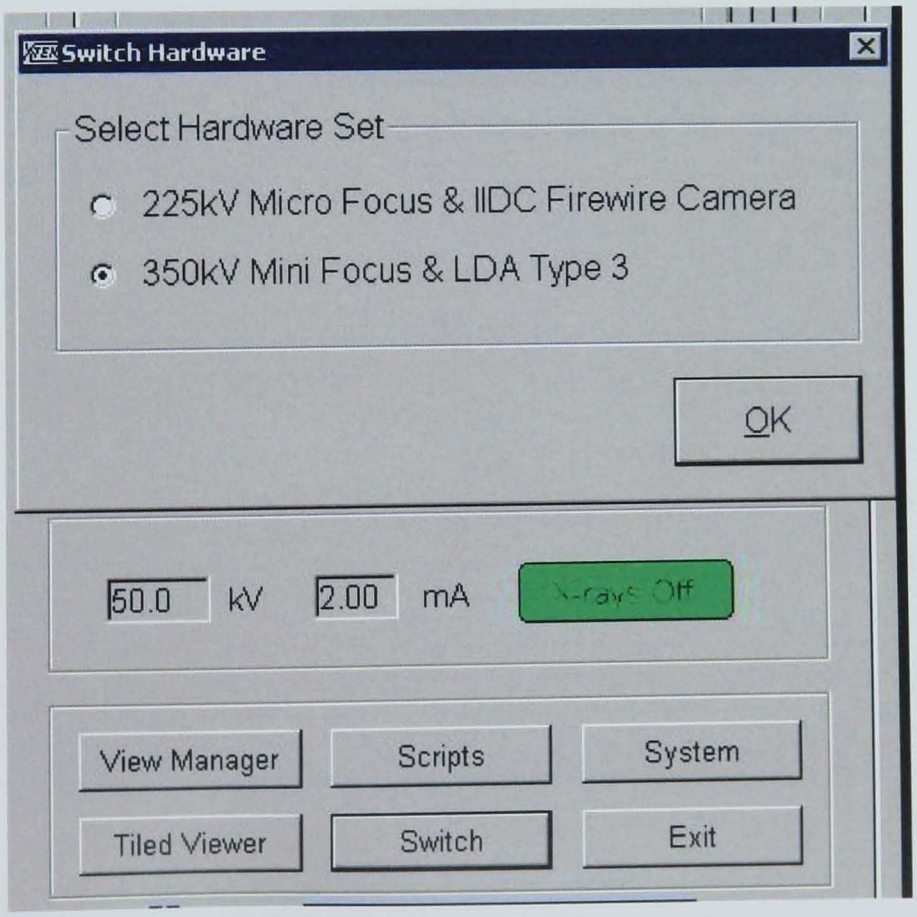

Figure 6 Switching from 225 kV to 350 kV

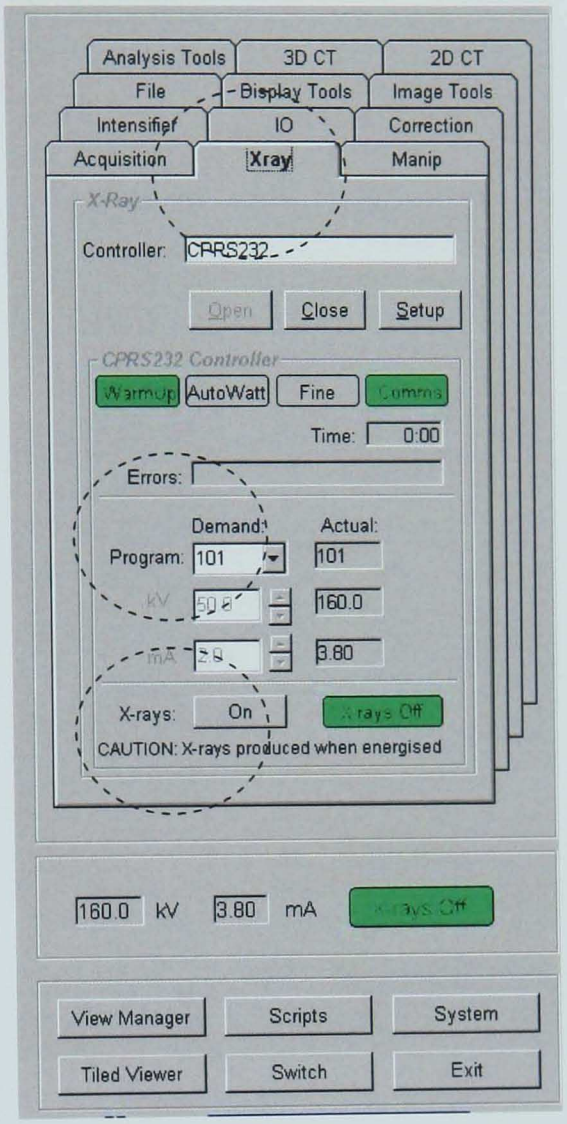

Figure 7 Warming Up The System

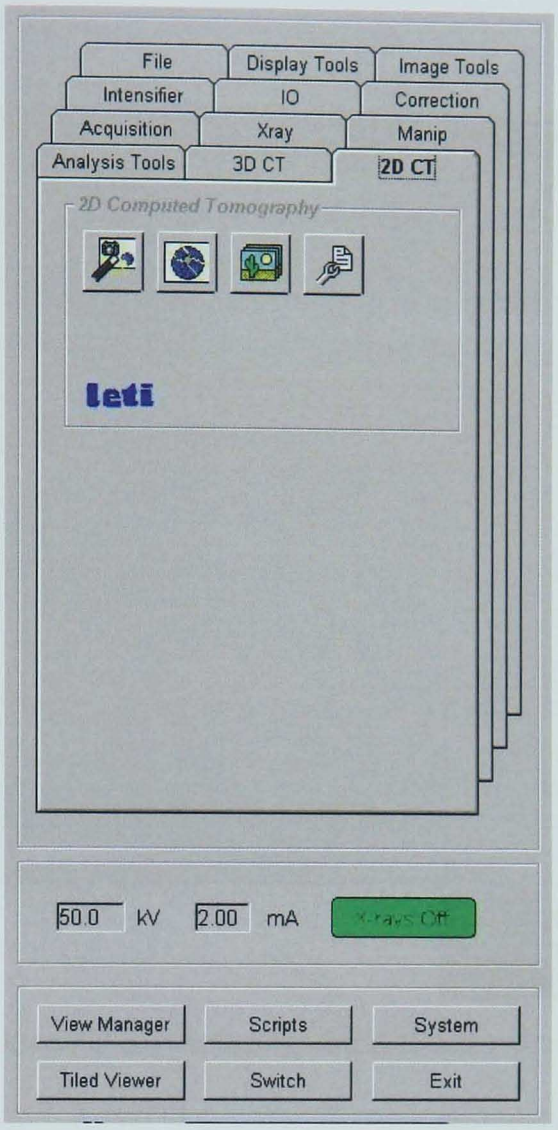

Figure 8 2D CT Wizard

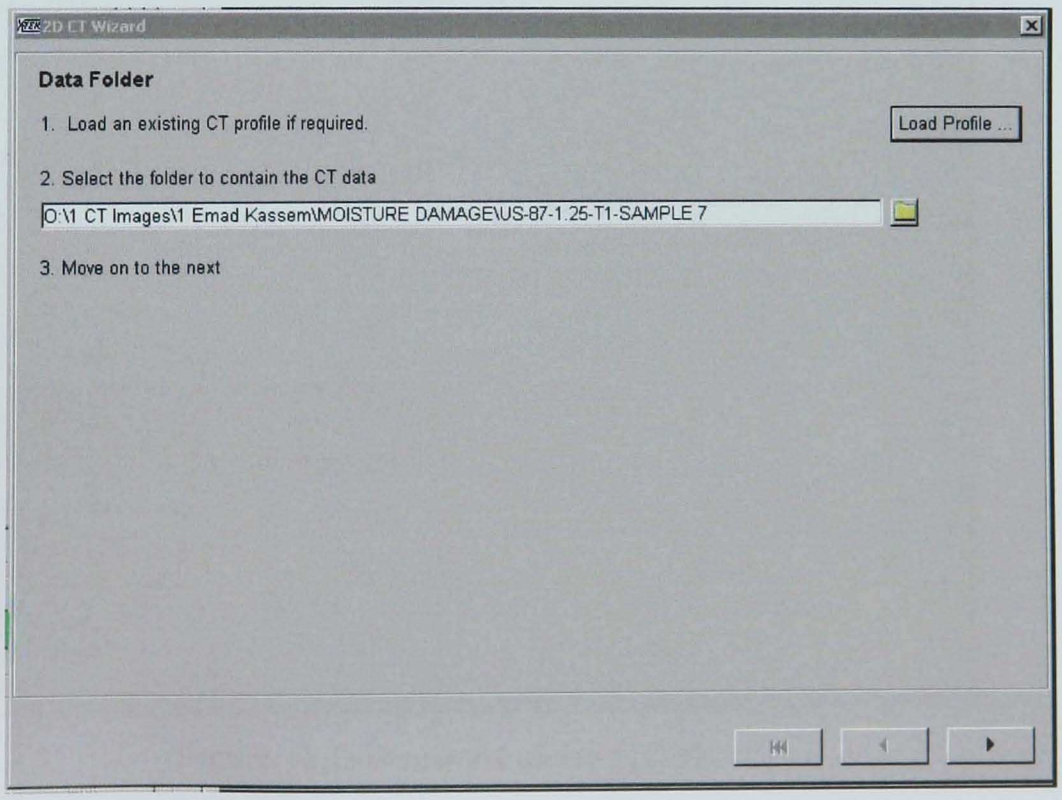

Figure 9 Load CT Profile

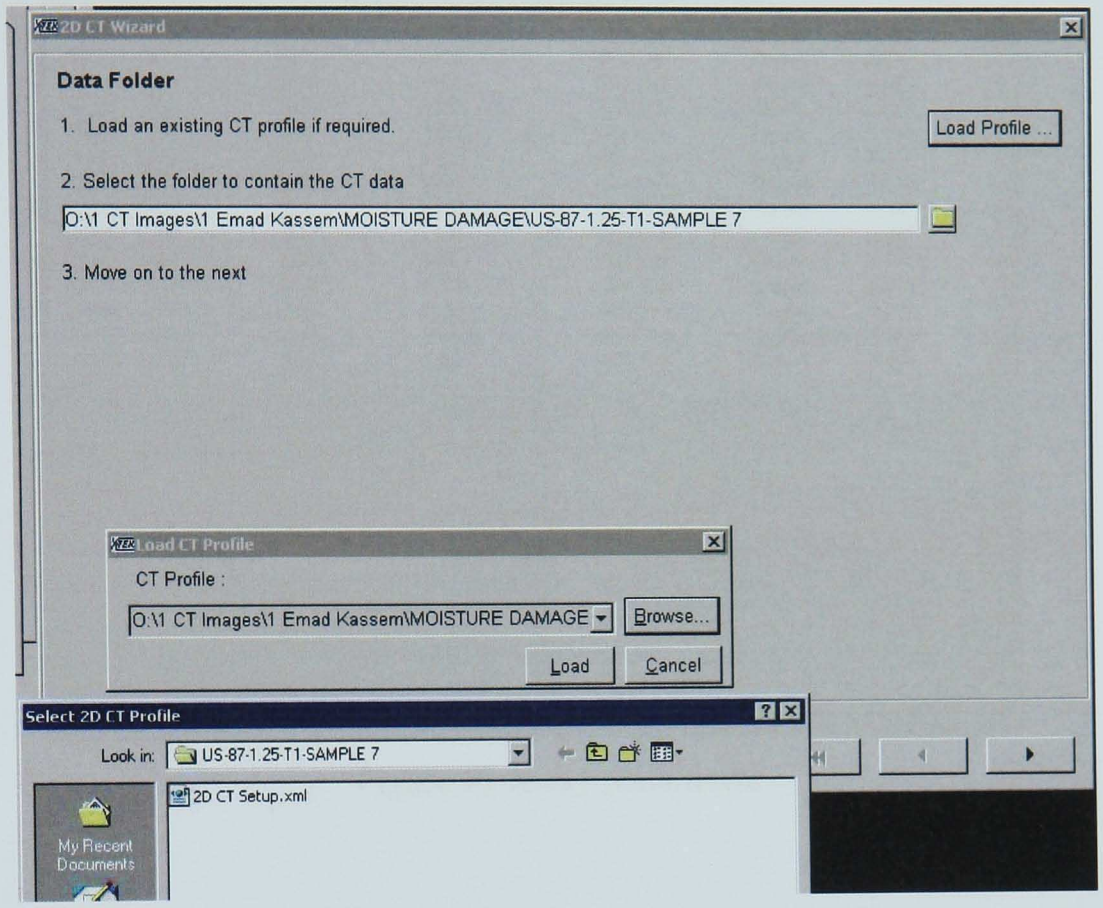

Figure 10 Choose 2D CT Setup from previous sample

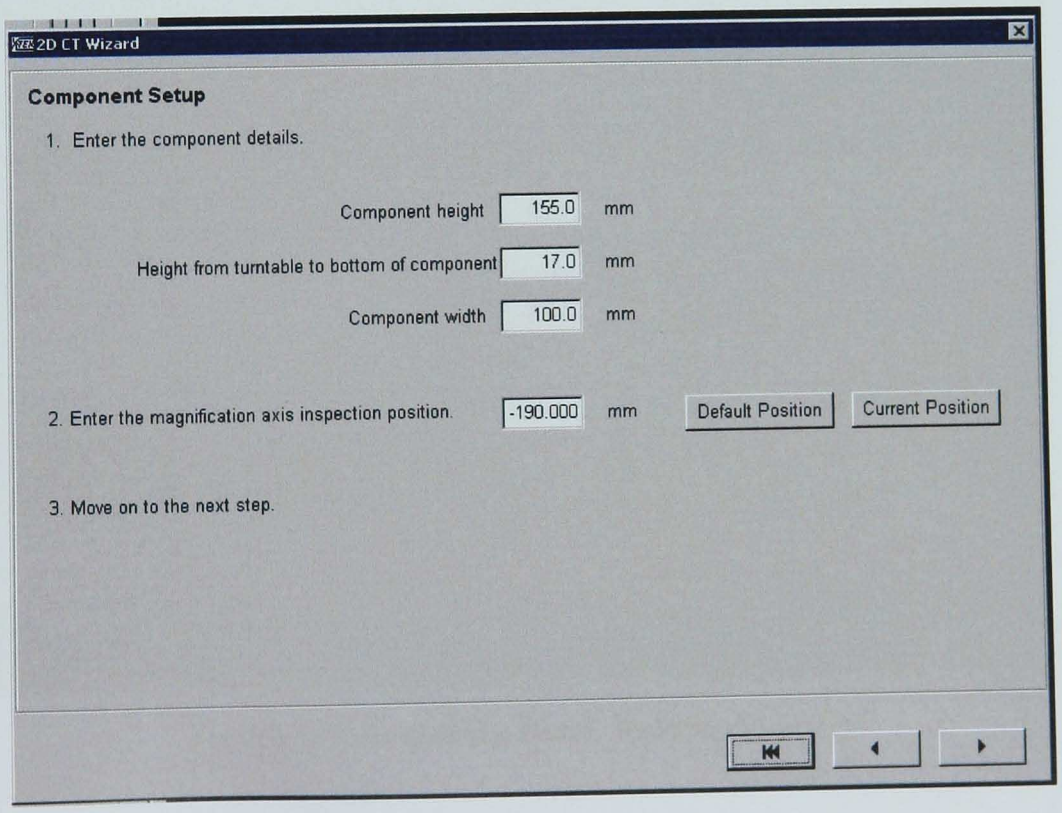

Figure 11 Dimensions of the Sample

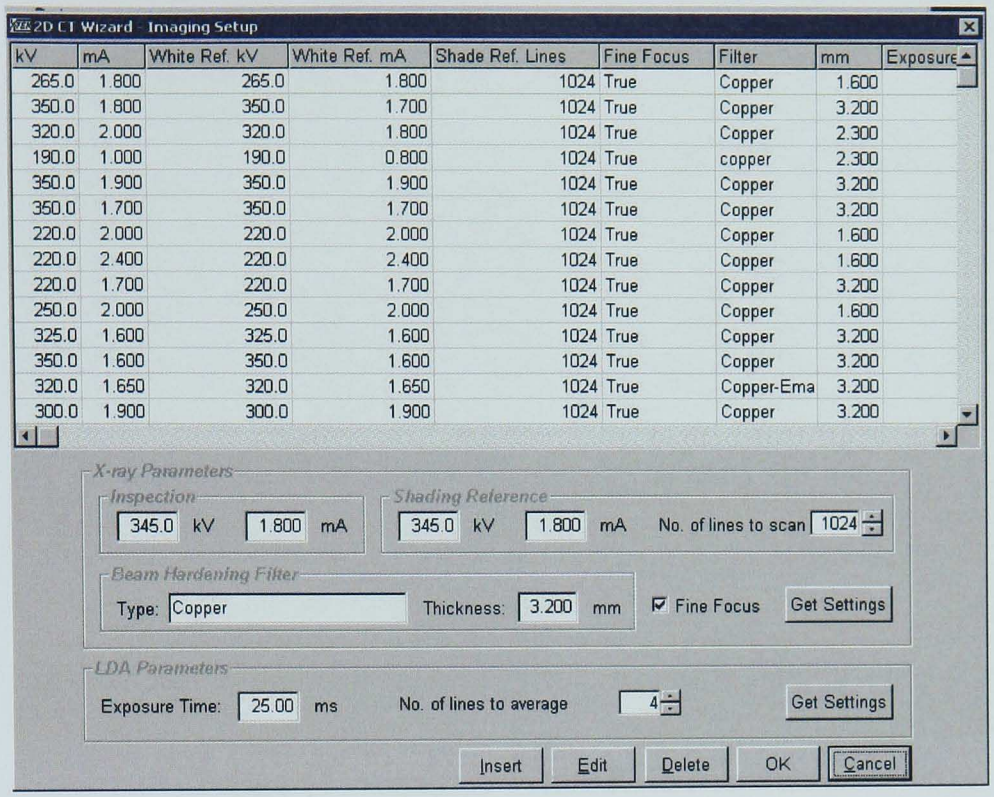

Figure 12 X-ray parameters

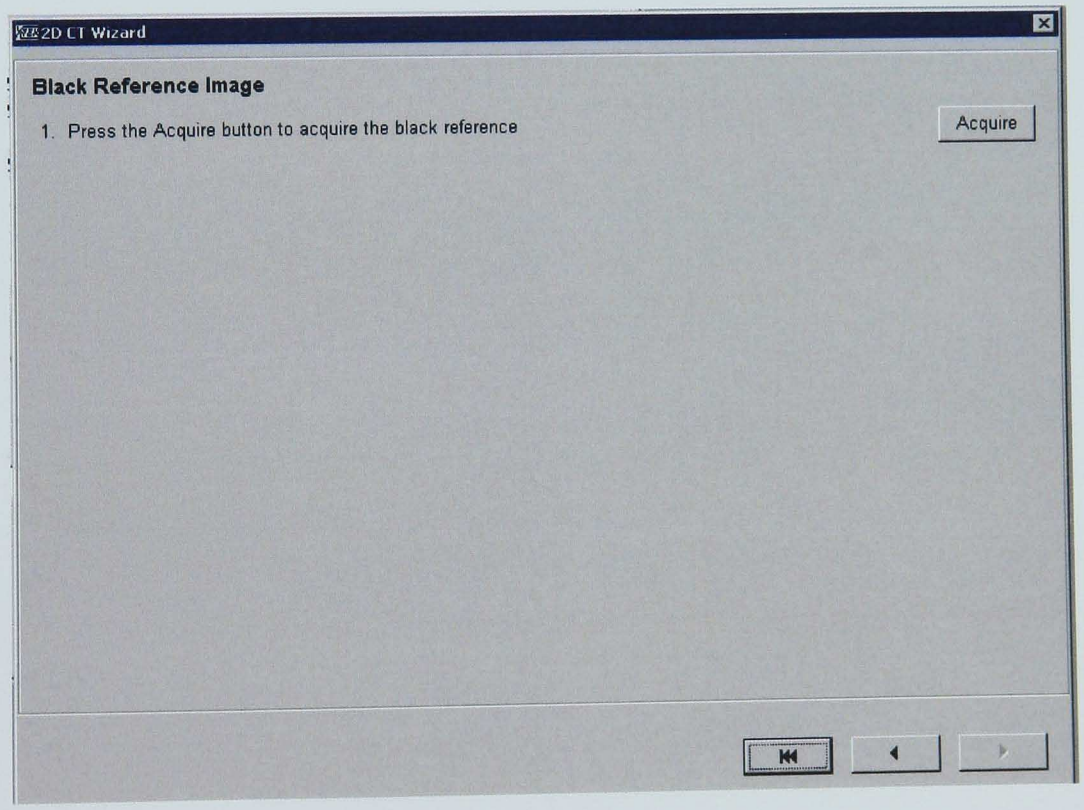

Figure 12a Acquiring Black Reference Image

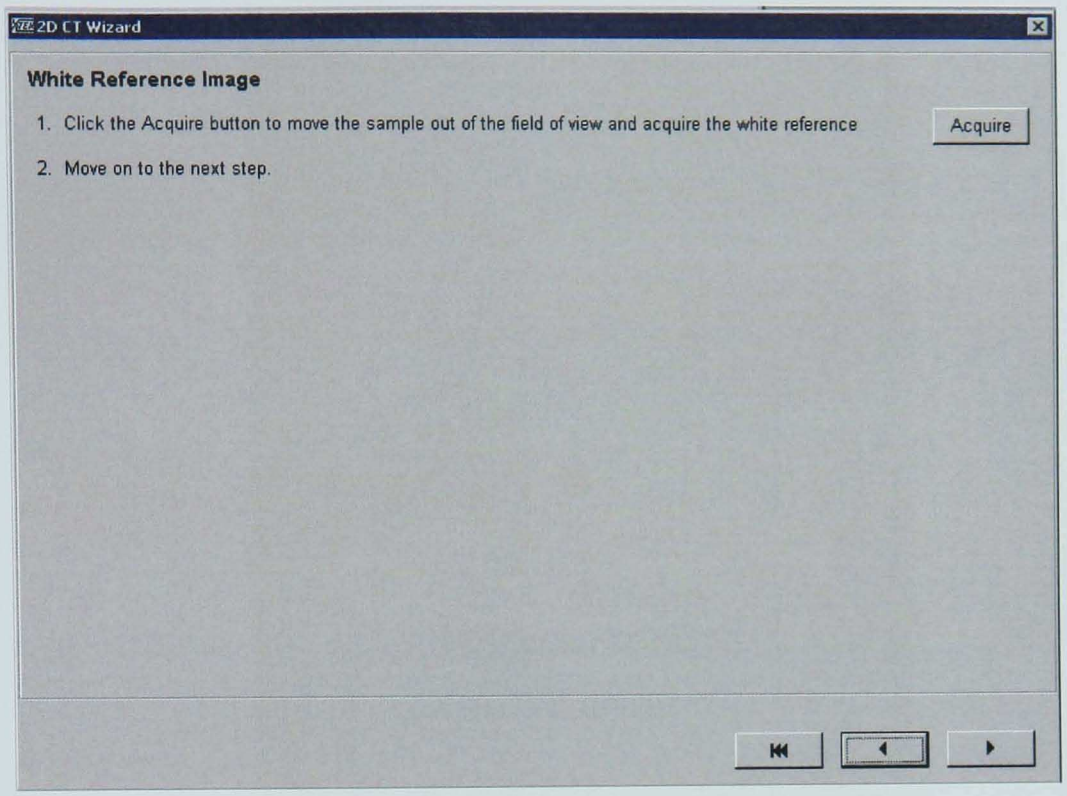

Figure 13 Acquiring White Reference Image

Figure 14 Highlight Saturation

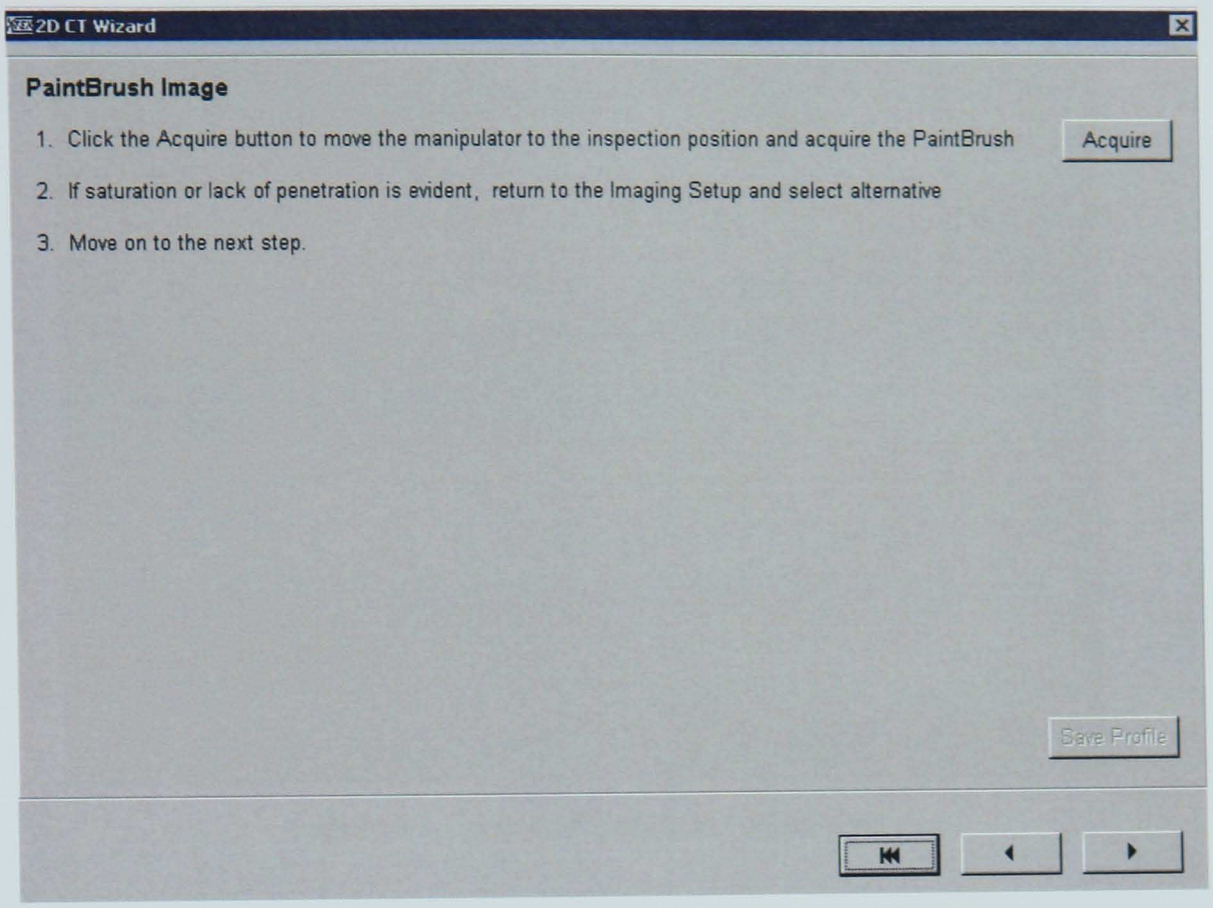

Figure 15 Acquiring PaintBrush Image

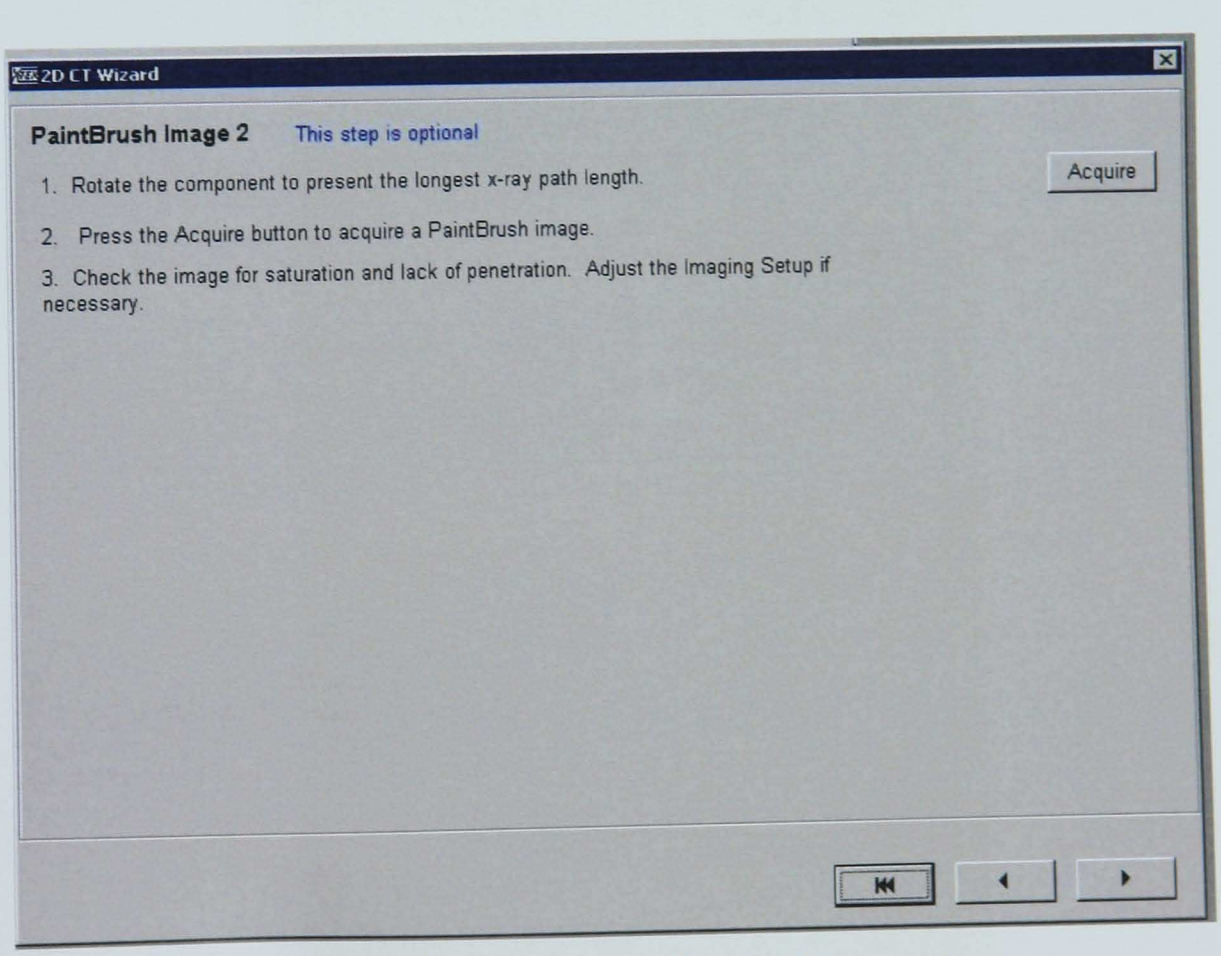

Figure 16 Acquiring PaintBrush Image 2

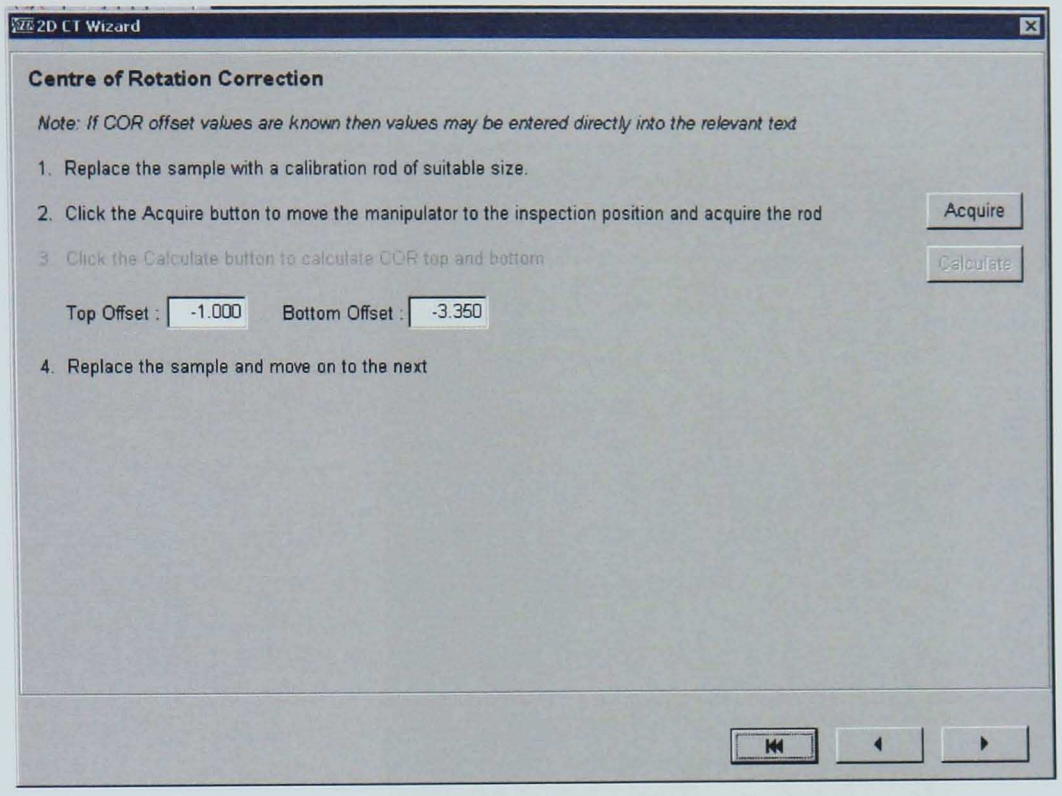

Figure 17 Centre of Rotation Correction

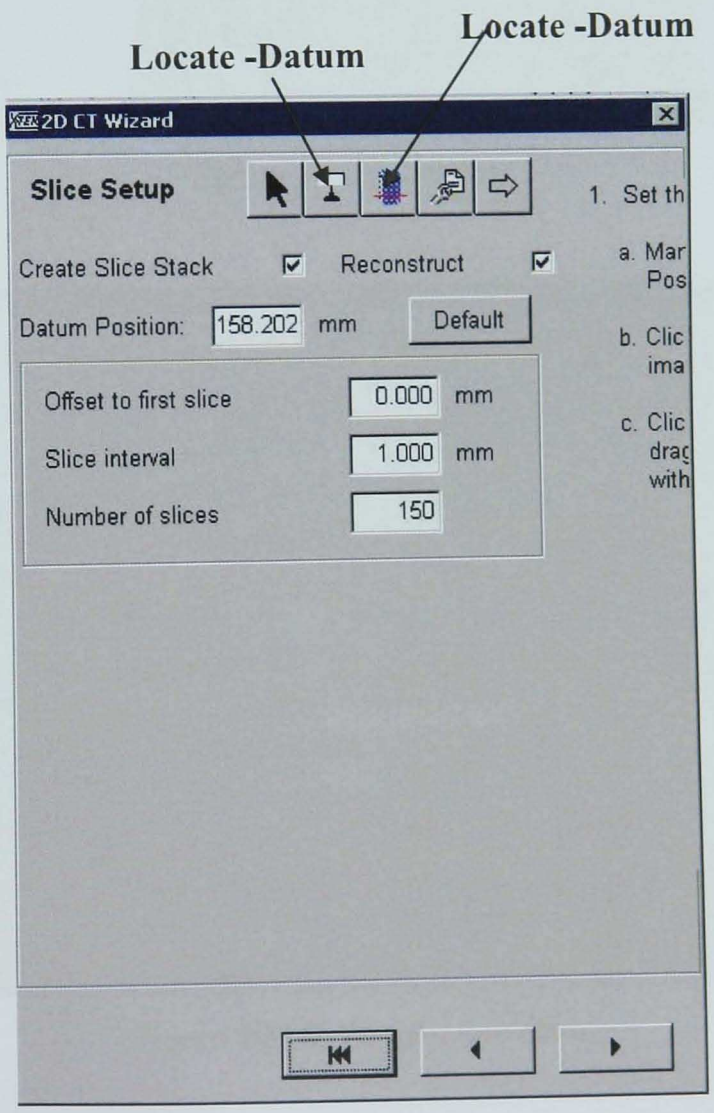

Figure 18 Slice Setup

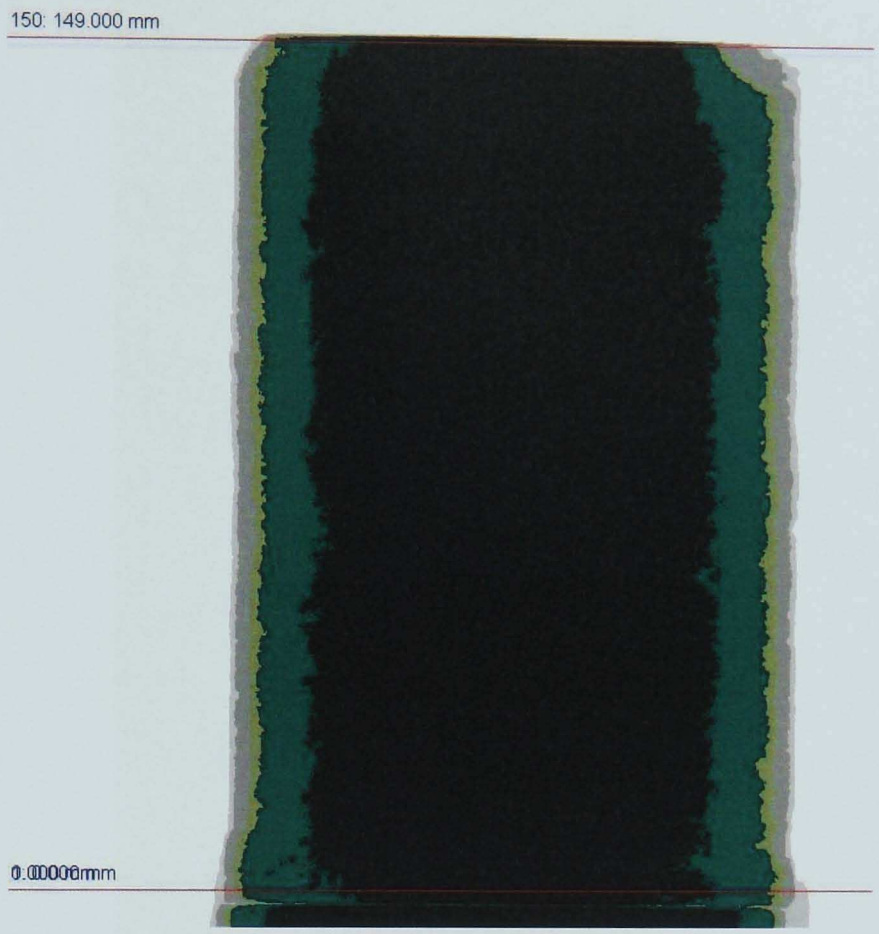

Figure 19 Slice Stack

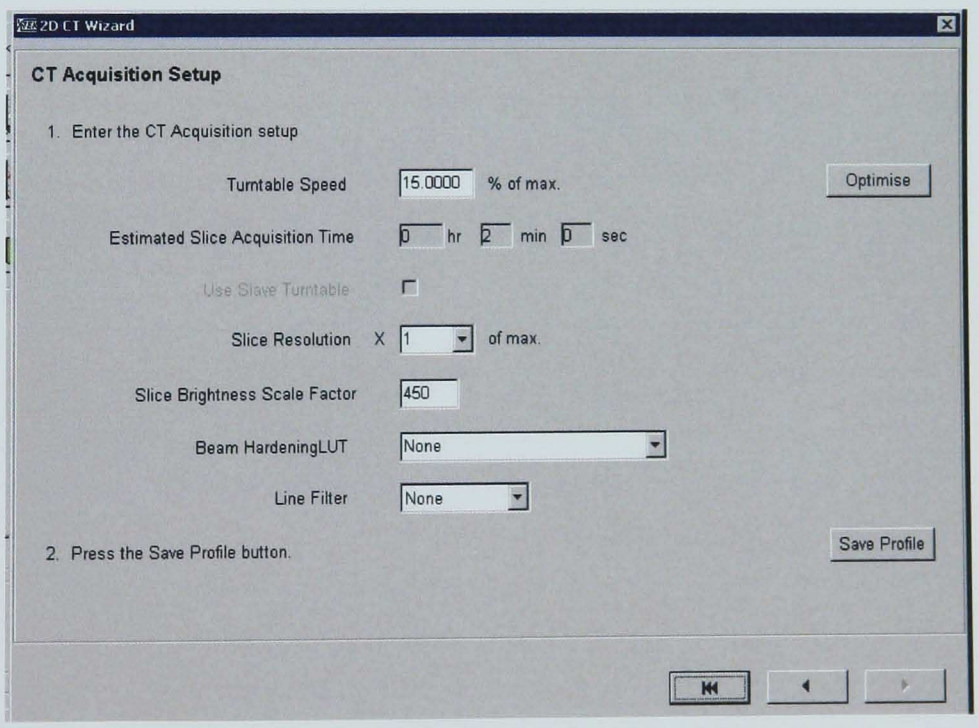

Figure 20 CT Acquisition Slice

Figure 21 2D Reconstruction Icon

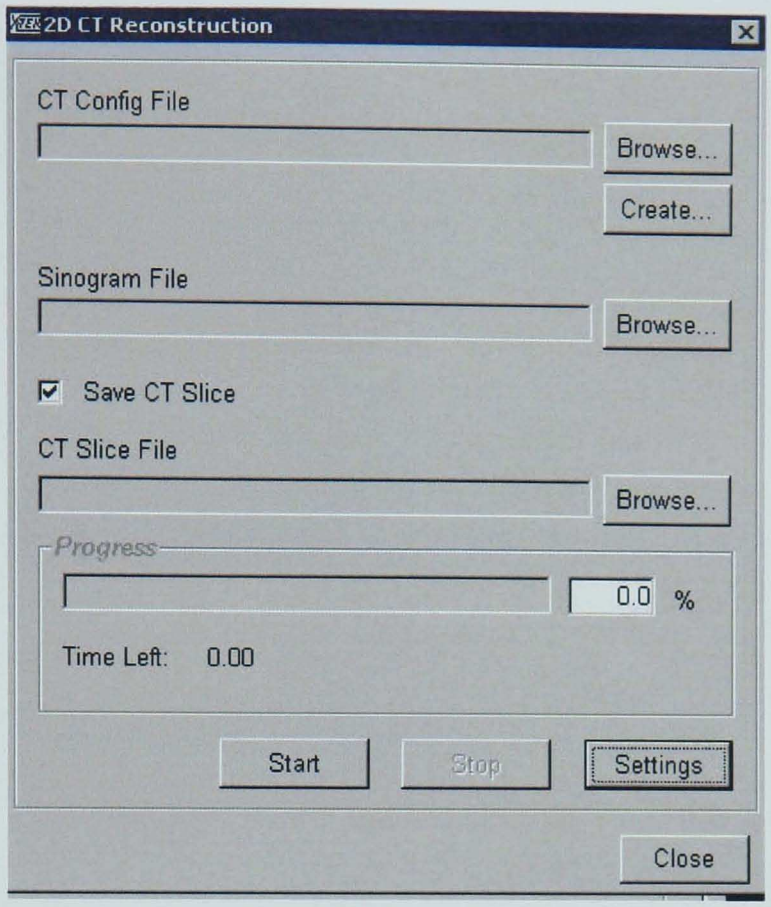

Figure 22 2D Reconstruction

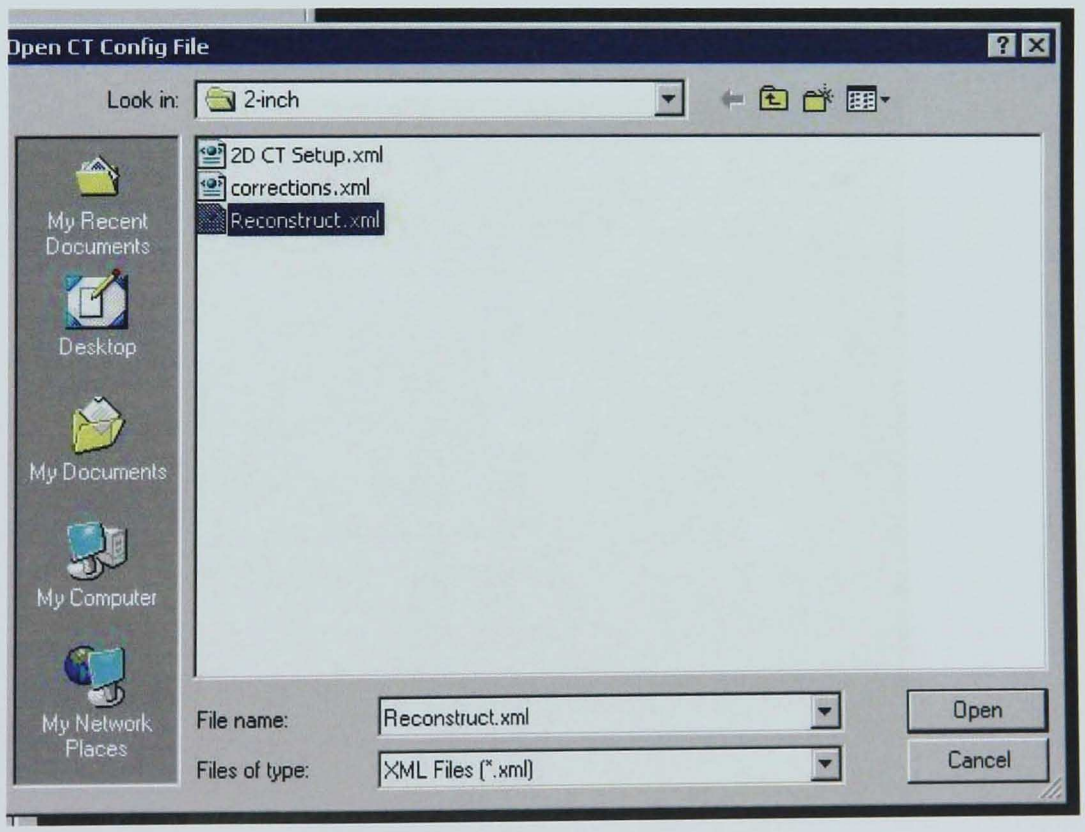

Figure 23 CT Config File

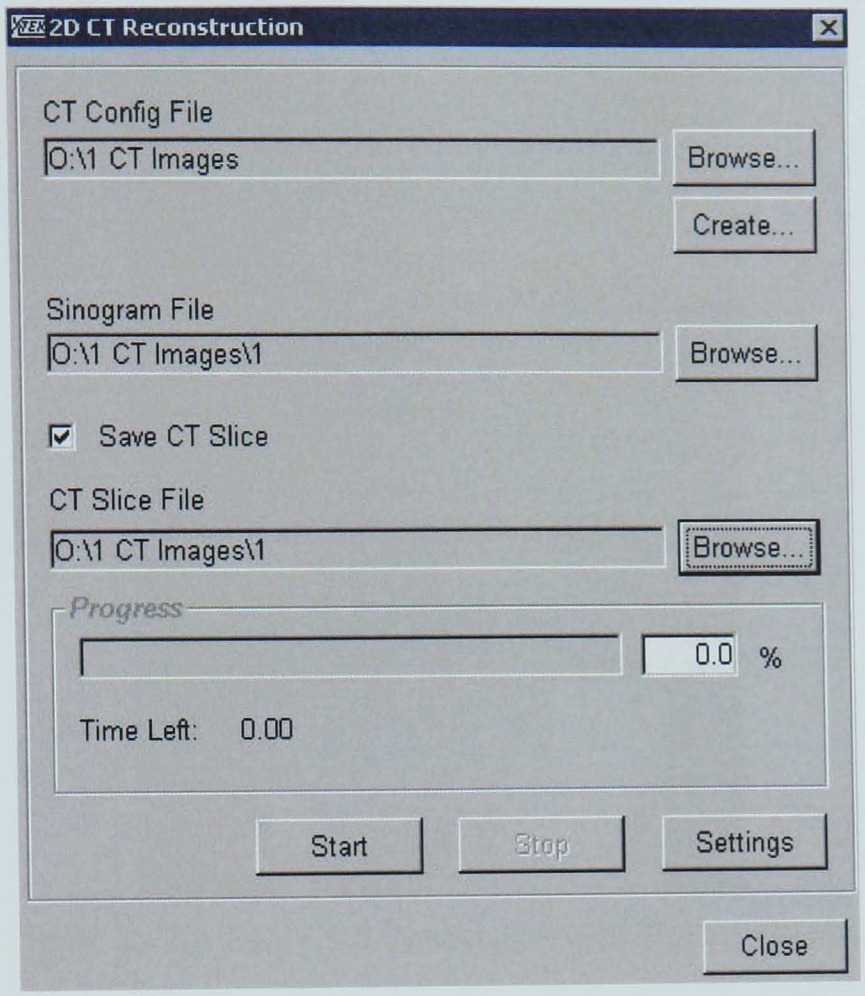

Figure 24 CT Config File

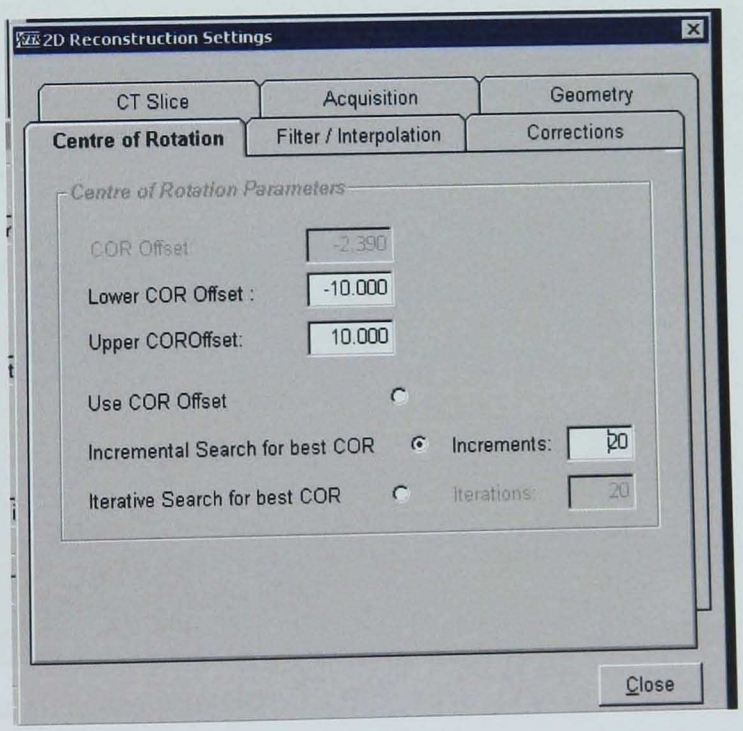

Figure 24a Center of Rotation

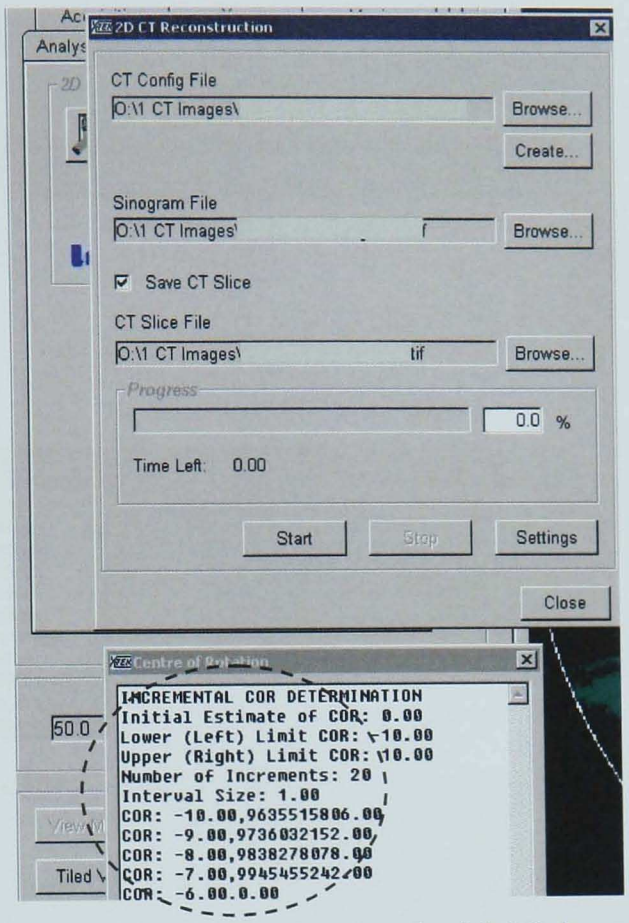

Figure 25 The Best COR Associated with Highest Number

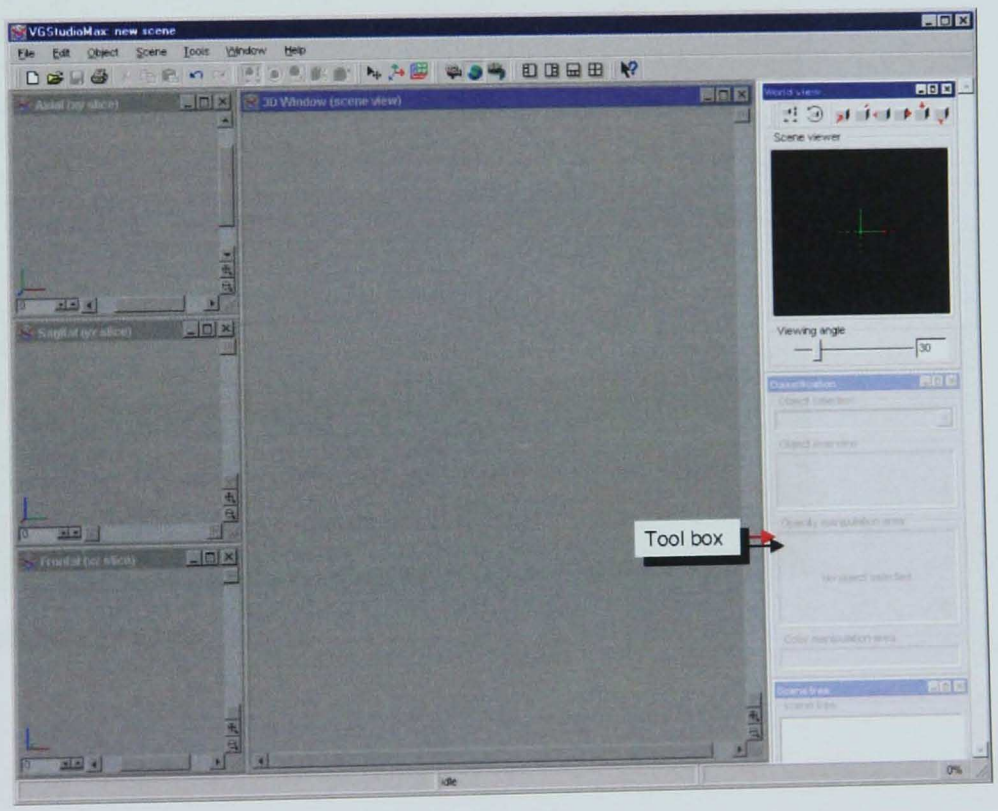

Figure 26 Main window

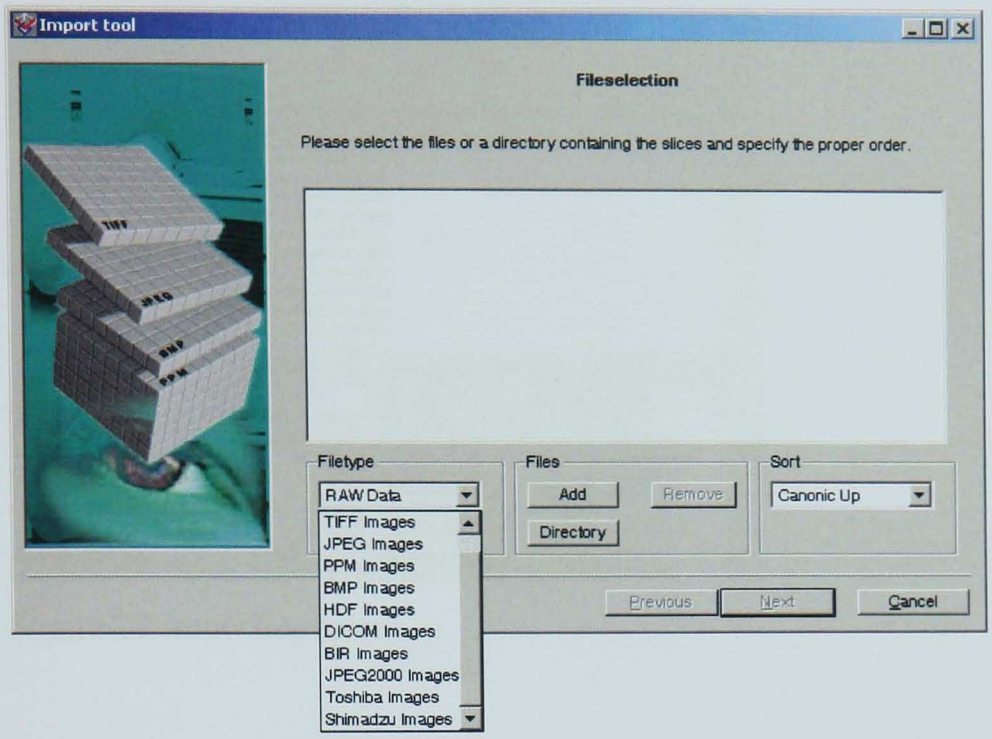

Figure 27 Importing 2D slices

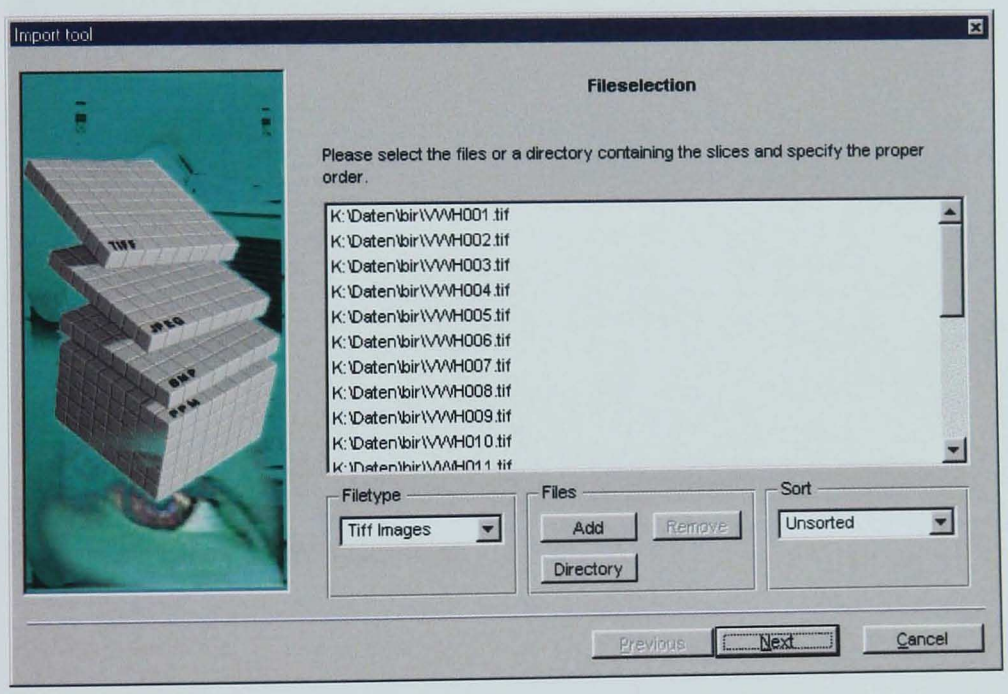

Figure 28 Selecting slices

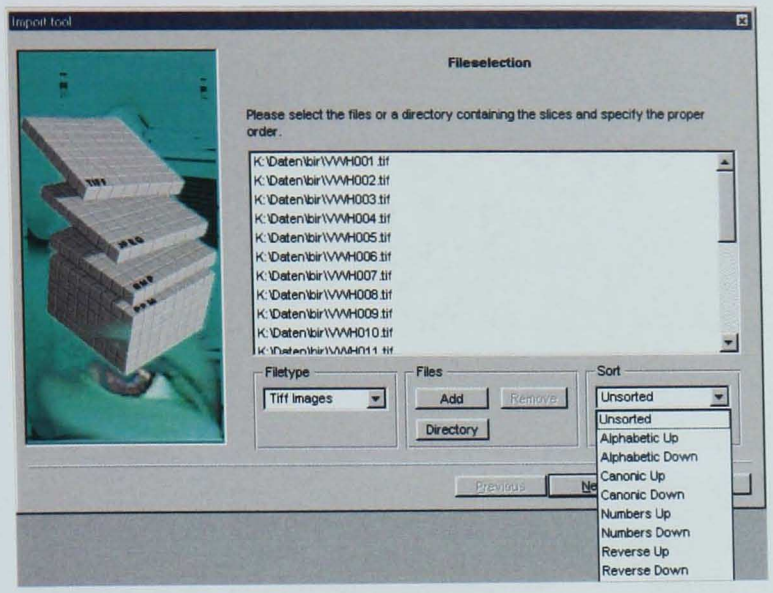

Figure 29 Importing slices

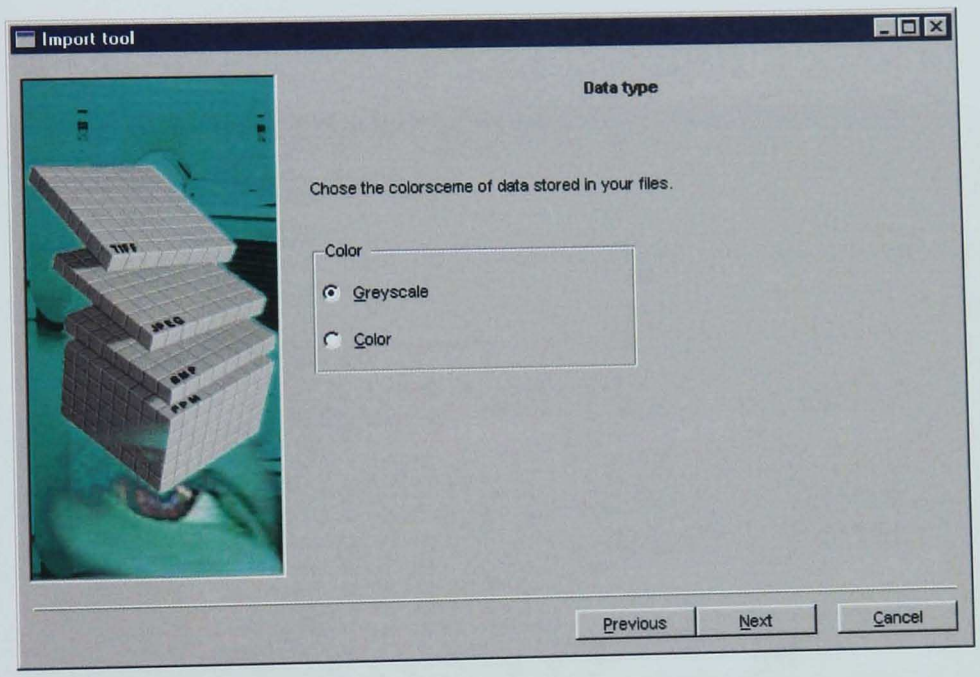

Figure 30 Grey scale selection

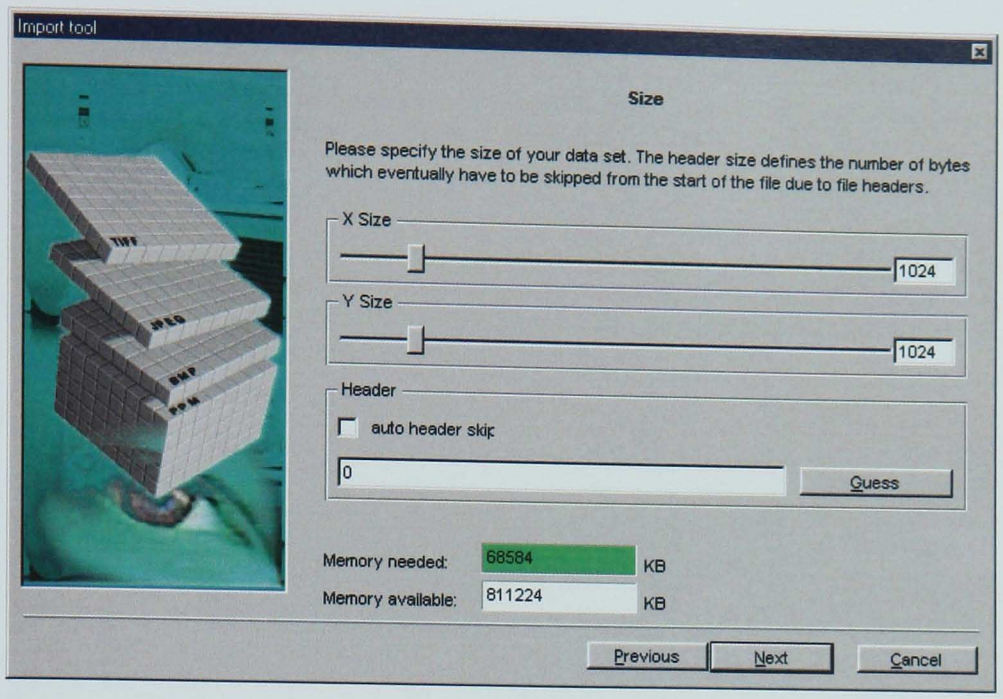

Figure 31 Selecting size of image

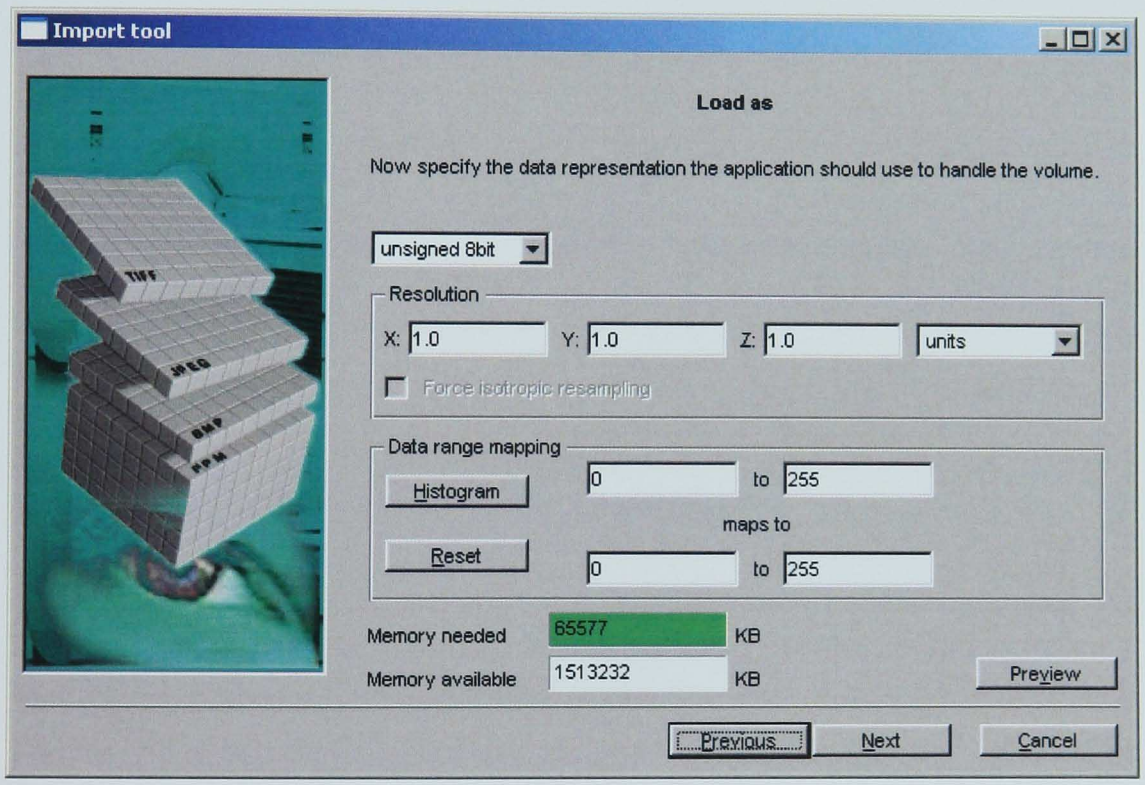

Figure 32 Fixing size of image

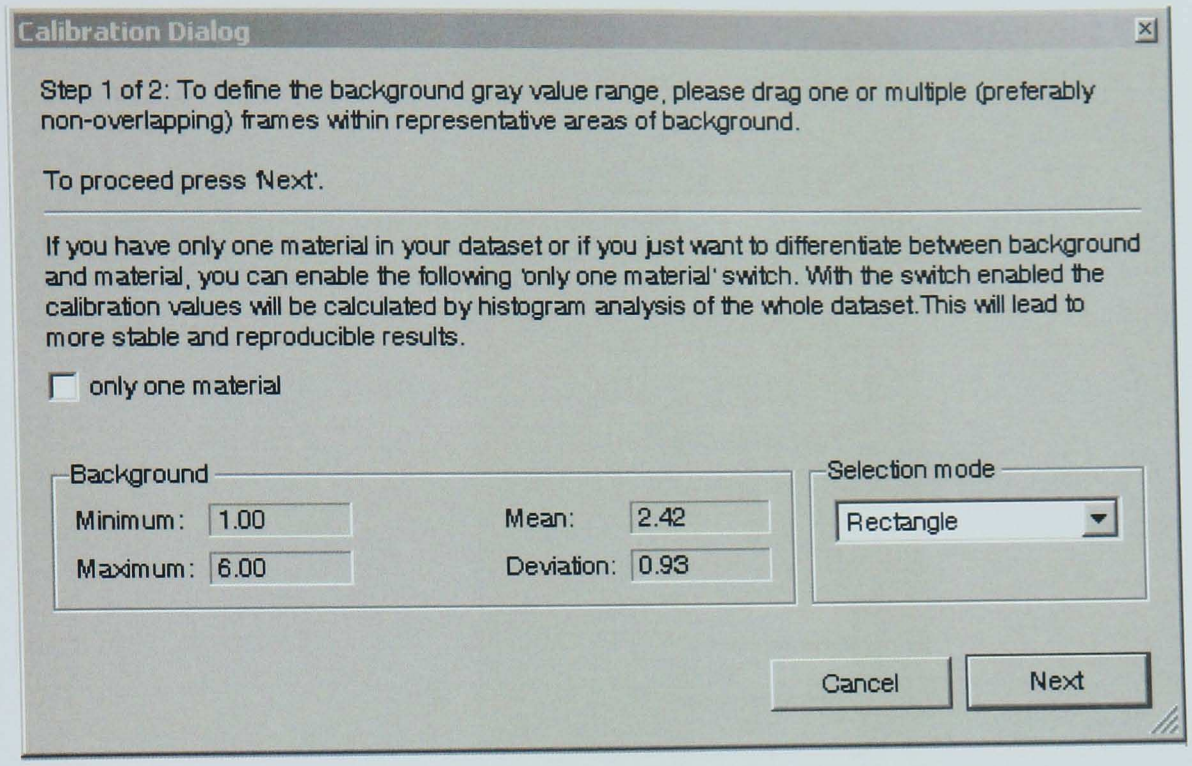

Figure 33 Selection of void parameters

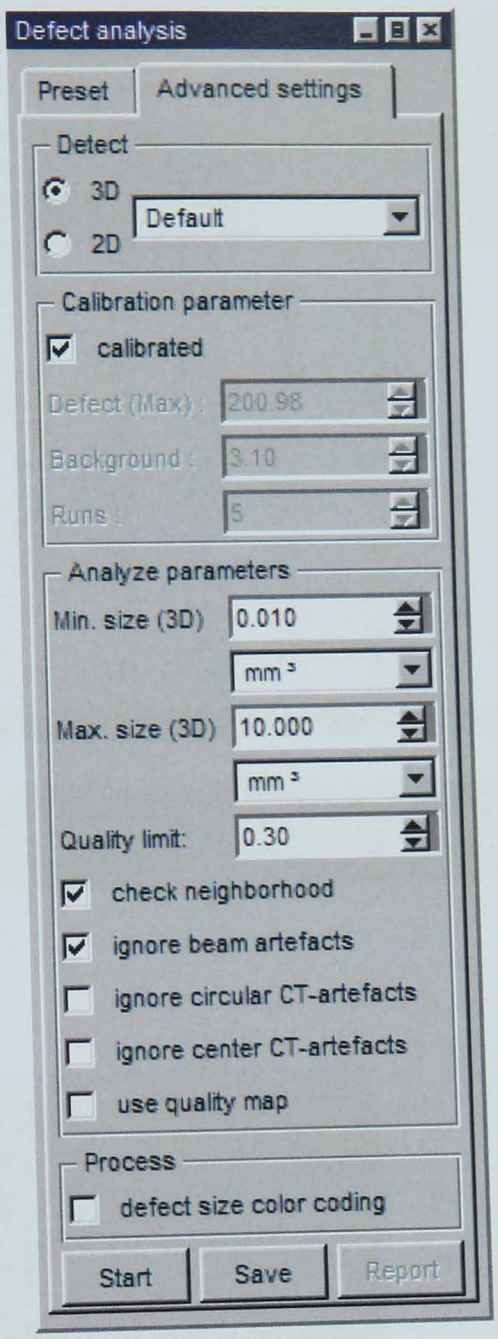

Figure 34 Selecting defects

Defect detection

Title: Test Defect analysis

Subtitle: First approach

22.01.2004

Subtitle: Ceramic (SI3N4) precombustion chamber

Defects | Porosity | Histogram | 3D view A | 3D view B | 3D view C | 3D view D

	ation	quality	surface [mm²]	SX [mm]	SY [mm]	SZ [mm]	PX [mm²]	PY [mm²]	PZ [mm²]	Text	Print slice?	Print slice?	Print slice?
1	2.44	0.75	1.080	0.50	0.40	0.60	0.18	0.19	0.17		☐ xy	☐ xz	☐ yz
2	2.66	0.89	0.720	0.50	0.50	0.30	0.11	0.10	0.15		☐ xy	☐ xz	☐ yz
3	2.88	1.04	2.100	0.70	0.50	1.10	0.32	0.44	0.26		☐ xy	☐ xz	☐ yz
4	3.82	1.83	3.040	0.90	1.10	1.00	0.53	0.46	0.49		☐ xy	☐ xz	☐ yz
5	3.81	1.83	2.200	0.80	0.80	0.60	0.34	0.31	0.43		☐ xy	☐ xz	☐ yz
6	4.48	2.52	3.200	1.10	0.90	0.90	0.47	0.47	0.61		☐ xy	☐ xz	☐ yz
7	4.96	3.09	4.060	1.00	1.10	0.80	0.57	0.55	0.73		☐ xy	☐ xz	☐ yz
8	5.04	3.19	3.000	1.00	0.90	0.70	0.40	0.48	0.56		☐ xy	☐ xz	☐ yz
9	6.12	4.70	2.820	0.80	1.10	0.60	0.37	0.38	0.60		☐ xy	☐ xz	☐ yz
10	6.85	5.89	1.720	0.80	0.60	0.60	0.24	0.32	0.30		☐ xy	☐ xz	☐ yz
11	6.88	5.94	4.200	1.00	1.00	0.80	0.58	0.64	0.83		☐ xy	☐ xz	☐ yz
12	7.99	8.00	2.640	0.90	0.70	0.70	0.42	0.42	0.48		☐ xy	☐ xz	☐ yz
13	8.87	9.88	3.340	0.80	1.00	0.80	0.53	0.51	0.62		☐ xy	☐ xz	☐ yz
14	11.89	17.74	2.480	1.00	0.50	0.70	0.29	0.54	0.41		☐ xy	☐ xz	☐ yz
15	12.89	20.87	3.660	1.10	0.80	0.80	0.52	0.69	0.62		☐ xy	☐ xz	☐ yz
16	27.95	98.02	2.860	0.80	0.80	0.70	0.47	0.44	0.52		☑ xy	☑ xz	☑ yz
17	33.27	135.06	1.440	0.70	0.50	0.40	0.14	0.21	0.32		☑ xy	☑ xz	☑ yz

Close | Remove selection | Save as ... | ☐ print all | Print Report

Figure 35 Output data

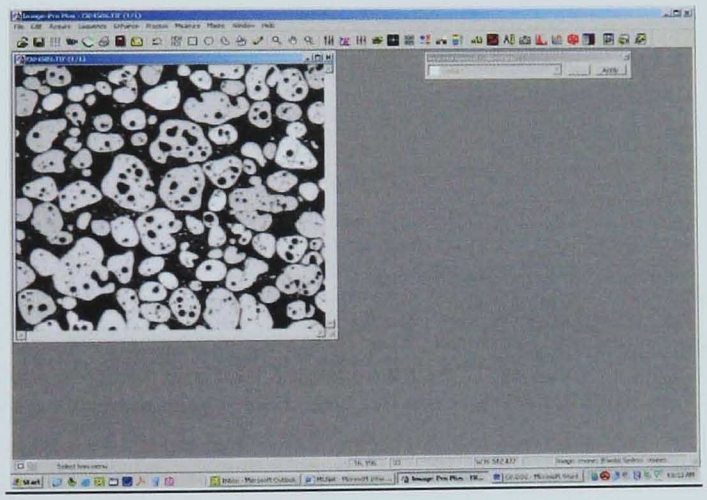

Figure 36 Output data

Appendix A-2

A-2-1 Programming in MATLAB for connectivity from top

```
clear all;
%The following statements will open the first two images for execution
and
%load the data in two matrices k1 and k2
k1 = load(strcat('trial',int2str(1),'.txt'));
k2 = load(strcat('trial',int2str(2),'.txt'));

%initialisation of variables takes place
total_volume =0;
n= k1(1,1);

N = input('enter the no. of images to be executed');

%this FOR loop will execute all the voids of the first image
if N>1
for i = 1:n
%to separate the data in simplified form
x1 = k1(:,1); y1 = k1(:,2);
x2 = k2(:,1); y2 = k2(:,2);
rad1 = k1(:,3); rad2 = k2(:,3);
vol1 = k1(:,4); vol2 = k2(:,4);
m = k2(1,1);
ff =0;z=3;min=100;
for   j=1:m
SI = sqrt(((x1(i+1)-x2(j+1))^2)+((y1(i+1)-y2(j+1))^2));
if SI<min
min = SI;
count = j+1;
end
end

%now the X and Y coordinates are saved in the xcoord and ycoord variables
xcoord = x2(count); ycoord = y2(count);
SImindef = rad1(i+1)+rad2(count)+15;
rad =rad2(count);
if    min<=SImindef
%disp('connectivity has been found in first two images.so can proceed
further');
volume = vol1(i+1)+vol2(count);
while  ff == 0 && z <= N
min=100;
ki = load(strcat('trial',int2str(z),'.txt'));
xreq = ki(:,1);yreq = ki(:,2);
radreq = ki(:,3);volreq = ki(:,4);
m = ki(1,1);
for k =1:m
SI = sqrt(((xcoord-xreq(k+1))^2)+((ycoord-yreq(k+1))^2));
if   SI< min
min = SI;
flag =k+1;
end
end
```

```
add_volume = volreq(flag);
xcoord = xreq(flag);ycoord = yreq(flag);
SImindef = rad+radreq(flag)+15;

if  min <= SImindef
%disp('further connectivity found');
rad =radreq(flag);
ff = 0;
z=z+1;
volume = volume+add_volume;
else
ff = 1;
end
end
total_volume =total_volume+volume;
else
%disp('first two images are not connected');
end
end
fprintf('the total connected volume%f\n',total_volume);
end
```

Programming in MATLAB for connectivity from bottom (opposite side)

```
clear all;
N = input('enter the no. of images to be executed');

%The following statements will open the first two images for execution
and
%load the data in two matrices k1 and k2
k1 = load(strcat('trial',int2str(N),'.txt'));
k2 = load(strcat('trial',int2str(N-1),'.txt'));

%initialisation of variables takes place
total_volume =0;
n= k1(1,1);

%this FOR loop will execute all the voids of the first image
for i = 1:n
x1 = k1(:,1); y1 = k1(:,2);
x2 = k2(:,1); y2 = k2(:,2);
rad1 = k1(:,3); rad2 = k2(:,3);
vol1 = k1(:,4); vol2 = k2(:,4);
m = k2(1,1);
ff =0;z=N-2;min=100;
for   j=1:m
SI = sqrt(((x1(i+1)-x2(j+1))^2)+((y1(i+1)-y2(j+1))^2));
if SI<min
min = SI;
count = j+1;
end
end
%now the X and Y coordinates are saved in the xcoord and ycoord variables
xcoord = x2(count); ycoord = y2(count);
%minimum similarity index is defined
SImindef = rad1(i+1)+rad2(count)+15;
rad =rad2(count);
if    min<=SImindef
volume = vol1(i+1)+vol2(count);
```

```
%disp('found connectivity');

while  ff == 0 && z >0
min=100;
ki = load(strcat('trial',int2str(z),'.txt'));
xreq = ki(:,1);yreq = ki(:,2);
radreq = ki(:,3);volreq = ki(:,4);
m = ki(1,1);
for k =1:m
SI = sqrt(((xcoord-xreq(k+1))^2)+((ycoord-yreq(k+1))^2));
if   SI< min
min = SI;
flag =k+1;
end
end
add_volume = volreq(flag);
xcoord = xreq(flag);ycoord = yreq(flag);
SImindef = rad+radreq(flag)+15;

if  min <= SImindef
% disp('further connectivity found');
%fprintf('the value of SImini:%6.4f\n',min);
%fprintf('the value of SImindefi:%6.4f\n',SImindef);
%fprintf('the value of x coord%6.4f\n',xcoord);
%fprintf('the value of y coord%6.4f\n',ycoord);
rad =radreq(flag);
ff = 0;
z=z-1;
volume = volume+add_volume;
else
ff = 1;
%disp('not connected')
end
end

%fprintf('connected volume%f\n',volume);
total_volume =total_volume+volume;
else
% disp('first two images are not connected');
end
end
fprintf('the total connected volume%f\n',total_volume);
```

A-2-2 An input data sheet of air voids for one slice

X-coordinate (mm)	Y-coordinate (mm)	Max. Radius (mm)	Volume (mm^3)
39.47	48.18	2.45642016	0.283
14.82	63.62	5.567764363	2.1871
62.87	45.94	11.3961397	10.1378
51.67	57.64	4.369897024	1.1064
76.57	52.91	2.889636655	0.4374
41.96	45.69	3.26557805	0.5918
7.35	56.65	2.635147055	0.3345
2.37	8.09	7.472750498	3.8081
5.1	81.05	11.43774453	11.45
60.63	51.42	2.405410568	0.2573
35.23	44.7	6.742996367	3.5508
1.62	34.98	8.295902603	4.9402
44.45	18.8	3.015625972	0.5146
47.93	73.08	8.558270853	5.0689
40.71	47.19	3.983967871	0.7462
72.09	70.59	4.035591654	0.952
47.19	67.35	2.681790447	0.3602
4.11	69.6	3.227382841	0.5661
0.37	67.6	2.431049156	0.3345
63.87	33.74	12.24246707	10.0091
71.84	50.92	2.53929124	0.283
76.07	14.32	3.328362961	0.5918
68.35	68.6	3.770676332	0.8748

References

Al-Omari, A., Masad, E. (2004). "Three dimensional simulation of fluid flow in X-ray CT images of porous media", *International Journal for Numerical and Analytical Methods in Geomechanics,* Vol. 28, pp. 1327–1360.

Amit Bhasin, (2006). "Development of methods to quantify bitumen-aggregate adhesion and loss of adhesion due to water", Phd thesis , Texas A &M University Uinted State.

Artamendi, I., and H. Khalid, (2005). "Characterization of fatigue damage for paving asphaltic materials", *Journal of fatigue and fracture of Engineering materials and structures,* Vol. 28, pp. 1113-1118.

Arambula, E., Eyad, Masad and Amy Epps Martin, (2007). "Moisture susceptibility of asphalt mixtures with known field performance: evaluated with dynamic analysis and crack growth model" *TRB Report*, pp. 20-28

Bodin Didier, Gilles Pijaudier-Cabot, Chantal de La Roche, Jean-Michel Piau and Armelle Chabot, (2004). "Continuum damage approach to asphalt concrete fatigue modeling", *Journal of Engineering mechanics*", Vol. 130, pp. 700-708.

Braz, D., Laura, M. and Ricardo, T. L. (1999). "Computed tomography in the fatigue test analysis of an asphaltic mixtures", *Journal of Applied Radiation and Isotopes,* Vol. 50.

Caro, S., E. Masad, A.Bhasin and D.N. Little, (2008). "Moisture susceptibility of asphalt mixtures, Part 1: mechanisms", *International Journal of pavement Engineering*, Vol. 9, pp.81-98.

Collop, AC. (1996). Lecture Notes, University of Nottingham.

Collop, A.C., Scarpas, A. T. , Kasbergen, C. and Bondt, A. (2003). "Development and finite element implementation of a stress dependent elasto-visco-plastic constitutive model with damage for asphalt", *Transportation Research Board 82nd Annual Meeting National Research Council*, Washington, D.C.

Collop, A.C., Choi,Y.K, Aiery,G.D. (2007). "Effect of pressure and ageing in SATS test", *ASCE Journal of Transportation Engineering*, pp. 618-624.

Collop, A.C., Choi, Y.K, Airey, G.D, Elliot, R.C. (2004). "Development of the saturation aging tensile stiffness (SATS) test" *Journal of Transport*, pp. 163-171.

Daigle, M., D.Frata and L.B. Wang, (2005). " Ultrasonic and X ray tomography imaging of high contrasting inclusion in concrete specimens", *Geo Frontier conference*, Texas.

Di Benedetto, H., C.de La Roche, H. Baaj, A Pronk and R. Lundstrom, (2004). "Fatigue of bituminous mixtures", *Journal of materials and structures* Vol. 37, pp. 202-216.

Dunhill, Stuart, (2002). "Quasi-static characterization of asphalt mixtures", PhD thesis University of Nottingham.

Dunhill, S., Airy, G., Collop, A. C. and Scarpas, A. (2006). "Advanced constitutive modeling of bituminous materials" *International Journal of pavement Engineering.*

Dailgle, M., Fratta, D. Wang, L.B. (2005). "Ultrasonic and X-ray tomography imaging of highly contrasting inclusion in concrete specimen" *Geofrontier conference. Austin, TX.*

Gross, D., Seeling T. (2006). "Fracture mechanics with an introduction to micromechanics".

Gregory, H. (2009). Detection of permeability and moisture damage in asphalt using X ray computer tomography, M. Eng. thesis , University of Nottingham.

Hunter, Robert, N. (2003). "The shell bitumen Handbook", fifth edition, Shell bitumen UK.

Huang, Y. H. (2004). "Pavement analysis and design" (Second edition). Prentice Hall, New Jersey, USA.

Kaseem, E., Lubinda W., Tom,S., Eyad M.,Andrew,W. (2008). "Evaluation of full depth asphalt pavement construction using X ray computed tomography and ground penetration radar." *Journal of performance of constructed facilities,* Vol. 22, pp. 408-416.

Kose, S., Guler, M., Bahia, H. U. and Masad, E. (2000). "Distribution of strains within hot-mix asphalt binders." *Transportation Research Record 1391*, Transportation Research Board, Washington, D.C., pp. 21–27.

Kibuuka, Ronald, (2007). "Surface energy measurement of bitumen and mastics", M.Sc. thesis, university of Nottingham.

Kim, Y. R., Lee, H. and Little, D. (1997). "Fatigue characterization of asphalt concrete using viscoelasticity and continuum damage theory." *Association of Asphalt Paving Technologists*, Vol. 66, pp. 520-569.

Kim Richard.Y, (2009). " Modeling of Asphalt Concrete" McGraw-Hill.

Khaleel, M. A., Zbib, H. M., and Nyberg, E. A. (2001). "Constitutive modeling of deformation and damage in superplastic materials." *International Journal of Plasticity*, Vol. 17, pp. 277-296.

Kose, S., Guler, M., Bahia, H. and Masad, E. (2000). "Distribution of strains within binders in HMA using imaging and finite element techniques." Transp. Res. Rec. 1728, *Transportation Research Board,* Washington, D.C., pp. 21–27.

Landis, E. and Keane, D. (1999). "X-ray micro-tomography for fracture studies in cement-based materials." *International Society of Optical Engineering*, pp. 105-113 cited in Tashman (2003).

Lee, H. and Y. Richard Kim, (1998). "Viscoelastic constitutive model for asphalt concrete under cyclic loading", *Journal of Engineering mechanics*, Vol. 124, pp.32-39.

Lee, H., Daniel, J. S. and Kim, Y. R. (2000). "Continuum damage mechanics-based fatigue model of asphalt concrete." *Journal of Materials in Civil Engineering*, Vol. 12(2), pp. 104-113.

Little, D., Lytton, R., Williams, D. and Kim, Y. R. (1999). "An analysis of the mechanism of microdamage healing based on the application of micromechanics first principles of fracture and healing." *Journal of Association of Asphalt Paving Technologists*, Vol. 68, pp. 501-542.

Lytton, R. L., Uzan, J., Fernando, E.G., Roque, R., Hiltmen, D., and Stoffesl, S. (1993). "Development and validation of performance of performance predication model and specifications for asphalt binders and paving mixtures", *SHARP A-357*, Strategic highway research program, Washington D. C.

Lytton, R. L. (2000). "Characterizing Asphalt Pavements Performance" *Transportation Research Record, 1767,* Transportation Research Board, Washington D. C., pp. 5-16.

Maire, E. , Babout, L. , Buffiere, J. Y. , and Fougeres, R. (2001). "Recent results on 3D characterization of microstructure and damage of metal matrix composites and a metallic foam using X-ray tomography." *Journal of Materials Science and Engineering*, A319-321, pp. 216-219 cited in Tashman (2003).

Masad, E., Muhunthan, B., Shashidhar, N. and Harman, T. (1999). "Internal structure characterization of asphalt concrete using image analysis." *ASCE Journal of Computing in Civil Engineering (Special Issue on Image Processing)*, Vol. 13(2).

Masad, E., Hussain, U. B. and Sadi, K. (2001). "Modeling and experimental measurements of Strain distribution in asphalt mixes" *Journal of Transportation Engineering*, Vol. 127 (6).

Masad, E., Niranjanan, S., Hussain U. B., and Sadi, K. (2002). "Modeling and experimental measurement of strain distribution in asphalt mixes" *Journal of transportation Engineering* Vol.127 (6).

Masad, E. (2006). "Thermo-mechanical framework for the constitutive modeling of the asphalt concrete" *International journal of geomechanics.*

Masad, E.,V.T.F. Castelo Branco, D.N. Little and R. Lytton,(2007). "A unified method for the analysis of controlled strain and controlled stress fatigue testing", *International Journal of pavement engineering,* Vol. 9, pp. 233-246.

Mummery, P. M., Derby, B., Anderson, P., Davis, G. and Elliott, J. C. (1993). "X-ray microtomography of damage in particle-reinforced metal matrix composites." *Journal De Physique*, Vol. 3, pp. 1857-1860 cited in Tashman (2003).

Nelson, H. G., Charles, W. S., Richard, A. S. and Mattew, W.W. (2003). "Viscoelastic, Viscoplastic, and Damage Modeling of Asphalt Concrete in Unconfined Compression" Transp. Res. Rec.1860, *Transportation Research Board,* Washington, D.C.,

Nicholls, J.C, Elliot, R.C, Grenfell, J, Airey, G.D, Collop, A.C. (2009). "Assessment of Asphalt Duribility Test part 1, Widening the applicability of the SATS Test (accepted for publication).

Papagiannakis, A. T., Abbas, A. and Masad, E. (2002). "Modeling the viscoelastic behavior of asphalt concretes". *Journal of the Transportation Research Board*, Record No. 1789.

Park, S. W., Kim, Y. R., and Schapery, R. A. (1996). "A viscoelastic continuum damage model and its application to uniaxial behavior of asphalt concrete." *Mechanics of Materials*, Vol. 24, pp. 241-255.

Richard, A. Ketcham, William, D Carlson. (2001). "Acquisition, optimization and interpretation of X ray computed tomographic imagery: application to the geosciences". *Journal of computers and geosciences* Vol. 27, pp. 381-400.

Ramachandran, G. N. and A. V. Lakshminarayanan. (1971). "Three dimensional reconstruction from radiographs and electron micrographs: application of convolutions instead of Fourier Transforms". *Proceedings of the national academy of science* Vol.68, pp. 2236-2240.

Russ, John C. (1999). "Practical Stereology" 2nd Edition Published by Plenum Press, New York, NY

Perzyna, P. (1984). "Constitutive modeling of dissipative solids for post critical behaviour and fracture." *Journal of Engineering Materials and Technology*, ASME, Vol. 106, pp. 410-419 cited in Tashman (2003).

Scarpas, A., Khoury- Al, R., Gurp, C.A. and Erkens, S.M. (1997). "Finite element simulation of damage development in asphalt concrete pavements." *8th international conference on asphalt pavements*, Vol. 01, pp. 673-692 cited in Staurt (2002).

Si, Zhiming, D.N.Little and R.L. Lytton, (2002), "Characterization of microdamage and healing of asphalt concrete mixtures", *Journal of Materials in Civil Engineering*, vol. 14, pp. 461-470

Shi, B., Murakami, Y., Wu, Z., Chen, J., and Inyang, H. (1999). "Monitoring of internal failure evolution in soils using computerization X-ray tomography." *Journal of Engineering Geology*, Vol. 54, pp. 321-328 cited in Tashman (2003).

Sinclair, I., Khor, K. H., Ludwig, W., Toda, H., Ubhi, H. S., Gregson, P. J. (2004). "In situ high resolution synchrotron X-ray tomography of fatigue crack closure micro mechanisms" *Journal of physics, condensed materials* Vol. 16.

Song, I. (2004). "Damage analysis in asphalt concrete mixtures based on parameter relationships" PhD thesis Texas A& M university.

Staurt, T. D. (2002). "Quasi-Static characteristic of asphalt mixtures" PhD thesis, Nottingham university.

Synolakis, C. E., Zhou, Z., and Leahy, R. M. (1996). "Determination of internal deformation field in asphalt cores using X-ray computer tomography." *Transportation Research Record 1526*, Transportation Research Board, Washington, D.C., pp. 135-141.

Tada H., Paris P.C., Irwin G. (2000). "The stress analysis of cracks handbook" 3rd Edition.

Tashman, L., Masad, E., Peterson, B., Habeeb, S. (2002). "Internal structure analysis of asphalt mixes to improve the simulation of superpave gyratory compaction to field conditions." *Journal of the association of asphalt paving technologists*, Vol. 70, pp. 605-645.

Tashman, L. (2003). "Microstructural viscoplastic continuum model for asphalt concrete" PhD thesis, Texas A&M University.

Tashman, L., Masad, E., Dallas, L., Hussein, Z. (2005). "A microstructure-based viscoplastic model for asphalt concrete". *International Journal of Plasticity* Vol. 21 pp. 1659–1685.

Tashman, L., L.B. Wang, and S. thyagarajan. (2007). "Microstructure characterization for modeling HMA behavior using imaging technology", *Journal of road materials and pavement design*, Vol.21, pp. 338-348.

Townend, R, (2005). "An investigation in to X ray Computed Tomography and its Application into the Damage Evolution of Dense Bitumen Macadam"

Van Der Poel, C. (1954). "A general system describing the visco-elastic properties of bitumen and its relation to routine test data" *Journal of applied chemistry* Vol. 4 cited in Song (2004).

Vallerga, B.A, (1982). "Pavement deficiencies related to asphalt durability". *Proceeding of the association of Asphalt Paving technologists*, pp. 481-491.

Voyiadjis,G.Z , Amin, H. (2007). "Experimental study and fabric tensor quantification of micro crack distributions in composite materials" *Journal of Composite Materials,* Vol. 41(6).

Walubita, Lubinda, F., Amy Epps Martine, Gregory S. Cleveland and Robert L. Lytton, (2006) "Computation of pseudo strain energy and Paris law fracture coefficient from surface energy and uniaxial strain controlled tension test data", *International journal of pavement engineering* , Vol. 7, pp. 167-178.

Wang, L.B. Frost, J.D. and Shashidhar, N. (2001). "Microstructure study of wes track mixes from X-ray tomography images",*TRR No. 1767*, pp. 85–94.

Wang, L.B., J.D. Frost, G.Z Voyiadjis and T.P. Harman, (2003). "Quantification of damage parameters using X ray tomography images", *Journal of mechanics of materials,* Vol. 35, pp.777-790.

Wang, L. B., Frost, J. D. and Lai, S. (2004). "Three dimensional digital representation of granular material microstructure from X ray tomography imaging". *Journal of computing in civil engineering*, Vol. 28(1), pp. 28-35.

Wang, L.B., H.S.Paul, T. Harman and J.d Anglo, (2004). "Characterization of aggregate and asphalt concrete using X ray tompgraphy", *AAPT*, Vol. 73, pp. 467-500.

Wen, Hafiang, (2001). "Fatigue performance evaluation of wes track asphalt mixtures based on viscoelastic analysis of indirect tensile test" M.Sc. thesis University of North Carolina USA.

Witezak, M.W. , Bonaquist, R. , Quintus, V. H. and Kaloush, K. (2000). "Specimen geometry and aggregate size effect in uniaxial compression and constant height shear test", *Association of Asphalt paving Technologists*, Vol. 69, pp. 733-793.

Wolf, P.R. and Ghilani, C. D. (2002). "Elementary surveying (Introduction to Geomatics)", 10th Edition, Prentice Hall, New Jersey.

Wang, Y. (2002). "Quantification of the spatial gradient of local volume fraction from tomography images". M.Sc. thesis Washington state university.

X Tek, (2005), "IMPS III operational manual", X Tek industries limited, UK.

Youngguk seo and Y. Richard Kim, (2008). "Using acoustic emission to monitor fatigue damage and healing in asphalt", *KSCE Journal of Civil Engineering*, Vol. 12, pp.237-243.